



HAL
open science

Modeling fibrous composite reinforcements and metamaterials: Theoretical development and engineering applications

Gabriele Barbagallo

► **To cite this version:**

Gabriele Barbagallo. Modeling fibrous composite reinforcements and metamaterials: Theoretical development and engineering applications. Materials. Université de Lyon, 2017. English. NNT : 2017LYSEI098 . tel-02068235

HAL Id: tel-02068235

<https://theses.hal.science/tel-02068235>

Submitted on 14 Mar 2019

HAL is a multi-disciplinary open access archive for the deposit and dissemination of scientific research documents, whether they are published or not. The documents may come from teaching and research institutions in France or abroad, or from public or private research centers.

L'archive ouverte pluridisciplinaire **HAL**, est destinée au dépôt et à la diffusion de documents scientifiques de niveau recherche, publiés ou non, émanant des établissements d'enseignement et de recherche français ou étrangers, des laboratoires publics ou privés.



N° D'ORDRE NNT : 2017LYSEI098

ANNÉE 2017

THÈSE DE DOCTORAT DE L'UNIVERSITÉ DE LYON

OPÉRÉE AU SEIN DE

INSA-Lyon

ECOLE DOCTORALE MÉCANIQUE, ENERGÉTIQUE, GÉNIE CIVIL, ACOUSTIQUE (MEGA)

SPÉCIALITÉ: MÉCANIQUE DES SOLIDES, DES MATÉRIAUX DES STRUCTURES ET DES SURFACES

SOUTENUE PUBLIQUEMENT LE 19/10/2017 PAR

Gabriele Barbagallo

Modeling fibrous composite reinforcements and metamaterials: theoretical development and engineering applications

Devant le jury composé de :

BOISSE Philippe	Professeur des Universités	INSA-Lyon	Examineur
CUOMO Massimo	Professeur des Universités	University of Catania	Rapporteur
DAOUADJI Ali	Professeur des Universités	INSA-Lyon	Invité
LOMBARD Bruno	Chargé de Recherche, HDR	Aix-Marseille Univ, CNRS	Rapporteur
MADEO Angela	Professeur des Universités	INSA-Lyon	Directrice de thèse
MORESTIN Fabrice	Professeur des Universités	INSA-Lyon	Directeur de thèse
NEFF Patrizio	Professeur des Universités	Universität Duisburg-Essen	Examineur

LaMCoS & SMS-ID, INSA-Lyon 20 avenue Albert Einstein, F-69621, Villeurbanne CEDEX – France

Département FEDORA – INSA Lyon - Ecoles Doctorales – Quinquennal 2016-2020

SIGLE	ECOLE DOCTORALE	NOM ET COORDONNEES DU RESPONSABLE
CHIMIE	CHIMIE DE LYON http://www.edchimie-lyon.fr Sec : Renée EL MELHEM Bat Blaise Pascal 3 ^e étage secretariat@edchimie-lyon.fr Insa : R. GOURDON	M. Stéphane DANIELE Institut de Recherches sur la Catalyse et l'Environnement de Lyon IRCELYON-UMR 5256 Équipe CDFA 2 avenue Albert Einstein 69626 Villeurbanne cedex directeur@edchimie-lyon.fr
E.E.A.	ELECTRONIQUE, ELECTROTECHNIQUE, AUTOMATIQUE http://edeea.ec-lyon.fr Sec : M.C. HAVGOUDOUKIAN Ecole-Doctorale.eea@ec-lyon.fr	M. Gérard SCORLETTI Ecole Centrale de Lyon 36 avenue Guy de Collongue 69134 ECULLY Tél : 04.72.18 60.97 Fax : 04 78 43 37 17 Gerard.scorletti@ec-lyon.fr
E2M2	EVOLUTION, ECOSYSTEME, MICROBIOLOGIE, MODELISATION http://e2m2.universite-lyon.fr Sec : Sylvie ROBERJOT Bât Atrium - UCB Lyon 1 04.72.44.83.62 Insa : H. CHARLES secretariat.e2m2@univ-lyon1.fr	M. Fabrice CORDEY CNRS UMR 5276 Lab. de géologie de Lyon Université Claude Bernard Lyon 1 Bât Géode 2 rue Raphaël Dubois 69622 VILLEURBANNE Cédex Tél : 06.07.53.89.13 cordev@univ-lyon1.fr
EDISS	INTERDISCIPLINAIRE SCIENCES-SANTE http://www.ediss-lyon.fr Sec : Sylvie ROBERJOT Bât Atrium - UCB Lyon 1 04.72.44.83.62 Insa : M. LAGARDE secretariat.ediss@univ-lyon1.fr	Mme Emmanuelle CANET-SOULAS INSERM U1060, CarMeN lab, Univ. Lyon 1 Bâtiment IMBL 11 avenue Jean Capelle INSA de Lyon 696621 Villeurbanne Tél : 04.72.68.49.09 Fax :04 72 68 49 16 Emmanuelle.canet@univ-lyon1.fr
INFOMATHS	INFORMATIQUE ET MATHEMATIQUES http://infomaths.univ-lyon1.fr Sec :Renée EL MELHEM Bat Blaise Pascal, 3 ^e étage Tél : 04.72. 43. 80. 46 Fax : 04.72.43.16.87 infomaths@univ-lyon1.fr	M. Luca ZAMBONI Bâtiment Braconnier 43 Boulevard du 11 novembre 1918 69622 VILLEURBANNE Cedex Tél :04 26 23 45 52 zamboni@maths.univ-lyon1.fr
Matériaux	MATERIAUX DE LYON http://ed34.universite-lyon.fr Sec : Marion COMBE Tél:04-72-43-71-70 –Fax : 87.12 Bat. Direction ed.materiaux@insa-lyon.fr	M. Jean-Yves BUFFIERE INSA de Lyon MATEIS Bâtiment Saint Exupéry 7 avenue Jean Capelle 69621 VILLEURBANNE Cedex Tél : 04.72.43 71.70 Fax 04 72 43 85 28 Ed.materiaux@insa-lyon.fr
MEGA	MECANIQUE,ENERGETIQUE,GENIE CIVIL,ACOUSTIQUE http://mega.universite-lyon.fr Sec : Marion COMBE Tél:04-72-43-71-70 –Fax : 87.12 Bat. Direction mega@insa-lyon.fr	M. Philippe BOISSE INSA de Lyon Laboratoire LAMCOS Bâtiment Jacquard 25 bis avenue Jean Capelle 69621 VILLEURBANNE Cedex Tél : 04.72 .43.71.70 Fax : 04 72 43 72 37 Philippe.boisse@insa-lyon.fr
ScSo	ScSo* http://recherche.univ-lyon2.fr/scso/ Sec : Viviane POLSINELLI Brigitte DUBOIS Insa : J.Y. TOUSSAINT Tél : 04 78 69 72 76 viviane.polsinelli@univ-lyon2.fr	M. Christian MONTES Université Lyon 2 86 rue Pasteur 69365 LYON Cedex 07 Christian.montes@univ-lyon2.fr

*ScSo : Histoire, Géographie, Aménagement, Urbanisme, Archéologie, Science politique, Sociologie, Anthropologie

Acknowledgments

Firstly, I would like to express my sincere gratitude to my supervisors Prof. Angela Madeo and Prof. Fabrice Morestin. In particular, Angela continuously supported me during my Ph.D study and related research with her patience, motivation and knowledge. Her guidance helped me during all my time in Lyon and I am very thankful to have had her supervise my Ph.D study. I know I am not always the easiest person to work with, thank you for sticking with me!

Besides my supervisors, I would like to thank Prof. Neff and Prof. Boisse for having inspired me during my Ph.D to step up my work from a theoretical, practical and sometimes even philosophical point of view. I really hope that Prof. Neff will be able to forgive me the new notation in this manuscript. I also have to thank Prof. Cuomo for having directed me through my master thesis to this Ph.D program and to research in general and for having accepted to be a part of this accomplishment by reviewing this manuscript. A special thank goes also to the SMS-ID lab at INSA-Lyon, its director Prof. Daouadji and the university staff (both academic and support staff) for creating an environment in which my research effort could thrive. My sincere thanks also go to the rest of my doctoral commission: Dr. Lombard, for his paramount role of reviewer, and Prof. Belouettar, for honoring us with his presence.

Furthermore, I have to acknowledge Marco and Alexis, with whom I lived my doctoral life in Lyon, for their friendship and support. Thank you, Alexis, for sharing my interest in *random facts* and for your invaluable help in the correction of this manuscript: the result would have not been the same without you. Thank you, Marco, for having shared with me both difficulties and successes during these three years of our shared life at INSA. A special thanks goes also to FranÃ§ois, whose wisdom and guidance helped me through the bureaucratic nightmare that is a Ph.D. at INSA.

I want to thank all of my friends, both new and old, from both foreign and familiar places, for sharing parts of your lives with me: I am a much better person for it. I have a list of marvelous people I should mention, but this *margin* is too narrow to contain it. Please know that, no matter what I accomplish, my life would be empty without you in it.

Last but not the least, I would like to thank my *family*: my parents, my brother and my sister for supporting me spiritually, emotionally and intellectually since long before I ever thought about joining this Ph.D. program. There is nothing in life as important as the love of your family.

I promise to never forget the part that you all had in this. This thesis would not have been ever written without you!

Abstract

The microstructure of materials is becoming an increasingly essential tool for the optimization of the mechanical properties of structures, however, the transition to a continuous description often leads to a too drastic simplification of reality and a significant loss of information rendering the optimization efforts useless. Nowadays, the developments of continuum mechanics, of the computational tools and of the experimental techniques make it possible to account for scale-effects observed in mechanics of materials and structures. The primary goal of this thesis is to integrate the effects of a complex microstructure, as well as the associated characteristic lengths, in a continuous framework. Therefore, enriched continuous models have been used to describe in detail the mechanical behavior of woven composite reinforcements and metamaterials. Within the framework of this thesis, numerical simulations have been developed using the software COMSOL Multiphysics and Mathematica to show the importance of the terms added for the correct description of the mechanical behavior of these materials.

There are several approaches that take into account the effects of micro-structure on the macroscopic behavior of materials, that can be divided in the two following categories:

- description of the behavior at the macroscopic scale starting from considerations at the microscopic scale;
- direct description of the macroscopic behavior indirectly taking into account the presence of a micro-structure.

There is an abundant literature based on the first point of view: obtaining the homogenized properties of the mechanical behavior of complex materials on a macroscopic scale from a detailed description of their microscopic properties. However, we must also mention the limits of this type of micro-macro approaches, most of which are related to the simplifying hypotheses necessary for the description of the microstructure. The second type of approach starts directly from the description at the macroscopic scale, by developing models capable of describing the average behavior of the material with a relatively limited set of parameters. The fundamental advantage of this type of approach lies in the possibility of describing the behavior of the microstructured material via the introduction, on a macroscopic scale, of this restricted number of parameters. Theories of enriched continuous media belong to the second class of the models cited. In this work, we tried to analyze the situations in which their use brings obvious advantages.

Within the framework of enriched continuous theories, the systematic use of a so-called Cauchy theory sometimes leads to an oversimplification of reality. Indeed, certain characteristics of the microstructure are implicitly neglected in these approaches. However, even if all the materials are heterogeneous on a sufficiently small scale and therefore possess a microstructure, this does not necessarily induce a specific behavior on a macroscopic scale. In this case, the Cauchy theory would be perfectly adapted to their description. On the other hand, other materials possess microstructures on a large-enough scale (micron, millimeter, centimeter), whose effects have repercussions on macroscopic behavior. The Cauchy model is then insufficient to describe their specific global behavior related to what occurs at smaller scales, e.g. concentration of forces or deformations, or strong local gradients.

One of the most promising fields of application of enriched continuous theories concerns the study of the mechanical behavior of woven composite reinforcements. This class of materials, made up by weaving yarns (made up themselves of many thinner fibers), possess very different rigidities in tension and in shear: the yarns are very stiff in tension but the angle between two yarns can vary very easily. This very marked contrast of material mechanical properties makes it necessary to describe its homogenized properties within the framework of a second gradient theory (or a constrained micromorphic one). The macroscopic manifestation of the meso-structure can indeed play a major role for composite reinforcements, since these reinforcements are forced to take very complex geometries during the forming process. It is mainly for this reason that a theory of enriched continuous media becomes an important tool for their macroscopic modeling.

In the case of woven composite reinforcements of textile composites, enriched models are suitable to integrate the effect of the bending of the yarns at the mesoscopic level in the continuous modeling. This has been demonstrated in the case of the bias extension test and the deep drawing of a composite 2.5D interlock. For the bias extension test, the second gradient terms allow for the description of certain boundary layers, i.e. transition zone between two regions with constant shear angle, and also asymmetric effects in the case of unbalanced reinforcements. Concerning the deep drawing of composite interlocks, it has been shown that second gradient terms are necessary to correctly describe the onset of wrinkling. In the two examples discussed, the effect of mesoscopic bending of the yarns is the main mechanism giving rise to effects that are not included in conventional models. The same line of reasoning could be followed for composites consisting of fibrous reinforcements in a soft matrix. In this case, the theories of enriched continuous media would be applied to the whole material: fibrous reinforcement + soft matrix.

Cauchy models are also not well-suited for the description of the dynamic response of certain microstructured materials showing dispersive behaviors or band-gaps. Enriched continuous theories (and in particular the relaxed micromorphic model) can be good candidates for modeling these materials in a more precise and realistic way, since they can include the macroscopic manifestation of their microstructure. In the current state of knowledge and technology, it is interesting to focus efforts on the design of microstructured materials that may have original properties, to improve and optimize the responses of the structures that use them. Indeed, these structures are designed using such microstructured materials - also known as metamaterials - to exhibit improved strengths, shaping facilities, minimized weights, and much more. They can also possess innovative properties in the field of vibration control or in the field of stealth technology. In particular, some microstructures possess very specific properties with respect to wave propagation, which give the resulting structures possible applications as a screen or a wave absorber. The new concept of metamaterials is attracting more and more physicists and mechanics. These materials are obtained by the optimal assembly of several individual elements arranged in periodic or quasi-periodic substructures, which makes it possible to obtain very original properties. Indeed, the shape, geometry, dimensions, contrast of the mechanical properties, orientation and arrangement of these elements can influence, for example, the propagation of waves in a way impossible in classical materials. The properties thus created can certainly lead to innovative applications in engineering.

Recent papers provided the evidence that the relaxed micromorphic model, even when restricted to the isotropic case, is usable to characterize the mechanical behavior of band-gap metamaterials, i.e. microstructured materials which are able to “stop” the propagation of elastic waves due to local resonances at the level of the microstructure. The enormous advantage of using the relaxed micromorphic model for the description of such metamaterials is undoubtedly that of mastering the behavior of complex media via the introduction of few elastic coefficients (Young modulus, Poisson ratio and few extra microstructure-related homogenized coefficients). This simplified modeling of metamaterials allows for the conception of “metastructures”, i.e. structures which are made up of metamaterials as basic building blocks and which preserve their unconventional behavior at the scale of the structure (i.e. wave absorption).

Keywords: enriched continua, relaxed micromorphic model, second gradient theories, woven fibrous composite reinforcements, metamaterials, phononic band-gaps, bias extension test, deep drawing of composite interlocks.

La microstructure des matériaux est un levier essentiel pour l'optimisation des propriétés mécaniques des structures. Le passage à la description continue de la matière conduit souvent à une simplification trop drastique de la réalité et à une perte significative d'informations. Les développements de la mécanique des milieux continus, des moyens de calcul numérique et des techniques expérimentales permettent aujourd'hui de rendre compte des effets d'échelle observés en mécanique des matériaux et des structures. Le but primaire de cette thèse a été celui de développer des modèles continus pour intégrer dans la modélisation continue les effets d'une morphologie complexe des microstructures ainsi que les longueurs caractéristiques associées. Ces modèles continus enrichis ont ensuite été utilisés pour décrire en détail le comportement mécanique des renforts de composites textiles et des metamatériaux. Des simulations numériques qui montrent l'importance des termes ajoutés pour la correcte description du comportement mécanique de ces matériaux ont été développées dans le cadre de cette thèse à l'aide des logiciels COMSOL Multiphysics et Mathematica.

Il existe plusieurs approches qui prennent en compte les effets de la micro-structure sur le comportement macroscopique des matériaux, elles appartiennent à l'une des catégories suivantes :

- description du comportement à l'échelle macroscopique à partir d'une description de celui-ci à l'échelle microscopique,
- description directe du comportement macroscopique tenant indirectement compte de la présence d'une micro-structure.

Il existe une littérature abondante qui se fonde sur le premier point de vue : obtenir les propriétés homogénéisées du comportement mécanique des matériaux complexes à l'échelle macroscopique en partant d'une description détaillée de leurs propriétés microscopiques. Cependant, on doit aussi mentionner les limites de ce type d'approches micro-macro, limites pour la plupart liées aux hypothèses simplificatrices nécessaires pour la description de la microstructure. Le deuxième type d'approche possible consiste à partir directement de la description à l'échelle macroscopique en développant des modèles capables de décrire le comportement moyen du matériau par un ensemble relativement limité de paramètres. L'avantage fondamental de ce type d'approche réside dans la possibilité de décrire le comportement du matériau microstructuré à partir de l'introduction, à l'échelle macroscopique, de ce nombre restreint de paramètres, ce qui est d'un grand intérêt pour les sciences de l'ingénieur. Les théories des milieux continus enrichis appartiennent à la deuxième classe des modèles cités. On essaiera d'analyser dans ce travail les situations dans lesquelles leur utilisation permet d'apporter des avantages évidents.

Dans le cadre des théories des milieux continus enrichis, l'utilisation systématique d'une théorie dite de Cauchy conduit souvent à des simplifications trop fortes de la réalité. En effet, certaines caractéristiques de la microstructure sont implicitement négligées dans ces approches. Cependant, même si tous les matériaux sont hétérogènes à une échelle suffisamment petite et possèdent donc une microstructure, celle-ci n'induit pas forcément un comportement spécifique à une échelle macroscopique. Dans ce cas, la théorie de Cauchy sera parfaitement adaptée à leur description. En revanche, d'autres matériaux possèdent des microstructures à une échelle beaucoup plus grande (micron, millimètre, centimètre), dont l'effet se répercute sur le comportement macroscopique. Le modèle de Cauchy est alors insuffisant pour décrire leur comportement global spécifique, lié par exemple à la concentration d'efforts ou de déformations, ou encore à des modes de déformations particuliers caractérisés par de forts gradients locaux induisant des comportements eux-mêmes liés à ce qui se passe à des échelles plus petites.

Un des domaines d'application les plus prometteurs des théories de milieux continus enrichis concerne l'étude du comportement mécanique des renforts tissés de composites. Cette classe de metamatériaux est en effet constituée par le tissage de mèches (constituées de nombreuses fibres plus fines), dont les rigidités sont très différentes en traction et en cisaillement : les mèches sont très raides en traction mais l'angle

entre deux mèches peut varier très facilement. Ce contraste très marqué des propriétés mécaniques de la meso-structure du matériau permet de décrire ses propriétés homogénéisées dans le cadre d'une théorie de deuxième gradient. La manifestation macroscopique de la meso-structure peut en effet jouer un rôle majeur lors de la mise en forme des renforts de composites puisque ces renforts sont contraints de prendre des formes très particulières pour permettre la réalisation d'éléments structuraux de géométrie complexe. C'est pour cette raison, principalement, qu'une théorie de milieux continus enrichis devient un outil important pour la modélisation.

Dans le cas des renforts de composites textiles, il a été montré que des modèles enrichis sont nécessaires pour intégrer dans la modélisation continue l'effet de la flexion des mèches au niveau mesoscopique. Ceci a été mis en évidence pour le cas du "bias extension test" et de l'emboutissage emisphérique d'un interlock 2.5D de composite. Pour le cas du "bias extension test" les termes de deuxième gradient permettent la description de certaines couches limites qui déterminent une zone de transition entre deux régions à angle de cisaillement constant et aussi des effets asymétriques dans le cas des renforts déséquilibrés. Pour ce qui concerne l'emboutissage des interlocks de composite, il a été montré que les termes de deuxième gradient sont nécessaires pour décrire correctement la formation des plis. Dans les deux exemples traités, l'effet de la flexion des mèches à l'échelle mesoscopique est le mécanisme principal donnant lieu aux effets qui ne sont pas descriptibles avec des modèles classiques. Des raisonnements du même type que ceux exposés jusqu'ici peuvent être formulés pour les composites constitués par des renforts fibreux englobés dans une matrice molle. Dans ce cas, les théories de milieux continus enrichis s'appliquent lorsque l'on considère l'ensemble du matériau fini : renfort fibreux + matrice molle.

Les modèles de Cauchy ne sont pas non plus adaptés à la description de la réponse dynamique de certains matériaux microstructurés montrant des comportements dispersifs ou des band-gaps. Les théories de milieux continus enrichis peuvent être des bonnes candidates pour modéliser ces matériaux d'une façon plus précise et plus réaliste, aussi bien en statique qu'en dynamique, puisqu'elles peuvent décrire, même d'une façon simplifiée, la manifestation macroscopique de la présence d'une microstructure. Dans l'état actuel des connaissances et de la technologie, il est intéressant de faire porter les efforts sur la conception de matériaux microstructurés pouvant présenter des propriétés originales afin d'améliorer et d'optimiser les réponses des structures qui les utilisent. En effet, ces structures conçues en utilisant de tels matériaux microstructurés – aussi connus sous le nom de matériaux architecturés ou métamatériaux – peuvent présenter des résistances améliorées, des facilités de mise en forme, des poids minimisés, etc. Elles peuvent également posséder des propriétés innovantes dans le domaine du contrôle des vibrations ou dans le domaine de la furtivité. Certaines microstructures génèrent en effet des propriétés très particulières vis à vis de la propagation d'ondes, ce qui confère aux structures résultantes des solutions de choix comme écran ou absorbeur d'ondes.

Des articles récents ont fourni la preuve que le modèle micromorphe relaxé, même s'il est restreint au cas isotrope, est utilisable pour caractériser le comportement mécanique des métamatériaux à bande, c'est-à-dire des matériaux microstructurés capables de "stopper" la propagation des ondes élastiques due aux résonances locales au niveau de la microstructure. L'avantage énorme de l'utilisation du modèle micromorphe relaxé pour la description de ces métamatériaux est sans aucun doute celui de maîtriser le comportement des milieux complexes grâce à l'introduction de peu de coefficients élastiques (module de Young, coefficient de Poisson et quelques coefficients supplémentaires liés à la microstructure homogénéisée). Cette modélisation simplifiée des métamatériaux permet d'ouvrir la porte vers la conception des "métastructures", c'est-à-dire des structures qui sont constituées de métamatériaux en tant que blocs de construction basiques et qui préservent leur comportement non conventionnel à l'échelle de la structure (c'est-à-dire l'absorption des ondes).

Le nouveau concept de métamatériaux est en train d'intéresser de plus en plus les physiciens et les mécaniciens. Ces matériaux sont obtenus par l'assemblage optimal de plusieurs éléments individuels disposés en sous-structures périodiques ou quasi-périodiques et permettent ainsi l'obtention de propriétés très originales. En effet, la forme, la géométrie, les dimensions, le contraste des propriétés mécaniques, l'orientation et la disposition de ces éléments peuvent influencer par exemple la propagation d'ondes, d'une façon telle qu'aucun matériau naturel n'est capable de concurrencer. Les propriétés ainsi créées peuvent certainement donner lieu à des applications innovantes en ingénierie.

Mots-Clés : milieux continus enrichis, modèle micromorphe relaxé, théories de second gradient, renforts fibreux de composite, métamatériaux, band gaps, bias extension test, mise en forme, emboutissage.

Acknowledgments	i
Abstract	ii
Résumé	iv
General introduction	1
Prelude	2
Notational agreement	3
Copyright statement	4
I Enriched continuous models	5
1 Classical vs enriched continuum mechanics	7
2 Micromorphic models	9
2.1 The standard Mindlin-Eringen model	10
2.2 Cosserat's micropolar model	11
2.3 The micro-stretch model	11
2.4 The micro-voids (or micro-dilatation) model	12
2.5 The microstrain model	12
2.6 The incompressible micromorphic model	12
2.7 The relaxed micromorphic model	13
3 Higher gradient models	15
4 The Principle of Virtual Work and the equilibrium of enriched continuous models	17
4.1 Space of configurations and spaces of admissible variations	18
4.2 The equilibrium of a first gradient continuum	19
4.3 The equilibrium of a micromorphic continuum	20
4.4 The equilibrium of a second gradient continuum	21
II Modeling fibrous composite reinforcements as second gradient materials	23
Introduction	25

1	The multi-scale structure and behavior of fibrous composite reinforcements	26
1.1	Microscopic scale: the fiber	27
1.2	Mesoscopic scale: the yarn	27
1.3	Macroscopic scale: the reinforcement	30
1.3.1	Types of reinforcement	30
1.3.2	Mechanical behavior of the reinforcement	31
1.3.3	Consolidation processes	34
2	Modeling of fibrous composite reinforcements	35
2.1	Modeling approaches for fibrous composite reinforcements	35
2.1.1	Microscopic modeling	35
2.1.2	Mesoscopic modeling	36
2.1.3	Macroscopic modeling	37
2.2	Macroscopic enriched continuous modeling	38
2.2.1	Hyperelastic first gradient model	39
2.2.2	Hyperelastic orthotropic second gradient strain energy density	40
2.2.3	Considerations on the numerical implementation of an enriched continuous model	41
2.3	Discrete mesoscopic 2D modeling	43
3	The Bias Extension Test	44
3.1	Characterization of the shear response of woven composite reinforcements	44
3.2	The BET on unbalanced fabrics	45
3.2.1	Experimental setup	45
3.2.2	Experimental results and physical interpretation	47
3.3	Modeling 2D woven fabrics	49
3.3.1	First gradient model	49
3.3.2	Second gradient model	50
3.3.3	Discrete model	51
3.4	Numerical results	51
4	Deep Drawing	56
4.1	Second gradient energy	57
4.2	Modeling geometry and contact interaction between the mold and the reinforcement	58
4.3	Numerical results	59
4.3.1	Influence of the second gradient on the wrinkling	59
4.3.2	Some considerations concerning mesh-dependency of the performed simulations	61
	Conclusion	64
III	The relaxed micromorphic model	67
	Introduction	69
1	Energy formulation of the relaxed micromorphic model	71
1.1	Strain energy density	71
1.2	Kinetic energy density	74
1.3	The relaxed micromorphic stress and its possible symmetry	75
1.4	Dynamic equilibrium equations	76
2	Analysis of the material symmetry classes	78
2.1	The strain energy density in the Mandel-Voigt vector notation	78
2.2	Constitutive tensors for various anisotropy classes	80

3	The macroscopic limit of the relaxed model – macroscopic consistency conditions	84
3.1	Some considerations on the isotropic macroscopic consistency condition	84
3.2	The static macroscopic limit and the dynamic long wavelength limit	86
3.3	The general relaxed anisotropic case in the limit $L_c \rightarrow 0$	86
3.4	Particularization for specific anisotropy classes	88
3.4.1	The isotropic case	88
3.4.2	The cubic symmetry case	89
3.4.3	The orthotropic case	90
	Conclusion	91
IV	Modeling phononic band-gaps via the relaxed micromorphic model	93
	Introduction	95
1	Bulk wave propagation in the relaxed micromorphic model	97
1.1	Solution of the dynamic problem	97
1.2	Necessary and sufficient conditions for real wave propagation	101
1.3	Dispersion curves for the relaxed micromorphic model	105
1.3.1	Longitudinal waves	105
1.3.2	Transverse waves	106
1.3.3	Uncoupled waves	108
2	Dispersion curves and band-gaps in other enriched continuum models	109
2.1	The classical Cauchy medium	110
2.2	The Cosserat micromorphic model	111
2.3	The internal variable model	112
2.4	The standard Mindlin-Eringen model	113
2.5	The relaxed micromorphic model with curvature $\ \text{Div } P\ ^2$	114
3	Reflection and transmission of waves at a Cauchy/relaxed micromorphic interface	115
3.1	Conservation of the total energy	115
3.1.1	The classical Cauchy medium	115
3.1.2	The relaxed micromorphic continuum	115
3.2	Interface jump conditions at a Cauchy/relaxed-micromorphic interface	116
3.2.1	Decomposition of the incident, transmitted and reflected waves	117
3.2.2	The case of purely longitudinal incident waves	118
3.3	Reflection and transmission coefficients at a Cauchy/relaxed-micromorphic interface	120
3.3.1	The degenerate limit case $L_c = 0$ (internal variable model)	120
4	Modeling real two dimensional phononic crystals	122
4.1	The steel plate with cross-shaped holes	122
4.1.1	Microstructure and FEM analysis of a phononic metamaterial	122
4.1.2	Identification of the material parameters	124
4.1.3	Validation of the relaxed micromorphic model via the transmission spectra	127
4.2	The steel plate with liquid-filled round holes	127
4.2.1	Experiments of wave transmission at a Cauchy/phononic-crystal interface	128
4.2.2	Identification of the parameters	129
	Conclusion	133

General conclusion and perspectives	135
End matter	139
Bibliography	139
A Appendix to part I	149
A.1 Micromorphic models as limiting cases of the relaxed micromorphic continuum	149
A.2 One-dimensional standard Mindlin-Eringen model versus new relaxed micromorphic model .	150
B Appendix to part II	151
B.1 Representation Theorems for Hyperelastic Materials	151
B.2 Alternative numerical implementation of the constrained micromorphic model: penalty method	152
B.3 Influence of cutting the corners on the onset of wrinkling for first and second gradient solutions	153
C Appendix to part III	153
C.1 Linear mapping for the Mandel-Voigt vector notation	153
C.2 Non reduction for the standard Mindlin-Eringen model	155
C.3 Some considerations about the anisotropic rotational coupling in the “relaxed micromorphic model”	157
C.4 Properties of the macroscopic constitutive tensors	159
C.4.1 Symmetry	159
C.4.2 Positive definiteness	159
D Appendix to part IV	160
D.1 Bulk wave propagation for the classical Cauchy medium	160
D.2 Bulk wave propagation for the linear Cosserat model	162
D.3 Inequality relations between material parameters	165
D.4 The 12×12 acoustic tensor for arbitrary direction	165

List of Figures

1	Enriched kinematics for a micromorphic continuum.	8
2	Classification of the micromorphic models based on the microdistortion tensor P	9
3	Multi-scale behavior of fibrous composite reinforcements [146].	27
4	Traction of the yarn and problems in the evaluation of the effective stress [34].	28
5	Bending of the yarn before the lateral expansion (a) and after (b) [34].	29
6	Schemes of weaving for 2D fibrous composite reinforcements.	30
7	X-ray tomography of a 2.5D woven interlock.	31
8	Validation of the hypothesis of non-slipping via a hemispherical punch [34].	32
9	Shear behavior in the plane of the yarns of fibrous composite reinforcements.	33
10	Microscopic modeling of fibrous composite reinforcements [61].	36
11	Mesoscopic modeling of fibrous composite reinforcements [107, 108].	37
12	Macroscopic modeling of fibrous composite reinforcements.	38
13	Lagrangian Shape Functions and their First Derivative	41
14	Schematics of the elastic interconnections between warp and weft yarns. (a) rotational spring, (b) translational spring, (c) interaction between thin yarns and (d) interaction between thick yarns.	43
15	Simplified description of the shear angle pattern in the bias extension test	44
16	Boundary layers between two regions at constant shear	45
17	(a) Sample I on top, (b) sample II at the bottom	46
18	X-ray tomography of the interlock I (left) and experimental setting during testing (right).	46
19	Force/displacement plot	47
20	Deformed shape for both specimens (sample I on top, sample II at the bottom)	47
21	Deformed shape for a displacement of 56 mm (a) and angle variation in the transition layers for the thick (b) and thin (c) yarns	48
22	Points identifying some sliding phenomena	49
23	Geometry of the discrete model: undeformed configuration.	51
24	Deformed shape for a displacement of 37 mm (left) and 56 mm (right). From top to bottom: (a) experimental shape, (b) first gradient simulation (cyan with black fibers), (c) second gradient simulation (red with black fibers) and (d) discrete simulation (green). The blue outline is the experimental shape.	52
25	Angle between the fibers in the first gradient (a), second gradient (b) and discrete (c) simulations for a displacement of 56 mm.	53
26	Load-Displacement curve for the first gradient (left), the second gradient (center) and the discrete (right) model	54
27	Double-force-Displacement curve \mathcal{T} (dual of i_{12}) versus sum of the discrete bending moments.	54
28	Vertical displacement of the axis for an imposed displacement of 56 mm and different values of α_1 (top) and d Deformed shape for a displacement of 37 mm and different values of K_{el} (bottom).	55
29	Experimental setup and deformation for a deep-drawing preforming with a hemispherical punch [35].	57
30	Geometry of the model for a deep-drawing preforming with a hemispherical punch.	58
31	Dependence of the solution on the second gradient parameter α	60

32	Solution of a first gradient model with linear shape functions and hexahedral meshes of different sizes.	62
33	Solutions for a first gradient model with linear shape functions and tetrahedral elements of different sizes.	62
34	Mesh-dependency for the first and the second gradient model with augmented continuity shape functions.	63
35	Material symmetry classes and their inclusions [113].	79
36	Dispersion relations for longitudinal waves in the <i>relaxed micromorphic model</i> with vanishing micro-inertia (left) and non-vanishing micro-inertia (right).	105
37	Dispersion relations for longitudinal waves in the <i>internal variable model</i> with vanishing micro-inertia (left) and non-vanishing micro-inertia (right).	106
38	Dispersion relations for transverse waves in the <i>relaxed micromorphic model</i> with vanishing micro-inertia (left) and non-vanishing micro-inertia (right).	107
39	Dispersion relations for transverse waves in the <i>internal variable model</i> with vanishing micro-inertia (left) and non-vanishing micro-inertia (right).	108
40	Dispersion relations for the uncoupled waves in the <i>relaxed micromorphic model</i> (left) and in the <i>internal variable model</i> (right).	108
41	Dispersion relations for the <i>relaxed micromorphic model</i> with non-vanishing gradient micro-inertia, longitudinal (left), transverse (center) and uncoupled (right) waves.	109
42	Dispersion relations for the <i>classical Cauchy medium</i> compared to the acoustic branches of the relaxed micromorphic model with vanishing (left) and non-vanishing gradient micro-inertia (right).	110
43	Longitudinal (left), transverse (center) and uncoupled (right) dispersion relations for the <i>Cosserat model</i> with vanishing (top) and non-vanishing (bottom) micro-inertia.	111
44	Dispersion relations for the <i>internal variable model</i> with vanishing (top) and non-vanishing (bottom) gradient micro-inertia, longitudinal (left), transverse (center) and uncoupled (right) waves.	112
45	Longitudinal (left), transverse (center) and uncoupled (right) dispersion relations for the <i>standard micromorphic model with $\ \nabla P\ ^2$</i> with vanishing (top) and non-vanishing (bottom) gradient micro-inertia.	113
46	Longitudinal (left), transverse (center) and uncoupled (right) dispersion relations for the <i>micromorphic model with $\ \text{Div } P\ ^2$</i> with vanishing (top) and non-vanishing (bottom) gradient micro-inertia.	114
47	Schematics of a macro internal clamp with free microstructure at a Cauchy/relaxed-micromorphic interface.	117
48	Incident, reflected and transmitted waves at a Cauchy/relaxed-micromorphic interface.	118
49	Incident, reflected and transmitted longitudinal waves at a Cauchy/relaxed-micromorphic interface.	119
50	Transmission coefficient of the relaxed micromorphic model with $L_c = 0$ for $\lambda_e = \mu_e = \lambda_m = \mu_m = 100 \text{ GPa}$ and $\eta = 1 \text{ kg/m}$	121
51	Microstructure of the considered metamaterial (left), values of the elastic parameters of the base material (aluminum) and geometric parameters relative to the unit cell (right).	122
52	Dispersion curves for waves propagating at 0° (left) and 45° (right) obtained with a Bloch wave analysis of the cell shown in Figure 51.	123
53	Schematic representation of the FEM model for the determination of the transmission spectrum, as implemented in COMSOL Multiphysics®.	123
54	Transmission coefficient as function of frequency for an incident longitudinal (top) and transverse (bottom) wave for the FEM model.	124

55	Comparison between the dispersion curves obtained with a Bloch wave analysis of the cell shown in Figure 51 (left) and dispersion curves for the relaxed micromorphic model with the parameters measured in [132] (center) and with the slightly modified set of the relaxed parameters value proposed in Table 4.1 (right). Longitudinal branches are in blue while the transverse ones are in green.	126
56	Transmission coefficient as function of frequency for an incident longitudinal wave for the FEM model (left) and for the relaxed micromorphic model (right).	127
57	Dimensionless displacement on the bottom edge for the vibrating modes in the range of angular frequencies $1.75 \times 10^7 - 1.9 \times 10^7$ rad/s (left) and $0.80 \times 10^7 - 1.5 \times 10^7$ (right) (FEM simulations).	128
58	Transmission coefficient as function of frequency for an incident transverse wave for the FEM model (left) and for the relaxed micromorphic model (right).	128
59	Schematics of the sample structure (a) and the experimental setup (b) ([127, Figure 1(b)]).	128
60	Transmission spectrum of the phononic crystal presented in Figure 59a, with liquid-filled holes [127, Figure 2b].	129
61	Profiles of the transmission coefficients obtained for different arbitrary values of the parameter μ_e (left).	130
62	Comparison of the profile obtained in [127] based on a real metamaterial and the one obtained with the relaxed micromorphic model with the values given in Table 4.3 and $L_c = 0$	131
63	Fitting of the parameter L_c on the experimental profile of the transmission coefficients.	132
64	Vertical displacement of the mean axis for a displacement of 56 mm and different values of K	153
65	Influence of cutting the corners on the onset of wrinkling for the first and the second gradient model with shape functions with augmented continuity.	154

List of Tables

3.1	Parameters of the first-gradient continuous model for the simulation of the BET.	50
3.2	Parameters of the second gradient continuous model for the simulation of the BET.	50
3.3	Parameters of the discrete model for the simulation of the BET.	51
4.1	Parameters of the first gradient energy for the simulation of the deep drawing.	58
4.1	Values of the material parameters (top) and of the micro-inertia parameters (bottom) of the weighted relaxed micromorphic model. All parameters are the same as the ones measured in [132] except for $\bar{\eta}_2$ and $\bar{\eta}_3$	126
4.2	Values of the constitutive parameters obtained via the solution (IV.116) for arbitrary values of the parameter μ_e (right).	130
4.3	Conditions used for the parameters identification (a) and corresponding values of the obtained elastic parameters of the relaxed micromorphic model (b).	130
B.1	Invariants of Deformation	151

General introduction

General introduction

Modeling in continuum mechanics is an art encompassing mathematics, mechanics, physics and experiments. Many researchers have been attracted to the field of enriched continuum mechanics, following the master works of Mindlin and Eringen, and have dealt with the description of particular aspects of enriched continuum theories, usually introducing “ad hoc” terms to provide sensational additional effects. Nonetheless, some fundamental questions concerning the range of applicability or the descriptive power of enriched continuum mechanics had not been settled, leading to an understandable skepticism of the majority of researchers in continuum mechanics. On the contrary, we believe in the usefulness of enriched continuum mechanical models, even if we are aware of their current shortcomings.

We are deeply convinced that scientific advancements do not consist in producing a zoo of possibilities and to combine more effects (which are themselves not yet properly understood), but in *reducing complexity* and in explaining in simpler terms previously non-connected ideas, without losing the accuracy of the mathematical description of the physical problem we are interested in. A major guidance for enlightened modeling certainly comes from the experimental side. Basing ourselves on the considered phenomena, we should not use superfluous information (superfluous because in practice, it cannot be determined) and, among valid competing hypotheses, the one with the *simplest* assumptions should be selected. In this work, we deal with enriched continuum models in this spirit: directed towards simplification. Whether we have achieved a step into this direction must be judged by the reader.

Recent years have seen a colossal increase of interest in so-called generalized or enriched continuum models. This exponential growth is mainly due to the need to incorporate additional phenomenological features like the discreteness of matter, characteristic length scales, dispersion of waves, etc. As a matter of fact, complex (meta-)materials may exhibit superior mechanical properties with respect to more commonly used engineering materials, also providing some advantages as easy formability processes, light weight and exotic behavior with respect to wave propagation. All these features are not fully captured by standard elasticity approaches. The idea of using enriched continuum models to account for the homogenized behavior of microstructured materials has extensively been exploited in the last years (e.g [71–75]).

The first main focus of this manuscript is a class of complex engineering materials which are known as woven fibrous composite reinforcements. These materials possess a hierarchical microstructure, since they are constituted by woven yarns which are themselves made up of thousand of fibers. We will show that the meso- and micro-structures of fibrous composites have a strong impact on the overall mechanical behavior of the macroscopic engineering piece. A classical Cauchy model is not able, alone, to take into account all the possible effects that the microstructure of considered materials have on their macroscopic deformation. More precisely, some particular loading conditions, associated to particular types of boundary conditions may cause some microstructure-related deformation modes which are not fully taken into account in Cauchy continuum theories. This is the case, for example, when observing some regions inside the materials in which high gradients of deformation occur, concentrated in relatively narrow regions. One way to deal with the description of such boundary layers, while remaining in the framework of a macroscopic theory, is to consider so-called “enriched continuum theories”. Such enriched theories allow for the introduction of a class of internal actions wider than in the case of classical Cauchy continuum theory. These more general contact actions excite additional deformation modes, which can be seen to be directly related with the properties of the microstructure of considered materials.

The second main focus of this manuscript is the relaxed micromorphic model. Recent papers [131, 132] provided the evidence that the relaxed micromorphic model, even when restricted to the isotropic case, is fit to characterize the mechanical behavior of metamaterials with unorthodox dynamical properties. More precisely, it has been shown that the isotropic relaxed micromorphic model can be effectively used to model band-gap metamaterials, i.e. microstructured materials which are able to “stop” the propagation of elastic waves due to local resonances at the level of the microstructure. The enormous advantage of using the relaxed

micromorphic model for the description of such metamaterials is undoubtedly the introduction of few elastic coefficients (Young modulus, Poisson ratio and few extra microstructure-related homogenized coefficients). This simplified modeling of metamaterials will allow for the conception of “metastructures”, i.e. structures which are made up of metamaterials as basic building blocks and which preserve their unconventional behavior at the scale of the structure (e.g. wave absorption).

The present manuscript is organized as follows:

- In Part I, some fundamental details concerning classical continuum mechanical models are recalled. Moreover, enriched continuum models are introduced and discussed presenting their characteristics and their differences with classical continuum mechanics. A brief presentation of the Principle of virtual work for enriched continuum models is presented.
- In Part II, a general description of fibrous composite reinforcements is given, with particular attention to the micro- and macro-structural mechanical properties. Furthermore, some discrete and continuum models are presented for the description of the mechanical behavior of 2.5D woven composites. In particular, it will be shown how to describe some deformation modes related to the effect of the local bending of fibers and the overall macroscopic deformation of fibrous composite reinforcements.
- In Part III, we present the relaxed micromorphic continuum model that will be used in Part IV to describe phononic band-gap metamaterials. This model allows for a very general set of micromorphic effects, while keeping the number of material coefficients reasonable. A homogenization formula is derived to relate the parameters of the relaxed micromorphic model to an equivalent macroscopic classical model.
- In Part IV, we study the dispersive behavior of the relaxed micromorphic model and of some other main micromorphic models. In particular, we focus on the description of phononic band-gap metamaterials and the relaxed micromorphic model is applied to some real engineering band-gap metamaterials.

Notational agreement

We denote by $\mathbb{R}^{3 \times 3}$ the set of real 3×3 second order tensors and by $\mathbb{R}^{3 \times 3 \times 3}$ the set of real $3 \times 3 \times 3$ third order tensors. The standard Euclidean scalar product on $\mathbb{R}^{3 \times 3}$ is given by $\langle X, Y \rangle_{\mathbb{R}^{3 \times 3}} = \text{tr}(X \cdot Y^T)$ and, thus, the Frobenius tensor norm is $\|X\|^2 = \langle X, X \rangle_{\mathbb{R}^{3 \times 3}}$. Moreover, the identity tensor on $\mathbb{R}^{3 \times 3}$ will be denoted by $\mathbf{1}$, so that $\text{tr}(X) = \langle X, \mathbf{1} \rangle$. We adopt the usual abbreviations of Lie-algebra theory, i.e.:

- $\text{Sym}(3) := \{X \in \mathbb{R}^{3 \times 3} \mid X^T = X\}$ denotes the vector-space of all symmetric 3×3 matrices
- $\mathfrak{so}(3) := \{X \in \mathbb{R}^{3 \times 3} \mid X^T = -X\}$ is the Lie-algebra of skew symmetric tensors
- $\mathfrak{sl}(3) := \{X \in \mathbb{R}^{3 \times 3} \mid \text{tr}(X) = 0\}$ is the Lie-algebra of traceless tensors
- $\mathbb{R}^{3 \times 3} \simeq \mathfrak{gl}(3) = \{\mathfrak{sl}(3) \cap \text{Sym}(3)\} \oplus \mathfrak{so}(3) \oplus \mathbb{R} \cdot \mathbf{1}$ is the *orthogonal Cartan-decomposition of the Lie-algebra*

For all $X \in \mathbb{R}^{3 \times 3}$, we consider the decomposition

$$X = \text{dev sym}X + \text{skew}X + \frac{1}{3} \text{tr}(X) \mathbf{1}, \quad (\text{INT.1})$$

where:

- $\text{sym}X = \frac{1}{2}(X^T + X) \in \text{Sym}(3)$ is the symmetric part,
- $\text{skew}X = \frac{1}{2}(X - X^T) \in \mathfrak{so}(3)$ is the skew-symmetric part,
- $\text{dev}X = X - \frac{1}{3} \text{tr}(X) \mathbf{1} \in \mathfrak{sl}(3)$ is the deviatoric part .

Throughout all the paper, we denote:

- the sixth order tensors $\widehat{\mathbb{L}} : \mathbb{R}^{3 \times 3 \times 3} \rightarrow \mathbb{R}^{3 \times 3 \times 3}$ by a hat
- the fourth order tensors $\overline{\mathbb{C}} : \mathbb{R}^{3 \times 3} \rightarrow \mathbb{R}^{3 \times 3}$ by overline
- without superscripts, i.e. \mathbb{C} , the classical fourth order tensors acting only on symmetric matrices $\mathbb{C} : \text{Sym}(3) \rightarrow \text{Sym}(3)$ or skew-symmetric ones $\mathbb{C}_c : \mathfrak{so}(3) \rightarrow \mathfrak{so}(3)$
- the second order tensors $\widetilde{\mathbb{C}} : \mathbb{R}^6 \rightarrow \mathbb{R}^6$ or $\widetilde{\mathbb{C}} : \mathbb{R}^3 \rightarrow \mathbb{R}^3$ appearing as elastic stiffness by a tilde.

Throughout this paper Latin subscripts take the values 1,2,3 while Greek subscripts take the values 1,2,3,4,5,6 and we adopt the Einstein convention of sum over repeated indices if not differently specified. We denote by $\overline{\mathbb{C}}X$ the linear application of a 4th order tensor to a 2nd order tensor and also for the linear application of a 6th order tensor $\widehat{\mathbb{L}}$ to a 3rd order tensor. In symbols:

$$(\overline{\mathbb{C}}X)_{ij} = \overline{\mathbb{C}}_{ijkh}X_{hk}, \quad (\widehat{\mathbb{L}}A)_{ijh} = \widehat{\mathbb{L}}_{ijhpqr}A_{pqr}. \quad (\text{INT.2})$$

The operation of simple contraction between tensors of suitable order is denoted by a central dot, for example:

$$(\widetilde{\mathbb{C}} \cdot v)_i = \widetilde{\mathbb{C}}_{ij}v_j, \quad (\widetilde{\mathbb{C}} \cdot X)_{ij} = \widetilde{\mathbb{C}}_{ih}X_{hj}. \quad (\text{INT.3})$$

Typical conventions for differential operations are implied, such as a comma followed by a subscript to denote the partial derivative with respect to the corresponding Cartesian coordinate, i. e. $(\cdot)_{,j} = \frac{\partial(\cdot)}{\partial x_j}$.

Given a skew-symmetric matrix $\overline{A} \in \mathfrak{so}(3)$ we consider:

$$\overline{A} = \begin{pmatrix} 0 & \overline{A}_{12} & \overline{A}_{13} \\ -\overline{A}_{12} & 0 & \overline{A}_{23} \\ -\overline{A}_{13} & -\overline{A}_{23} & 0 \end{pmatrix}, \quad \text{axl}(\overline{A}) = (-\overline{A}_{23}, \overline{A}_{13}, -\overline{A}_{12})^T. \quad (\text{INT.4})$$

ore equivalently in index notation:

$$[\text{axl}(\overline{A})]_k = -\frac{1}{2}\epsilon_{ijk}\overline{A}_{ij} = \frac{1}{2}\epsilon_{kij}\overline{A}_{ji}, \quad (\text{INT.5})$$

where ϵ is the Levi-Civita third order permutation tensor.

Inversely, we introduce the canonical identification of R^3 with $\mathfrak{so}(3)$, A can be expressed as a function of $a \in \mathbb{R}^3$ as:

$$A = \text{anti}(a) = \begin{pmatrix} 0 & -a_3 & a_2 \\ a_3 & 0 & -a_1 \\ -a_2 & a_1 & 0 \end{pmatrix}. \quad (\text{INT.6})$$

Copyright statement

Some passages have been quoted verbatim from the published papers of the author [11–13, 49, 50, 129–131, 136–138, 179].

Part I

Enriched continuous models

Contents of Part I

1	Classical vs enriched continuum mechanics	7
2	Micromorphic models	9
2.1	The standard Mindlin-Eringen model	10
2.2	Cosserat's micropolar model	11
2.3	The micro-stretch model	11
2.4	The micro-voids (or micro-dilatation) model	12
2.5	The microstrain model	12
2.6	The incompressible micromorphic model	12
2.7	The relaxed micromorphic model	13
3	Higher gradient models	15
4	The Principle of Virtual Work and the equilibrium of enriched continuous models	17
4.1	Space of configurations and spaces of admissible variations	18
4.2	The equilibrium of a first gradient continuum	19
4.3	The equilibrium of a micromorphic continuum	20
4.4	The equilibrium of a second gradient continuum	21

CHAPTER I.1

Classical vs enriched continuum mechanics

This part of the thesis is meant as an introduction to enriched continuum mechanics. Most of the concepts presented are taken from [176] and from the work of the late professor Maugin [149,150].

The study of enriched continuum mechanics can not be developed without considering its fundamentals, namely what is usually referred to as “classical continuum mechanics”. The huge possibilities of the continuous modeling of materials have been shown since Gabrio Piola (1789–1857) and Augustin L. Cauchy (1789–1857) in the 19th century. In his pioneering work [196], Piola theorized the need of complex constitutive equations including derivatives of the displacement of higher order than the usual first gradient. Nowadays, this feature would not be considered proper of “classical continuum mechanics” due to the great impact of Cauchy’s approach to modeling [32]; the French mathematician presented a rather simplified model that was still rich enough to describe a wealth of mechanical behaviors. This impressive feature was the outcome of his novel concepts and the work of other major researchers: Leonard Euler (1707–1783), Joseph L. Lagrange (1736–1813) and George Green (1793–1841) (see [150]).

In his work, Cauchy generalized Euler’s notion of pressure, valid in the case of fluids, stating that the interactions between parts of a solid can be described via the symmetric Cauchy force-stress tensor $\sigma : \Omega \subset \mathbb{R}^3 \rightarrow \mathbb{R}^{3 \times 3}$. The proof of this concept was obtained via its celebrated tetrahedron argument, which is still part of almost every continuum mechanics class worldwide. Afterwards, Cauchy determined the equations of motion that balance inertiae, external forces and stresses (see [32, Eq. (35)]) considering the equilibrium of an elementary parallelepiped (as Euler did for fluids). In the equations of motion, one can recognize the divergence operator, even if the term “divergence” was not used by Cauchy since the operation was formally defined by Green in the same year [87].

The simplicity of the entire theory is based on two fundamental assumptions that, even if reasonable in most applications, can be restrictive in some specific cases, namely:

1. the displacement $u : \Omega \subset \mathbb{R}^3 \rightarrow \mathbb{R}^3$ from a reference configuration is the only kinematic field, which is equivalent to assume that the only possible motion of each point of the body is a translation;
2. the stress σ in each material point X is a symmetric tensor (Boltzmann’s axiom of symmetry) and depends only on the gradient ∇u of the displacement evaluated in the same material point X .

Following Green and considering the entirety of the described properties, the resulting model can be defined in the case of infinitesimal deformations via a strain energy density and a kinetic energy density as:

$$W = \frac{1}{2} \langle \mathbb{C}_M \text{sym}(\nabla u), \text{sym}(\nabla u) \rangle_{\mathbb{R}^{3 \times 3}}, \quad J = \frac{1}{2} \rho \|u_{,t}\|^2, \quad (\text{I.1})$$

where $\mathbb{C}_M : \text{Sym}(3) \rightarrow \text{Sym}(3)$ is a fourth order tensor with 21 independent coefficients and ρ is a scalar mass density. This format (with its non-linear/plastic variations) is still the standard for engineering and it is still general enough to comprehend a huge variety of engineering applications. However, the new fields of research on metamaterials and their unconventional behaviors demand more complex models. As a matter of fact, the Cauchy model falls short for most of the materials in which a micro-structure, with a high contrast of material properties, determines the overall behavior of the resulting piece. For example, as it will be shown in the rest of this work, both phononic crystals (see [129,131,132] and Part IV) and fibrous composite reinforcements (see [11,13,70,130,134] and Part II) need more refined models to fully describe their experimental behaviors.

In order to set up an enriched continuum model, it is sufficient to discard one of the two basic assumptions made by Cauchy. Indeed, most of the newly proposed models can be described in this manner, assuming either:

1. the displacement u is NOT the ONLY kinematic field;

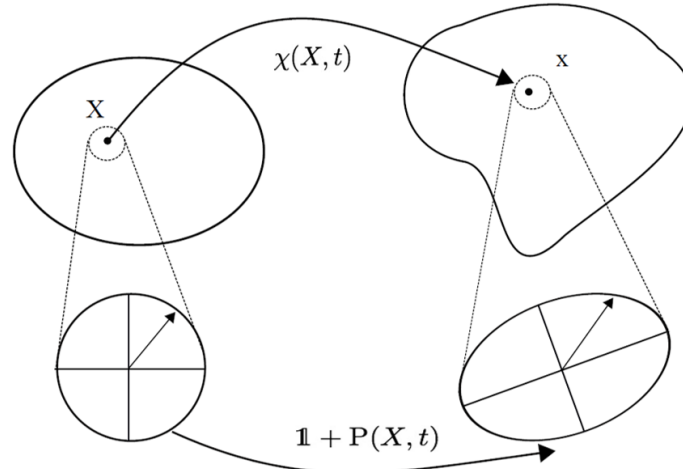


Figure 1: Enriched kinematics for a micromorphic continuum.

2. the stress σ in each material point X is NOT necessarily a symmetric tensor AND does NOT depend ONLY on the gradient ∇u of the displacement evaluated in the same material point X .

The most prominent examples of case 1 are the *micromorphic continuum models*: the kinematics is enriched by introducing an additional field of micro-distortions P , beyond the classical macroscopic displacement u (see Fig. 1, chapter I.2, and Parts III and IV). This new set of degrees of freedom can be used to describe a substructure attached to each macroscopic material point $x \in \Omega$, so describing micro-structure related phenomena.

To understand the possible models generated in the case 2, we must analyze the reasoning behind the corresponding Cauchy's assumption. The functional dependence derive from the notion of contiguity introduced by Euler: the mechanical action on each material point is caused only by its "direct environment" [150], which excludes the influence of different points in the body. However, it is possible to find cases in which other parts of the continuum have an influence, even if secondary, on the local response (e.g. molecular dynamics). Such models are usually referred to as *peridynamics* (from the Greek prefix $\pi\epsilon\rho\iota$ - (peri-, "around, surrounding")). Applications of such models can be also found in the study of crack propagation, in which the possibility to introduce an energy depending on the derivatives of the displacement is rendered impossible by the discontinuity on the displacement fields. The peridynamic models are strongly non-local, but we can also assume a weaker kind of non-locality, whose response depends only on the local displacement field but includes its higher derivatives. The non-locality is given by the influence that a broader neighborhood of the material point exerts on the local response. Such models are the so-called *higher gradient models* and will be the object of chapter I.3 and Part II.

In what follows, a presentation of the main micromorphic models and of the higher gradient models will be made. For a more detailed treatise, we refer the reader to [149, 150, 176]. In the final chapter, the Principle of Virtual Work is presented and some aspects of its application to enriched continua are analyzed. We remark here that the following presentation will be made under the hypothesis of a linearized strain measure on ∇u (and P for the micromorphic continua) while some applications in Part II will employ non-linearized strain measures on the Cauchy-Green deformation tensor C .

CHAPTER I.2

Micromorphic models

The French Cosserat brothers, the mathematician-astronomer Eugène (1866–1931) and the civil engineer François (1852–1914), were among the first researchers to propose the introduction of additional kinematical fields to the standard displacement for the description of micro-structured materials. In their model, the added micromorphic displacements were meant to describe rigid rotations at the microscopic level (see [44] and section I.2.2), therefore the additional degrees of freedom take the structure of a skew-symmetric tensor $A \in \mathfrak{so}(3)$, complementing the classical macroscopic displacement $u : \Omega \subset \mathbb{R}^3 \rightarrow \mathbb{R}^3$.

The worth of the Cosserats' contribution wasn't really appreciated and built upon until the second half of the 20th century, when Mindlin [155, 156], Green and Rivlin [86], Toupin [225, 226], Eringen [65, 67–69] and Germain [78] developed their work lending it credibility. In Mindlin and Eringen's work, the kinematics was enriched introducing an additional non-symmetric field of micro-distortions $P \in \mathbb{R}^{3 \times 3}$: in each macroscopic material point $x \in \Omega$ there is a substructure attached. This micro-deformation was generalized to include micro-stretches, micro-strains, micro-shear, micro-distortions and micro-rotations, and it was described by an affine mapping $\mathbf{1} + P$ (see Fig. 1 and section I.2.1).

In time, many variations of the micromorphic model have been proposed to take into account microstructures with specific deformation modes. Not considering the full non-symmetric field of micro-distortions, the resulting models are simpler and easier to apply, but lose the generality of the standard Mindlin-Eringen model. However, the gained simplicity is of paramount importance for some applications, giving value to the proposed models. This variety of models, that differ for the deformation modes of the microstructure and for the resulting format assumed for P , (see Figure 2 for a graphic representation) includes:

- the Mindlin-Eringen micromorphic model in which P describes micro-shearing, micro-rotation and micro-stretch (isotropic expansion and contraction), i.e. $P \in \mathbb{R}^{3 \times 3}$ (see [67, 156] and I.2.1)
- the Cosserat micropolar model in which P describes only micro-rotations, i.e. $P \in \mathfrak{so}(3)$ (see [44] and I.2.2)

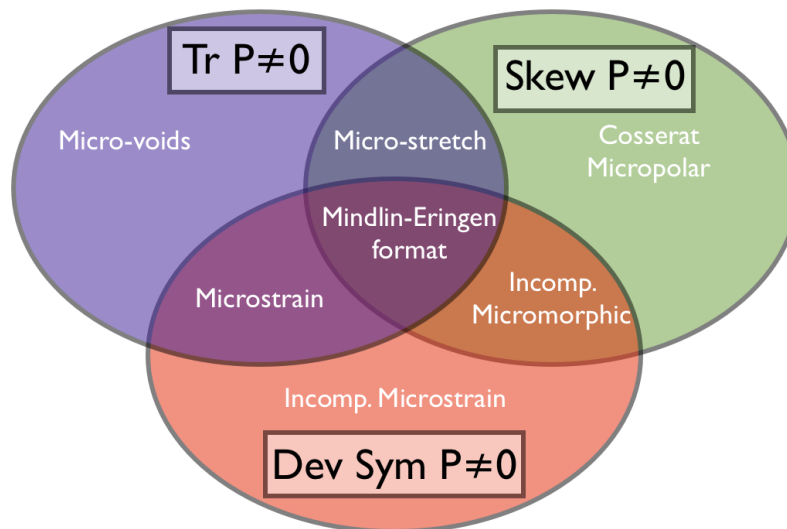


Figure 2: Classification of the micromorphic models based on the microdistortion tensor P .

- the micro-stretch model in which P describes micro-rotations and micro-stretch (isotropic expansion and contraction), i.e. $P \in \mathbb{R} \cdot \mathbf{1} \oplus \mathfrak{so}(3)$ (see [66] and I.2.3)
- the micro-voids (or micro-dilatation) model in which P describes only micro-stretch (isotropic expansion and contraction), i.e. $P \in \mathbb{R} \cdot \mathbf{1}$ (see [46, 186] and I.2.4)
- the micro-strain model in which P describes microshearing and micro-stretch (isotropic expansion and contraction), i.e. P is a symmetric tensor $P \in \text{Sym}(3)$ (see [74] and I.2.5)
- the incompressible micro-strain model in which P describes only microshearing, i.e. P is a traceless symmetric tensor $P \in \{\mathfrak{sl}(3) \cap \text{Sym}(3)\}$ (see [74] and I.2.5)
- the incompressible micromorphic model in which P describes micro-rotations and microshearing, i.e. $P \in \mathfrak{sl}(3)$ (see [74] and I.2.6)

A different approach to the simplification of the the standard Mindlin-Eringen's is the relaxed micromorphic model, which was first proposed in [176] (see section I.2.7 and Part III). Instead of reducing the generality of the micro-distortions described by P , the authors propose to consider a more structured energy leading to an important decrease in the number of constitutive parameters and to an easier interpretation of the associated micro-macro deformation modes.

In the following sections, we present briefly the already mentioned enriched micromorphic models, referring the reader to [74, 150, 176] for more details.

2.1 The standard Mindlin-Eringen model

One of the most known enriched continuum models is the micromorphic continuum model introduced by Mindlin and Eringen [43, 65, 67–69, 155, 156] in the early sixties of the last century. It includes many special cases among which the much older Cosserat-type models [44]. Considering $P \in \mathbb{R}^{3 \times 3}$ (9 additional degrees of freedom), the elastic energy of the general anisotropic centro-symmetric micromorphic model in the sense of Mindlin-Eringen (see [156] and [67, p. 270, eq. 7.1.4]) can be represented as:

$$\begin{aligned}
 W = & \underbrace{\frac{1}{2} \langle \bar{\mathbb{C}}_e (\nabla u - P), (\nabla u - P) \rangle_{\mathbb{R}^{3 \times 3}}}_{\text{full anisotropic elastic - energy}} + \underbrace{\frac{1}{2} \langle \mathbb{C}_m \text{sym } P, \text{sym } P \rangle_{\mathbb{R}^{3 \times 3}}}_{\text{micro - self - energy}} \\
 & + \underbrace{\frac{1}{2} \langle \bar{\mathbb{E}}_{\text{cross}} (\nabla u - P), \text{sym } P \rangle_{\mathbb{R}^{3 \times 3}}}_{\text{anisotropic cross - coupling}} + \underbrace{\frac{\mu L_c^2}{2} \langle \hat{\mathbb{L}} \nabla P, \nabla P \rangle_{\mathbb{R}^{3 \times 3 \times 3}}}_{\text{full anisotropic curvature}}, \tag{I.2}
 \end{aligned}$$

where $\bar{\mathbb{C}}_e : \mathbb{R}^{3 \times 3} \rightarrow \mathbb{R}^{3 \times 3}$ is a 4th order micromorphic elasticity tensor which has at most 45 independent coefficients and which acts on the *non-symmetric elastic distortion* $e = \nabla u - P$ and $\bar{\mathbb{E}}_{\text{cross}} : \mathbb{R}^{3 \times 3} \rightarrow \text{Sym}(3)$ is a 4th order cross-coupling tensor with the symmetry $(\bar{\mathbb{E}}_{\text{cross}})_{ijkl} = (\bar{\mathbb{E}}_{\text{cross}})_{jikl}$ having at most 54 independent coefficients. The fourth order tensor $\mathbb{C}_m : \text{Sym}(3) \rightarrow \text{Sym}(3)$ has the classical 21 independent coefficients of classical elasticity, while $\hat{\mathbb{L}} : \mathbb{R}^{3 \times 3 \times 3} \rightarrow \mathbb{R}^{3 \times 3 \times 3}$ is a 6th order tensor that shows an astonishing 378 parameters. The parameter $\mu > 0$ is a typical shear modulus and $L_c > 0$ is one characteristic length, while $\hat{\mathbb{L}}_{\text{aniso}}$ is, accordingly, dimensionless. Here, for simplicity, we have assumed just a decoupled format of the energy: mixed terms of strain and curvature have been discarded by assuming *centro-symmetry*. Counting the number of coefficients we have $45 + 21 + 54 + 378 = 498$ independent coefficients.

Even assuming an isotropic behavior of the curvature, we obtain that the 6th order tensor $\hat{\mathbb{L}}$ has still 11 independent non-dimensional constants [67]¹. On the other hand, the local energy has 7 independent coefficients in the isotropic case: $\bar{\mathbb{C}}_e$ has 3, $\mathbb{C}_m \sim 2$, $\bar{\mathbb{E}}_{\text{cross}} \sim 2$ adding up to the usual 18 constitutive coefficients to be determined in the isotropic case. One of the major obstacles in using the micromorphic approach for specific materials is the impossibility to determine such multitude of new material coefficients.

¹This is due to the fact that the general isotropic 6th order tensor has 15 coefficients which, considering that in a quadratic form representation we can assume a major symmetry of the type $\hat{\mathbb{L}}_{ijklmn} = \hat{\mathbb{L}}_{lmnij k}$, reduce to 11 (see [160, 214]). The 11 coefficients of the curvature in the isotropic case reduce to 5 in the particular case of second gradient elasticity (see [57]) which is obtained from a micromorphic model by setting $P = \nabla u$.

Not only is the huge number a technical problem, but also the interpretation of coefficients is problematic [37–39]. Some of these coefficients are size-dependent while others are not. A purely formal approach, as is often done, cannot be the final answer.

2.2 Cosserat’s micropolar model

In Cosserat’s micropolar model [44], the underlying microstructure is assumed to have two orthogonal rigid directions and, therefore, the microdeformation field can only describe micro-rotations. With this hypothesis, it is sufficient to consider a skew-symmetric micromorphic distortion field $A \in \mathfrak{so}(3)$ (3 additional degrees of freedom) instead of $P \in \mathbb{R}^{3 \times 3}$. It would be possible to obtain this particular case from a general micromorphic model, but we refrain here from showing the proof. The strain energy density of the resulting model is²:

$$W = \underbrace{\frac{1}{2} \langle \mathbb{C}_M \operatorname{sym} \nabla u, \operatorname{sym} \nabla u \rangle_{\mathbb{R}^{3 \times 3}}}_{\text{anisotropic elastic – energy}} + \underbrace{\frac{1}{2} \langle \mathbb{C}_c (\operatorname{skew} \nabla u - A), \operatorname{skew} \nabla u - A \rangle_{\mathbb{R}^{3 \times 3}}}_{\text{invariant local anisotropic rotational elastic coupling}} + \underbrace{\frac{\mu L_c^2}{2} \langle \tilde{\mathbb{L}} \nabla \operatorname{axl} A, \nabla \operatorname{axl} A \rangle_{\mathbb{R}^{3 \times 3}}}_{\text{curvature}}. \quad (\text{I.3})$$

where $\mathbb{C}_M : \operatorname{Sym}(3) \rightarrow \operatorname{Sym}(3)$ is the classical 4th order constitutive tensors acting on the symmetric strains $\operatorname{sym} \nabla u$, $\mathbb{C}_c : \mathfrak{so}(3) \rightarrow \mathfrak{so}(3)$ is a 4th order tensor acting on the 2nd order tensor skew-symmetric strain $\operatorname{skew}(\nabla u - A)$ and $\tilde{\mathbb{L}} : \mathbb{R}^{3 \times 3} \rightarrow \mathbb{R}^{3 \times 3}$ is a 4th order constitutive tensor acting on the 2nd order tensor $\nabla \operatorname{axl} A$.

Even if a wide set of materials seems to fit the hypothesis of a microstructure that can only rotate, it is still difficult to fit the additional parameters in a reliable manner [150]. Some success has been obtained by Lakes to describe natural porous bone, metallic foams and cellular materials [116, 117], where the author has been able to determine and verify for consistency the Cosserat elasticity constants and to show how a Cosserat model obtains better results than the classical elasticity ones. Among the resulting properties of this application of the Cosserat model, some notable ones were the size effects, the negative Poisson ratio and the dispersive behavior.

2.3 The micro-stretch model

The micro-stretch model presents an intermediate possibility between the Cosserat micropolar model and the full Mindlin-Eringen micromorphic model. In particular, Eringen (see [66]) proposed a micro-structure that can have rotations (as in the Cosserat model) but also stretch (expand and contract, as in the micro-voids model) leading to a micro-distortion tensor $P \in \mathbb{R} \cdot \mathbb{1} \oplus \mathfrak{so}(3)$ (4 additional degrees of freedom). The micro-distortion tensor can be decomposed as $P = \zeta \mathbb{1} + A$, where the skew-symmetric part $A \in \mathfrak{so}(3)$ represent the rotations and ζ is a scalar function that represents the stretch. The energy associated with this model can be written as:

$$W = \underbrace{\frac{1}{2} \langle \mathbb{C}_e \operatorname{sym}(\nabla u - \zeta \mathbb{1}), \operatorname{sym}(\nabla u - \zeta \mathbb{1}) \rangle_{\mathbb{R}^{3 \times 3}}}_{\text{anisotropic elastic – energy}} + \underbrace{\frac{1}{2} \langle \mathbb{C}_c (\operatorname{skew} \nabla u - A), \operatorname{skew} \nabla u - A \rangle_{\mathbb{R}^{3 \times 3}}}_{\text{invariant local anisotropic rotational elastic coupling}} + \underbrace{\frac{1}{2} \kappa_m \zeta^2}_{\text{micro – self}} + \underbrace{\frac{\mu L_c^2}{2} \left(\langle \tilde{\mathbb{L}} \nabla \zeta, \nabla \zeta \rangle_{\mathbb{R}^3} + \langle \tilde{\mathbb{L}} \nabla \operatorname{axl} A, \nabla \operatorname{axl} A \rangle_{\mathbb{R}^{3 \times 3}} \right)}_{\text{curvature}}. \quad (\text{I.4})$$

where $\mathbb{C}_e : \operatorname{Sym}(3) \rightarrow \operatorname{Sym}(3)$ is a classical 4th order constitutive tensor acting on symmetric tensors, $\mathbb{C}_c : \mathfrak{so}(3) \rightarrow \mathfrak{so}(3)$ is a 4th order tensor acting on the 2nd order tensor skew-symmetric strain $\operatorname{skew}(\nabla u - A)$,

²The operator axl gives a vector with the three independent components of a skew symmetric tensor, as defined in the Equation (INT.4).

$\kappa_m > 0$ is a constitutive parameter, $\tilde{\mathbb{L}} : \mathbb{R}^3 \rightarrow \mathbb{R}^3$ is a 2^{nd} order tensor acting on vectors and $\bar{\mathbb{L}} : \mathbb{R}^{3 \times 3} \rightarrow \mathbb{R}^{3 \times 3}$ is a 4^{th} order constitutive tensor acting on the 2^{nd} order tensor $\nabla \text{axl } A$.

2.4 The micro-voids (or micro-dilatation) model

The micro-voids (or micro-dilatation) model was proposed by Cowin and Nunziato [46, 186] (see also [99]) for thermomechanical applications. The fundamental idea of this model is that the micro-structure attached to the material can only expand or compress isotropically. Therefore, the micro-distortion tensor $P \in \mathbb{R} \cdot \mathbb{1}$ (1 additional degree of freedom) can be described with a scalar function as $P = \zeta \mathbb{1}$. This case can be considered as a limiting case of microstretch elasticity (see section I.2.3) in which no internal-rotation is considered. The energy associated to this model can be written as:

$$W = \underbrace{\frac{1}{2} \langle \mathbb{C}_e \text{sym}(\nabla u - \zeta \mathbb{1}), \text{sym}(\nabla u - \zeta \mathbb{1}) \rangle_{\mathbb{R}^{3 \times 3}}}_{\text{anisotropic elastic - energy}} + \underbrace{\frac{1}{2} \kappa_m \zeta^2}_{\text{micro - self}} + \underbrace{\frac{\mu L_c^2}{2} \langle \tilde{\mathbb{L}} \nabla \zeta, \nabla \zeta \rangle_{\mathbb{R}^3}}_{\text{curvature}}. \quad (\text{I.5})$$

where $\mathbb{C}_e : \text{Sym}(3) \rightarrow \text{Sym}(3)$ is a classical 4^{th} order constitutive tensor acting on symmetric strains, $\kappa_m > 0$ is a constitutive parameter and $\tilde{\mathbb{L}} : \mathbb{R}^3 \rightarrow \mathbb{R}^3$ is a 2^{nd} order tensor acting on vectors.

2.5 The microstrain model

In the microstrain model proposed in [74], the micro-distortion tensor assumes the form of a symmetric strain $P \in \text{Sym}(3)$ (6 additional degrees of freedom). Therefore, this model does not account for possible rotations in the microstructure. This model respects Boltzmann's axiom of symmetry because the symmetry of the micro-distortion tensor allows for symmetric stresses. The resulting energy is:

$$W = \underbrace{\frac{1}{2} \langle \mathbb{C}_e \text{sym}(\nabla u - P), \text{sym}(\nabla u - P) \rangle_{\mathbb{R}^{3 \times 3}}}_{\text{anisotropic elastic - energy}} + \underbrace{\frac{1}{2} \langle \mathbb{C}_m \text{sym } P, \text{sym } P \rangle_{\mathbb{R}^{3 \times 3}}}_{\text{micro - self - energy}} \quad (\text{I.6})$$

$$+ \underbrace{\frac{\mu L_c^2}{2} \langle \hat{\mathbb{L}} \nabla P, \nabla P \rangle_{\mathbb{R}^{3 \times 3 \times 3}}}_{\text{full anisotropic curvature}},$$

where $\mathbb{C}_e, \mathbb{C}_m : \text{Sym}(3) \rightarrow \text{Sym}(3)$ are classical 4^{th} order constitutive tensors acting on symmetric tensors and $\hat{\mathbb{L}} : \mathbb{R}^{3 \times 3 \times 3} \rightarrow \mathbb{R}^{3 \times 3 \times 3}$ is a 6^{th} order tensor acting on 3^{rd} order tensors.

In [74], the incompressible micro-strain model was proposed as a possible variation of the micro-strain model. In this case P would be a traceless symmetric tensor $P \in \{\mathfrak{sl}(3) \cap \text{Sym}(3)\}$ (5 additional degrees of freedom). The energy assumes the same form and will not, therefore, be written again.

2.6 The incompressible micromorphic model

The micro-incompressible micromorphic model was proposed in [74] to complete the set of possible micromorphic models. In this case the micro-distortion tensor is assumed to be traceless (i.e. $P \in \mathfrak{sl}(3)$ with 8 additional degrees of freedom). The energy would assume the same form of the Mindlin-Eringen format (for simplicity the cross coupling tensor $\bar{\mathbb{E}}_{\text{cross}}$ is discarded):

$$W = \underbrace{\frac{1}{2} \langle \bar{\mathbb{C}}_e (\nabla u - P), (\nabla u - P) \rangle_{\mathbb{R}^{3 \times 3}}}_{\text{full anisotropic elastic - energy}} + \underbrace{\frac{1}{2} \langle \mathbb{C}_m \text{sym } P, \text{sym } P \rangle_{\mathbb{R}^{3 \times 3}}}_{\text{micro - self - energy}} + \underbrace{\frac{\mu L_c^2}{2} \langle \hat{\mathbb{L}} \nabla P, \nabla P \rangle_{\mathbb{R}^{3 \times 3 \times 3}}}_{\text{full anisotropic curvature}}, \quad (\text{I.7})$$

where $\bar{\mathbb{C}}_e : \mathbb{R}^{3 \times 3} \rightarrow \mathbb{R}^{3 \times 3}$ is a 4^{th} order micromorphic elasticity tensor, $\mathbb{C}_m : \text{Sym}(3) \rightarrow \text{Sym}(3)$ is a classical fourth order elastic tensor, and $\hat{\mathbb{L}} : \mathbb{R}^{3 \times 3 \times 3} \rightarrow \mathbb{R}^{3 \times 3 \times 3}$ is a 6^{th} order tensor.

2.7 The relaxed micromorphic model

The *relaxed micromorphic model* [139, 140, 175, 176] is one of the main objects of this work. It will be briefly presented in this section, see Part III for the theoretical framework and Part IV for dynamic applications. The model has been introduced in 2013 in [176] and endows the standard Mindlin-Eringen's representation with more geometric structure. In particular, the full $P \in \mathbb{R}^{3 \times 3}$ is considered with its 9 additional degrees of freedom, but the energy assumed for the model is:

$$\begin{aligned}
 W = & \underbrace{\frac{1}{2} \langle \mathbb{C}_e \operatorname{sym}(\nabla u - P), \operatorname{sym}(\nabla u - P) \rangle_{\mathbb{R}^{3 \times 3}}}_{\text{anisotropic elastic - energy}} + \underbrace{\frac{1}{2} \langle \mathbb{C}_m \operatorname{sym} P, \operatorname{sym} P \rangle_{\mathbb{R}^{3 \times 3}}}_{\text{micro - self - energy}} \\
 & + \underbrace{\frac{1}{2} \langle \mathbb{C}_c \operatorname{skew}(\nabla u - P), \operatorname{skew}(\nabla u - P) \rangle_{\mathbb{R}^{3 \times 3}}}_{\text{invariant local anisotropic rotational elastic coupling}} + \underbrace{\frac{\mu L_c^2}{2} \langle \bar{\mathbb{L}} \operatorname{Curl} P, \operatorname{Curl} P \rangle_{\mathbb{R}^{3 \times 3}}}_{\text{curvature}}. \tag{I.8}
 \end{aligned}$$

For the energy, the underlying assumptions are the decoupled format and the replacement of the full gradient ∇P with the dislocation density tensor $\alpha = -\operatorname{Curl} P^3$. Therefore, the energy has separate parts for the symmetric part of $\nabla u - P$, the skew-symmetric part of $\nabla u - P$, the symmetric part of P and the curvature $\alpha = -\operatorname{Curl} P$. This simplification leads to:

- the 4th order constitutive tensors $\mathbb{C}_e : \operatorname{Sym}(3) \rightarrow \operatorname{Sym}(3)$ and $\mathbb{C}_m : \operatorname{Sym}(3) \rightarrow \operatorname{Sym}(3)$, which have the same structure as in classical elasticity with at most 21 independent constants, acting on the 2nd order symmetric strains $\operatorname{sym}(\nabla u - P)$ and $\operatorname{sym} P$, respectively;
- the 4th order tensor $\mathbb{C}_c : \mathfrak{so}(3) \rightarrow \mathfrak{so}(3)$, which has at most 6 independent constants, acting on the 2nd order skew-symmetric strain $\operatorname{skew}(\nabla u - P)$;
- the 4th order constitutive tensor $\bar{\mathbb{L}} : \mathbb{R}^{3 \times 3} \rightarrow \mathbb{R}^{3 \times 3}$, which has at most 45 independent constants, acting on the 2nd order tensor $\alpha = -\operatorname{Curl} P$ (for comparison the 6th order $\hat{\mathbb{L}} : \mathbb{R}^{3 \times 3 \times 3} \rightarrow \mathbb{R}^{3 \times 3 \times 3}$ acting on ∇P has at most 378 parameters);
- the absence of Mindlin-Eringen's cross coupling constitutive tensor $\bar{\mathbb{E}}_{\text{cross}}$, which is of difficult interpretation.

Counting coefficients we now have $21+21+6+45=93$, instead of Mindlin-Eringen's 498 coefficients. The main advantage at this stage is that \mathbb{C}_e and \mathbb{C}_m , unlike $\bar{\mathbb{C}}_e$, possess all the symmetries that are peculiar to the classical elasticity tensors acting on $\operatorname{sym} \nabla u$. Nevertheless, the structure of the model continues to be very rich.

The large number of constants in the standard Mindlin-Eringen model (even in the isotropic case) has always been of concern. Previous attempts to endow the Mindlin-Eringen model with more structure include Koh's [112, 190] so-called micro-isotropy postulate which requires, among others, that $\operatorname{sym} \sigma$ is an isotropic function of $\operatorname{sym} \nabla u$ only. This reduces the number of isotropic coefficients to 5 (similarly to our relaxed model) but the fact of connecting $\operatorname{sym} \sigma$ to $\operatorname{sym} \nabla u$ only cannot be considered a well-grounded hypothesis.

Another interesting property of the relaxed micromorphic model is that certain limiting cases of the anisotropic relaxed micromorphic model give as a result other micromorphic models (e.g. the Cosserat model, the micro-voids theory, the micro-incompressible micromorphic model, the micro-stretch theory and the microstrain model), as shown in Appendix A.1.

Some variation of the relaxed micromorphic model have also been proposed in [138]. For example, a curvature term depending on the second order tensor $\operatorname{Div} P$ could be considered in the strain energy density

³The dislocation tensor is defined as $\alpha_{ij} = -(\operatorname{Curl} P)_{ij} = -P_{ih,k} \epsilon_{jhk}$, where ϵ is the Levi-Civita tensor.

leading to:

$$\begin{aligned}
 W = & \underbrace{\frac{1}{2} \langle \mathbb{C}_e \operatorname{sym}(\nabla u - P), \operatorname{sym}(\nabla u - P) \rangle_{\mathbb{R}^{3 \times 3}}}_{\text{anisotropic elastic - energy}} + \underbrace{\frac{1}{2} \langle \mathbb{C}_m \operatorname{sym} P, \operatorname{sym} P \rangle_{\mathbb{R}^{3 \times 3}}}_{\text{micro - self - energy}} \quad (\text{I.9}) \\
 & + \underbrace{\frac{1}{2} \langle \mathbb{C}_c \operatorname{skew}(\nabla u - P), \operatorname{skew}(\nabla u - P) \rangle_{\mathbb{R}^{3 \times 3}}}_{\text{invariant local anisotropic rotational elastic coupling}} + \underbrace{\frac{\mu L_c^2}{2} \langle \bar{\mathbb{L}} \operatorname{Div} P, \operatorname{Div} P \rangle_{\mathbb{R}^{3 \times 3}}}_{\text{curvature}}.
 \end{aligned}$$

Imposing that the curvature term vanishes, we obtain as a limit case the so-called internal variable model:

$$\begin{aligned}
 W = & \underbrace{\frac{1}{2} \langle \mathbb{C}_e \operatorname{sym}(\nabla u - P), \operatorname{sym}(\nabla u - P) \rangle_{\mathbb{R}^{3 \times 3}}}_{\text{anisotropic elastic - energy}} + \underbrace{\frac{1}{2} \langle \mathbb{C}_m \operatorname{sym} P, \operatorname{sym} P \rangle_{\mathbb{R}^{3 \times 3}}}_{\text{micro - self - energy}} \quad (\text{I.10}) \\
 & + \underbrace{\frac{1}{2} \langle \mathbb{C}_c \operatorname{skew}(\nabla u - P), \operatorname{skew}(\nabla u - P) \rangle_{\mathbb{R}^{3 \times 3}}}_{\text{invariant local anisotropic rotational elastic coupling}}.
 \end{aligned}$$

CHAPTER I.3

Higher gradient models

Higher gradient models derive from the hypothesis that the stress σ in each material point X does not depend only on the displacement u of the material points and its first gradient, but also on higher gradients of u . The idea of a higher gradient theory seems to be a natural generalization of the classical Cauchy model in a more inclusive setting. However, due to the inherent complexity of the model, the definition of a well-posed higher gradient model directly by the stress σ is very complex, if not downright impossible. On the other hand, it is possible to define a gradient theory of the n -th order via strain and kinetic energy densities that do not depend only on ∇u but also on its successive gradients up to order n , i.e.,

$$W = W(\nabla u, \nabla^2 u, \nabla^3 u, \dots), \quad J = J(u, t, \nabla u, t, \nabla^2 u, t, \nabla^3 u, t, \dots). \quad (\text{I.11})$$

The classical Cauchy model is included as a gradient theory of the first order¹, see chapter I.1. Moreover, we will call second gradient continua (sometimes referred to a first strain-gradient continua) those media whose strain energy density depends both on the first and second gradients of the displacement field, i.e.:

$$W = W(\nabla u, \nabla^2 u). \quad (\text{I.12})$$

In a second gradient model, the concept of contact actions needs more general treatment than the one due to Cauchy, for example new types of actions can be applied: surface double-forces and edge forces. As mentioned before, higher gradient models are weakly non-local, i.e. the response depends only on the local displacement field but it is influenced by a neighboring region via the higher derivatives of the displacement. This is a weaker non-locality with respect to the peridynamic models, whose strain energy density depends on the displacement of the entire body.

Since the first formulation of higher gradient models, their spreading has been limited by the complexity of the underlying mathematical structure and by a still unclear physical interpretation of the boundary conditions. Furthermore, different approaches to the determination of the boundary conditions lead to different results rising doubts on the validity of the resulting conditions [135]. For this reason, it makes sense to come up with two possible strategies to deal with second gradient continua:

- directly use kinematics uniquely based on the macroscopic displacement field and consider higher gradients of the displacement in the strain and kinetic energy densities;
- start from a richer kinematics (as done for micromorphic media) and then impose suitable constraints on the extra kinematical descriptors in order to obtain the desired second gradient model as a limiting case.

Let us first consider the first approach and the simple case of a second gradient model. The characteristic which makes a second gradient theory different from a first gradient one is the fact that the strain energy density does not depend only on first gradient of the displacements. A simple, infinitesimal strain theory would give, therefore, an energy of the type²:

$$W = \frac{1}{2} \langle \mathbb{C}_M \text{sym } \nabla u, \text{sym } \nabla u \rangle_{\mathbb{R}^{3 \times 3}} + \frac{\mu L_c^2}{2} \langle \widehat{\mathbb{L}} \nabla (\text{sym } \nabla u), \nabla (\text{sym } \nabla u) \rangle_{\mathbb{R}^{3 \times 3 \times 3}} \quad (\text{I.13})$$

On the other hand, the second approach would lead to an energy of the type:

$$W = \frac{1}{2} \langle \mathbb{C}_M \text{sym } \nabla u, \text{sym } \nabla u \rangle_{\mathbb{R}^{3 \times 3}} + \frac{\mu L_c^2}{2} \langle \widehat{\mathbb{L}} \nabla \text{sym } P, \nabla \text{sym } P \rangle_{\mathbb{R}^{3 \times 3 \times 3}} + \frac{1}{2} \Lambda \| \nabla u - P \|_{\mathbb{R}^{3 \times 3}}^2, \quad (\text{I.14})$$

¹From now on, we will refer to the Cauchy model also as first gradient model.

²For the sake of simplicity, the cross terms between the first and the second gradient of the displacement are omitted.

where Λ is a Lagrangian multiplier that weakly enforces the condition $\nabla u = P$. We note here that it is not possible to suitably restrict the parameters of the relaxed micromorphic model, which is one of the main subjects of this manuscript, to obtain a full higher gradient elasticity model, in sharp contrast to the standard Mindlin-Eringen model where $\bar{C}_e \rightarrow \infty$ implies $\nabla u = P$ and $\|\nabla P\|^2 \rightarrow \|\nabla \nabla u\|^2$, see Appendix A.2 for the one dimensional case.

Which of the two strategies has to be used to deal with the application of a second gradient theory is a matter of convenience. In this manuscript, we mention all the available possibilities for the sake of a complete description of enriched continuum theories. The direct implementation of a second gradient model has the following advantages with respect to the micromorphic theories:

- the number of degrees of freedom is lower;
- the differential system of associated Euler-Lagrange equations counts less equations.

On the other hand, the strategy with micromorphic theories gives three main advantages:

- easier physical interpretation of internal and external internal actions related to microstructure (see section I.4.4);
- the differential system of associated Euler-Lagrange equations is of lower order;
- FEM implementation with traditional shape functions: no need to impose the continuity of the derivatives on the mesh boundaries.

Notwithstanding the previous considerations, we want to stress the fact that the correct continuum framework which we found to be well-adapted for describing the mechanical behavior of fibrous composite reinforcements is the one of second gradient theories, even if the numerical implementation could be eased by passing through a constrained micromorphic model.

CHAPTER I.4

The Principle of Virtual Work and the equilibrium of enriched continuous models

The Principle of Virtual Work (PVW) is one of the first quantitative laws in the history of mechanics. Historically, the principle of virtual work and the associated calculus of variations were formulated to analyze systems of rigid bodies, but it has been extended for the study of the mechanics of deformable bodies. Let us consider the following statement of the Principle of Virtual Works:

Considering a Galilean frame with an absolute Newtonian chronology, the virtual work of internal actions \mathcal{P}^{int} , spent by the inertial forces minus the internal ones, balances the virtual work of external actions \mathcal{P}^{ext} , spent by the external forces impressed on the system, for any virtual displacement field.

In formulas, the Principle of virtual work says that a configuration is in dynamical equilibrium if and only if¹:

$$\mathcal{P}^{int} + \mathcal{P}^{ext} = 0. \quad (\text{I.15})$$

Suitable generalizations of the Principle of Virtual Work can be introduced to account for dissipative effects, but we refrain here from presenting such more complex framework. Therefore, the most fundamental questions which have to be confronted to properly set up a mechanical theory by means of the Principle of Virtual Work is to establish:

- the constitutive form of the *work of internal actions* \mathcal{P}^{int} in terms of the displacement and, eventually, of the micro-descriptor (such constitutive choice is related to the intrinsic nature of the medium that one wants to study),
- the expression of the *work of external actions* \mathcal{P}^{ext} , which allows to establish how the external world acts on the considered medium and to define the concept of force, double force, or other more complex interactions.

Furthermore, we can consider different kinds of external actions applied to the boundary (or to the bulk) of the continuum body that either restrict the set of admissible configurations or that spend some energy on its displacement². As a matter of fact, we can imagine acting on the boundary of the considered body by imposing either

- kinematic (or essential or geometric) boundary conditions: the displacement and/or eventually the micro-descriptor are assigned on some portion of the boundary ∂B ,
- traction (or natural) boundary conditions: forces and/or, eventually, other more complex external interactions are assigned on some portion of the boundary ∂B and/or of the bulk B .

Imposing a kinematic boundary condition is tantamount to reduce the admissible deformed configurations that the body can assume, so reducing the number of admissible fields. This will be analyzed with more care in section I.4.1. On the other hand, imposing traction boundary conditions means that an external action is acting on the body and therefore a corresponding term must be considered in the work of external forces. However, the set of actions that can be applied to the body depends on the kind of model considered, see sections I.4.2, I.4.3 and I.4.4.

¹We remark that, depending on the conventions which are used for the signs in the definition of the work of internal and external actions, slightly different versions of the Principle of Virtual Work can be found in the literature.

²In what follows, we will call *continuum body* a set of material particles occupying the volume B in its reference configuration and its boundary will be denoted with ∂B .

4.1 Space of configurations and spaces of admissible variations

Depending on the intrinsic nature of the considered body (first gradient or micromorphic or second gradient), the expressions for the work of internal and external actions take specific forms which will be better specified later on. However, independently of the specific form taken by the internal and external work and the type of continuum, finding the equilibrium configuration under specific kinematic boundary conditions is equivalent to searching, in some *suitable set*, for the kinematic fields which satisfy the Principle of Virtual Work for any admissible virtual variation. Therefore, the definition of a *suitable set* Q , that contains all the possible solutions of the equilibrium problem, is of paramount importance. The set Q is called *space of configurations* of the considered medium and contains information about the kinematical constraints applied on the body, which must be verified by the kinematic fields.

In the case of a Cauchy continuum, the form assumed by the space of configurations is:³

$$Q = \{u \mid u = \bar{u} \text{ on } \Sigma_{K_1} \subseteq \partial B\}, \quad (\text{I.16})$$

where \bar{u} is a suitably assigned function and Σ_{K_1} is the subset of ∂B on which the kinematic boundary conditions are applied. Roughly speaking, the set Q represents the set in which we look for the solution of our minimization problem and contains only those displacement fields which satisfy the imposed kinematical boundary conditions. Furthermore, we define the set of admissible variations (i.e. the admissible virtual displacement field) as:

$$T_u = \{\delta u \mid u + \delta u \in Q\}. \quad (\text{I.17})$$

We explicitly remark that, since $u = \bar{u}$ on Σ_{K_1} , in order to have δu belonging to the set of admissible variations, one must have that $\bar{u} + \delta u = \bar{u}$ on Σ_{K_1} . This clearly implies that $\delta u = 0$ on Σ_{K_1} , and hence the set of admissible variations takes the form $T_u = \{\delta u \mid \delta u = 0 \text{ on } \Sigma_{K_1}\}$.

Setting up suitable minimization problems can be extended in a natural way to higher gradient continua by suitably restricting the space of configurations Q with a richer set of possible kinematic constraints. Considering for instance a second gradient continuum, Q assumes a form analogous to the first gradient case but some boundary condition can be applied to components of the gradient ∇u on ∂B and/or to the displacement u on boundary of the boundary $\partial\partial B$ (e.g. constrained edges in the 3D case). The components of ∇u that can be constrained depend on the form of the second gradient energy, therefore we show only one of the possible space of configurations:

$$Q = \{u \mid u = \bar{u} \text{ on } \Sigma_{K_1} \subseteq \partial B, \nabla u \cdot n = \bar{u}_n \text{ on } \Sigma_{K_2} \subseteq \partial B\}, \quad (\text{I.18})$$

where \bar{u} and \bar{u}_n are suitably assigned functions and Σ_{K_1} and Σ_{K_2} are the subsets of ∂B on which the kinematic boundary conditions are applied. The set of admissible variations T_u is formally analogous to the first gradient case. It could be noted that all the considerations made on the first gradient type boundary conditions apply now to the richer set allowed in the higher order gradient case.

The equilibrium problem for a micromorphic continuum can be set up by suitably generalizing what was done for Cauchy continua. In particular, a supplementary set D must be defined to specify the space of configurations for such a continuum:

$$D = \{P \mid P = \bar{P} \text{ on } \Sigma_{K_2} \subseteq \partial B\}, \quad (\text{I.19})$$

where \bar{P} is a suitably assigned function and Σ_{K_2} is the subsets of ∂B on which the kinematic boundary conditions are imposed. Roughly speaking, the set D represents the set in which we look for the solution for the micro-motion of our minimization problem and contains only those micro-motions which satisfy the imposed kinematical boundary conditions. We remark that, in the spirit of Mindlin [156] and Eringen [67], such a supplementary kinematical field represents the motion of a microstructure which is embedded in the considered body. In principle, such micro-motion is completely independent of the macroscopic motion of the matrix. Nevertheless, in some cases of physical interest, it is worth relating such micro-descriptors to the derivatives of the macroscopic displacement field. Moreover, we define a supplementary set of admissible variations as

$$T_P = \{\delta P \mid P + \delta P \in D\}. \quad (\text{I.20})$$

³The space of configurations should also contain informations concerning the desired regularity on the corresponding kinematic fields, but we limit ourselves here by talking about “suitably regular” functions.

4.2 The equilibrium of a first gradient continuum

The equilibrium of a Cauchy continuum body subjected to given boundary conditions can be studied by means of the Principle of Virtual Work. This fundamental principle of Mechanics states that a body, subjected to specific external actions, is in equilibrium if the work of internal actions is balanced by the work of external actions. In formulas, we say that a displacement field u^* is in dynamic equilibrium if and only if:

$$\mathcal{P}^{int}(u^*, \delta u) + \mathcal{P}^{ext}(u^*, \delta u) = 0, \quad (\text{I.21})$$

for any admissible δu . With the introduced notations, we can formulate the equilibrium problem for a Cauchy continuum as:

$$\text{Find } u^* \in Q \text{ such that } \mathcal{P}^{int}(u^*, \delta u) + \mathcal{P}^{ext}(u^*, \delta u) = 0, \quad \forall \delta u \in T_{u^*}.$$

In most cases, the external and internal works can be seen as the first variation of suitable functionals $\mathcal{A}^{int}(u) : Q \rightarrow \mathbb{R}$ and $\mathcal{A}^{ext}(u) : Q \rightarrow \mathbb{R}$, so that the Principle of Virtual Work (I.21) actually implies the minimization of a functional $\mathcal{A} := \mathcal{A}^{int} + \mathcal{A}^{ext}$. More specifically, we can write

$$\mathcal{P}^{int}(u, \delta u) + \mathcal{P}^{ext}(u, \delta u) = \delta \mathcal{A}(u, \delta u) := \lim_{t \rightarrow 0^+} \frac{\mathcal{A}(u + t \delta u) - \mathcal{A}(u)}{t}, \quad u \in Q, \quad \delta u \in T_u, \quad (\text{I.22})$$

where the sets Q and T_u were defined in the previous section and $\delta \mathcal{A}$ is the first variation of the functional \mathcal{A} .

As it has been previously pointed out, to establish the equilibrium problem for a given continuum body subjected to specific external interactions, the expressions of both the work of internal and external actions must be specified. For a first gradient continuum, the work of internal actions can be defined by the action functional \mathcal{A}^{int} :

$$\mathcal{A}^{int} = - \int_0^T \int_B (W(\nabla u) - J(\dot{u})) \, dB \, dt, \quad (\text{I.23})$$

where W is the strain energy density which, in a Cauchy continuum, constitutively depends only on the first gradient of displacement, and J is the kinetic energy density.

In the case of first gradient theories, the work of internal actions can be written as ⁴

$$\begin{aligned} \mathcal{P}^{int}(u, \delta u) &= - \int_0^T \int_B (\delta W - \delta J) \, dB \, dt = - \int_0^T \int_B \left(\left\langle \frac{\partial W}{\partial \nabla u}, \nabla \delta u \right\rangle - \left\langle \frac{\partial J}{\partial \dot{u}}, \delta \dot{u} \right\rangle \right) \, dB \, dt \\ &= \int_0^T \int_B \left(\left\langle \text{Div} \left(\frac{\partial W}{\partial \nabla u} \right) - \frac{d}{dt} \frac{\partial J}{\partial \dot{u}}, \delta u \right\rangle \right) \, dB \, dt - \int_0^T \int_{\partial B} \left\langle \frac{\partial W}{\partial \nabla u} \cdot n, \delta u \right\rangle \, ds \, dt \\ &\quad + \left[\int_B \left\langle \frac{\partial J}{\partial \dot{u}}, \delta u \right\rangle \, dB \right]_0^T, \end{aligned} \quad (\text{I.24})$$

where, to obtain the last identity, the divergence theorem and the integration by parts have been used. Equation (I.24) provides the *irreducible expression of the work of internal actions* for a first gradient continuum. Following Lagrange, it is generally assumed that the set of admissible motions is included in the set of isochronous motions between two instants, i.e. motions which start from a given configuration at instant 0 and arrive to another given configuration at the instant T. Therefore the term $\left[\int_B \left\langle \frac{\partial J}{\partial \dot{u}}, \delta u \right\rangle \, dB \right]_0^T$ vanishes. No more integrations by parts can be performed to ulteriorly manipulate this expression of \mathcal{P}^{int} . We remark here that, from this irreducible form of the internal work, only quantities expending work on the virtual displacement δu (i.e. forces) appear. It is for this reason that, based on the validity of the Principle of Virtual

⁴The operator Div stands for the classical divergence operator. For a tensor field A of any order $n > 0$, we define its divergence as the $n - 1$ tensor $(\text{Div} A)_{i_1, \dots, i_{n-1}} = A_{i_1, \dots, i_n, i_n}$. Finally $\langle a, b \rangle = a_{i_1, \dots, i_n} b_{i_1, \dots, i_n}$ is the scalar product between two tensors of any order $n \geq 1$ and the Einstein convention of sum over repeated indices is used.

Work, we can affirm that the only external actions which can be sustained by a first gradient continuum are forces per unit area or volume, i.e. external actions expending work on δu . These observations are at the heart of introducing the work of external actions for first gradient continua in the form

$$\mathcal{P}^{ext}(u, \delta u) = \int_B \langle b, \delta u \rangle dv + \int_{\partial B} \langle f, \delta u \rangle ds, \quad (\text{I.25})$$

where $b : B \rightarrow \mathbb{R}^3$ and $f : \partial B \rightarrow \mathbb{R}^3$ are external actions in the bulk and on the boundary of B , respectively.

Having assigned the specific form for the work of internal and external actions, the equilibrium problem for a first gradient continuum can be reformulated as follows (\mathcal{P}^{int} , \mathcal{P}^{ext} , Q and T_{u^*} being as in Eqs. (I.24), (I.25), (I.16) and (I.17)):

$$\int_0^T \int_B \left(\left\langle \text{Div} \left(\frac{\partial W}{\partial \nabla u} \right) - \frac{d}{dt} \frac{J}{\partial \dot{u}} + b, \delta u \right\rangle \right) dB dt - \int_0^T \int_{\partial B} \left\langle \frac{\partial W}{\partial \nabla u} \cdot n - f, \delta u \right\rangle ds dt = 0,$$

which is identically verified for every variation δu if and only if:

$$\begin{aligned} \frac{d}{dt} \frac{J}{\partial \dot{u}} &= \text{Div} \left(\frac{\partial W}{\partial \nabla u} \right) + b, & \forall X \in B, \\ \frac{\partial W}{\partial \nabla u} \cdot n &= f, & \forall X \in \partial B. \end{aligned} \quad (\text{I.26})$$

Defining the stress $\sigma = \frac{\partial W}{\partial \nabla u}$ and considering a simple kinetic energy of the type $J = \rho \|\dot{u}\|^2$, the equilibrium equations take the usual form:

$$\rho \ddot{u} = \text{Div} \sigma + b, \quad \forall X \in B, \quad \sigma \cdot n = f, \quad \forall X \in \partial B. \quad (\text{I.27})$$

4.3 The equilibrium of a micromorphic continuum

Suitably generalizing the definitions given above for first gradient continua, the Principle of Virtual Work can be reformulated for a micromorphic continuum by saying that a couple (u^*, P^*) is in equilibrium if

$$\mathcal{P}^{int}(u^*, P^*, \delta u, \delta P) + \mathcal{P}^{ext}(u^*, P^*, \delta u, \delta P) = 0, \quad (\text{I.28})$$

for any compatible $(\delta u, \delta P)$. With the introduced notations, we can formulate the equilibrium problem for a micromorphic continuum as:

$$\begin{aligned} & \text{Find } (u^*, P^*) \in Q \times D \text{ such that} \\ & \mathcal{P}^{int}(u^*, P^*, \delta u, \delta P) + \mathcal{P}^{ext}(u^*, P^*, \delta u, \delta P) = 0, \quad \forall (\delta u, \delta P) \in T_{u^*} \times T_{P^*}. \end{aligned}$$

Once again, the external and internal works can be seen as the first variation of suitable functionals $\mathcal{A}^{int}(u, P) : Q \times D \rightarrow \mathbb{R}$ and $\mathcal{A}^{ext}(u, P) : Q \times D \rightarrow \mathbb{R}$, so that the Principle of Virtual Work (I.28) actually implies the minimization of a functional $\mathcal{A} := \mathcal{A}^{int} + \mathcal{A}^{ext}$. More specifically, we can write

$$\mathcal{P}^{int}(u, P, \delta u, \delta P) + \mathcal{P}^{ext}(u, P, \delta u, \delta P) = \delta \mathcal{A}(u, P, \delta u, \delta P) := \lim_{t \rightarrow 0^+} \frac{\mathcal{A}(u + t \delta u, P + t \delta P) - \mathcal{A}(u, P)}{t}, \quad (\text{I.29})$$

where we denoted again by $\delta \mathcal{A}$ the first variation of the functional \mathcal{A} , where $(u, P) \in Q \times D$, $(\delta u, \delta P) \in T_u \times T_P$ and the sets Q , D , T_u and T_P will be defined in more detail later on.

For a micromorphic continuum, the work of internal actions can be defined through the definition of the action functional \mathcal{A}^{int} as:

$$\mathcal{A}^{int} = - \int_0^T \int_B \left(W(\nabla u, P, \nabla P) - J(\dot{u}, \dot{P}) \right) dB dt, \quad (\text{I.30})$$

where, once again, W is the strain energy density which and J is the kinetic energy density .

The internal work can be rewritten as in the case of a first gradient theory but the variation must be done also in δP . The power of internal actions \mathcal{P}^{int} contains a set of terms which depends on δu that are formally analogous to the first gradient case with the addition of the following terms in δP :

$$\begin{aligned}
& - \int_0^T \int_B \left(\left\langle \frac{\partial W}{\partial \dot{P}}, \delta P \right\rangle + \left\langle \frac{\partial W}{\partial \nabla P}, \nabla \delta P \right\rangle - \left\langle \frac{J}{\partial \dot{P}}, \delta \dot{P} \right\rangle \right) dB dt \\
& = \int_0^T \int_B \left(\left\langle -\frac{\partial W}{\partial P} + \text{Div} \left(\frac{\partial W}{\partial \nabla P} \right) - \frac{d}{dt} \frac{J}{\partial \dot{P}}, \delta P \right\rangle \right) dB dt - \int_0^T \int_{\partial B} \left\langle \frac{\partial W}{\partial \nabla P} \cdot n, \delta P \right\rangle ds dt \\
& \quad + \left[\int_B \left\langle \frac{J}{\partial \dot{P}}, \delta P \right\rangle dB \right]_0^T,
\end{aligned} \tag{I.31}$$

where, to obtain the last identity, the divergence theorem and integration by parts have been used. Equation (I.31) furnishes the *irreducible expression of the additional terms in the work of internal actions* for a micromorphic continuum. As in the first gradient case, the term $\left[\int_B \left\langle \frac{J}{\partial \dot{P}}, \delta P \right\rangle dB \right]_0^T$ vanishes. We remark here that, from this irreducible form of the internal work, only quantities expending work on the virtual displacement δP can be recognized. Therefore, we include additional external actions expending work on δP , since they can be sustained by a micromorphic continuum. These considerations are at the origin of a work of external actions of the form

$$\mathcal{P}^{ext}(u, \delta u) = \int_B (\langle b_u, \delta u \rangle + \langle b_P, \delta P \rangle) dB + \int_{\partial B} (\langle f_u, \delta u \rangle + \langle f_P, \delta P \rangle) ds, \tag{I.32}$$

where $b_u, b_P : B \rightarrow \mathbb{R}^3$ and $f_u, f_P : \partial B \rightarrow \mathbb{R}^3$ are external actions in the bulk and on the boundary of B , respectively.

Once the specific form for the work of internal and external actions is assigned, the equilibrium problem can be reformulated as follows:

$$\begin{aligned}
& \int_0^T \int_B \left(\left\langle \text{Div} \left(\frac{\partial W}{\partial \nabla u} \right) - \frac{d}{dt} \frac{J}{\partial \dot{u}} + b_u, \delta u \right\rangle \right) dB dt - \int_0^T \int_{\partial B} \left\langle \frac{\partial W}{\partial \nabla u} \cdot n - f_u, \delta u \right\rangle ds dt \\
& \quad + \int_0^T \int_B \left(\left\langle -\frac{\partial W}{\partial P} + \text{Div} \left(\frac{\partial W}{\partial \nabla P} \right) - \frac{d}{dt} \frac{J}{\partial \dot{P}} + b_P, \delta P \right\rangle \right) dB dt \\
& \quad - \int_0^T \int_{\partial B} \left\langle \frac{\partial W}{\partial \nabla P} \cdot n - f_P, \delta P \right\rangle ds dt = 0,
\end{aligned} \tag{I.33}$$

which holds for every variation δu and δP if and only if:

$$\begin{aligned}
\frac{d}{dt} \frac{J}{\partial \dot{u}} &= \text{Div} \left(\frac{\partial W}{\partial \nabla u} \right) + b_u, & \frac{d}{dt} \frac{J}{\partial \dot{P}} &= -\frac{\partial W}{\partial P} + \text{Div} \left(\frac{\partial W}{\partial \nabla P} \right) + b_P, & \forall X \in B, \\
\frac{\partial W}{\partial \nabla u} \cdot n &= f_u, & \frac{\partial W}{\partial \nabla P} \cdot n &= f_P, & \forall X \in \partial B.
\end{aligned} \tag{I.34}$$

This expression can be simplified by assigning a strain and a kinetic energy. The equations obtained for the relaxed micromorphic model will be shown in Part III.

4.4 The equilibrium of a second gradient continuum

The second gradient continuum is analogous to the first gradient case, apart from the functional dependency of the strain energy density. The equilibrium problem for a second gradient continuum is therefore:

$$\text{Find } u^* \in Q \text{ such that } \mathcal{P}^{int}(u^*, \delta u) + \mathcal{P}^{ext}(u^*, \delta u) = 0, \quad \forall \delta u \in T_{u^*}.$$

However, the work of internal actions is defined through the action functional \mathcal{A}^{int} that depends on the first and the second gradient of displacement:

$$\mathcal{A}^{int} = - \int_0^T \int_B (W(\nabla u, \nabla \nabla u) - J(\dot{u})) dB dt, \quad (\text{I.35})$$

where W is the strain energy density and J is the kinetic energy density. As we did in the other cases we can write the power of internal actions \mathcal{P}^{int} that has an additional term compared to the first gradient continuum, namely:

$$\mathcal{P}^{int}(u, \delta u) = - \int_0^T \int_B \left(\left\langle \frac{\partial W}{\partial \nabla \nabla u}, \nabla \nabla \delta u \right\rangle + \left\langle \frac{\partial W}{\partial \nabla u}, \nabla \delta u \right\rangle - \left\langle \frac{J}{\partial \dot{u}}, \delta \dot{u} \right\rangle \right) dB dt. \quad (\text{I.36})$$

Once again, we can work on this expression obtaining terms in the bulk B , on the boundary ∂B and on also the boundary of the boundary $\partial \partial B$ (e.g. constrained edges in the 3D case), meaning that a second gradient model is able to react to bulk, surface and also edge forces. However, the interpretation of boundary contact actions, namely forces and double-forces, depends on the type of manipulation which is done on the work of internal actions by means of integration by parts (see e.g. [135, 156, 157]). More particularly, if one decides to stop after integrating by parts a specific amount of times, or to continue the procedure, the definition of force and double force is not the same⁵. On the other hand, when considering micromorphic continua in which only first gradient of the introduced kinematical fields appear in the strain energy density, integration by parts is possible only once: the boundary contact actions are uniquely defined and take immediate physical meaning when framed in the considered physical problem. Therefore, it is possible to keep a more general micromorphic model and to subsequently constrain its strain energy density in order to let it tend to a second gradient one. This choice is preferable to directly interpret in a unique way the external actions of the considered continuum.

⁵We need to mention the fact that no common agreement is currently available concerning the choice of different but equally legitimate sets of boundary conditions deriving to different levels of integration by parts.

Part II

Modeling fibrous composite reinforcements as second gradient materials

Contents of Part II

Introduction	25
1 The multi-scale structure and behavior of fibrous composite reinforcements	26
1.1 Microscopic scale: the fiber	27
1.2 Mesoscopic scale: the yarn	27
1.3 Macroscopic scale: the reinforcement	30
1.3.1 Types of reinforcement	30
1.3.2 Mechanical behavior of the reinforcement	31
1.3.3 Consolidation processes	34
2 Modeling of fibrous composite reinforcements	35
2.1 Modeling approaches for fibrous composite reinforcements	35
2.1.1 Microscopic modeling	35
2.1.2 Mesoscopic modeling	36
2.1.3 Macroscopic modeling	37
2.2 Macroscopic enriched continuous modeling	38
2.2.1 Hyperelastic first gradient model	39
2.2.2 Hyperelastic orthotropic second gradient strain energy density	40
2.2.3 Considerations on the numerical implementation of an enriched continuous model	41
2.3 Discrete mesoscopic 2D modeling	43
3 The Bias Extension Test	44
3.1 Characterization of the shear response of woven composite reinforcements	44
3.2 The BET on unbalanced fabrics	45
3.2.1 Experimental setup	45
3.2.2 Experimental results and physical interpretation	47
3.3 Modeling 2D woven fabrics	49
3.3.1 First gradient model	49
3.3.2 Second gradient model	50
3.3.3 Discrete model	51
3.4 Numerical results	51
4 Deep Drawing	56
4.1 Second gradient energy	57
4.2 Modeling geometry and contact interaction between the mold and the reinforcement	58
4.3 Numerical results	59
4.3.1 Influence of the second gradient on the wrinkling	59
4.3.2 Some considerations concerning mesh-dependency of the performed simulations	61
Conclusion	64

Introduction

In material science, a composite material is defined as a heterogeneous material with two or more distinct components whose resulting material properties exceed the ones of the single components. Such a wide definition can be interpreted to include a wide set of materials both natural (e.g. wood and bones) and man-made (as the well-known reinforced concrete). As in most engineering cases, the development of our ability to design and build composite materials has been driven mainly by the wish to optimize both the resulting mechanical pieces and the economical investments; nonetheless, applications which were unthinkable centuries ago are now feasible through this endeavor. Among the sectors influenced by composites, it is worth mentioning the domains of aeronautical and aerospace engineering, where the need for light materials, which still possess outstanding mechanic properties, lead to big investments in the field.

The most widespread kind of composite are built from two components which have a very different function: a reinforcement, that gives the material the desired physical properties, and a matrix, that gives cohesion to the assembly. Certainly, it is possible to find composites made by more than two components (e.g. if more than one physical property is targeted) but the two-phase composite is already adaptive enough for most applications. The matrices of composite materials currently developed are generally classified into two categories:

- organic matrices (thermoplastic polymers, thermosetting polymers and elastomers): they represent the vast majority of matrices used industrially due to their low cost and ease of implementation of the manufacturing process;
- Mineral matrices: ceramic (oxides and carbides) and metallic matrices (aluminum, magnesium, iron, cobalt, copper) are intended for advanced applications where hostile environmental conditions do not allow the use of an organic matrix (high temperatures, unfavorable hygrometry).

The other component of this kind of composite materials is the reinforcement. We can define a classification considering their geometry: particle reinforcements, staple fiber reinforcements and continuous fiber reinforcements. In *particle reinforcements*, the matrix is reinforced by a dispersed phase of particles (granular inclusions, lamellar or short fibers) with or without a preferred orientation. On the other hand, considering *staple fiber reinforcements*, the matrix is reinforced by a dispersed phase of short fibers (lengths less than 100 times their diameters) with or without a preferred orientation. Finally, *in fiber reinforcements* the matrix is reinforced by a dispersed phase of continuous fibers whose length is close to that of the final part, whose privileged directions give the final part its main mechanical properties. Our focus will be put on fibrous composite reinforcements, in which two distinct sets of continuous fibers are interlaced to form a fabric or a cloth.

This part is structured as follows:

- in chapter II.1, the multi-scale structure and behavior of fibrous composite reinforcements is analyzed in detail;
- in chapter II.2, an overview of the possible models for the description of fibrous composite reinforcements is presented, with particular attention to the enriched continuous model put forth in this manuscript;
- in chapter II.3, a first application of enriched continuous modeling in the case of the bias extension test on an unbalanced fabric is presented;
- in chapter II.4, the enriched continuous model is applied to the case of the dry preforming of woven fabrics with particular attention to the phenomenon of wrinkling.

CHAPTER II.1

The multi-scale structure and behavior of fibrous composite reinforcements

In the last decades, one kind of material has sparked an ever increasing amount of interest among engineers: textile composites made of woven fabrics. The range of applicability includes fields such as aircraft engineering, aerospace engineering, automotive and various other industrial applications. Moreover, even greater potentialities are related to the use of such kind of materials, but a comprehensive model capable of describing their mechanical behavior is needed to exploit their excellent mechanical properties (e.g. a very high specific-strength and excellent formability characteristic). Therefore, our effort is directed to the development of new theories and softwares for the modeling of the response of such materials during the forming processes of industrial products and components.

The internal micro-structure of the woven fabrics strongly characterizes their mechanical properties and complicate the modeling of these kind of materials. During the process of weaving, small yarns or tows are woven in order to form a very complex texture. These yarns are made by materials which possess high specific mechanical properties such as the almost traditional carbon and glass fibers or even polymeric and ceramic fibers. Furthermore, in the case of carbon fiber reinforcements each yarn is itself a composition of thousands of small carbon fibers. This very complex microstructure characterizes the global features of the material response, mainly due to the interaction between the yarns and their behavior at a mesoscopic level.

The two main directions of woven yarns (warp and weft), each composed by a high number of fibers, define the structure of the fabric. These direction, which are usually orthogonal, possess a very high extensional rigidity. Moreover, the friction between the fibers both prevents slipping and generates the shear rigidity of the fabric that, being usually different orders of magnitude lower than the elongation stiffness of the yarns, fundamentally determines the overall behavior of the fabric. The characteristics of the fabric are also influenced by the weaving scheme and, consequently, to each kind of weaving correspond different mechanical properties of the relative woven composite. One more characteristic that can profoundly determine the response of the material is the ratio between the weight (or size) of the yarns in the warp and weft directions. If the ratio is different from one, the woven fabric is called “unbalanced”, otherwise it is called “balanced”. In an unbalanced fabric, the properties in the two weaving directions differ generating a stiffer and stronger direction that can be of use for particular engineering applications. For instance, if there is one main direction of loading, the use of an unbalanced fabric allows for the optimization of the material bringing real designing advantages.

Woven fabrics are materials that possess very important features in terms of specific stiffness and strength, deformability, dimensional stability, thermal expansion, corrosion resistance, and many more due to the efficient exploitation of the fiber material. Of all these positive features, the deformability allows for these materials to be formed in various shapes without complex forming processes. However, without tools to forecast of phenomena such as the onset of wrinkling and slipping that limit the admissible deformation during the forming process, it is not possible to fully exploit the huge potential of these materials. Hence, it is of paramount importance to develop a comprehensive model for the description of the forming of this kind of materials.

As already pointed out, woven reinforcements consist of a succession of subassemblies resulting to a multiscale material. The overall mechanical behavior of the woven fabric is inherited from the behavior of its constituents and their interactions at lower scales (see Figure 3). Three scales of observation can be distinguished:

- microscopic scale for the fibers;
- mesoscopic scale for the yarns;
- macroscopic scale for the reinforcement.

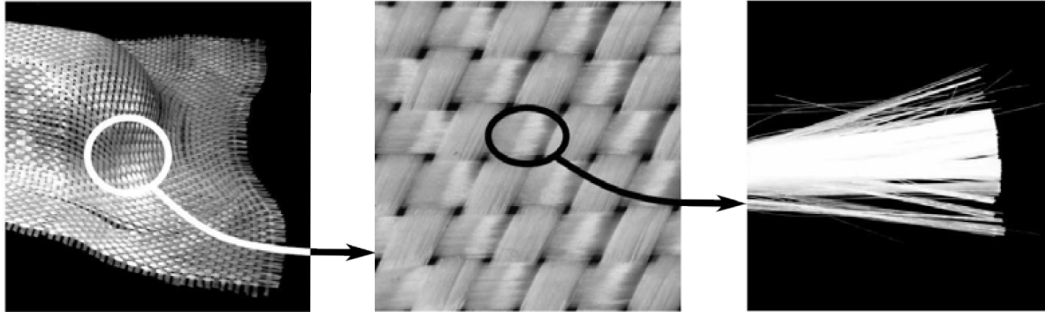


Figure 3: Multi-scale behavior of fibrous composite reinforcements [146].

To comprehensively describe the macroscopic behavior of woven fabric, it is not enough to describe the macroscopic shear stiffness of the fabric and the elongation stiffness given by the yarns since each scale includes specific problems of mechanical behavior, interactions and defects. When the yarns that compose the fabric are thick they possess a relevant bending stiffness at the meso-level, leading to some particular experimental response and, in the case of unbalanced fabrics, some interesting asymmetric phenomena (see section II.3.2). The aim of this work is to model the macroscopic behavior of dry composite reinforcements including some mesoscopic phenomena that are overlooked by the classical models. The purpose of the following sections is to describe the known mechanisms governing the behavior at each scale to understand both the material as a whole and the assumptions necessary for modeling.

1.1 Microscopic scale: the fiber

The behavior of a fiber, the smallest components of woven reinforcements, is studied at the microscopic scale. The fibers' behavior is given by the properties of the constituting material, even if treatments or transformations of the fibers can influence the resulting properties. Moreover, the constituting material can be of various nature and with very different properties. For example, we can find applications for:

- organic fibers (carbon, thermoplastic, aramid, high-modulus polyethylene);
- glass fibers;
- ceramic fibers (oxide, silica, alumina, silica/alumina, silicon);
- metal fibers (aluminum, aluminized plastic and nylon, and historically also gold and silver);
- vegetable fibers (seed, leaf, bast, core, stalk);
- animal fibers (animal hair, silk, avian fibers) constituted by proteins.

Carbon fibers will constitute the main focus of this manuscript. In the case of carbon fibers, a non-linear behavior is observed: the tangent stiffness of the fiber increases slightly as the applied force is increased until rupture [48, 98]. This non-linearity is quite low, often leading to the use of linear models in simulations. For ceramic fibers also, the mechanical behavior is generally accepted as linear (the studies on these materials are rather focused on problems of creep, influence of temperature and the chemical treatments they undergo).

The mechanical characterization of the fibers used for the fibrous composites can be complicated due to their small size, in the order of a micrometer. A single fiber is generally tested to determine the mechanical properties (see [98]); however, at such a scale both the precise measurement of the deformation and the initial diameter and constraining a single fiber with an experimental device are real challenges.

1.2 Mesoscopic scale: the yarn

The fibers are assembled to form yarns, with possible additional treatments such as:

- milling or twisting to improve their mechanical characteristics and to reduce their separation;

- texturing to give swelling and elasticity, thus modifying the appearance and comfort of the fabrics;
- wrapping that consists of covering a core wire by a helical winding of one or more single wires called cover wires, to protect certain fragile yarns such as carbon or ceramic fibers during the transformation operations of yarns into textile surfaces.

Once assembled, each yarn generally contains between 3000 and 50000 fibers in the case of carbon and less than 500 fibers for ceramics. The characteristic quantities generally used to describe a yarn are the following: material, type of assembly, number of fibers, diameter of fibers, linear mass (in tex, 1 tex = 1 g.km), rigidity and strength in traction.

The mechanical behavior of the fibers and their interactions defines the overall behavior of the yarn. Therefore, the only effective mean to study the yarn's behavior is by observing these microscopic phenomena via a X-microtomography. This technique is promising for the precise evaluation of the yarns' movements, that constitutes nowadays a widespread problem of research [59, 119, 165]. This method has the additional advantages of being non-intrusive, non-destructive and usable in conjunction with mechanical experiments. The phenomena associated with the stress of the yarns are identifiable by physical considerations and simple experiments.

Longitudinal behavior of the yarn As said before, the yarns are made up of a large number of fibers. However, not all the fibers tighten simultaneously when a yarn is pulled, but one after the other. The progressive traction of the fibers causes a non-linearity of the yarns' behavior at the beginning of the stress. This phenomenon is strongly dependent on the characteristics of the yarn and its method of manufacture. For example, a twisted yarn will behave in an only slightly non-linear manner.

The notion of stress is not easily adaptable to the yarns to evaluate the stiffness. For instance, let us consider the case of two different yarns with the same number of fibers, but distributed in sections of different area (i.e. the space between the fibers is different). In this case, the force needed to obtain a specific deformation is identical for the two yarns but, considering the sections' area, the stress obtained is not, see Figure 4. Since the behavior is based on the fibers' number and stiffness, considering a force per unit area is not coherent. It is more logical to characterize the tension behavior by a rigidity in N (ratio of the force on the deformation), rather than by a modulus.

For *compression* behavior, it is difficult to evaluate a longitudinal stiffness, which is of the order of the one in tension, because the relatively low rigidity to bending causes an almost immediate buckling of the yarn.

Transversal compression of the yarn The behavior in transverse compression of the yarns is associated with a change of area in the transverse plane: when the yarn is compressed, the fibers come closer to each other and fill the vacuum. This mechanism can be divided into two main steps, namely the rearrangement

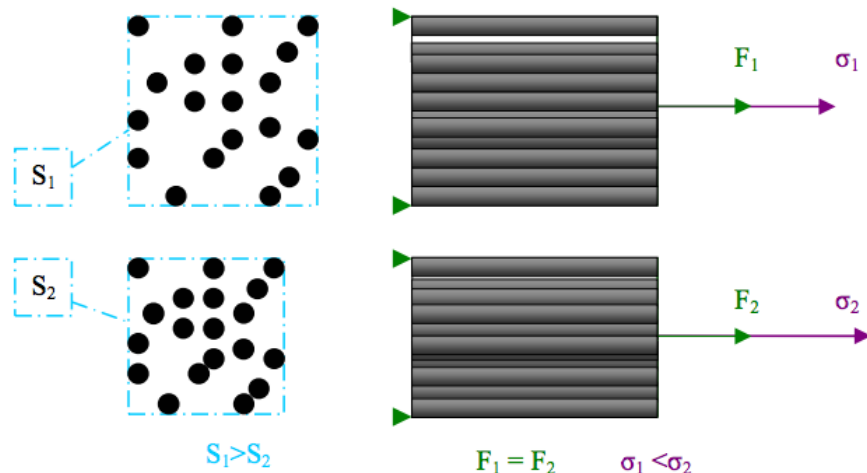


Figure 4: Traction of the yarn and problems in the evaluation of the effective stress [34].

and compression of the fibers. Initially, the fibers rearrange filling the empty spaces and, when no free space can be filled by fibers, the compression rigidity of the yarn will progressively tend towards the stiffness of compression of the material constituting the fibers. Directly related to the compression of the yarns, the density of fibers within the yarn has a considerable influence on the local permeability, and therefore on the quality of the resin injection carried out after the shaping of the woven reinforcement. The quality of the modeling of this behavior directly impacts the studies of permeability which could follow.

Shear of the yarn Two shear deformation modes can be identified for a yarn: a distortion mode (shear in the transverse plane of the yarn) and a transverse shear in the main direction of the fibers. The direct identification of these modes, as well as for transverse compression, appears difficult.

The distortion refers to the change in the shape of the yarn's section without the intervention of transverse compression. During this process, the fibers slide against each other and rearrange themselves in a new shape. It is clear that distortion is facilitated if no compression is present, because, the fibers will have less space and more friction during their rearrangement if the yarn is compressed. This coupling mechanism is difficult to identify directly. Furthermore, a slight bending of the fibers can also occur during the stress.

The transverse shear refers to the longitudinal sliding of the fibers against each other. This sliding is constrained, ideally, only by the friction existing between the fibers but the twisting of the yarns stiffens this mode of deformation. Even in this case, it can be assumed that the transverse shear is stiffened by the presence of transverse compression.

Bending behavior of the yarn Although the bending behavior of the yarns is relatively unknown, it influences the weaving process and even the flexural response of the entire reinforcement during forming. There are many phenomena related to the bending of the yarns. For instance, three deformation mechanisms are likely to occur in the simple case of the three-point bending (see Figure 5):

- transverse shear of the yarn, linked to the almost inextensibility of the fibers (strong longitudinal rigidity) compared to its low shear strength;
- bending of the fibers composing the yarn, directly related to the variation of their curvatures;
- lateral buckling of the fibers at the central support, strongly reduced by cohesion treatments such as sizing, twisting or wrapping.

The bending behavior of the yarns is thus controlled by both the transverse shear and the flexural behavior of the fibers, i.e. their resistance to a local change in curvature. This behavior is, moreover, very interesting from the point of view of continuous media, because it is directly related to the local curvature of the material (a variable, linked to the second derivative of the displacement, that is not influential in classical theories). This influence of the local curvature of the fibers on the overall behavior of the yarns makes it possible to affirm that, even at the mesoscale, woven fabrics do not respond to the hypotheses of classical continuous medium: the dependence on local rotations makes it a higher gradient or micromorphic medium, see Part I. Bending stiffness characterization devices exist, but were developed initially for the characterization of the flexural behavior of the woven fabrics and need, therefore, some adaptation.

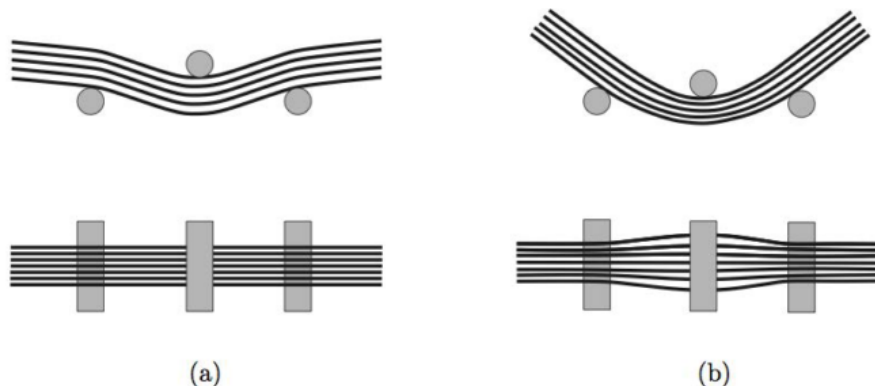


Figure 5: Bending of the yarn before the lateral expansion (a) and after (b) [34].

1.3 Macroscopic scale: the reinforcement

1.3.1 Types of reinforcement

The focus of this manuscript is put on composite reinforcements obtained by weaving. Depending on the type of weaving and on their thickness they can be divided into three categories:

- 2D (surface);
- 2.5D (interlock);
- 3D (three-dimensional).

The 2D reinforcements, usually referred to as reinforcement armor, are an intersection of yarns in two preferred perpendicular directions, warp and weft. For the 2D case, the traditional weaves of the textile industry are used. On the other hand, a third yarn direction is added in the thickness of the reinforcement to obtain a 3D weaving. The weaves called 2.5D are located at the border between 2D and 3D woven fabrics: some of the yarns connect the upper and lower layers to bond them together. These fabrics are often derived from conventional 2D armor, making it possible to obtain woven fabrics that are resistant to delamination and very thick (of the order of about ten centimeters). Only 2.5D armor will be studied in this manuscript, but it is interesting to detail the 2D armor that is the basis of these more complex armors and can also be used to obtain thick pieces of composite materials.

Weave 2D In the case of 2D fabrics, there are three main kinds of weaves (Figure 6):

- plain weave (or taffeta weave) is the simplest weave: each warp yarn alternately passes above and below each weft yarn;
- twill NxM: the weft yarn passes over N and then below M warp yarns by shifting one yarn at each pass;
- satin: the binding points of the warp and weft are disseminated so as to attenuate the diagonal effect present on the twill. The weft yarn passes over N warp yarns and then below 1.

The combination of these three families of armor, with the multiplicity of geometries and materials available for the yarn, allows for a wide variety of woven reinforcements. In general, a fabric can be characterized by its weave, the relative arrangement of the warps and wefts, and its the relative difference between the length of the fabric in one direction and the length of a yarn in that same direction.

Thick pieces can be made with these 2D armors by superimposing them. The structure thus obtained makes it possible to optimize the stiffness of the finished material by playing on the orientation of the layers, but the different armors do not possess links other than the resin. These materials are then very sensitive to delamination, which can propagate leading to a complete failure of the piece. In addition, the stacking of the various layers (a few millimeters thick each), results in long manufacturing times for parts of considerable thickness.

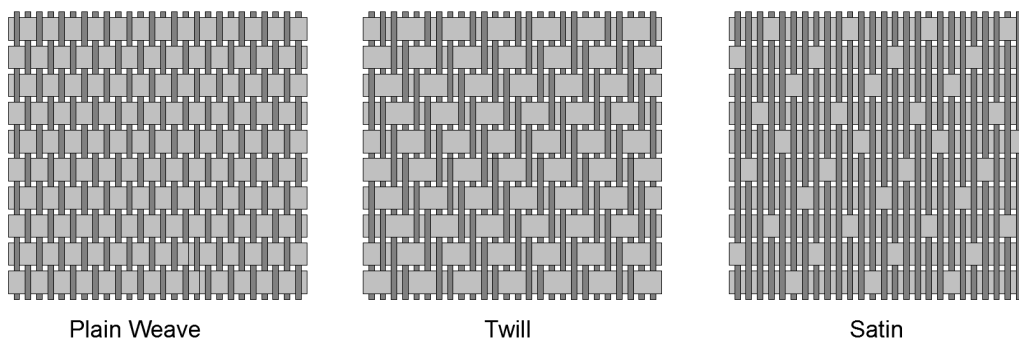


Figure 6: Schemes of weaving for 2D fibrous composite reinforcements.

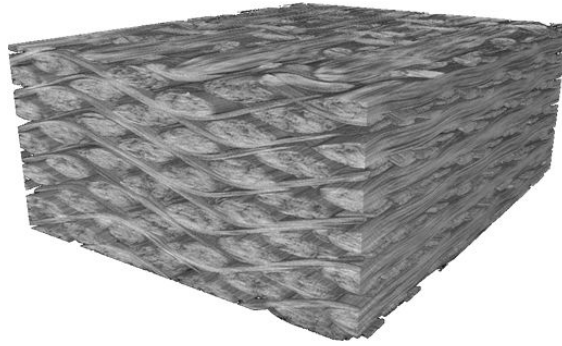


Figure 7: X-ray tomography of a 2.5D woven interlock.

Weave 2.5D To overcome the delamination problems inherent in superimposed 2D armors, thick woven reinforcements have been designed [19]. These reinforcements can be seen as the superimposition of different layers that are structurally assembled together during weaving. Instead of continuously intersecting in the same plane, the weft yarns intersect several layers in the thickness of the material (see Figure 7). The fabric obtained can then reach thicknesses of the order of ten centimeters, making it possible to manufacture parts with comparable mechanical qualities to superimposed 2D armors that avoid the phenomenon of delamination.

The geometry can become quite complex by varying the weaving pattern within the same preform. However, this possibility allows for an optimization of the resulting characteristics as a function of the stresses undergone. The use of 2.5D woven fabrics also makes it possible to minimize the variations in mechanical properties between two finished composite parts which are supposed to be identical, a common problem for 2D laminates where the operator's working method is preponderant.

1.3.2 Mechanical behavior of the reinforcement

When considering the macroscopic scale, the reinforcement is considered as a whole. However, woven reinforcements are influenced by the properties associated with the yarns, of which they are assemblages, thus leading to a complex resulting behavior. Some characteristics can be directly linked to the yarns' structure, and in particular to their weaving (e.g. the non-slipping between warp and weft yarns, the variations of stitching, the locking for in-plane shear and the transverse shear stiffening). Specific tests aimed to the interpretation of the deformation modes are necessary. In what follows, we will briefly describe the main deformation modes and the related characterization challenges.

Non-slipping between warp and weft At the macroscopic scale, it is usually assumed that there is no relative slipping between the warp and weft yarns. Considering the complexity of the slipping problem, it should not come as a surprise that this hypothesis is conventionally used for the macroscopic simulation of woven fibrous media. However, there is one main implication of this fundamental hypothesis: strong interactions must exist between the constituent networks of the woven fabric, so that relative sliding can be considered negligible and the displacement of the two sets of yarns can be considered continuous. When dealing with materials, geometries and loading cases for which this consideration can be thought as sensible, the material can be modeled as a continuous medium. However, the results obtained with the theory of continuous media cannot be considered reliable when relative movements appear.

To validate this hypothesis, a study based on stamping with a hemispherical punch can be carried out (see Figure 8). This test consists in stamping a woven reinforcement plate at low speed, shaping it in a hemispherical shape. Before stamping, traces are drawn in the warp and weft directions at regular intervals. After the experiment, a crossing of the lines at the same points as in the initial state indicates that there was no relative sliding between the locks. The relative non-slipping hypothesis, which will be considered in the remainder of this manuscript, can also be tested for complex loads.

Traction behavior Let us consider the sollicitation of a woven fabric in *uniaxial traction* in the warp (or weft) direction. This loading case is influenced by two successive phenomena induced by the reinforcement's weaving studied:

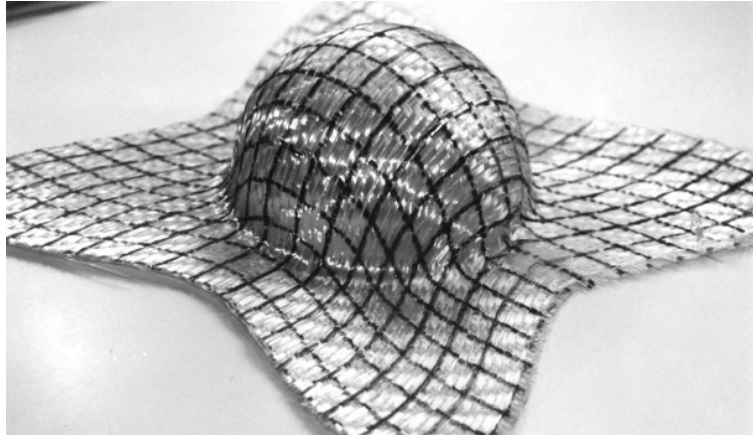


Figure 8: Validation of the hypothesis of non-slipping via a hemispherical punch [34].

- the gradual straightening of the yarns in the direction of stress, due to the strong increase in the traction of the yarn and a bending of the yarns in the orthogonal direction;
- the elongation of the yarns once they are totally straightened.

From these two mechanisms results a strong non-linearity of the traction behavior for the first percentages of deformation: the initial rigidity is low because the yarns can easily straighten without important stress. Afterwards, the yarns themselves must elongate to allow for bigger deformations increasing sharply the rigidity of the reinforcement. The actual length of the woven fabric decreases in this orthogonal direction with a corresponding bending of the yarns.

The *simultaneous traction* of two orthogonal directions is interesting to study. As in the case of uniaxial tension, the traction in one direction has an effect in the orthogonal direction leading to complex results. The biaxial traction test consists in subjecting both of the directions to a tensile stress which is not necessarily identical. However, the implementation of this type of test is difficult for 2D woven fabrics, and even more so for thick woven fabrics, since the user must ensure that all the warp and weft yarns are stressed at the same time.

Compression behavior The compression behavior *in the direction of the yarns* of the woven reinforcements is difficult to characterize. Taken individually, a yarn will tend to buckle in compression, but when woven they are bonded together in the reinforcements. Their movements are constrained by the positioning of the neighboring yarns. Therefore, the weaving directly influences the behavior of the yarns in compression and, thus, the macroscopic behavior of the material. No test is commonly accepted or even used for the characterization of woven fabrics compressed in the direction of the yarns. Furthermore, buckling appears fairly rapidly, allowing for a characterization only for small deformations. However, considering the usual loading during the shaping of the woven reinforcements, knowledge of the compression behavior for small deformations could be sufficient.

The *transverse compression* of a thick woven fabric can be easily characterized experimentally. This deformation mechanism directly influences the parameters and the quality of the injection during the RTM process. The volume density of fibers, mainly associated to the compression behavior, must be controlled to optimize the mechanical performance, the permeability and the flow of the resin inside the reinforcement [18, 89].

Shear behavior in the plane of the yarns During the forming tests, the shear flexibility of the fabric allows for a shape with a double curvature. Also, the low stiffness associated with this mode of deformation makes it possible to give the reinforcement a non-developable geometry¹. Hence, the characterization of shear behavior is essential for the study of the characteristics of the reinforcement (see Figure 9), namely:

- the deformability, i.e. the capacity to take complex forms without defects appearing;

¹A developable surface can be flattened onto a plane without distortion (i.e. "stretching" or "compressing").



Figure 9: Shear behavior in the plane of the yarns of fibrous composite reinforcements.

- the permeability that determines the resin injection process.

The shear behavior of the reinforcement is highly non-linear because various mechanisms of deformation are involved. From the kinematic point of view, these can be divided into three stages:

- for low shear deformation, the yarns pivot almost as rigid bodies and the stiffness is generated principally by the friction of the yarns on each other;
- progressively, the interstices fill up and a transverse compression of the yarns is added to this friction;
- the transverse compression increases and it becomes the only mode of deformation.

All the interstices do not fill simultaneously, which results in a progressive stiffening. Once the interstices are filled, the phenomenon of locking in shear appears, for which the weaving of the material plays a fundamental role. The average distance between the yarns conditions the freedom of movement: the higher the volume of fiber induced by the armor, the lower the clearance will be and the sooner the locking will occur. Furthermore, when the shear locking angle is reached, the local permeability of the reinforcement is considerably reduced, rendering the resin injection more difficult. Apart from the kinematic constraints, the shear also presents several sources of dissipation such as the inelastic dissipation caused by the rearrangement of fibers within the yarns and the friction. Therefore, the sample does not return to its initial position at the end of the test but a residual deformation persists. Two conventional tests can be used to study the shear behavior: the frame test and the bias extension test, see section II.3.

Transverse shear behavior Contrary to the majority of the woven materials studied in the literature, the 2.5D interlocks do not have a negligible thickness. The transverse shear becomes a predominant mode of deformation in the shaping of these woven fabrics. This mode of deformation has been studied little so far because of the current low use of thick woven fabrics, but it is possible to find a test protocol in Charmetant [36]. In the work of [235], a new test device is proposed, taking into account the specificities of transverse shear behavior of thick woven fabrics. At present, no device or experimental protocol is commonly accepted due to the small number of studies performed.

Bending In analogy to the mesoscopic scale, a local flexural rigidity is present for each yarn constituting the woven reinforcement. This local rigidity is accentuated on a macroscopic scale by the existence of an armor. This presence of local resistance to curvature was notably demonstrated by the development of wrinkling during shaping tests [28, 90]. Several experimental devices enable the characterization of this

rigidity of curvature. However, there is no common agreement on how to measure it and its influence on the global behavior. This characteristic is commonly overlooked when the modeling of the fibrous composite reinforcement is made in a continuous framework. The object of this manuscript is to find a continuous model to include the effects of this mode of deformation in an enriched continuous model.

1.3.3 Consolidation processes

Liquid Composite Molding (LCM) processes are used to form woven reinforced composites with *organic matrix*. The principle of these processes is to mold the dry reinforcement and then to inject the resin to solidify the part. Molding the dry reinforcement makes it possible to obtain a final composite part very close to the desired part and, thus, to minimize the production steps and costs. These processes, known as closed mold processes, allow strict control of the volatile organic compounds emitted during manufacture, the resin then not being in direct contact with the atmosphere. Among the LCM methods, the most widely used are:

- the vacuum infusion: the dry woven reinforcement is placed between a mold and a sealed membrane, afterwards the pump presses the reinforcement against the mold and initiates the flow of the resin by vacuuming the area;
- the Resin Transfer Moulding (RTM): the dry woven reinforcement is shaped (or stamped) in a mold by means of a punch. Afterwards the resin is injected and the assembly is then heated to polymerize the resin (in the case of a thermosetting matrix).

The advantage of the RTM is to have two rigid parts which allow to better control the compression of the reinforcement during shaping and therefore its final thickness. The ability of the reinforcement to deform, adapting to the mold, has a major influence on both the injection step (quality of impregnation, mold filling time) and the mechanical characteristics of the part. During the forming processes, some problems can be encountered such as fiber fracture, the appearance of wrinkles and/or the creation of either dry zones or parts without yarns. These defects are usually due to uneven mechanical solicitations during the dry forming that locally result in large tension in the yarns, excessive shearing or compression and/or uneven fiber density. Therefore, to check the feasibility of a mechanical piece by RTM, the dry forming must be studied in detail and its results must be used for a permeability study. The final mechanical qualities are intimately linked to this stage that will be analyzed in detail in chapter II.4.

On the other hand, woven reinforced composites with *ceramic matrix* are commonly manufactured by infiltration methods. This means that the ceramic matrix is formed by the infiltration of a matrix into the fibrous structure, in this case a woven reinforcement. Depending on the nature of the injected matrix it is possible to differentiate between:

- the Chemical Vapor Infiltration (CVI) in which the matrix is introduced as a gaseous constituent;
- the Liquid Phase Infiltration (LPI) (e.g. Polymer Infiltration and Pyrolysis (PIP)) in which the matrix is introduced as a liquid constituent.

Many other molding processes exist, but their recollection goes beyond the scope of this work. We will limit ourselves to point out that such processes vary according to the nature of the materials constituting the reinforcement and the matrix, the importance of the series to be carried out, the rate and cost of production sought.

CHAPTER II.2

Modeling of fibrous composite reinforcements

The reliable simulation of the forming processes of fibrous composites is a strong need for every industrial manufacturer, since a thorough understanding and predictability of the reinforcements' behavior would improve the efficiency and affordability of the production processes. Furthermore, the characteristics of the finished piece could also be enhanced considerably. In the common practice, the production processes are characterized by a series of iterations that lead to the final result. Therefore, the aim of modeling is to avoid (or at least shorten) this iterative process via an effective numerical modeling. Such a model should be able to predict both the mechanical and geometrical resulting characteristics, including:

- the mechanical characteristics of the piece, before and after curing;
- the eventual onset of wrinkling, unweaving and fracture of the fibers;
- the fiber orientation after forming;
- the permeability in every point of the deformed interlock.

The problems in describing precisely all of these characteristics lie in the multi-scale behavior of fibrous composite reinforcements: each problem must be studied at a different scale. This issue led to the creation of a variety of models that, considering their scale, can be divided in microscopic, mesoscopic and macroscopic models (see section II.2.1). The object of this thesis is the definition of a macroscopic enriched continuous model for the description of the mechanical behavior of fibrous composite reinforcements, whose fundamentals will be described in section II.2.2. Finally, in section II.2.3 a discrete mesoscopic model, used as a comparison/validation for the enriched continuous model in the case of the bias extension test (chapter II.3), will be put forward.

2.1 Modeling approaches for fibrous composite reinforcements

In this section, a brief description of the possible approaches for the numerical simulation of thick composite reinforcements is made (see [146] for more details):

- microscopic models;
- mesoscopic models;
- macroscopic models.

2.1.1 Microscopic modeling

The underlying idea in the microscopic modeling is to simulate the behavior of the most fundamental part of the fibrous composite reinforcements: the fiber. This concept implies the determination of the fibers' material behavior and the mechanisms governing the interaction between different fibers. The evaluation of the mechanical properties of the materials constituting the fibers is straightforward, but managing the description of the contact between different fibers can be very complex. On this subject, a wealth of different studies have been conducted, considering simplified models with a limited number of fibers which geometry is somewhat descriptive of the woven yarn (see for example [106,166]). However, the application to the yarns used for composite reinforcements is less common, due to the elevated number of fibers per yarn. For the case with a limited number of fiber, we can refer to [236] as a possible example. Moreover, it has been proposed to model groups of fibers as continuous to reduce the computational cost while accounting for their repositioning (see [61] and Figure 10). This approach is very effective for computational purposes, but big groups of fibers lead to lack of accuracy in the results: big groups tend to behave as yarns more than as single fibers.

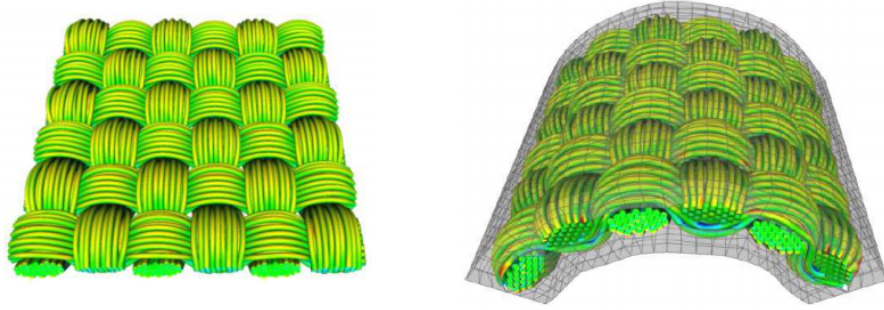


Figure 10: Microscopic modeling of fibrous composite reinforcements [61].

2.1.2 Mesoscopic modeling

The mesoscopic approach is based on the simulation of the yarn as a continuous elementary component, instead of describing the behavior of the single fiber. Therefore, it is necessary to define and describe the mechanical behavior of the yarns and their interactions within an armor, from which it is possible to deduce the overall behavior of the reinforcement. The macroscopic mechanical behavior of the reinforcement can be derived from the mesoscopic modeling with two possible approaches: modeling the entire mechanical piece from the mesoscopic scale up, or by characterizing a small macroscopic part with a mesoscopic model and then injecting the results in macroscopic calculations. An example of a mesoscopic analysis that is commonly made is the determination of the local permeability that directly feeds injection flow calculations.

The simulation at the mesoscopic scale allows to directly observe the influence of the interlock's properties on the overall behavior of a woven fabric and to determine the weaving adapted to the needs. Therefore, the access to the actual geometry of an elementary mesh is of paramount importance. X-ray microtomography is the most promising method for the experimental observation of the positioning of the yarns, see for example [14, 59, 95]. This technique consists of scanning a representative sample of a reinforcement in order to obtain a 3D mapping. The images obtained are, then, processed by isolating the constituent elements (the yarns) and meshing them.

The models at the mesoscopic level can be divided into two different sets:

- analytical approaches;
- finite element modeling.

Analytical approaches have been developed to access the mechanical and geometric quantities of the interlocks. These approaches are generally based on a simplification of the geometry of the yarns and on assumptions of mechanical behavior. A model based on the discretization of the mean line by segments, with a rigidity associated to each segment and at each point of intersection between warp and weft, was proposed by Kawabata [107, 108] (see Figure 11). The behavior of the model is satisfactory for traction stresses of the reinforcement but remains too poor for transverse compression and shear. In another analytical approach, the geometry of the reinforcement is obtained by minimizing the deformation energy of each yarn until a static equilibrium configuration is found, taking into account various mechanical contributions (traction, bending, torsion, compression of the yarns and interactions) (see [124, 125]).

Analytical approaches provide consistent results in the determination of the mechanical behavior of tension yarns but are more limited in more complex applications involving, for example, shear. Therefore, the use of finite elements seems a good alternative, but it requires two prerequisites: the geometry and the boundary conditions of the reinforcement. These two inputs must be obtained either theoretically, from the characteristics of the yarn and the armor, or experimentally. With FEMs, it is also possible to consider yarns with variable non-symmetrical sections along their mean line and with complex geometries. However, the mesoscopic modeling of an entire composite woven reinforcement during shaping remains difficult because of the major issue of modeling interpenetration. Therefore, the modeling of a Representative Unit Cell (RUC), that is the smallest elementary pattern that can be repeated to obtain the entire armor, is commonly used. The aim is then to study the behavior of the weaving on a smaller scale before extending it to the whole of the piece.

2.1.3 Macroscopic modeling

The simulation at the macroscopic scale aims to describe the shaping of woven reinforcements at the scale of the whole piece. This is the ultimate goal of the research on modeling preforming composite reinforcements: predicting (and possibly avoiding) the appearance of the various observable defects in the woven fabrics. The possibility of detecting few or many observable defects arises both from the type of modeling approach chosen and from the richness of the mechanical characteristics conferred upon them. The input quantities of such models may be derived from woven-scale tests or from observations/simulations at microscopic and mesoscopic scales.

In the past years, researchers have proposed different approaches to the problem. One of the first attempts was based on a kinematic algorithm called “fishnet” that, thanks to its simplicity and fast computability, was suitable for the implementation in commercial software [128]. This approach is usually referred to as *geometric or kinematic*, since it is based on strong purely non-mechanical assumptions:

- the inextensibility of the yarns;
- non-slipping between warp and weft;
- free rotation at intersection points between warp and weft;
- the absence of complex contact considerations (friction) with the shaping tools.

In other words, the reinforcement is described as if composed by articulated bars connected at the crossing points between networks. The algorithm then calculates the position of the related points on geodesics traced on the surface to be draped from the current point.

Nevertheless, this approach presented some limitations because it does not take the mechanical behavior of the fabric into account. For instance, one of the main problems of the fishnet algorithm was the impossibility to impose static boundary conditions. Furthermore, removing all mechanical and weaving considerations, the results are identical regardless of the stiffness of the locks and the chosen weave. Shear kinematic locking and thickness variation in compression are also absent in the basic modeling. The use of this method for thick woven fabrics is, of course, not recommended other than for preliminary analysis.

A different path can be followed considering macroscopic *mechanical approaches*, whose models can be divided into:

- discrete models;
- continuous models;
- semi-discrete models.

Discrete approaches consist in considering the textile as a discontinuous assembly of deformable elements [40, 110, 210]. These are generally extensions of the theory of the net, that is to say the introduction of mechanical characteristics in the resolution of the problem of shaping. The reinforcement is modeled by nodes connected to each other by bars and springs designed to model the elongation, shear, torsion and bending response.

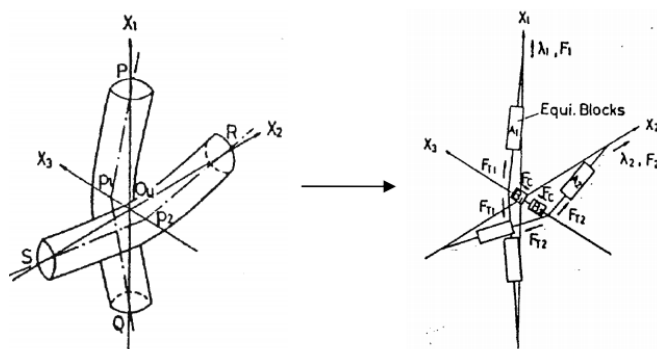


Figure 11: Mesoscopic modeling of fibrous composite reinforcements [107, 108].

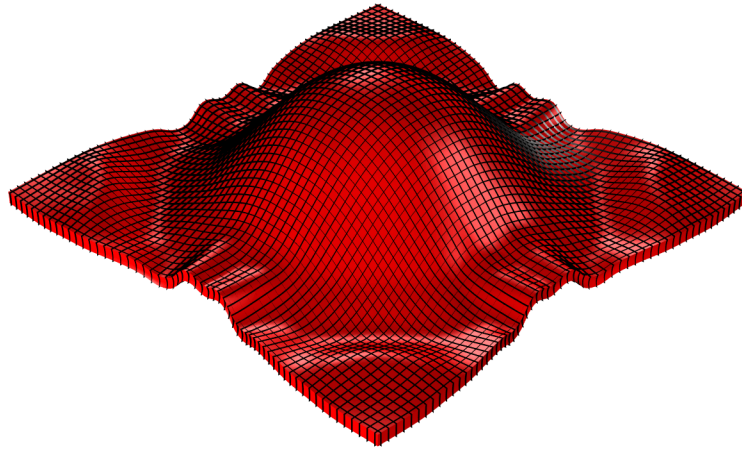


Figure 12: Macroscopic modeling of fibrous composite reinforcements.

On the other hand, continuous approaches assume a continuous material on a macroscopic scale. This hypothesis stems directly from the consideration of non-slipping between yarns during the shaping phase leading to a textile that is a homogenized anisotropic continuous medium, see Figure 12. The most crucial part of continuous modeling is the definition of proper constitutive relations that realistically reflect the mechanical properties of the analyzed material, whether hypo-elastic [9, 109, 193] or hyperelastic [35, 215, 224], that yield convincing results. The same material is considered in all the points of the fibrous reinforcement and does not take into account the variations of the mechanical characteristics inherent to the weave studied. In the literature, reliable constitutive models for the description of the mechanical behavior of fibrous composite reinforcements at finite strains can be found in [2, 35, 36]. Moreover, the mechanical behavior of composite preforms with rigid organic matrix (see e.g. [153, 154, 189]) is quite different from the behavior of the sole fibrous reinforcements (see e.g. [35]) rendering the mechanical characterization of such materials a major scientific and technological issue. Traditionally, the energy used in the simulation of continuous media comprises only deformations defined as the first derivative of the displacement, thus giving rise to so-called first gradient theories. However, in various papers dealing with woven composites, it is shown how the addition of energies related to the local stiffness of the yarns is useful, if not necessary, to describe the macroscopic deformation behavior of the interlocks (e.g. [11, 35, 70, 130, 134]).

Semi-discrete approaches are a combination of the two approaches discussed above. Part of the behavior is modeled by a continuous solid, while the rest by discrete elements. The interaction between discrete and continuous parts can be associated in the same Lagrangian element [52, 91] or considered totally independent [47]. In the first case, the discrete and continuous portions are fixed relative to one another in the isoparametric configuration but the forces generated by any deformation are subdivided between a traction contribution associated with the discrete parts and the other contributions (shear, compression) associated with the continuous part. The advantage of such an element is that it is possible to more accurately and simply represent the local directions of the yarns in the preform and to account for the complex anisotropy of these materials. In the second case, the reinforcements are represented by layers of solid elements while bar elements are added to represent the yarns. Here, the continuous parts are totally decoupled from the discrete parts, implying the complication of managing their contact.

2.2 Macroscopic enriched continuous modeling

To model the macroscopic behavior of composite reinforcements, the traditional approach is a continuous model in which a first gradient energy describes all the deformation effects in the material. However, in [35] it is also underlined that Cauchy continuum theory may not be sufficient to model a class of complex

contact interactions which are related to local stiffness of the yarns and which macroscopically affect the overall deformation of interlocks. It has been known since the pioneering works by Piola [196], Cosserat [44], Mindlin [156], Toupin [225], Eringen [67], Green and Rivlin [86], and Germain [78] that many microstructure-related effects in mechanical systems can be still modeled by means of continuum theories. More recently, these enriched continuum theories have been widely developed to describe the mechanical behavior of many complex systems, such as e.g. porous media [54, 133, 208], capillary fluids [51, 56], exotic media obtained by homogenization of heterogeneous media [3, 195, 209]. Therefore, our approach has been the implementation of a second gradient material that describes the energy related to micro-structural properties such as the bending of the fibers. However, any enriched continuous model must be compared to the classical continuous one and will therefore be presented in subsection II.2.2.1. Afterwards, the proposed second gradient hyperelastic model will be presented in subsection II.2.2.2.

2.2.1 Hyperelastic first gradient model

In this subsection, the constitutive equations for the first gradient strain energy density $W_I(C)$, which will be used to simulate the mechanical behavior of this fibrous composite reinforcement in the finite strain regime, is presented. With this scope, we introduce a Lagrangian configuration $B_L \subset \mathbb{R}^3$ and a suitably regular kinematical field $\chi(X, t)$ which associates to any material point $X \in B_L$ its current position x at time t in order to describe the deformation of the considered continuum. The image of the function χ gives, at any instant t the current shape of the body $B_E(t)$: this time-varying domain is usually referred to as the Eulerian configuration of the medium and, indeed, it represents the system during its deformation. Since they will be used in the following, we define the displacement field $u(X, t) := \chi(X, t) - X$, the tensor $F := \nabla \chi$ and the Right Cauchy-Green deformation tensor.

Even at finite strains, well-known expressions for isotropic strain energies descriptive of the behavior of isotropic materials are available in the literature (see e.g. [187, 219]). Quite the opposite happens in the case of orthotropic materials, for which suitable specific strain energies, well descriptive of real material behaviors are more difficult to be found. Some results are provided in [102], where some polyconvex energies are proposed to describe the deformation of rubbers in uniaxial tests. Explicit anisotropic hyperelastic potentials for soft biological tissues are also proposed in [97] and reconsidered in [10, 206], in which their polyconvex approximations are derived. Other examples of polyconvex energies for anisotropic solids are given in [220].

Notwithstanding the research efforts devoted to the study of polyconvexity, which certainly introduce rigorous theoretical frameworks for the study of the mechanical behaviors of hyperelastic materials, the use of such polyconvex models is often limited due to the difficult attribution of a sensible physical meaning to the wealth of constitutive parameters which are introduced. The approach adopted in this manuscript is the Ockham's razor approach, introducing the minimum possible number of physically sensible constitutive parameters which are needed to describe the targeted phenomena.

In this work, the directions D_1 and D_2 denote the unit vectors in the directions of the warp and weft yarns in the reference configuration and the direction $D_3 = D_1 \times D_2$ denotes the unit normal to the plane containing the two sets of fibers. It is possible to fully describe a first gradient orthotropic energy with an expression of the type (see e.g. [200] and the Appendix B.1 where a theorem for the complete representation of a first gradient energy is presented):

$$W_I(C) = W_I(i_{11}, i_{22}, i_{33}, i_{12}, i_{13}, i_{23}), \quad (\text{II.1})$$

where $i_{ii} = D_i \cdot C \cdot D_i$, $i = \{1, 2, 3\}$ represents the elongation strain in the direction D_i and $i_{ij} = D_i \cdot C \cdot D_j$ represents the shear strain (angle variation) between the directions D_i and D_j with $i, j \in \{1, 2, 3\}$ and $i \neq j$.

It is possible to develop complex non-linear energies that capture all the details of the mechanical nonlinearities observable in the experimental testing, as done in [2, 35, 36], but this is not one of the aims of the present manuscript. Instead, using only a simple quadratic first gradient energy, it is possible to thoroughly analyze the influence of both meshing and additional second gradient terms on the performed numerical simulations. Thus, the chosen constitutive expression for the first gradient energy is:

$$W_I(C) = \frac{1}{2}K_{11}(\sqrt{i_{11}} - 1)^2 + \frac{1}{2}K_{22}(\sqrt{i_{22}} - 1)^2 + \frac{1}{2}K_{33}(\sqrt{i_{33}} - 1)^2 + \frac{1}{2}K_{12}i_{12}^2 + \frac{1}{2}K_{13}i_{13}^2 + \frac{1}{2}K_{23}i_{23}^2, \quad (\text{II.2})$$

where K_{ii} are the extensional stiffnesses in the direction of the yarns as well as in the orthogonal direction, while K_{ij} with $i \neq j$ are the in-plane and out-of plane shear stiffnesses. The numerical values of the material

parameters define a material in which the extensional stiffness is much higher than the shear stiffness and the shear behavior in the plane of the fibers is stiffer than the out of plane. Moreover, the extensional stiffness in the orthogonal plane is much lower than the in-plane ones, due to the fact that no yarns are effectively present in the thickness of the interlock. Even if more refined hyperelastic laws can be certainly be introduced in the spirit of [2, 35, 36], the proposed expression for the first gradient energy density is representative of the main macroscopic deformation modes of fibrous interlocks.

2.2.2 Hyperelastic orthotropic second gradient strain energy density

A hyperelastic, orthotropic, second gradient model can be applied to the case of fibrous composite reinforcements at finite strains. The first gradient kinematics of the continuum must be enriched by considering the second order tensor field ∇C which accounts for terms that can be associated with the macro-inhomogeneity of micro-deformation in the microstructure of the continuum. For the strain energy density $W(C, \nabla C)$ which shall be used to simulate the mechanical behavior of the fibrous composite reinforcements in the finite strain regime we will assume a decomposition of the form:

$$W(C, \nabla C) = W_I(C) + W_{II}(\nabla C) \quad (\text{II.3})$$

Considering linear elastic isotropic second gradient media, it is possible to find constitutive laws that are able to describe a very wide set of behaviors (see for example [57]). In the case of the woven fabrics, the bending stiffness of the yarns is the main micro-structure-related deformation mechanism which takes place at the mesoscopic level and is, therefore, the only one that will be considered here. The modeling of the bending stiffness of the yarns is decisive for the description of some specific phenomena, such as shear transition layers in 2D experimental tests and wrinkling during the deep-drawing of dry woven fabrics. A second gradient theory is potentially able to account for other effects related to the derivatives of the elongations but, in this work, they will be disregarded. The second gradient energy considered is, thus, a function only of the derivatives of the invariants i_{ij} ($i \neq j$), that can be used to define rough descriptors of the curvatures of the two sets of yarns of the fabric.

As a matter of fact, it can be inferred (see also [11, 58, 70, 130, 134]) that, given the family of yarns initially oriented in the direction D_1 , the quantity $i_{12,1}$ is a measure of their in-plane bending¹. Analogously $i_{12,2}$ is a measure of the in-plane bending of the family of yarns initially oriented in the direction D_2 . The quantities $i_{13,1}$ and $i_{23,2}$ are descriptors of the out-of-plane bending of the yarns initially oriented in the D_1 and D_2 directions, respectively. Since no material fibers are present in the thickness of the considered interlocks, quantities related to their bending ($i_{13,3}$ and $i_{23,3}$) are not likely to play a role in the deformation of such materials. In light of these remarks, the following constitutive form is introduced for the second gradient strain energy density:

$$W_{II}(\nabla C) = \frac{1}{2} \alpha_1 i_{12,1}^2 + \frac{1}{2} \alpha_2 i_{12,2}^2 + \frac{1}{2} \beta_1 i_{13,1}^2 + \frac{1}{2} \beta_2 i_{23,2}^2, \quad (\text{II.4})$$

where with α_1 , α_2 and β_1 , β_2 are the in-plane and out-of-plane bending stiffnesses of the two families of yarns, respectively. For unbalanced fabrics, i.e. fabrics whose warp and weft yarns do not have the same characteristics, it is likely that $\alpha_1 \neq \alpha_2$ and $\beta_1 \neq \beta_2$ (see also [11, 130]). Moreover, it is possible that the two families of yarns have different in-plane and out of plane bending stiffnesses.

Further investigations are needed to establish a strict theoretical relationship between the microscopic structure of considered reinforcements and the macroscopic parameters here introduced: it is indeed well known that the second gradient parameters are intrinsically related to a characteristic length L_c which is, in turn, associated to the micro-structural properties of considered materials. Many identification methods have been introduced to relate the macroscopic second gradient parameter to the microscopic properties of the considered medium, e.g. see [3, 209]. Suitable multi-scale methods as the one introduced in [163] may be generalized to be applied to the present case. Moreover, the description of the considered system at the microscopic scale may exploit some of the results proposed in [6, 94, 218].

¹Here and in the sequel the term $(\cdot)_{,i}$ denotes the partial derivative of the quantity (\cdot) with respect to the space coordinates ξ_i of a reference frame oriented within the directions D_i .

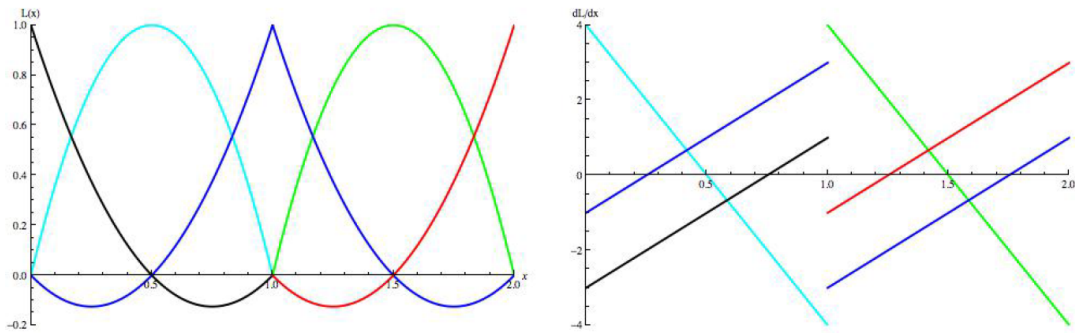


Figure 13: Lagrangian Shape Functions and their First Derivative

2.2.3 Considerations on the numerical implementation of an enriched continuous model

As explained in the introductory part on higher gradient models (Chapter I.3), the two following approaches are possible for the numerical implementation of a second gradient model:

- directly use kinematics uniquely based on the macroscopic displacement field and consider higher gradients of the displacement in the strain and kinetic energy densities;
- start from richer kinematics (as done for micromorphic media) and then impose suitable constraints on the extra kinematical descriptors in order to obtain the desired second gradient model as a limiting case.

Some consideration on the numerical implementations of the two models are proposed in this subsection.

Direct implementation of a second gradient model: augmented continuity shape functions In the finite element method the solution of the problem is searched among a subset of functions approximating the space of configurations. As well explained in [237], it is implicitly assumed in the derivation of the equations in the finite element model that no contribution to the virtual work arises at element interfaces. Therefore, it is necessary to choose displacement functions such that the strains at the interface between elements are finite (even though they may be discontinuous). In the first gradient models, the strain is defined by first derivatives and, therefore, the displacements only have to be continuous. If, however, the strains depend on the second derivatives, as in the second gradient model, the continuity of the first derivatives must also be granted.

The most used kind of shape functions are the Lagrangian shape functions, that can be found already implemented in almost every finite element software. These functions are polynomials that, given a set of nodes, are zero at all the points but one. Considering the one dimensional case, this gives rise to an expression of the kind:

$$\mathbb{L}_i = \prod_{\substack{j=1, \dots, n \\ j \neq i}} \frac{x - x_j}{x_i - x_j} \quad (\text{II.5})$$

Let us work with the case of a polynomial of degree 2 and on 2 adjacent elements. Figure 13 shows that, despite having imposed continuity, the first derivatives are still discontinuous. This is due to the continuity class C^0 of the Lagrangian functions.

Having said that, it is now important to choose one class of shape functions fit for the analysis of a second gradient model. In the one dimensional case, there would be various possible choices to be made. For instance, the Hermitian polynomials were born to evaluate problems such as the beam in which the second derivatives of the displacement (the curvature of the beam in particular) play an important role. A different possibility are the Spline functions which guarantee a higher level of continuity (class C^{n-1} for polynomials of degree n) between elements and would therefore be fit for this application.

In the case of 2D and 3D solids the problem becomes even more complicated: instead of having to consider one derivative we have to face the full gradient of the displacements ∇u . As a matter of fact, the 2D and 3D Hermite functions have continuous derivatives between mesh elements, but only at the mesh vertices. In the 2D case, the Argyris functions (5th order polynomials) or B-splines would assure the continuity in the entire edge of the element (for the use of B-Splines in high continuity 2D problems see for example [84, 85]). Going to the complete 3D case the only existing compatible elements (C^1 continuity) are of at least 9th order [234] based on the Ženišek element [233]. Unfortunately those kind of elements imply such a high order of polynomials that are not currently implemented in the most widespread finite element softwares.

However, it has to be reminded again that the need for continuity is due to the absence of contribution to the virtual work at element interfaces. We chose to implement third order Lagrangian polynomials with *augmented continuity* adding an a posteriori penalty energy related to the discontinuity of the deformations i_{12} , i_{13} and i_{23} at the element interfaces of the type²:

$$W_{\text{Interface}} = K_{\text{Penalty}} ([[i_{12}]]^2 + [[i_{13}]]^2 + [[i_{23}]]^2). \quad (\text{II.6})$$

This energy depends only on the discontinuity of the in-plane and out-of-plane shear deformations i_{12} , i_{13} and i_{23} and it is, therefore, not sufficient to render the entire ∇u continuous. Nonetheless, the derivatives of the deformations i_{12} , i_{13} and i_{23} are the only ones appearing in the presented second gradient energy and, therefore, are the only ones on which the continuity has to be imposed.

With this workaround, it is possible to obtain almost continuous deformations and, thus, to implement directly a second gradient 3D model. In order to use this method on a constant basis, other studies on the numerical stability and convergence should be made, but the problem remains open for now. The possibility of adding an energy on the interface between mesh elements is not always granted, but COMSOL Multiphysics[®], the software used for the simulations, has it already built-in.

Implementation of a micromorphic model as limiting case of the second gradient model At this point, the reader may believe that the fact of considering a micromorphic medium is redundant for treating the considered problem of fibrous composite reinforcements, since a second gradient model could have been directly introduced, instead of constraining a micromorphic model to become a second gradient one. Nevertheless, the intermediary step of passing through a micromorphic model could be helpful, at least for two reasons:

- the imposed boundary conditions take a simple and more precise meaning;
- the numerical implementation of the considered problem involves lower order differential equations.

The first point, i.e. the unique meaning of the imposed boundary conditions, is crucial to have an easily-recognizable physically-grounded interpretation. In fact, as far as second gradient theories are concerned, the boundary conditions that can be imposed may take different, but equally legitimate, forms for the same physical problem (see e.g. [135]): for example, in a second gradient theory, a given angle can be imposed either by directly assigning the angle or by suitably choosing the components of the normal derivative of displacement on the boundary. Depending on whether one choice of the kinematic conditions or the other one is made, the dual traction counterparts (dual of the angle variation or of the normal derivative) have different expressions and the definition of the force can be also shown to be non-equivalent in the two cases. Such non-uniqueness of the way of imposing second gradient boundary conditions is directly related to the number of integration by parts which one decides to make in the expression of the internal work: in second gradient theories, the second gradient of the virtual displacement can be integrated by parts twice, by making use of the standard divergence theorem and of the surface divergence theorem.

On the other hand, micromorphic models only involve first gradients of the introduced kinematical fields, so that we can integrate by parts only once (only the standard divergence theorem is used in a micromorphic model). This fact, avoids any sort of indeterminacy for the imposable boundary conditions when micromorphic models are considered (see e.g. also [21]). Moreover, the absence of higher order derivatives allows for the use of traditional shape functions for both the displacement and the additional degrees of freedom. However, it is not clear how the coupling between the micromorphic degrees of freedom, discretized by the continuous traditional shape functions, and the macroscopic strains, discretized by the discontinuous derivatives of the same shape function, could impact the numerical stability and robustness of the model and, therefore, more detailed numerical studies should be made to choose the best approach.

²The term $[[\cdot]]$ denotes the jump at the interface of the quantity \cdot .

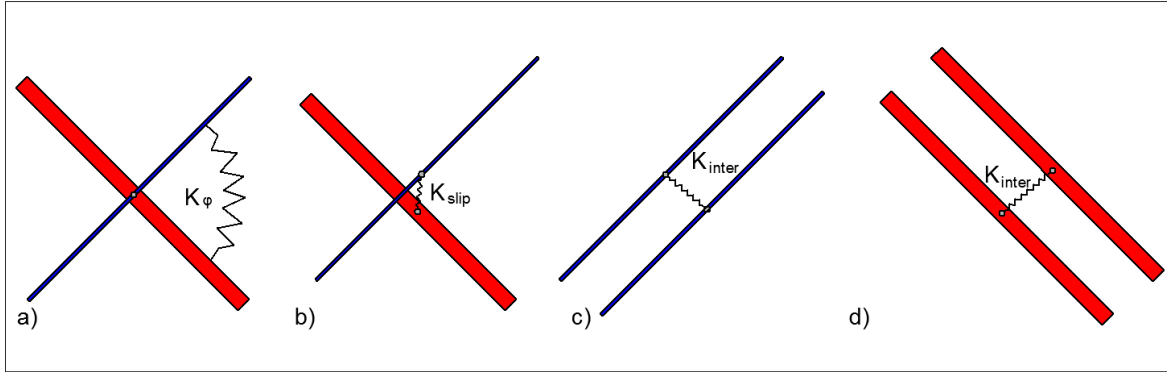


Figure 14: Schematics of the elastic interconnections between warp and weft yarns. (a) rotational spring, (b) translational spring, (c) interaction between thin yarns and (d) interaction between thick yarns.

2.3 Discrete mesoscopic 2D modeling

In this section, we set up a suitable discrete model in which the motions of the single yarns are singularly taken into account. The aim of this model is to have a clear comparison/validation for the proposed enriched continuous model. This discrete 2D model employs long Euler-Bernoulli beams, disposed at 90 degrees with respect to each other, to describe the two sets of yarns. Their connection is made via rotational and translational springs that mimic their physical interaction, see Figure 14, and both beams and springs are considered to behave linearly. The main features of this discrete model are that it allows to:

- explicitly account for the slipping of the yarns;
- better understand the potentialities and limitations of the enriched continuous model introduced.

More particularly, the two families of beams have axial stiffness $K_1 = EA_1$ and $K_2 = EA_2$ and bending stiffness $K_3 = EI_1$ and $K_4 = EI_2$, respectively, where E is the Young modulus of the material constituting the yarns, A_1 and A_2 are the equivalent cross sections and I_1, I_2 the equivalent moments of inertia. To model the yarns' interactions, the set of points in which the two families of beams intersect have been defined in COMSOL Multiphysics®. In this set of points, the interactions between the two yarns are supposed to be (see Fig 14):

- the shear stiffness, i.e. the resistance to the variation of angle between the yarns, which is accounted for via a set of rotational springs of stiffness K_φ ;
- the friction between two yarns, i.e. the resistance to the slippings, which is described by a set of translational springs with stiffness K_{slip} ;
- the transverse compression stiffness, i.e. the mutual interactions between parallel yarns due to the contact and the weaving of the orthogonal yarns, which is modeled with a set of springs with stiffness K_{inter} applied to every couple of adjacent points belonging to two different yarns of the same family.

A possible downside of such a discrete model is that a very large number of degrees of freedom is needed for a proper description of big specimens. In this optic, continuum models are preferable to discrete ones in view of the design of engineering structures. Another main limitation of the discrete model presented is that the interactions between adjacent yarns are all considered elastic. Even if this simplification is reasonable up to a certain extent, there are some irreversible mechanisms, such as friction, that are not accounted for. Indeed, when unloading the experimental specimen, it is not sufficient to let the specimen return in its initial configuration, therefore a certain part of the deformation is not elastic, but related to irreversible mechanisms such as friction. Nevertheless a big amount of the imposed deformation is recovered and, hence, this discrete mode can be a reasonable compromise between the complexity of the real microstructural motions and the simplicity of the model that one wants to introduce. To make a comprehensive model, the methods presented in [76] should be followed.

CHAPTER II.3

The Bias Extension Test

3.1 Characterization of the shear response of woven composite reinforcements

The behavior of woven composite reinforcements must be analyzed under different types of loads and, in particular, the most important feature to be determined is the in-plane shear response of the woven composite. In fact, due to the quasi-inextensibility of the fibers, the main deformation mode of the woven composites reinforcements during a forming process is the in-plane shear deformation (angle variation between the warp and weft).

Two main tests are of current use for the determination of the in-plane shear stiffness of the fabrics. The first test developed was the Picture Frame Test (PFT), in which a square specimen of the woven composite is ideally subjected to a state of pure shear deformation. Nevertheless, the state of pure shear is only theoretical: any misalignment of the specimen leads to an increase of the measured load [120, 125, 184]. In addition, the yarns are tightly clamped fixing their direction inside the four clamps and generating bending of the yarns during the motion. This effect usually implies an overestimation of the shear parameter due to these boundary effects. The second test used for the measure of the in-plane shear stiffness is the bias-extension test (BET). In this test one of the edges of a rectangular sample of woven composite reinforcement, whose yarns are initially oriented at $\pm 45^\circ$ with respect to the loading direction, is displaced in the direction of the axis [31, 93, 122, 194, 199, 231]. The length/width ratio of the specimen must be larger than 2, while in the present manuscript the ratio is fixed at 3. When one of the ends of the specimen is displaced by a given amount, three types of regions appear to have an almost homogeneous behavior in their interior (A, B and

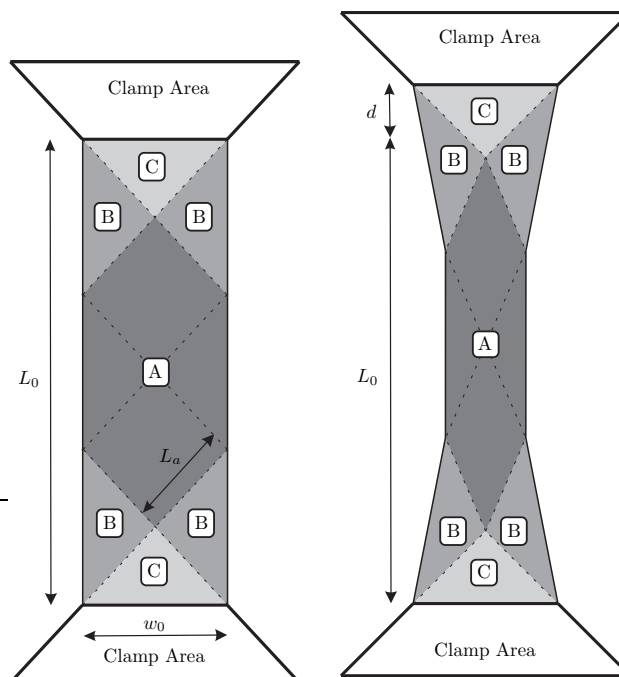


Figure 15: Simplified description of the shear angle pattern in the bias extension test

C in Figure 15). In each of these areas, the angle between the warp and weft direction is almost constant. These specific kinematics are due to the quasi-inextensibility of the yarns and the absence of slipping between warp and weft yarns at the crossover points. The advantage of the BET, with respect to the PFT, is that each yarn has at least one edge which is free, and this free edge is thought to be sufficient to avoid spurious tensions in the yarns as observed in [92, 120].

Nevertheless, there are some phenomena that are not described in the schematics of Figure 15 that are important for the complete understanding of the BET. As a matter of fact, the transition between two different areas at constant shear angle is not concentrated in a line, instead it is distributed in a transition layer with a gradual variation of the angle, as shown in Figure 16. In such transition layers, the angle variation between the two constant values is achieved by a smooth pattern directly associated to the local bending of the yarns. One more feature that can be highlighted is that the free boundary does not remain straight during the test, as is assumed in the scheme of Figure 15, but it shows a small curvature (Figure 9). Both of these phenomena can be understood by considering that the yarns possess a non-vanishing bending stiffness that depends on the micro-structure of the fabric: a variation of orientation cannot be concentrated in a point, creating a boundary layer of non-vanishing size. With the usual first-gradient models, it is not possible to include such micro-structural related phenomena while, with the aid of second-gradient theories, promising results have been obtained in [70]. In those models, a specific constitutive coefficient can be introduced, which can be directly related to the bending energy of the fibers. The second-gradient continuum model introduced in the present manuscript is able to describe the main macroscopic and mesoscopic deformation mechanisms taking place during a bias extension test on woven composite reinforcement.

3.2 The BET on unbalanced fabrics

One of the main aims of the present part is to show and discuss some specific results obtained during an uniaxial BET on an unbalanced specimen of fibrous composite reinforcement. The task of fully exploring what theoretical tools are needed to optimize the modeling of such unbalanced materials is left as a subsequent work, the scope of the present manuscript being that of explaining the principal micro and macro deformation mechanisms of such unbalanced fabrics. In fact, based on a phenomenological observation of some experimental results, it will be shown that the deformation modes which take place in a BET on an unbalanced fabric are completely different from those specific of the BET on standard fabrics described above. Moreover, the proposed second-gradient continuum model will be employed for the description of such unbalanced materials, pointing out the strong and weak points regarding its application to the design of complex engineering parts. It has to be explicitly remarked that mechanical conditioning was not accounted for in the present study with the aim of being closer to the conditions of a real forming process.

3.2.1 Experimental setup

In an unbalanced fibrous composite reinforcement, the warp and weft yarns are comprised of a very different number of fibers and, therefore, the mechanical properties in the two directions can differ considerably. The material studied in this manuscript is an unbalanced 2.5 D composite interlock with a characteristic weaving

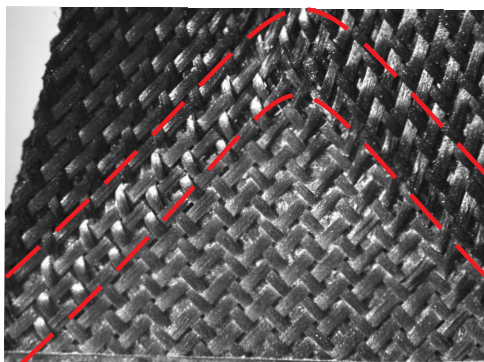


Figure 16: Boundary layers between two regions at constant shear

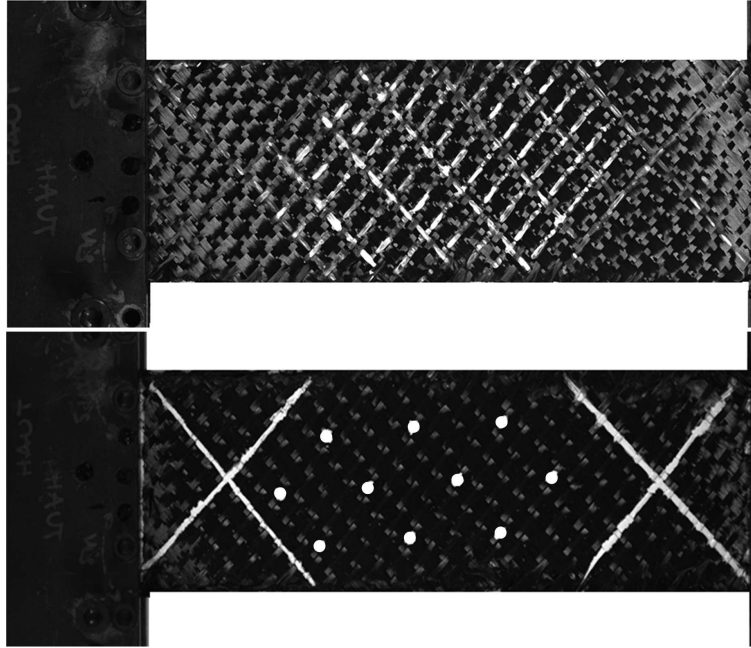


Figure 17: (a) Sample I on top, (b) sample II at the bottom

pattern in the direction of the thickness. The BET is performed on two samples of 3x3 twill unbalanced carbon interlocks with different unbalance ratios (Figure 17). For specimen I, a Tomographic image was obtained (Figure 18 (left)) showing the high unbalance of the specimen and the characteristic weaving pattern of the 2.5 D interlock.

To conduct the BET, the samples are positioned between the upper and lower jaws of a 100 kN Zwick Meca tensile machine (Figure 18 (right)). The force needed to deform the specimen is of the order of 100 N and, therefore, an auxiliary load cell of 500 N is used to allow for good resolution of the data from the test. During the test, the lower clamp is static while the upper clamp is set, with a displacement-control, to move up from 0 to 60 mm. The displacement speed of the movable clamp is set to 4 mm/min.

To analyze the experimental results and to reveal the characteristic deformation modes of the mesostructure, high-quality pictures of the samples during the deformation process are valuable. Therefore, a 16MP camera in combination with a 200x optical zoom and two LED adjustable color lights were used during the test, nonetheless, the detailed analysis of pictures of a black carbon specimen are still difficult to perform. For this reason, a white grid of lines aligned with the warp and weft yarns was added on the shear area A of the specimen I (Figure 17 (a)). However, during the analysis of the first specimen some difficulties following the deformation of the specimen were still present, therefore, for specimen II, it was decided to locate only a couple of white points on top of area A that, with a post-processing step, can lead to an easier access

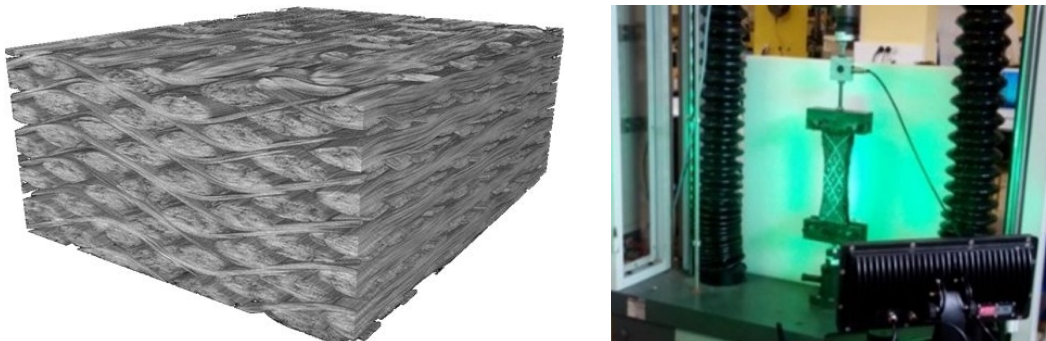


Figure 18: X-ray tomography of the interlock I (left) and experimental setting during testing (right).

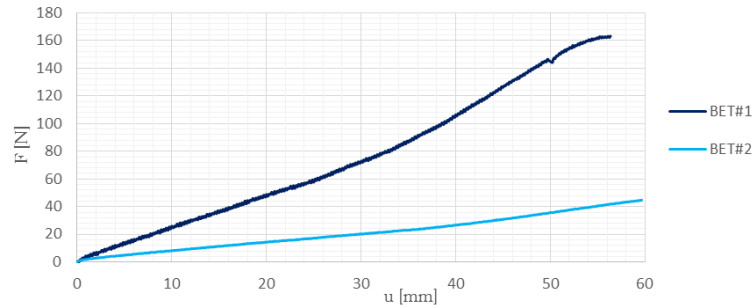


Figure 19: Force/displacement plot

to important data like the local shear angle or the sliding between yarns. The initial configuration of the interlock specimens and the added reference lines and points are illustrated in Figure 17.

3.2.2 Experimental results and physical interpretation

The results of the tests in terms of the load-displacement curve are shown in Figure 19. The force response of both of the specimens is almost linear except for a slight increase of stiffness at the end of the test. It is also easy to notice that the two materials present very different macroscopic stiffnesses due to their different internal architecture. To precisely identify the maximum strain that the material can withstand before failure due to excessive slipping, more experimental campaigns should be carried out. We limit ourselves here to remark that:

- after a first threshold the material behavior presents a softening which can be directly related to slipping;
- if the experiment is prolonged, the slipping becomes so important that some yarns are pulled out of the specimen compromising the integrity of the material rendering a continuous model unreliable.

Figure 20 shows the deformed shapes for both specimens during the development of the test. The quality of the test on the second specimen is much lower than that performed on the first one due to a non-perfect cutting. For this reason, the considerations will be illustrated by using the images relative to the specimen I, but analogous ones can be drawn for the specimen II.

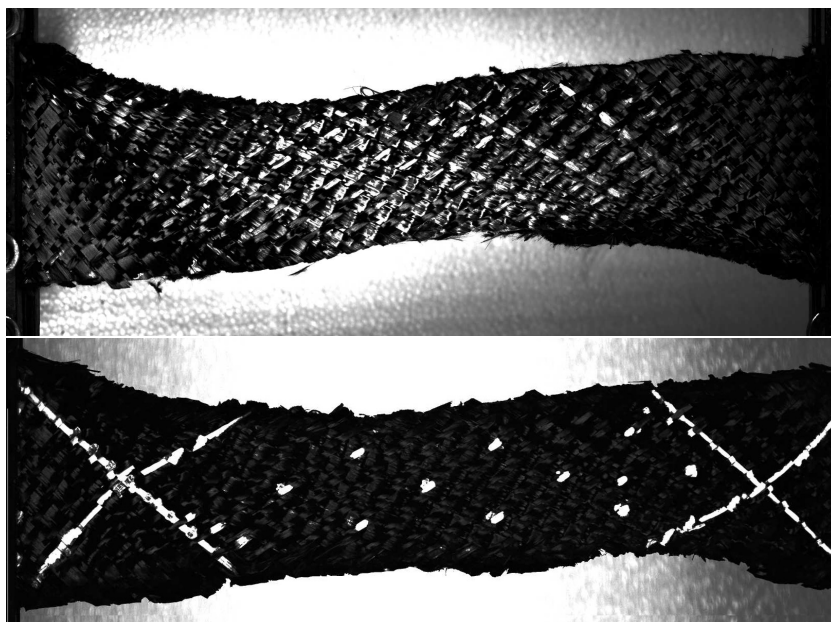


Figure 20: Deformed shape for both specimens (sample I on top, sample II at the bottom)

The main remark which may be inferred from the observation of the macroscopic deformed shape of the two specimens (Figure 20) is the asymmetric S-shape, which is due to the fact that the properties of the two families of yarns are very different in the two directions. What needs to be highlighted is that such an asymmetric shape is related to precise deformation mechanisms of the meso-structure which determine the behavior of such unbalanced materials. To represent with sufficient detail the mechanical behavior of unbalanced fabrics, a model must describe accurately:

- the macroscopic S-shaped deformation of the material;
- the mesoscopic deformations of the yarns inside the material.

To this goal, it is essential to observe the characteristic deformation patterns of the yarns inside the unbalanced fabric subjected to a BET. As will be better demonstrated in the remainder of this chapter, the main mesoscopic deformation mechanisms which take place during a BET performed on an unbalanced fabric are

- the in-plane shear deformation (angle variation between the yarns with respect to their initial configuration),
- the local differential bending of the warp and weft yarns due to the unbalance of the fabrics,
- the relative slipping of the contact points between warp and weft yarns.

Ideally, if perfect pivots were placed to connect the warp and weft without interrupting the continuity of the yarns and if the two families of fibers could be modeled as wires with infinite rigidity with respect to elongation and vanishing bending stiffness, the observed motion would be the ideal one presented in Figure 15. Thus, the only deformation mode would be the variation of the direction of the fibers which could be directly related to the angle variation between warp and weft. Nevertheless, in the considered material the yarns present a non-vanishing bending stiffness and a relative slipping of the warp with respect to weft changing the macroscopic mechanical behavior.

More particularly, the thin yarns possess a very low bending stiffness and, as it is possible to see in Figure 21 (c), there is a very sharp variation of direction that is concentrated in a very narrow layer. Instead, in the case of the thick yarns (Figure 21 (b)), there is almost no measurable change in direction along the whole fiber, a feature that can be uniquely related to an extremely high bending stiffness. As a consequence of this

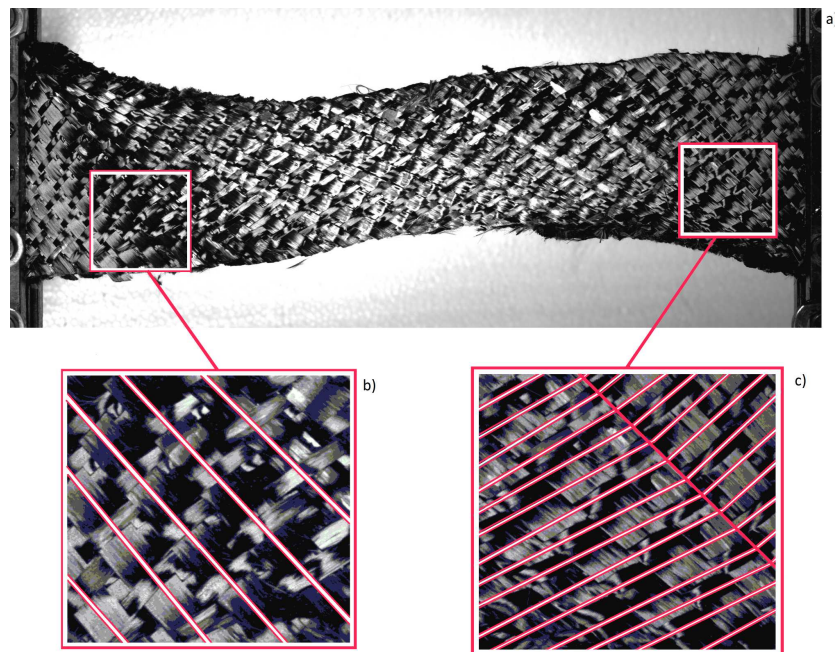


Figure 21: Deformed shape for a displacement of 56 mm (a) and angle variation in the transition layers for the thick (b) and thin (c) yarns

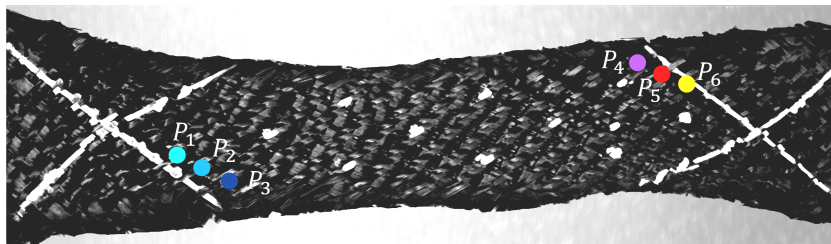


Figure 22: Points identifying some sliding phenomena

observation, it must be inferred that it is not possible to describe this specific behavior without accounting for the bending of the yarns at the mesoscopic level.

It is finally noted that the presence of measurable slipping of the fibers (up to a maximum that is around 10% of the total length of the yarns) strongly characterize this test. This phenomenon should be included in a complete model for this test and in general for woven composites. Such slippings can be qualitatively recognized when comparing the undeformed and deformed shape: three points which were initially located on the white cross marks which were drawn on the specimen have moved, thereby breaking the continuity of the cross marks themselves (see also points $P_1 - P_6$ in Figure 22).

A macroscopic indicator of the sliding may be found in the global in-plane thickness of the specimen. If relative sliding of the fibers is permitted, the height of the specimen measured in the middle of the specimen itself can be much higher than the height that the specimen would have if no relative motions were permitted. In some sense, such effect of the sliding can be modeled as a “fictive elongation” of the fibers in the two directions. More precisely, since the yarns can slide in the real situation, the resulting apparent in-plane thickness of the specimen is much higher than the theoretical one obtained if the yarns were considered hinged together. It is clear that the presence of such internal sliding weakens the basis on which a continuum theory is founded.

Nonetheless, we can continue using a continuum model with the limit of modeling such internal sliding as a “fictive” elongation of the yarns in the two directions. The price to pay for this modeling assumption is that the result of the simulations is a microstructure which is not perfectly superposable to the real one (the “real” sliding is replaced by “fictive” elongations of the yarns). In spite of this, the overall macroscopic pattern of the deformation can be recovered, together with the main features of the deformation of the underlying microstructure. Finally, we remark that the presence of the described relative sliding does not allow a direct interpretation of the in-plane shear deformation as the angle variation between the warp and weft directions. In fact, the in-plane shear is simply defined as the angle variation between the current direction of the considered yarn and its initial direction.

Summarizing, it is possible to say that the main mesoscopic deformation mechanisms which take place during the BET on an unbalanced fabric have been isolated. These significant contributions include the in-plane shear of the yarns, the differential local bending of the yarns and the sliding of the yarns. In the next section, three models will be used to capture such mesoscopic deformation mechanisms together with their macroscopic counterpart:

- a discrete mesoscopic 2D model;
- a first gradient continuous model;
- an enriched continuous model.

These models show how to obtain a sensible description of the macroscopic S-shaped deformation of the considered unbalanced fabric, as well as a reasonable prediction of the mesoscopic deformation of the yarns.

3.3 Modeling 2D woven fabrics

3.3.1 First gradient model

The first-gradient models are not able to capture the entire set of microstructural-related complex behaviors. However, it could be possible that the asymmetric S-shape of the macroscopic specimen, which can be

A_1	B_1	K_2
0.55 MPa	110 MPa	0.11 MPa

Table 3.1: Parameters of the first-gradient continuous model for the simulation of the BET.

K_{el}	K_{sh}	α_1	α_2
0.7 MPa	21 kPa	2 kN	0.02 kN

Table 3.2: Parameters of the second gradient continuous model for the simulation of the BET.

observed during the BET on unbalanced fabrics, could actually be reproduced by using a simple first-gradient theory with very different material properties in the two directions. This approach would mean that an energy of the type in Eq. II.2 could reproduce the observed phenomena. Considering that the invariants i_{13} and i_{23} represent out-of-plane angle variations of the yarns and i_{33} the out-of-plane extensional stiffness, we will consider a simplified energy for the 2D case of the type:

$$\Psi_I(C, \nabla C) = \frac{1}{2}A_1(\sqrt{i_{11}} - 1)^2 + \frac{1}{2}B_1(\sqrt{i_{22}} - 1)^2 + \frac{1}{2}K_2i_{12}^2. \quad (\text{II.7})$$

The chosen first-gradient coefficients are given in Tab. 3.1. Indeed, when suitably tuning the coefficients appearing in Eq. (II.7) by choosing significantly different values for A_1 and B_1 , it is true that an asymmetry can be produced in the macroscopic shape of the specimen which qualitatively agrees with the macroscopic experimental S-shape. Nevertheless, such macroscopic shape is not associated to any reasonable motions of the yarns at the mesoscopic level. With the considered constitutive choice, the main first gradient deformation modes allowed for the considered material are:

- the angle variation i_{12} between the warp and weft direction;
- the equivalent elongations i_{11} and i_{22} in the directions of the warp and weft which account for decrimping and, eventually for slipping.

It must be remarked that this simple quadratic choice for the first gradient strain energy density, even if providing geometric non-linearities, could be not sufficiently general to describe larger deformations, for which more complex hyperelastic constitutive laws should be introduced. More than that, since for very large strains the integrity of the material starts to be compromised by an excessive slipping, there is no interest in modeling the targeted unbalanced materials after a given strain threshold. We also remind how the macroscopic effects of the sliding are here modeled as a “fictive elongation” of the fibers in the two directions.

3.3.2 Second gradient model

For the second gradient model, we consider a decomposition between the first and the second gradient energy. The first gradient energy is the same used in the first gradient model (Eq. II.7):

$$W_I(C) = \frac{1}{2}K_{el} [(\sqrt{i_{11}} - 1)^2 + (\sqrt{i_{22}} - 1)^2] + \frac{1}{2}K_{sh}i_{12}^2, \quad (\text{II.8})$$

where the parameters K_{el} and K_{sh} are different from the first gradient case. The two elongation modes have the same stiffness to underline the difference in bending that drives the asymmetry of the macroscopic deformation. We also remind how the macroscopic effects of the sliding are here modeled as a “fictive elongation” of the fibers in the two directions (see section II.2.2.1). On the other hand, the second gradient energy (II.4) reduces in the 2D case to an energy of the type:

$$W_{II}(\nabla i_{12}) = \frac{1}{2}(\alpha_1 i_{12,1} + \alpha_2 i_{12,2}), \quad (\text{II.9})$$

where α_1 and α_2 are the micromorphic elastic parameters that have to be different to account for the imbalance of the microscopic characteristics of the material. The parameters used in the simulations are shown in the table 3.2. We notice that even with the insertion of the equivalent elongation the shear stiffness

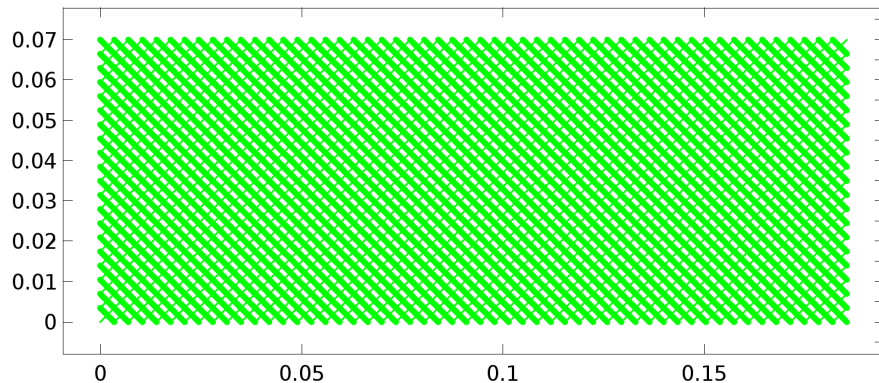


Figure 23: Geometry of the discrete model: undeformed configuration.

K_1	K_2	K_3	K_4	K_φ	K_{slip}	K_{inter}
50000 N	50000 N	0.4 N·m ²	10 ⁻³ N·m ²	2.510 ⁻⁴ N·m	11 N/m	11 N

Table 3.3: Parameters of the discrete model for the simulation of the BET.

is much lower and, therefore, the main deformation mode is still the shear one as the common knowledge on the behavior of these materials suggests.

The model was implemented in COMSOL Multiphysics[®] using a micro-descriptor φ numerically constrained to be equal to the angle variation i_{12} . The resulting second gradient energy is:

$$W_{II}(\nabla\varphi) = \frac{1}{2}(\alpha_1\varphi_{,1} + \alpha_2\varphi_{,2}), \quad (\text{II.10})$$

If, for example, we let φ tend to i_{12} , then expression (II.10) for the strain energy density tends to (II.9) and, therefore, accounts for space derivatives of the angle variation and the bending of the yarns. Based on the physics of the problem discussed in the previous sections, we do not introduce second gradient effects related to the gradients of the other invariants. We are then excluding that sharp spacial changes of elongation occur in the considered material. The results obtained with this energy in the simulations are presented in the section II.3.4.

3.3.3 Discrete model

To have a comparison for the continuous models, the discrete model presented in section II.2.3 was implemented in COMSOL Multiphysics[®] for the Bias Extension Test. The elastic parameters used have been chosen to be reasonably compatible with yarns of small cross section area and Young moduli of carbon (see table 3.3). The two elongation stiffnesses K_1 and K_2 have the same value to underline how the difference in the bending stiffness drives the asymmetry of the macroscopic deformation. Furthermore, it must be pointed out that, as long as the elongation stiffness is high enough, it does not strongly influence the results in terms of both displacement and reactions. The parameters relative to the bending stiffness, the slipping and the interaction between two fibers of the same set were chosen via a fit of the experimental shape of the specimen. In particular, the following characteristics were used to fit the different parameters: the width of the specimen in the central part, the macroscopic S-deformation, the slipping of the fibers and the distance between the fibers of the same set. The shear stiffness K_φ , was chosen in order to fit the experimental force with the reaction evaluated with the simulations.

3.4 Numerical results

In this section, the results obtained with the different models presented are shown. To better evaluate the models, we show the experimental shape for a displacement of 37 and 56 mm (Figure 24(a)) as reference for all the following considerations. The numerical results shown in this section are obtained with three very different models, namely:

- a first gradient continuum model,
- a second gradient continuum model,
- a discrete model.

For each model all the results in terms of displacement, deformations and forces are shown.

Deformed Shape The most interesting feature shown in the experimental results is the S-shape. Even with a first gradient model, with an appropriate choice of the constitutive parameters it is possible to describe roughly the outline of the test as shown in Figure 24(b). Even if this results seems promising, the deformation presented in this picture is completely different from the experimental one. Indeed, the black lines describe the position of the yarns in the deformed specimen and we see that the lines corresponding to the thick yarns do change sensibly direction while the thin yarns remain almost unbent. This is opposite to the experimental evidence and it is a sign of a profound mismatch of the bulk deformation between the first gradient model and the actual response of the fabric.

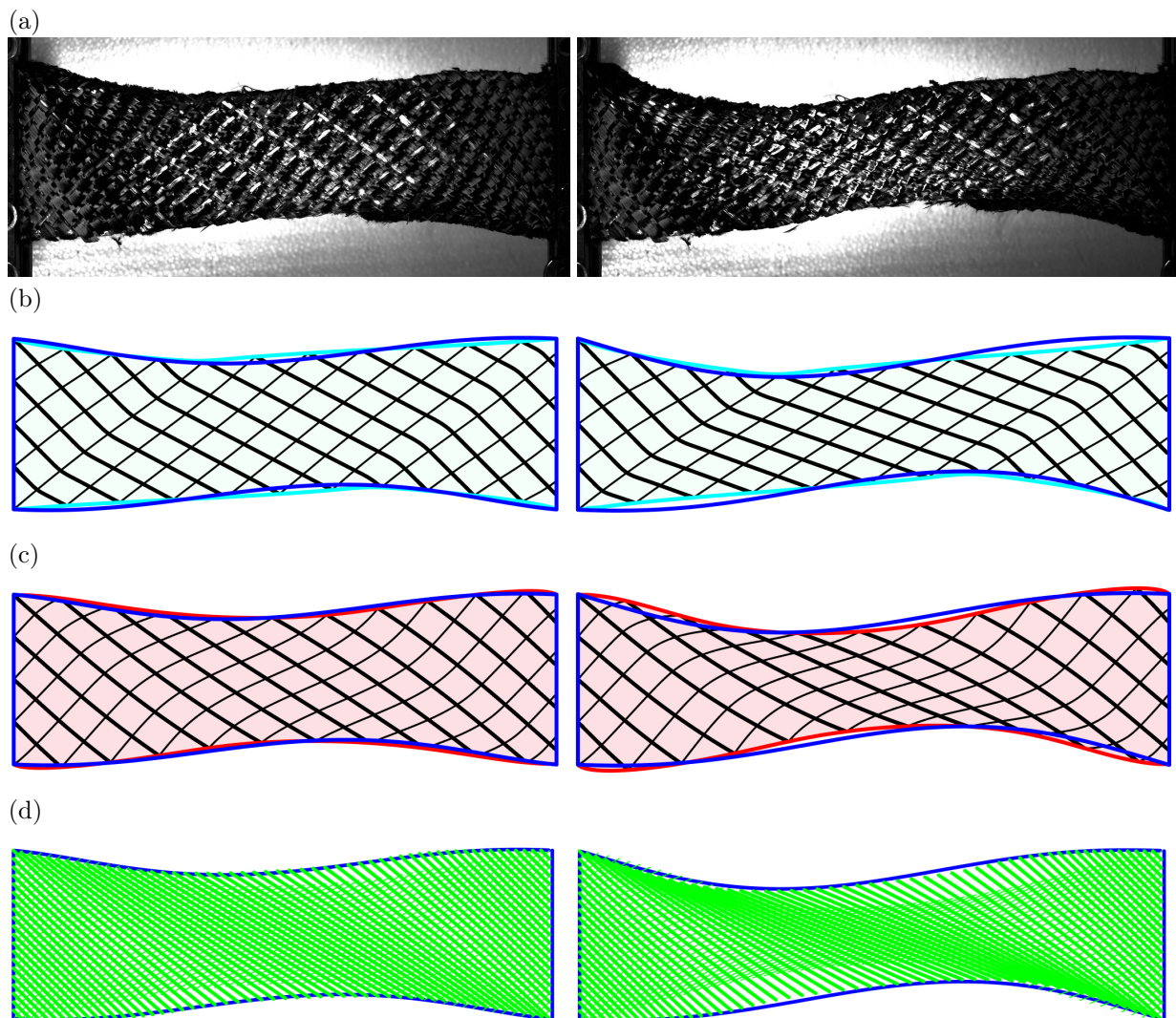


Figure 24: Deformed shape for a displacement of 37 mm (left) and 56 mm (right). From top to bottom: (a) experimental shape, (b) first gradient simulation (cyan with black fibers), (c) second gradient simulation (red with black fibers) and (d) discrete simulation (green). The blue outline is the experimental shape.

Considering instead a second gradient energy, we notice in Figure 24(c) that the simulation matches the experimental response very well even for different values of displacement both in the outline and in the internal deformation. Indeed, the fiber lines are coherent with the experimental evidence and even the width of the specimen matches the experimental results. This width is obtained with the insertion of “equivalent” elongation that describe the presence of the slipping and its consequent increase of width.

As for the continuum models, Figure 24(d) shows that the discrete model well describes the s-response even at different values of displacement. Furthermore, the slippings forecast by the model fit qualitatively the experimental observation, even if the constitutive law is a simple linear one. The response of this model shows strong similarities with the second gradient models. Indeed, the different bending stiffness of the two family of fibers lead to a set of straight thick fibers and a set of strongly bent thin fibers like the continuous case.

Angle Variation In a material for which the shear is the main deformation mode, one of the most important features to check is the angle between the fibers. To confirm the errors on the description of the deformation behavior of the fabrics with a first gradient model, Figure 25 (a) shows that the direction of constancy of the angle between the fibers is along the thin fibers while the experimental results and the other models show a constancy along the thick fibers.

On the other hand, we can see in Figure 25 (b) that, in the second gradient model, the angle between the set of fibers is almost constant along the strong fibers direction well describing the experimental evidence. This feature is due to the high bending stiffness of the thick fibers that keeps the angle with the orthogonal fibers almost constant along their fiber direction.

Also in the case of the discrete model, the angle between the fibers has been plotted. As we can see in Figure 25 (c), even in this model the angle between the set of fibers is almost a constant along the strong fibers direction, but drastically changes along the think yarns. The results of both the discrete and second gradient models, even with their very different natures, present the same qualitative description of the experimental behavior reconfirming the good analogy between the bending stiffness of the yarns and the second gradient effects in the continuum. This is another hint toward the importance of the insertion of a second gradient energy in a continuous model in order to fully describe the phenomenological mechanical response of the woven fabrics.

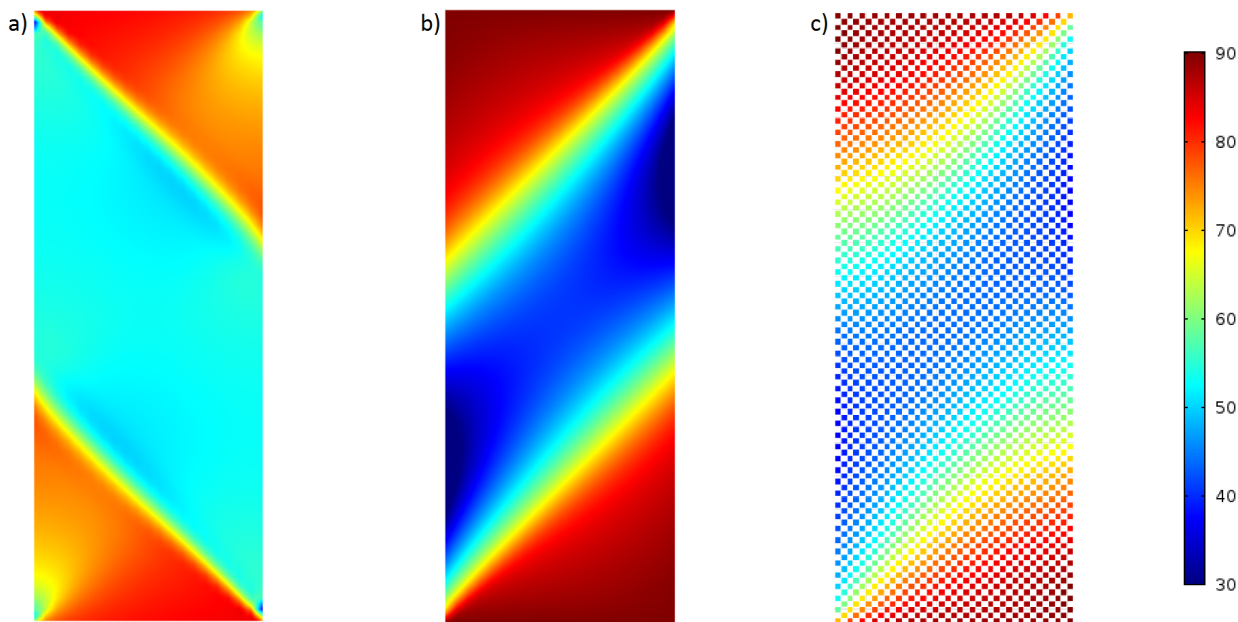


Figure 25: Angle between the fibers in the first gradient (a), second gradient (b) and discrete (c) simulations for a displacement of 56 mm.

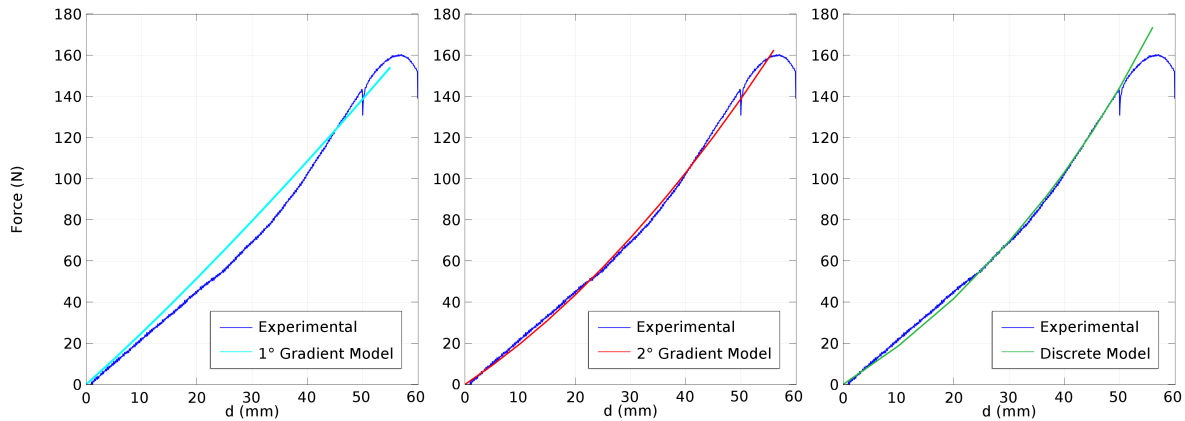


Figure 26: Load-Displacement curve for the first gradient (left), the second gradient (center) and the discrete (right) model

Load-Displacement Curve To evaluate the overall behavior of the model, an important feature to check is the response in terms of forces. Considering a first gradient model, we can describe the magnitude of the response at different values of displacement but there are no sensible increases of the stiffness of the specimen during the test. The results for this model are shown in Figure 26 (left).

Also in the case of the second gradient model, Figure 26 (center) shows a very good fit between the simulations and the experimental results in terms of force-displacement curve, despite the simplicity of the model. The slight non-linearity in the simulated response, that partially reflects the experimental increase of stiffness, is due only to the geometric non linearity of the problem while the constitutive laws of the problem are linear. Furthermore, the approximation of the slipping as an elongation seems to not affect the ability to describe the global response of the specimen.

Finally, the results in terms of a force-displacement curve are shown in Figure 26 (right) for the discrete model. Once again the force shows a good fit with both the experimental results and the second gradient model confirming once again the analogy between such different models.

Double Force-Displacement Curve The second gradient model possesses a feature that the first gradient model does not: the reaction in the clamps is not limited to a force and a moment. Since i_{12} is fixed, there is a reaction in terms of double-force; the results obtained are shown in Figure 27 in terms of the double-force. As far as the discrete model is concerned, it is possible to consider a discrete equivalent of the double-force. Indeed, for each beam there is a moment reaction to the local bending of the beams: an analog to the double-force. We must point out that the sum of these moments is not the resulting moment acting on the clamp but a description of an average local bending. While the models are very different in nature, this

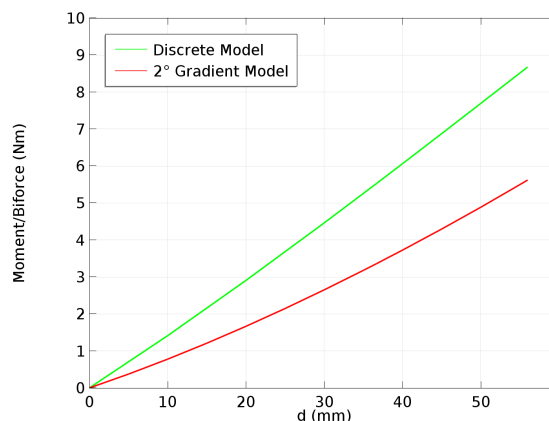


Figure 27: Double-force-Displacement curve \mathcal{T} (dual of i_{12}) versus sum of the discrete bending moments.

possibly far-fetched analog of the double-force, as shown in Figure 27, has a magnitude comparable with the double-force evaluated in the continuous model and is also linear. This analogy can be useful to hint to the physical meaning of the insertion of a second gradient energy and of second gradient boundary conditions.

Influence of the constitutive parameters on the results Now, we analyze the influence of the constitutive parameters on the response of the second gradient model. As was said before, the peculiar S-shape assumed during the test was modeled in this work with an asymmetric second gradient energy. Figure 28 (top) shows that when $\alpha_1 = \alpha_2$ the axis remains straight and that the S-shape is more pronounced with the increase of the parameter's value. The other parameter that strongly determines the deformed shape is K_{el} , that accounts for the slipping of the fibers by means of an equivalent elongation. It is possible to see in figure 28 (bottom) that the thickness of the specimen in the central part varies with the elongation stiffness. Once again we remark that this is only an equivalent continuous analysis of the slipping aimed to qualitatively describe the overall experimental behavior. Finally, we mention that the second gradient model could be implemented as a classical micromorphic model by weakening the constraint $i_{12} = \varphi$. The results obtained in this case are shown in Appendix B.2.

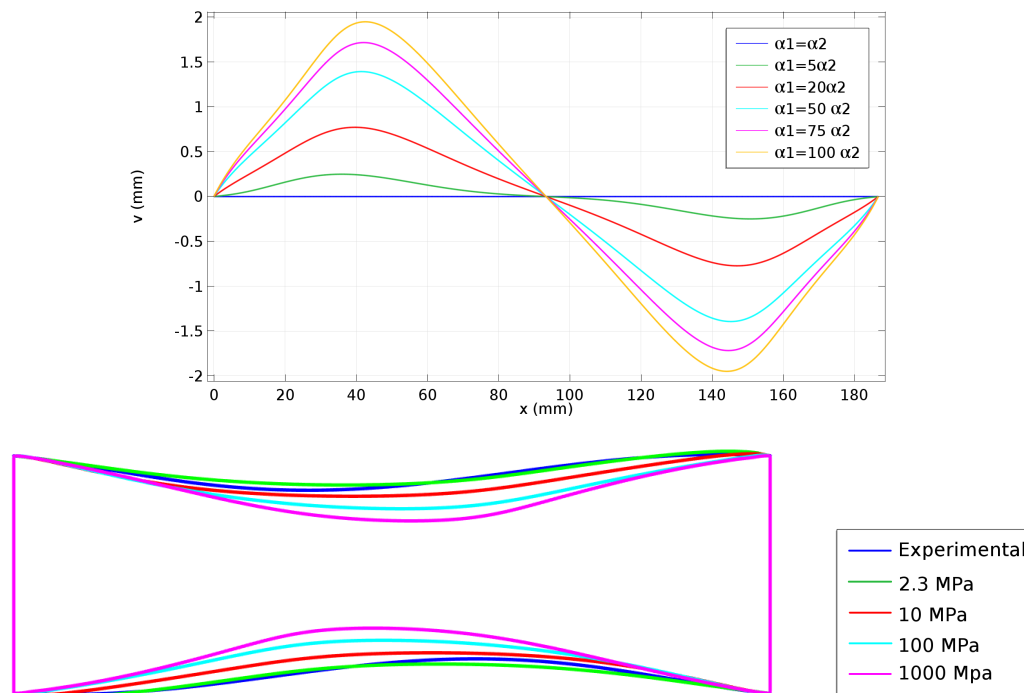


Figure 28: Vertical displacement of the axis for an imposed displacement of 56 mm and different values of α_1 (top) and d Deformed shape for a displacement of 37 mm and different values of K_{el} (bottom).

CHAPTER II.4

Deep Drawing

Woven composite materials are the most widespread choice in the case of mechanical reinforcement, due to their great formability and the subsequent possibility of designing rather complex mechanical pieces. The forming processes, such as the Resin Transfer Moulding, (RTM), have received a great deal of attention in the literature (see subsection II.1.3.3 and [191, 198, 202]). The most current forming processes consists basically of two stages:

- the dry woven fabric is preformed to obtain the desired geometry for the final part;
- a thermoset resin is injected into the woven fabrics filling the pores of the fibrous reinforcement.

The process used in the forming stage is thus followed by the injection and curing of a resin in the woven fabrics, after which the finished material, union of the reinforcement and the matrix, is obtained. The quality of the obtained piece is greatly influenced by several factors, such as the characteristics of the preformed woven fabric and, in particular, its permeability, the characteristic of the resin and the temperature at which the injection process takes place. In the literature, it is possible to find a great number of articles studying in detail the injection processes and the characteristic of the resins (see [191, 198, 202]) and also the preforming processes of thin woven reinforcements (see [25–28, 30, 52, 53, 76, 90, 232, 238]). Nonetheless, few research endeavors concern 2.5D or 3D composite reinforcement forming simulation [35, 147, 192]. The focus of this chapter will be on the first stage of the forming process, namely the preforming of 2.5D or 3D dry reinforcements. The understanding of this step is very important to determine if the preforming process is even possible. Indeed, the woven fabrics can withstand only a certain amount of shear deformation between the fibers without dissociating and, thus, an accurate modeling becomes crucial for optimal design.

The process of preforming can become fairly intricate when the geometries are complex (e.g. double curved geometries) and the prediction of the entirety of the properties of the deformed fabrics is, therefore, challenging. Several experimental devices have been set up to investigate the deformation modes and the possible occurrence of defects during forming of textile reinforcements [31, 122]. Among them, the hemispherical punch and die systems (Figure 29) were especially studied because of their simple shape, double curvature and large shear angle variations between the yarns in the final state.

Reliable models for the preforming process should include information about the fiber directions and densities in the deformed state, so aiding the simulation of the resin injection and of the structural behavior of the final composite part. Indeed, the permeability of the 3D interlock fabric is strongly influenced by some deformation states that can alter or even close the interstices in the micro-structure affecting profoundly the resulting material properties. Furthermore, the direction and positioning of the yarns, that are determined solely by the preforming process, have a predominant role in the resulting mechanical properties of the composite structure (stiffness, damage and fracture, etc.).

Different approaches have been proposed to model the raw fibrous composite materials that can be found in the literature (see chapter II.2 and [25, 27, 30, 52, 53, 76, 90]). The most widespread approach to the simulation of fibrous composite materials is, nowadays, the finite element model that needs the determination of specific constitutive laws to describe the complex experimental evidences shown by woven composites. In the present manuscript, additional evidence is provided regarding the fact that neglecting the bending rigidities of the yarns in the modeling phase can produce inaccurate results of the simulation of 3D woven fabrics (thickness ~ 1 cm) during the modeling phase. In order to support this statement, a 3D FEM is implemented and a rather simple constitutive form of the strain energy density is introduced, accounting for:

1. initial orthotropy,
2. geometric non-linearities,

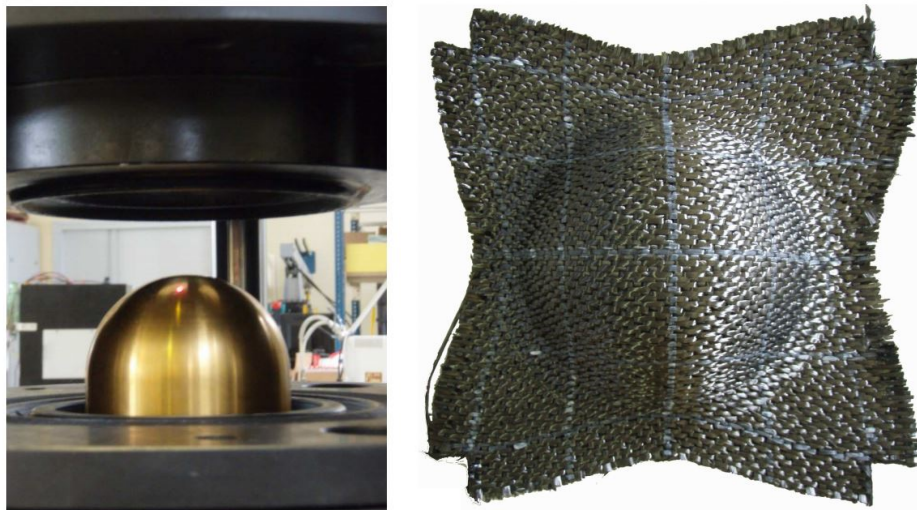


Figure 29: Experimental setup and deformation for a deep-drawing preforming with a hemispherical punch [35].

3. in-plane and out-of-plane bending of the yarns (through the introduction of suitable second gradient terms).

This second gradient model is implemented in COMSOL Multiphysics[®] looking for solutions that are continuous, as it is usual in FEM, but that also grant continuity of the first derivatives of the displacement field.

In this way, the following desirable results are obtained:

- the solution is in agreement with the observed experimental shapes (Figure 29);
- the second gradient energy has a beneficial effect on the mesh-dependency of the solution;
- the presence of suitable second gradient terms which are descriptive of the yarns' bending allows to control the onset and evolution of wrinkles during the deep-drawing process. More particularly, if the second gradient parameter (viz the bending stiffness of the yarns) is sufficiently high, no wrinkling is observed during the simulation. This result is in agreement with the common observations of experimental results.

The results presented here should be used as a guide towards the throughout implementation of FEM codes including second gradient constitutive laws for the complete modeling of the mechanical behavior of fibrous composite reinforcements during their forming process.

4.1 Second gradient energy

The description of woven composites' mechanical behavior demands important efforts. Through the analysis of the deformation patterns during experimental testing, it is easy to notice that the condition of material continuity is not always strictly fulfilled, due for example to some relative slipping of warp and weft. However, if the amount of slipping between the fibers is low, a continuous model can still be used [35, 36]. This is the approach adopted here, but it must be noted that the possibility of modeling each fiber as a single detached element still exists, even if it is of difficult applicability for big mechanical pieces [60]. Continuum models with "fictive" elongations can be also introduced to account for a certain amount of slipping while remaining in a continuum framework (see for example II.3 and [130]).

Considering the specific case of deep-drawing preforming, one of the phenomena which is most difficult to control, with a first gradient energy, is the onset of wrinkling in the deformed fabric. In first gradient simulations, the presence of wrinkles is observed when a certain amount of in-plane shear stiffness is present

K_{11}	K_{22}	K_{33}	K_{12}	K_{13}	K_{23}
5 MPa	5 MPa	0.5 MPa	50 kPa	0.5 kPa	0.5 kPa

Table 4.1: Parameters of the first gradient energy for the simulation of the deep drawing.

(see for example [29]). Nevertheless, the number and amplitude of such wrinkles is a mesh-dependent phenomenon and such wrinkling is not descriptive of the experimental results. In what follows, this result will be obtained again for a traditional first gradient finite element model with linear shape functions.

Once again, we choose a very simple constitutive energy, so that it is possible to thoroughly analyze the influence of both meshing and additional second gradient terms on the performed numerical simulations. The chosen constitutive expression for the first gradient energy is (see Eq. II.2):

$$W_I(C) = \frac{1}{2}K_{11}(\sqrt{i_{11}} - 1)^2 + \frac{1}{2}K_{22}(\sqrt{i_{22}} - 1)^2 + \frac{1}{2}K_{33}(\sqrt{i_{33}} - 1)^2 + \frac{1}{2}K_{12}i_{12}^2 + \frac{1}{2}K_{13}i_{13}^2 + \frac{1}{2}K_{23}i_{23}^2, \quad (\text{II.11})$$

where K_{ii} are the extensional stiffnesses in the direction of the yarns as well as in the orthogonal direction, while K_{ij} with $i \neq j$ are the in-plane and out-of plane shear stiffnesses. The parameters chosen are the ones shown in Tab. 4.1.

The following constitutive form is introduced for the second gradient strain energy density (see Eq. II.4):

$$W_{II}(\nabla C) = \frac{1}{2}\alpha_1 i_{12,1}^2 + \frac{1}{2}\alpha_2 i_{12,2}^2 + \frac{1}{2}\beta_1 i_{13,1}^2 + \frac{1}{2}\beta_2 i_{23,2}^2, \quad (\text{II.12})$$

where with α_1 , α_2 and β_1 , β_2 are the in-plane and out-of-plane bending stiffnesses of the two family of yarns, respectively. For unbalanced fabrics, i.e. fabrics whose warp and weft yarns do not have the same characteristics, it is likely that $\alpha_1 \neq \alpha_2$ and $\beta_1 \neq \beta_2$ (see also [11, 130]). However, the object of this chapter are interlocks which are balanced and, hence, it is assumed that $\alpha_1 = \alpha_2 = \alpha$ and $\beta_1 = \beta_2 = \beta$. Moreover, it is possible that the two families of yarns have different bending stiffnesses in-plane and out of plane, but we will neglect this difference setting $\alpha = \beta$. The chosen second gradient energy thus takes the form:

$$W_{II}(\nabla C) = \frac{1}{2}\alpha (i_{12,1}^2 + i_{12,2}^2 + i_{13,1}^2 + i_{23,2}^2), \quad (\text{II.13})$$

4.2 Modeling geometry and contact interaction between the mold and the reinforcement

The object of this chapter is the simulation of the deep-drawing process performed on 2.5D composite interlocks. In particular, the focus will be on a hemispherical punch and die system, as the one shown in Figure 30. In such test, a square dry woven composite interlock is formed by a hemispheric punch that, along with the presence of a horizontal plane, makes the deformed shape assume a double-curvature shape.

To implement the contact between the woven composite and the testing machine, a penalty function was introduced such that, to each interpenetration, it associates a stress t normal to the surface which is applied

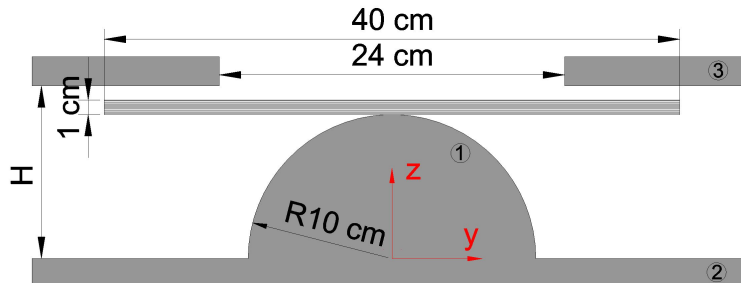


Figure 30: Geometry of the model for a deep-drawing preforming with a hemispherical punch.

on the fabric, in symbols:

$$t = K_{\text{contact}} \Delta n, \quad (\text{II.14})$$

where K_{contact} is an opportune stiffness that is set to increase in each non-linear iteration to obtain the minimum interpenetration possible, Δ is the interpenetration between the woven fabrics and the machine, and n is the normal to the surface of the punch or the die. The perpendicularity of the stress is equivalent to assuming that no friction is present between the experimental setup and the specimen. This could be considered a strong hypothesis, but the results seem to be qualitatively correct and this suffices for the purposes of this manuscript.

In the presented model, we chose to model the punch and the die as rigid bodies since they are supposed to have a stiffness of various orders of magnitude higher than the specimen. Thus, the position of the die and the punch is known a priori in each step of the test, leading to a much easier determination of the contact stresses in Eq. (II.14). Indeed, considering as origin of the reference system the center of the basis of the hemispherical punch, the Z axis as the vertical loading direction and the current position (x, y, z) of a point of the fabric, the interpenetrations between the woven fabric and the hemisphere, the lower plane and the die, respectively, can be expressed as:

$$\Delta_1 = \max(R - \sqrt{x^2 + y^2 + z^2}, 0), \quad \Delta_2 = \max(-z, 0), \quad \Delta_3 = \max(z - H + w_0, 0), \quad (\text{II.15})$$

where R is the radius of the hemispherical punch, H_0 and w_0 are the initial position and the applied displacement of the die in the considered step, respectively. The direction of the resulting stress is radial for the hemispherical punch and vertical for the plane and the die. Therefore, considering once again the center of the hemispherical punch as the origin of the reference system, we can write:

$$n_1 = \frac{(x, y, z)}{\sqrt{x^2 + y^2 + z^2}}, \quad n_2 = (0, 0, 1), \quad n_3 = (0, 0, -1), \quad (\text{II.16})$$

The resulting stresses t_1 and t_2 were applied to the lower surface of the specimen, while t_3 was applied to the upper surface. Finally, the resulting contact stresses can be written as:

$$\begin{aligned} t_1 &= K_{\text{contact}} \max\left(\frac{R}{\sqrt{z^2 + y^2 + z^2}} - 1, 0\right) \cdot (x, y, z), \\ t_2 &= K_{\text{contact}} \max(-z, 0) \cdot (0, 0, 1), \\ t_3 &= K_{\text{contact}} \max(z - H + w_0, 0) \cdot (0, 0, -1). \end{aligned} \quad (\text{II.17})$$

4.3 Numerical results

In this section, the results obtained by the FEM simulation of deep-drawing are presented as follows:

- in the first subsection, the influence of the second gradient parameter α on the onset of wrinkles during the simulation of the deep-drawing is studied;
- the second subsection presents some observed mesh-dependency results for the first gradient model, when using linear shape functions or the *augmented continuity shape functions*, and for the second gradient solutions in the case of the *augmented continuity shape functions*. It is concluded that second gradient simulations are not significantly affected by the choice of the mesh, provided that the size of the elements is sufficiently small;
- the third subsection shows the influence of cutting the corners of the specimen on the onset of wrinkling.

4.3.1 Influence of the second gradient on the wrinkling

The model here presented implements the *augmented continuity shape functions* (see II.2.2.3) in a COMSOL Multiphysics[®] finite element model. The energy considered was the sum of the first gradient energy presented in Eq. (II.11) and of the second gradient one given in Eq. (II.13), for which the directions of the fibers D_1

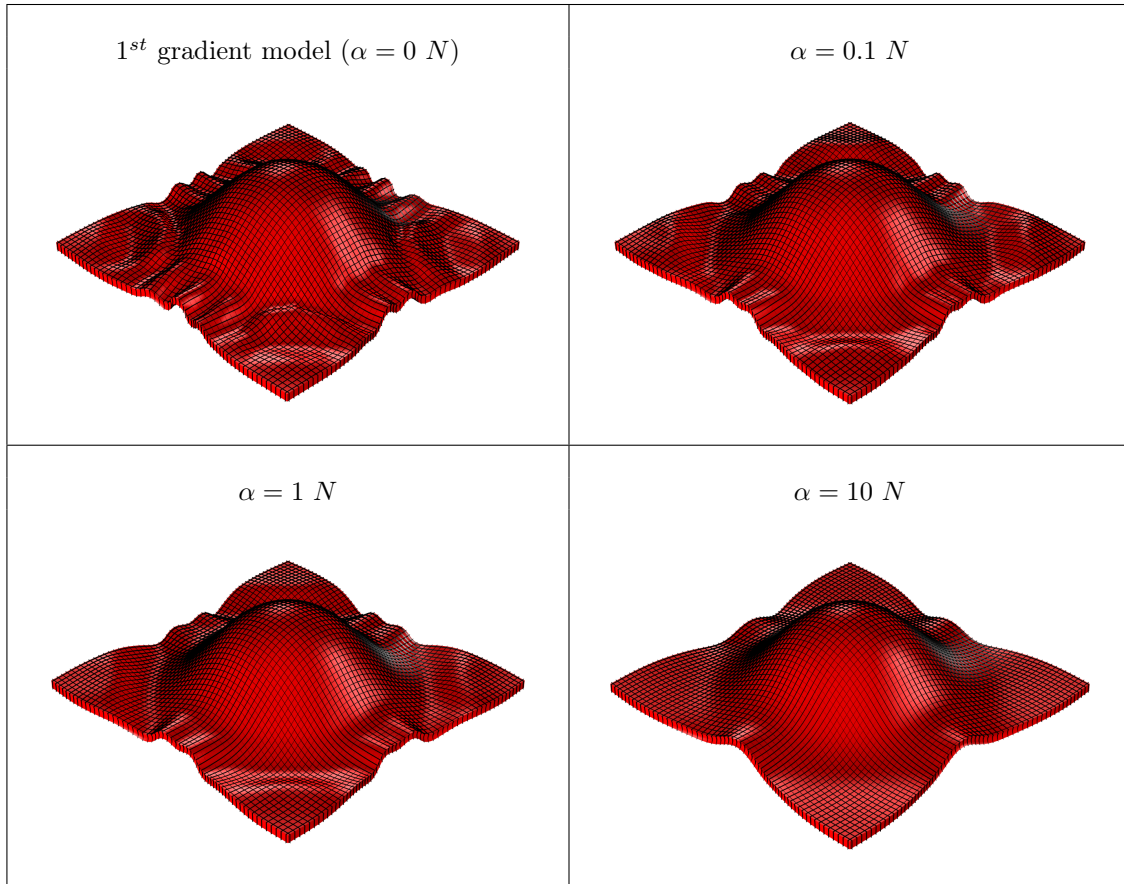


Figure 31: Dependence of the solution on the second gradient parameter α .

and D_2 were chosen to be parallel to the edges of the specimen. The first gradient parameters are the ones shown in the Tab. 4.1, while various values of the second gradient parameter α were considered. It must be noted that, in the case $\alpha = 0$, the model reduces to a first gradient model with the energy in Eq. (II.11).

The results, obtained for $\alpha = 0, 0.1, 1, 10 N$, are shown in Figure 31 for an imposed displacement of 90% of the punch's radius (9 cm). In the first gradient case, it is possible to notice the presence of a significant number of wrinkles in the fibers direction causing a considerable out-of-plane curvature of the fibers. Instead, the insertion of a second gradient energy depending on the curvature reduces the wrinkling effect. If the value of α increases to the value $10 N$, all the secondary wrinkling disappears and the only principal wrinkle remaining is due to the natural evolution of the double curvature of the macroscopic configuration. During experimental testing, it is a spread routine to cut the corners of the specimen as in the simulations shown in Figure 65, see [35]. The influence that this change in the geometry can have on the onset of wrinkling during the deep drawing of the fabric is studied in Appendix B.3.

As will be shown in subsection II.4.3.2, the first gradient model appears to be mesh-dependent even after the introduction of the *augmented continuity shape functions* (see Figure 34) and it is, therefore, impossible to show a representative solution for this case. Thus, it was chosen to show the deformed shape evaluated with the thinner used mesh, even if it is reasonable to assume that more wrinkles could appear for thinner meshes. On the other hand, even for small values of the second gradient parameter α , a stabilization of the deformed configuration is obtained (see Figure 34) and the deformed shape presented can be considered a representative solution.

The possibility of controlling the onset and evolution of wrinkling during the deep-drawing simulation via the introduction of a constitutive parameter could be of great use in the forecast of the material behavior in view of structure design. It must be reminded that the presented simulations are relative to an experimental test meant for the characterization of the material constitutive properties. It is, therefore not enough to correctly describe the experimental results but the final goal is to predict the behavior of the woven fabric in

generic engineering applications.

An issue that has to be covered is the determination of the second gradient parameter via experimental testing. Considering the proposed simple energy, it could be possible to heuristically choose α in order to have a qualitative description of the wrinkling phenomenon during a test such as the one proposed here. Furthermore, there are several experimental phenomena whose description would be useful for the calibration of a second gradient energy. During a Bias Extension Test, it is possible to observe the formation of some shear boundary layers the description of which can be used to calibrate the second energy parameters, as shown in [70]. In the case of a Bias Extension Test on strongly unbalanced fabrics, the bending stiffness of the fibers can lead to some macroscopic effects like the asymmetric deformed shape analyzed in [11, 130]. Finally, the calibration of the second gradient parameter could be attempted via a three point bending of an interlock, as in [134]. Which combination of these tests is best suited for the determination of the second gradient parameters is still to be decided, but it is important to have multiple observable effects so that it is possible to validate the chosen parameters.

The results obtained here are a confirmation of the great potential of a second gradient model for the description of the wrinkling phenomenon and, more generally, of the behavior of composite materials. In the author's opinion, the results presented here and in [11, 70, 130, 134] are starting to clearly show how a second gradient model can be a potential solution for most of the issues relative to the description of the behavior of dry woven fibrous composite.

4.3.2 Some considerations concerning mesh-dependency of the performed simulations

First gradient model with linear shape functions As stated above, the results obtained via a first gradient model appear to be mesh-dependent, due to the non-stability of the wrinkling description. The aim of this subsection is to present this issue in the case of a classical first gradient implementation and, hence, to show the stabilization effect obtained with the insertion of a second gradient energy.

The *augmented continuity shape functions* introduced for the second gradient model are temporarily discarded, enabling us to frame the mesh-dependency problem in a more traditional setting. In the simulations of this subsection, we implement a model with the Lagrange linear shape functions. The study of the mesh-density's influence on the first gradient solution is made with two types of mesh, namely:

- hexahedral meshes obtained by sweeping quadrilateral meshes on the boundary over the thickness of the specimen (Figure 32);
- tetrahedral elements (Figure 33).

The same results cannot be obtained for the second gradient model because with such low continuity shape functions the insertion of a second gradient energy cannot be detected and, hence, it plays no actual role in the results.

Figure 32 shows the hexahedral meshes and the resulting deformed shapes of the specimen. It is important to remark that in this set of meshes the directions of the yarns D_1 and D_2 , which are parallel to the edges of the specimen, coincide with the normals to the mesh interfaces. This property makes it possible to have a discontinuity on the derivatives in one of the fiber directions without losing the smoothness in the other direction. In other words, a wrinkle can form at the element interfaces for one set of fibers keeping the other set of fibers unaffected. This uncoupling can cause the formation of several wrinkles without interfering in other deformation mechanisms. This effect is strongly related to the positioning and number of interfaces between meshes, therefore it is not surprising that the result appears to be mesh-dependent. As a matter of fact, Figure 32 shows how the increase in mesh-density is connected to an increment in the number of wrinkles.

Changing the type of mesh to tetrahedral elements as shown in Figure 33, the improvement obtained in the stability is very clear. Despite the solution being once again mesh-dependent, the differences obtained in the output are much less significant compared to the hexahedral mesh. The explanation for this result is that, in this case, the normals to the interfaces between the meshes do not always coincide with the direction of the fibers making the appearance of a wrinkling phenomenon at the interfaces more difficult.

The conclusion on the results presented in this subsection is that a first gradient model with linear shape function may present unphysical wrinkling phenomena. It is still possible to obtain realistic results from such

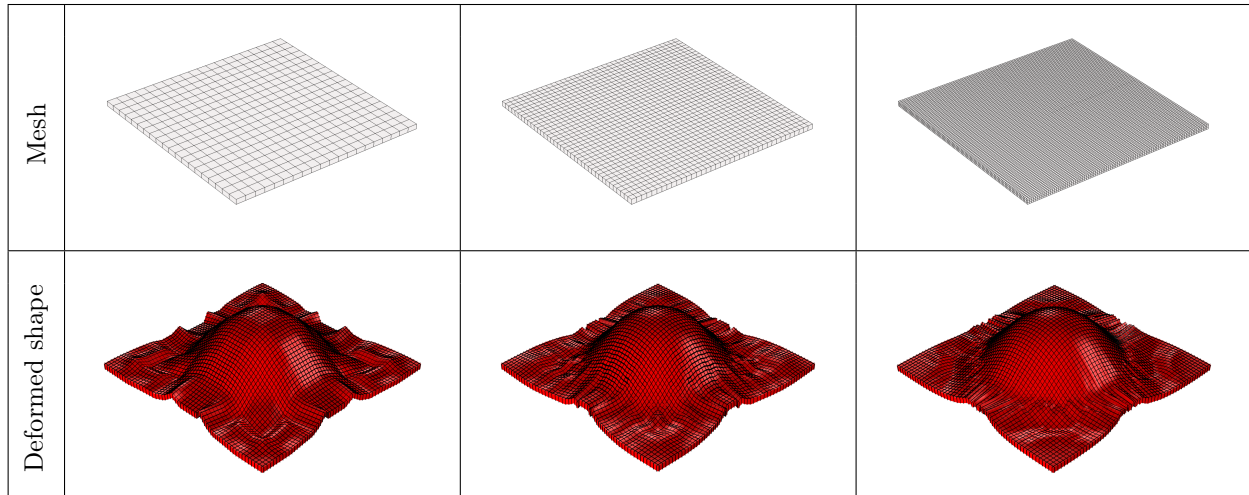


Figure 32: Solution of a first gradient model with linear shape functions and hexahedral meshes of different sizes.

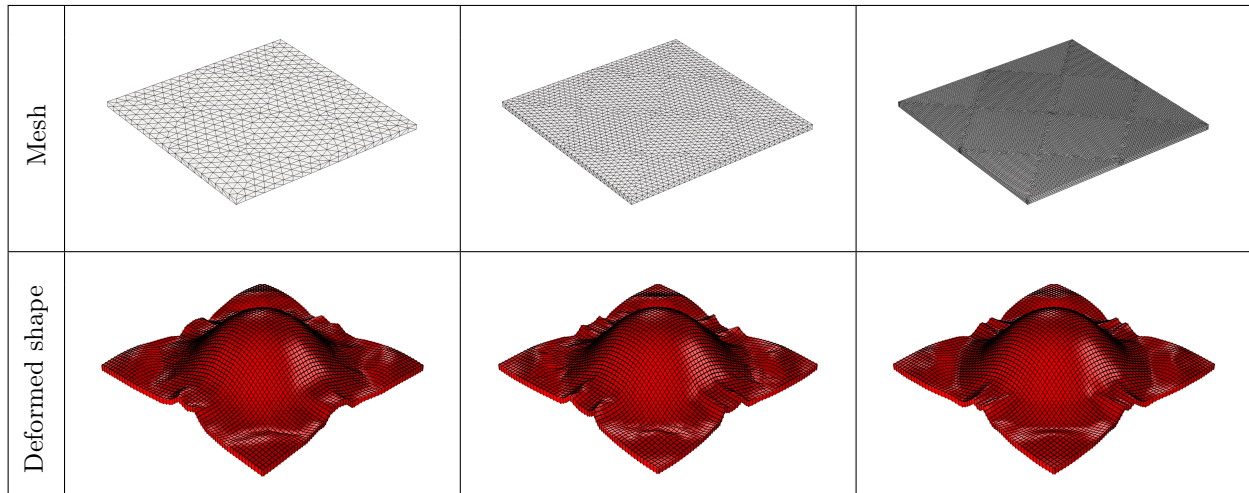


Figure 33: Solutions for a first gradient model with linear shape functions and tetrahedral elements of different sizes.

a model, but the dimension and the orientation of the elements should be carefully chosen to avoid unphysical wrinkling.

First and second gradient models with augmented continuity shape functions Here, a study of first and second gradient solutions obtained considering *augmented continuity shape functions* is presented in Figure 34. At first glance, it could seem that the mesh considered is poorer with respect to the previous case but, with the third degree polynomials used as shape functions, the number of nodes is comparable to the linear case.

We see that the first gradient solution still seems to depend on the size of the mesh. The wrinkles are not spikes corresponding to an interface between two mesh-elements, as they were in Figure 32, because the *augmented continuity shape functions* impose the smoothness of the strain during the deformation process.

Figure 34 explicitly shows that the stability of the model seems to increase by adding a second gradient energy. Indeed, the wrinkling phenomenon is controlled by the second gradient terms and the corresponding result appears to be mesh-independent even with a small constitutive parameter ($\alpha = 0.1 N$). The fact that second gradient terms stabilize the numerical onset of wrinkling, thus producing more realistic results, is not surprising. Indeed, the presence of an out-of-plane bending stiffness of the yarns (which is of course evident from a phenomenological point of view) makes the formation of wrinkles energetically expensive. On the

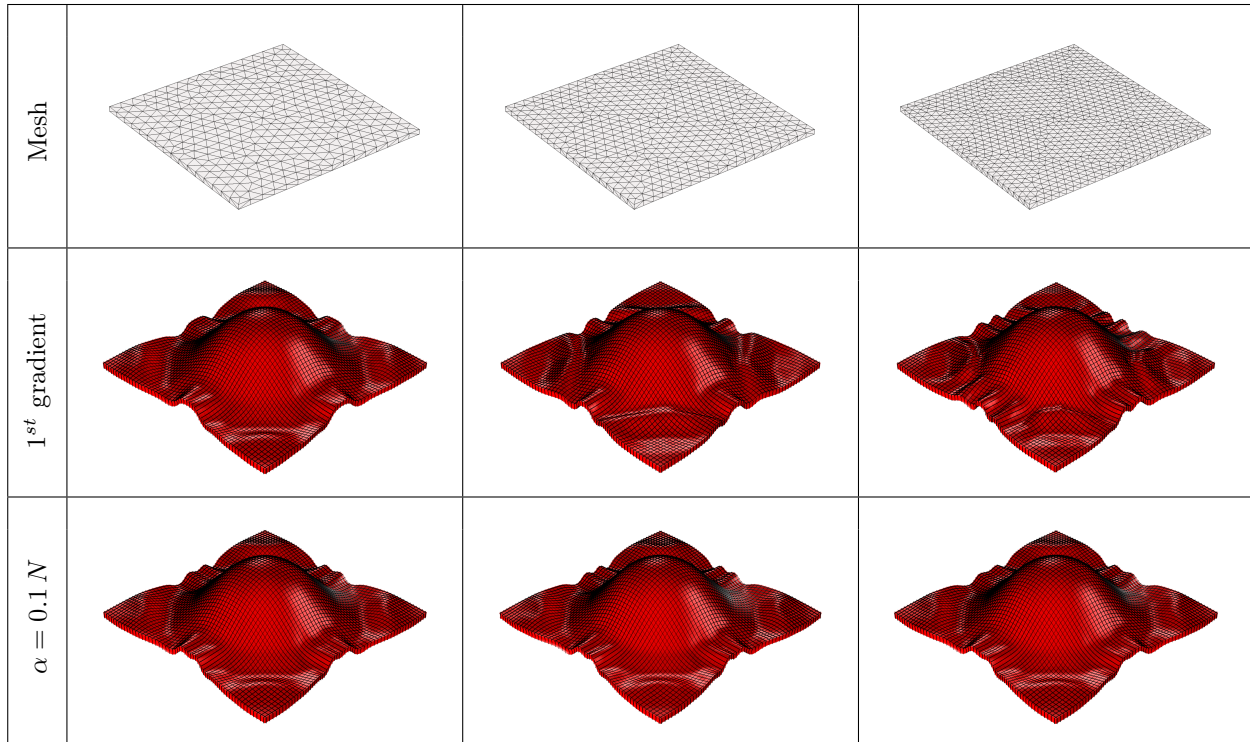


Figure 34: Mesh-dependency for the first and the second gradient model with augmented continuity shape functions.

other hand, since no energetic cost is associated to out-of-plane bending within first gradient theories, the onset of a myriad of wrinkles is allowed, even if this solution deviates from experimental evidence. If the value of α is increased, the results obtained with the different meshes considered are the same as in Figure II.11 and are, therefore, not included here.

The presented results are very promising, but it must be noted that the *augmented continuity shape functions* are just a workaround for the real problem which is that of implementing robust finite elements for the simulation of woven composite reinforcements in view of structure design. The continuity of the derivatives is weakly imposed and it is, therefore, not strictly granted. A study on the validity of a model implementing the *augmented continuity shape functions* should be made, even if the presented model seems to be reliable in the description of the analyzed phenomenon. Alternative methods to stabilize the solution can also be found in the literature [148] consisting in the insertion of small structural elements (such as beams) in the interior of the FE in the direction of the yarns, so indirectly accounting for the bending stiffness of the yarns.

Conclusion

The features of the woven fabrics are very peculiar and possess huge potentialities. Therefore, the engineering interest towards this kind of materials led to the conduction of various benchmark tests and to the definition of numerous models. However, there is still no commonly agreed upon approach to describe such materials during the forming. The opinion of the author is that a comprehensive model is not achievable without the insertion of higher order terms (or micromorphic terms) in the energy to describe the deformation energy of the microstructure. The classical models used for the woven composite preforming fail to describe a wealth of observed experimental evidences. In particular, the description of the wrinkling phenomenon is one of the weakest points of such models.

This thesis aims to support the validity of an enriched continuous model for the description of the behavior of woven materials. Therefore an orthotropic second gradient model for an unbalanced composite fabric was implemented and the onset of these particular phenomena was analyzed. The simple quadratic energy here used is not likely to be fit for the general description of their non-linear behavior but it does catch qualitatively all the peculiar phenomena observed during the experimental campaigns.

In this part, an enriched continuous model is introduced to reproduce the Bias Extension Test and the deep drawing for woven composite interlocks. We have shown that the model is able to account for the main microstructure related deformation mechanisms up to moderate strains, namely

- the angle variation between warp and weft yarns;
- the onset of boundary layers for the shear deformation;
- the curvature of the boundary;
- the different bending stiffness of the two families of yarns;
- the asymmetry in the case of the BET on unbalanced fabrics;
- the wrinkling during the deep drawing preforming;

The results obtained with the model are satisfactory up to moderate deformations so that it is conceivable to fit the proposed models on more extended experimental campaigns. This would allow for a more precise identification of the introduced constitutive parameters, above all for what concerns the different bending stiffnesses which are the main microstructural related characteristics of fibrous composite interlocks.

However, extra experimental campaigns are needed for a complete validation of the proposed enriched continuous model. More particularly, such more comprehensive campaigns would need the setting up of the following experiments:

- Bias Extension Test on a set of specimens with the same dimensions and characteristics. These tests would be needed to identify experimental errors that can be introduced during the experimental campaign and to precisely account for such variability in the performed study;
- realization of the Bias Extension Test and the deep drawing on specimens with various dimensions to unveil possible size effects which can occur in higher gradient or micromorphic materials;
- conception of independent tests (other than the Bias Extension Test and the deep drawing) which are suitably engineered to give rise to the same microscopic deformation modes (fibers' bending and slipping), but with different loading conditions. This test would allow the confirmation of the values of the parameters evaluated for the considered materials;

- realization of specific measurements which are devoted to measure local deformation mechanisms with due precision. Digital Image Correlation Techniques could represent a good choice to effectively proceed in this direction.

Notwithstanding the undiscussed interest of the aforementioned tests and their necessity for a complete validation of the presented model, they are not the primary objective of this work. The primary aim is to identify the main microstructure-related deformation modes in woven fabrics and to show, via a reasonable enriched continuous model, that they cannot be neglected. The phase of conception of such extra experimental campaigns for a precise identification of second-gradient parameters on a given class of fibrous woven materials is postponed.

Further studies should be also focused on the improvement of the proposed model to precisely describe non-linearities and irreversible phenomena such as friction, which can have a non-negligible role during the deformation of woven reinforcements. Moreover, the experimental campaigns should also determine which is the strain threshold until which the integrity of the material is preserved and a continuum model can be considered predictive. In fact, after a given macroscopic deformation, some yarns start to be pulled out from the specimen, so that further modeling efforts intrinsically lose their interest. The fundamental importance of the results shown in this part stands in the potential impact on the modeling of the forming processes in important engineering applications. It is very important to stress the potentialities of a simple enriched continuous model for the description of the apparently complex response of the woven fabrics and the hope of the author is that effort will be put into further studies on this subject.

Part III

The relaxed micromorphic model

Contents of Part III

Introduction	69
1 Energy formulation of the relaxed micromorphic model	71
1.1 Strain energy density	71
1.2 Kinetic energy density	74
1.3 The relaxed micromorphic stress and its possible symmetry	75
1.4 Dynamic equilibrium equations	76
2 Analysis of the material symmetry classes	78
2.1 The strain energy density in the Mandel-Voigt vector notation	78
2.2 Constitutive tensors for various anisotropy classes	80
3 The macroscopic limit of the relaxed model – macroscopic consistency conditions	84
3.1 Some considerations on the isotropic macroscopic consistency condition	84
3.2 The static macroscopic limit and the dynamic long wavelength limit	86
3.3 The general relaxed anisotropic case in the limit $L_c \rightarrow 0$	86
3.4 Particularization for specific anisotropy classes	88
3.4.1 The isotropic case	88
3.4.2 The cubic symmetry case	89
3.4.3 The orthotropic case	90
Conclusion	91

Introduction

In principle, the modeling framework for the micromorphic approach had been completed by Eringen, Mindlin, and Germain. Mindlin and Eringen also provided extensions of the micromorphic model to anisotropy, even if such anisotropic models are almost impossible to be applied to real cases, due to the impressive number of coefficients provided (498 coefficients in the general anisotropic case).

The existence and uniqueness questions for the linear micromorphic model have been completely settled both for the static and dynamic case, based on the assumption of *uniform positive definiteness* of the appearing constitutive elasticity tensors. However, the over-reliance on uniform positive definiteness, we believe, has blinded the eyes for the real possibilities inherent in the micromorphic model. These possibilities have been consistently overlooked until very recently, when, in a series of articles [80, 139, 140, 175, 176], the novel concept of *relaxed micromorphic continuum* has been introduced. This model provides a drastic reduction of the number of constitutive coefficients with respect to Mindlin-Eringen's one while remaining well-posed.

A fundamental contribution of the relaxed micromorphic model is given by the proof of well-posedness [176] also for the case where the strain energy density violates strict positive-definiteness¹. In other words, even if the relaxed micromorphic model can be apparently seen as a particular case of the Mindlin-Eringen model by suitably setting some constitutive parameters of their model to zero (see [140, p. 555]), such choice is not acceptable in the Mindlin-Eringen setting due to the loss of positive-definiteness of the energy. Nevertheless, it is exactly this feature which makes the relaxed micromorphic model unique for the description of a wealth of unorthodox material behaviors. The existence results proposed in [176], as well as the drastic reduction of the number of the introduced elastic coefficients, allowed us to open the way to the application of the relaxed micromorphic model to cases of real interest.

Indeed, the relaxed micromorphic model has already been a source of inspiration for researchers working on granular materials [158]. Moreover, the clear and transparent application of the relaxed micromorphic model in the isotropic case has recently been successfully achieved for the description of band-gap metamaterials (see [131, 132]). The isotropic relaxed micromorphic model has proven its ability to fit the dispersion curves of phononic crystals for large windows of frequencies and wavelengths, arriving down to wavelengths which are comparable to the size of the unit cell. The most interesting aspect of the description of such metamaterials via the relaxed micromorphic model is undoubtedly that of predicting their macroscopic dynamical response through the introduction of *few macroscopic elastic coefficients* which are *independent of the frequency*. This means that the coefficients of the relaxed micromorphic model can be seen as *true material parameters*, exactly as is the case for the Young modulus and the Poisson ratio when dealing with classical materials. Of course, in order to extend the range of applicability of the relaxed model to a wider class of actual metamaterials, the model must be generalized to the anisotropic setting. This generalization is one of the principal aims of the present part.

We restrict our attention to the linearized framework noting that the first existence result for the geometrically nonlinear static case has been obtained in [104], which includes a previous result for the nonlinear Cosserat model [168]. For more details about existence results for micromorphic models at finite deformations, we refer the reader to [118, 169, 172, 173]. Further existence results are supplied in [62, 63, 144, 145]. There are many applications treated within the nonlinear micromorphic framework, among which we limit ourselves to mention [83, 88, 96, 100, 103, 111, 121, 151, 201, 203, 204, 227, 228].

In this part, we want to present an approach to anisotropy for the relaxed micromorphic model. Our modeling perspective is to simplify as much as possible and indeed to reduce to an essential minimum

¹It has to be noted that the new approach is only formally included in the standard Mindlin-Eringen micromorphic model since we consistently give up uniform positive-definiteness in the elastic distortion e and the curvature tensor ∇P which are instead strictly requested in the standard model in order to have well-posedness. For example, controlling only the elastic strain $\varepsilon_e = \text{sym}(\nabla u - P)$ in the energy does not locally control the elastic distortion $e = \nabla u - P$ and working with $\text{Curl} P$ does not control the curvature ∇P .

the bewildering possibilities of the standard micromorphic model. Indeed, there is no point in exclaiming happily that the standard micromorphic model has more than 1000 constitutive coefficients which need to be determined. The true aim of modeling should consist of the opposite: to discard all unclear complications without compromising the essence of the model. We believe that the relaxed micromorphic model is just going in this direction, thereby opening the way for clear-cut experimental campaigns to determine the remaining fewer extra parameters.

The plan of this part is as follows:

- In chapter III.1, we first recall our new relaxed model showing that it supports a clear group-invariant framework, opening the way to speak about anisotropy classes. This hinges mainly on transformation properties of the dislocation density tensor $\alpha = -\text{Curl} P$. The general anisotropic setting for the kinetic energy to be used in the relaxed micromorphic model is provided. This step is strongly complementary to the constitutive choice for the static case featured in equation (III.1). Indeed, if some deformation mechanisms are introduced in the definition of the strain energy densities, analogous inertiae must be introduced in the kinetic energy to have a well-posed problem in the dynamical case. This step is essential to securely proceed towards controllable applications on actual metamaterials subjected to dynamical loading. Afterwards, a further reduction of coefficients is proposed for those cases in which one wants to feature a symmetric stress. The dynamic problem is set and the resulting equations of motion and boundary conditions are derived.
- In chapter III.2, we study the format of possible anisotropic constitutive tensors, including the local rotational coupling term acting on skew $(\nabla u - P)$ and the curvature term acting on $\text{Curl} P$. This is done using classical Voigt-notation in order to facilitate future applications.
- In chapter III.3, we consider the long-wavelength limit (characteristic length $L_c \rightarrow 0$) which must coincide with a linear elastic model that has lost any characteristic length (improperly called internal variable model). From this hypothesis, we are able to relate coefficients of the micromorphic scale to the macroscopic ones. The result is a convincing homogenization formula for all considered anisotropy classes.

CHAPTER III.1

Energy formulation of the relaxed micromorphic model

1.1 Strain energy density

The novel relaxed micromorphic model endows Mindlin-Eringen's representation with more geometric structure. Unlike Mindlin-Eringen's model, the relaxed model mainly works with *symmetric elastic (relative) strains* $\varepsilon_e := \text{sym}(\nabla u - P)$, so that standard 4th order symmetric elasticity tensors can be used in order to define elastic stresses. Moreover, regarding the curvature, the relaxed model considers the *second order dislocation-density tensor* $\alpha = -\text{Curl } P$ instead of the third order curvature tensor ∇P with the effect (among others) that the description of the anisotropy of curvature only needs 4th order tensors, instead of 6th order ones. Since Mindlin-Eringen's cross coupling $\overline{\mathbb{E}}_{\text{cross}}$ (see equation (I.2)) is difficult to interpret, it is discarded right-away. Nevertheless, the structure of the model continues to be very rich. We write:

$$\begin{aligned}
 W = & \underbrace{\frac{1}{2} \langle \mathbb{C}_e \text{sym}(\nabla u - P), \text{sym}(\nabla u - P) \rangle_{\mathbb{R}^{3 \times 3}}}_{\text{anisotropic elastic - energy}} + \underbrace{\frac{1}{2} \langle \mathbb{C}_m \text{sym } P, \text{sym } P \rangle_{\mathbb{R}^{3 \times 3}}}_{\text{micro - self - energy}} \\
 & + \underbrace{\frac{1}{2} \langle \mathbb{C}_c \text{skew}(\nabla u - P), \text{skew}(\nabla u - P) \rangle_{\mathbb{R}^{3 \times 3}}}_{\text{local anisotropic rotational elastic coupling}} + \underbrace{\frac{\mu L_c^2}{2} \langle \overline{\mathbb{L}} \text{Curl } P, \text{Curl } P \rangle_{\mathbb{R}^{3 \times 3}}}_{\text{curvature}}.
 \end{aligned} \tag{III.1}$$

Here $\mathbb{C}_e, \mathbb{C}_m : \text{Sym}(3) \rightarrow \text{Sym}(3)$ are both classical 4th order elasticity tensors *acting on symmetric second order tensors* only: \mathbb{C}_e acts on the *symmetric elastic strain* $\varepsilon_e := \text{sym}(\nabla u - P)$ and \mathbb{C}_m acts on the *symmetric micro-strain* $\text{sym } P$ and both map to symmetric tensors. The tensor $\mathbb{C}_c : \mathfrak{so}(3) \rightarrow \mathfrak{so}(3)$ is a 4th order tensor that acts only on skew-symmetric matrices and yields only skew-symmetric tensors and $\overline{\mathbb{L}} : \mathbb{R}^{3 \times 3} \rightarrow \mathbb{R}^{3 \times 3}$ is a dimensionless 4th order tensor with at most 45 constants acting on the second order tensor $\alpha := -\text{Curl } P$, that it is usually called the *dislocation density tensor*.¹ Counting coefficients we now have 21+21+6+45=93, instead of Mindlin-Eringen's 498 coefficients. The main advantage at this stage is that our \mathbb{C}_e , unlike $\overline{\mathbb{C}}_e$, possesses all the symmetries that are peculiar of the classical elasticity tensors acting on $\text{sym } \nabla u$.

Let us remark here that the relaxed micromorphic curvature expression can also be written as:

$$\text{Curl } P = -\text{Curl}(\nabla u - P), \tag{III.2}$$

because $\text{Curl } P$ is invariant under $P \rightarrow P + \nabla \vartheta$, see [175]. We need to highlight also the fact that $\text{Curl } P$ is not just an arbitrary combination of first derivatives of P (and as such included in the standard Mindlin-Eringen most general anisotropic micromorphic format), but that the formulation in $\text{Curl } P$ supports a completely invariant setting, as seen in [161, 170]. Since $\text{Curl } P$ is a second order tensor, it allows us to discard the 6th order tensors of classical Mindlin-Eringen micromorphic elasticity and to work instead with 4th order tensors whose anisotropy classification is much easier and well-known [33], see chapter III.2.

The large number of isotropic constants in the standard Mindlin-Eringen model has always been of concern. Previous attempts to endow the Mindlin-Eringen model with more structure include Koh's [112, 190] so-called micro-isotropy postulate which requires, among other things, that $\text{sym } \tilde{\sigma}$ is an isotropic function of $\text{sym } \nabla u$ only. This reduces the number of isotropic coefficient also to 5 (similarly to our relaxed model) but the fact of connecting $\text{sym } \tilde{\sigma}$ to $\text{sym } \nabla u$ only cannot be considered a well-grounded hypothesis.

¹The dislocation tensor is defined as $\alpha_{ij} = -(\text{Curl } P)_{ij} = -P_{ih,k} \epsilon_{jhk}$, where ϵ is the Levi-Civita tensor.

Reduction for a centro-symmetric case In the same spirit as done with the local energy terms, a possible simplification of the curvature expression is given by:

$$\langle \bar{\mathbb{L}} \text{Curl } P, \text{Curl } P \rangle_{\mathbb{R}^{3 \times 3}} = \langle \mathbb{L}_e \text{sym Curl } P, \text{sym Curl } P \rangle_{\mathbb{R}^{3 \times 3}} + \langle \mathbb{L}_c \text{skew Curl } P, \text{skew Curl } P \rangle_{\mathbb{R}^{3 \times 3}}. \quad (\text{III.3})$$

Here, $\mathbb{L}_e : \text{Sym}(3) \rightarrow \text{Sym}(3)$ is a classical, positive definite elasticity tensor with at most 21 independent (non-dimensional) coefficients and $\mathbb{L}_c : \mathfrak{so}(3) \rightarrow \mathfrak{so}(3)$ is a positive definite tensor with at most 6 independent (non-dimensional) coefficients.

Therefore, we propose the following representation of the energy for the relaxed anisotropic centro-symmetric model, which has maximally $21+21+6+21+6=75$ independent coefficients:

$$\begin{aligned} W = & \underbrace{\frac{1}{2} \langle \mathbb{C}_e \text{sym}(\nabla u - P), \text{sym}(\nabla u - P) \rangle_{\mathbb{R}^{3 \times 3}}}_{\text{anisotropic elastic - energy}} + \underbrace{\frac{1}{2} \langle \mathbb{C}_m \text{sym } P, \text{sym } P \rangle_{\mathbb{R}^{3 \times 3}}}_{\text{micro - self - energy}} \quad (\text{III.4}) \\ & + \underbrace{\frac{1}{2} \langle \mathbb{C}_c \text{skew}(\nabla u - P), \text{skew}(\nabla u - P) \rangle_{\mathbb{R}^{3 \times 3}}}_{\text{local anisotropic rotational elastic coupling}} \\ & + \underbrace{\frac{\mu L_c^2}{2} [\langle \mathbb{L}_e \text{sym Curl } P, \text{sym Curl } P \rangle_{\mathbb{R}^{3 \times 3}} + \langle \mathbb{L}_c \text{skew Curl } P, \text{skew Curl } P \rangle_{\mathbb{R}^{3 \times 3}}]}_{\text{curvature}}. \end{aligned}$$

This constitutive expression of the strain energy density for the relaxed micromorphic model is the most general one that can be provided in the anisotropic and centrosymmetric framework and it already it provides a drastic reduction of the constitutive coefficients with respect to the standard Mindlin-Eringen model (75 coefficients against the 498 of Mindlin-Eringen). In a first instance and with a look towards immediate applications, we can consider non-local effects to be isotropic, so that the curvature coefficients reduce from $21+6=27$, to at most 2. We end up with a fully anisotropic model which features at most 51 parameters for describing:

- the full anisotropy at the microstructural level.
- the full anisotropy at the macroscopic level.
- non-localities through the introduction of suitable characteristic lengths.

Of course, considering metamaterials with particular symmetries, this number of parameters can be further reduced.

Definite positiveness of the strain energy density It must also be observed that the relaxed micromorphic model can be used with \mathbb{C}_c positive semi-definite or indeed zero (in the isotropic case $\mu_c = 0$), while we always assume that the constitutive tensors \mathbb{C}_e , \mathbb{C}_m (and later \mathbb{C}_M) are strictly positive definite tensors. Furthermore, we assume the curvature constitutive tensor $\bar{\mathbb{L}}$ is positive definite (or the tensors \mathbb{L}_e and \mathbb{L}_c), and the length scale L_c and the constitutive parameter μ are positive. Assuming that \mathbb{C}_e , \mathbb{C}_m and $\bar{\mathbb{L}}$ are positive definite tensors means that:

$$\begin{aligned} \exists c_e^+ > 0 : \forall S \in \text{Sym}(3) : & \quad \langle \mathbb{C}_e S, S \rangle_{\mathbb{R}^{3 \times 3}} \geq c_e^+ \|S\|_{\mathbb{R}^{3 \times 3}}^2, \quad (\text{III.5}) \\ \exists c_m^+ > 0 : \forall S \in \text{Sym}(3) : & \quad \langle \mathbb{C}_m S, S \rangle_{\mathbb{R}^{3 \times 3}} \geq c_m^+ \|S\|_{\mathbb{R}^{3 \times 3}}^2, \\ \exists c_l^+ > 0 : \forall X \in \mathbb{R}^{3 \times 3} : & \quad \langle \bar{\mathbb{L}} X, X \rangle_{\mathbb{R}^{3 \times 3}} \geq c_l^+ \|X\|_{\mathbb{R}^{3 \times 3}}^2. \end{aligned}$$

In sharp contrast to the standard Mindlin-Eringen format, we assume for the rotational coupling tensor \mathbb{C}_c only positive semi-definiteness, i.e:

$$\forall \bar{A} \in \mathfrak{so}(3) : \quad \langle \mathbb{C}_c \bar{A}, \bar{A} \rangle_{\mathbb{R}^{3 \times 3}} \geq 0. \quad (\text{III.6})$$

As already noted, this allows the rotational coupling tensor \mathbb{C}_c to vanish, in which case the relaxed micromorphic model is *non-redundant* [201].

The reader might ask himself: how is it possible that the rotational coupling tensor \mathbb{C}_c can be absent but the resulting model is still well-posed? This is possible because in that case, the skew-symmetric part of P is not controlled locally but as a result of the boundary value problem and boundary conditions. In this sense, allowing for $\mathbb{C}_c \equiv 0$ is one of the decisive new possibilities offered by the relaxed micromorphic model.

However, in [140] it has been shown that in the isotropic case ($\mathbb{C}_c = \mu_c \mathbf{1}$) the presence of \mathbb{C}_c allows to control the onset of band-gaps. In subsection III.2.2 we discuss the possible forms that \mathbb{C}_c may have for certain given anisotropy classes.

The case of isotropy The fully isotropic case requires to determine ($\mathbb{C}_e \sim 2, \mathbb{C}_m \sim 2, \mathbb{C}_c \sim 1, \mathbb{L}_e \sim 2, \mathbb{L}_c \sim 1$) altogether 8 constitutive coefficients of which the rotational coupling coefficient μ_c can be set to zero to enforce *symmetric* elastic stresses $\tilde{\sigma}$. As seen before, Eringen's formulation has 18 coefficients and Koh's [112] micro-isotropic model still has 10.² This simplified framework, which allows to describe the full micro-macro anisotropy and the presence of non-localities via the introduction of "only" 51 parameters, is of fundamental importance to proceed towards an enlightened characterization of the actual metamaterial.

In general, if we consider an isotropic curvature term, we obtain the following representation:

$$\frac{\mu L_c^2}{2} \langle \bar{\mathbb{L}}_{\text{iso}} \text{Curl } P, \text{Curl } P \rangle_{\mathbb{R}^{3 \times 3}} = \frac{\mu L_c^2}{2} \left(\alpha_1 \|\text{dev sym Curl } P\|^2 + \alpha_2 \|\text{skew Curl } P\|^2 + \frac{\alpha_3}{3} [\text{tr}(\text{Curl } P)]^2 \right), \quad (\text{III.7})$$

with scalar weighting parameters $\alpha_1, \alpha_2, \alpha_3 \geq 0$. Since the curvature energy does not usually play a major role, we mostly just use $\|\text{Curl } P\|^2$, corresponding to $\alpha_1, \alpha_2, \alpha_3 = 1$.

If we consider the isotropic case and the simplest curvature form, we can reduce the relaxed representation to (see [131, 138–140, 176, 179]):

$$\begin{aligned} W = & \underbrace{\mu_e \|\text{sym}(\nabla u - P)\|^2 + \frac{\lambda_e}{2} \text{tr}(\text{sym}(\nabla u - P))^2}_{\text{isotropic elastic - energy}} + \underbrace{\mu_m \|\text{sym } P\|^2 + \frac{\lambda_m}{2} (\text{tr}(\text{sym } P))^2}_{\text{micro - self - energy}} \\ & + \underbrace{\mu_c \|\text{skew}(\nabla u - P)\|^2}_{\text{invariant local isotropic rotational elastic coupling}} + \underbrace{\frac{\mu L_c^2}{2} \|\text{Curl } P\|^2}_{\text{isotropic curvature}}. \end{aligned} \quad (\text{III.8})$$

In the case of isotropy, strict positive definiteness of the potential energy reduces to the following simple relations for the introduced parameters [176]:

$$\mu_e > 0, \quad 2\mu_e + 3\lambda_e > 0, \quad \mu_m > 0, \quad 2\mu_m + 3\lambda_m > 0, \quad \mu_c \geq 0, \quad L_c > 0. \quad (\text{III.9})$$

For very large sample sizes, a scaling argument easily shows that the relative characteristic length scale L_c of the micromorphic model must vanish.

For future use we define the elastic bulk modulus κ_e and the microscopic bulk modulus κ_m , respectively:

$$\kappa_e = \frac{2\mu_e + 3\lambda_e}{3}, \quad \kappa_m = \frac{2\mu_m + 3\lambda_m}{3}. \quad (\text{III.10})$$

In terms of these moduli, strict positive-definiteness of the energy is equivalent to:

$$\mu_e > 0, \quad \kappa_e > 0, \quad \mu_m > 0, \quad \kappa_m > 0, \quad \mu_c \geq 0, \quad L_c > 0. \quad (\text{III.11})$$

Linear elasticity as upper energetic limit The relaxed micromorphic model admits linear elasticity as an upper energetic limit for any characteristic length scale $L_c > 0$. This can be seen by noticing that an admissible field for the micro-distortion P is always $P = \nabla u$. Thus, we see that the relaxed model is always energetically *weaker than a linear elastic comparison material* with elastic stiffness \mathbb{C}_m , for any given stiffness \mathbb{C}_e . This, again, is in contrast to the standard Mindlin-Eringen format which will, in general,

²Note that establishing positive-definiteness of the energy is now an easy matter as compared to [212]: we only need to require positive definiteness of the occurring standard 4th order tensors $\mathbb{C}_e, \mathbb{C}_m, \mathbb{C}_c, \mathbb{L}_e, \mathbb{L}_c$.

generate arbitrary stiffer response as $L_c \rightarrow \infty$ and $C_e \rightarrow \infty$ simultaneously. This can be proven via a standard minimization argument:³

$$\begin{aligned} \min_{(u, P)} \left\{ \int_{\Omega} \frac{1}{2} \langle C_e \operatorname{sym}(\nabla u - P), \operatorname{sym}(\nabla u - P) \rangle_{\mathbb{R}^{3 \times 3}} + \frac{1}{2} \langle C_m \operatorname{sym} P, \operatorname{sym} P \rangle_{\mathbb{R}^{3 \times 3}} \right. \\ \left. + \frac{1}{2} \langle C_c \operatorname{skew}(\nabla u - P), \operatorname{skew}(\nabla u - P) \rangle_{\mathbb{R}^{3 \times 3}} + \frac{\mu L_c^2}{2} \langle \bar{\mathbb{L}}_{\text{aniso}} \operatorname{Curl} P, \operatorname{Curl} P \rangle_{\mathbb{R}^{3 \times 3}} dx \right\} \\ \leq \int_{\Omega} \frac{1}{2} \langle C_m \operatorname{sym} \nabla u, \operatorname{sym} \nabla u \rangle_{\mathbb{R}^{3 \times 3}} dx. \end{aligned} \quad (\text{III.12})$$

1.2 Kinetic energy density

The dynamical formulation of the proposed relaxed micromorphic model is obtained in the following way. We define a joint Hamiltonian and obtain the equations from the postulate of stationary action. In order to generalize the kinetic energy density to the anisotropic micromorphic framework, we need to introduce a micro-inertia density contribution of the type:

$$J = \underbrace{\frac{1}{2} \rho \|u_{,t}\|^2}_{\text{Cauchy inertia}} + \underbrace{\frac{1}{2} \langle \bar{\mathbb{J}}_m P_{,t}, P_{,t} \rangle}_{\text{free micro-inertia}} + \underbrace{\frac{1}{2} \langle \bar{\mathbb{J}}_g \nabla u_{,t}, \nabla u_{,t} \rangle}_{\text{gradient micro-inertia}}, \quad (\text{III.13})$$

Here $\bar{\mathbb{J}}_m : \mathbb{R}^{3 \times 3} \rightarrow \mathbb{R}^{3 \times 3}$ is the 4th order free micro-inertia density tensor and $\bar{\mathbb{J}}_g : \mathbb{R}^{3 \times 3} \rightarrow \mathbb{R}^{3 \times 3}$ is the 4th order gradient micro-inertia density tensor with, in general, 45 independent coefficients each. Eringen has added a conservation law for the free micro-inertia density tensor $\bar{\mathbb{J}}_m$, but in this work we assume constant micro-inertia density tensors $\bar{\mathbb{J}}_m$ and $\bar{\mathbb{J}}_g$ as well as a constant mass density $\rho > 0$ ($[\rho] = \text{kg}/\text{m}^3$). If the first two terms appearing in Eq. (III.13) can be directly related to those introduced by Mindlin [156], the terms of gradient micro-inertia are currently used only when dealing with second gradient continua [16, 126], but usually not when considering micromorphic models. Indeed, Mindlin [156] recognized inertia terms which are similar to our gradient micro-inertia terms when considering the particular case of the long-wavelength limit of his micromorphic model. The expression (III.13) of the energy that we propose here is more general (i.e. not restricted to large wavelengths) and indeed the gradient micro-inertia will show its higher effect for relatively small wavelengths (high wavenumbers). Nevertheless, basing ourselves on our first comparisons with experimental results [131, 132], we are persuaded that gradient micro-inertia is essential also when considering enriched models of the micromorphic type if the ultimate goal is that of describing the behavior of actual physical systems.

Considering dimensional consistency, we can always write the micro-inertia density tensor $\bar{\mathbb{J}}$ as:

$$\bar{\mathbb{J}}_m = \rho \hat{L}_c^2 \bar{\mathbb{J}}_{m0}, \quad \bar{\mathbb{J}}_g = \rho \hat{L}_c^2 \bar{\mathbb{J}}_{g0}, \quad (\text{III.14})$$

where $\bar{\mathbb{J}}_{m0}, \bar{\mathbb{J}}_{g0} : \mathbb{R}^{3 \times 3} \rightarrow \mathbb{R}^{3 \times 3}$ are dimensionless. Here, $\hat{L}_c \geq 0$ is another characteristic length $[\hat{L}_c] = m$. We also propose a split of the micro-inertia densities, similar to that adopted for the other elastic tensors like:

$$\begin{aligned} \frac{1}{2} \langle \bar{\mathbb{J}}_m P_{,t}, P_{,t} \rangle &= \frac{1}{2} \langle \mathbb{J}_m \operatorname{sym} P_{,t}, \operatorname{sym} P_{,t} \rangle + \frac{1}{2} \langle \mathbb{J}_c \operatorname{skew} P_{,t}, \operatorname{skew} P_{,t} \rangle, \\ \frac{1}{2} \langle \bar{\mathbb{J}}_g \nabla u_{,t}, \nabla u_{,t} \rangle &= \frac{1}{2} \langle \mathbb{J}_g \operatorname{sym} \nabla u_{,t}, \operatorname{sym} \nabla u_{,t} \rangle + \frac{1}{2} \langle \mathbb{J}_d \operatorname{skew} \nabla u_{,t}, \operatorname{skew} \nabla u_{,t} \rangle. \end{aligned} \quad (\text{III.15})$$

Here, $\mathbb{J}_m, \mathbb{J}_g : \operatorname{Sym}(3) \rightarrow \operatorname{Sym}(3)$ map symmetric tensors into symmetric tensors while $\mathbb{J}_c, \mathbb{J}_d : \mathfrak{so}(3) \rightarrow \mathfrak{so}(3)$ map skew-symmetric tensors to skew-symmetric tensors. We assume then that both $\mathbb{J}_m, \mathbb{J}_g, \mathbb{J}_c$ and \mathbb{J}_d are positive definite.

³The strict equality in (III.12) is trivial considering that replacing $P = \nabla u$ on the left hand side and recalling that $\operatorname{Curl} \nabla \vartheta = 0$. On the other hand, the inequality can be justified by thinking that a solution (u^*, P^*) of the relaxed micromorphic problem is a minimizer, in the sense that $W(u^*, P^*) \leq W(u, P)$ for any admissible field (u, P) . Hence, taking a generic field $P = \nabla u$ (which is of course admissible) justifies equation (III.12).

In the isotropic case, the micro-inertia density tensor $\bar{\mathbb{J}}_{m0}, \bar{\mathbb{J}}_{g0}$ can be represented by six micro-inertia parameters $\eta_1, \eta_2, \eta_3, \bar{\eta}_1, \bar{\eta}_2, \bar{\eta}_3 \geq 0$ such that:

$$J = \frac{1}{2}\rho \|u_{,t}\|^2 + \frac{1}{2}\eta_1 \|\operatorname{dev} \operatorname{sym} P_{,t}\|^2 + \frac{1}{2}\eta_2 \|\operatorname{skew} P_{,t}\|^2 + \frac{1}{6}\eta_3 (\operatorname{tr} P_{,t})^2 + \frac{1}{2}\bar{\eta}_1 \|\operatorname{dev} \operatorname{sym} \nabla u_{,t}\|^2 + \frac{1}{2}\bar{\eta}_2 \|\operatorname{skew} \nabla u_{,t}\|^2 + \frac{1}{6}\bar{\eta}_3 \operatorname{tr} (\nabla u_{,t})^2. \quad (\text{III.16})$$

Definite positiveness of the kinetic energy As for the kinetic energy, we assume that the mean mass density ρ is positive and $\bar{\mathbb{J}}_m$ and $\bar{\mathbb{J}}_g$ are positive definite, i.e.:

$$\begin{aligned} \exists c_1^+ > 0 : \forall X \in: \mathbb{R}^{3 \times 3} : \quad & \langle \bar{\mathbb{J}}_m X, X \rangle_{\mathbb{R}^{3 \times 3}} \geq c_1^+ \|X\|_{\mathbb{R}^{3 \times 3}}^2, \\ \exists c_2^+ > 0 : \forall X \in: \mathbb{R}^{3 \times 3} : \quad & \langle \bar{\mathbb{J}}_g X, X \rangle_{\mathbb{R}^{3 \times 3}} \geq c_2^+ \|X\|_{\mathbb{R}^{3 \times 3}}^2. \end{aligned} \quad (\text{III.17})$$

In the isotropic case, positive-definiteness is equivalent to having the mean mass density and the six micro-inertia parameters positive, i.e.:

$$\rho > 0, \quad \eta_1 > 0, \quad \eta_2 > 0, \quad \eta_3 > 0, \quad \bar{\eta}_1 > 0, \quad \bar{\eta}_2 > 0, \quad \bar{\eta}_3 > 0. \quad (\text{III.18})$$

1.3 The relaxed micromorphic stress and its possible symmetry

Considering the energy in equation (III.1), the resulting elastic stress is:

$$\tilde{\sigma}(\nabla u, P) = \mathbb{C}_e \operatorname{sym}(\nabla u - P) + \mathbb{C}_c \operatorname{skew}(\nabla u - P), \quad (\text{III.19})$$

which is solely related to elastic distortions $e = \nabla u - P$. One of the main results of the present part is to provide a simple but effective homogenization formula which relates the elastic tensors \mathbb{C}_e and \mathbb{C}_m to the macroscopic elastic properties of the considered medium that will be encoded in the effective elastic tensor \mathbb{C}_M .

In this subsection, we recall some arguments which allow the possibility of featuring a symmetric stress tensor for the relaxed micromorphic model by setting the 6 components of the tensor \mathbb{C}_c to be vanishing. Considering the scalar product $\langle X, Y \rangle = \operatorname{tr}(X \cdot Y^T)$, we start by noticing that, given the definition of the fourth order tensors \mathbb{C}_e and \mathbb{C}_c , they respect a generalized version of the *orthogonal decomposition* of second order tensors ($X = \operatorname{sym}X \oplus \operatorname{skew}X$), in the sense that:

$$\begin{aligned} \operatorname{sym}[\mathbb{C}_e \operatorname{sym}X + \mathbb{C}_c \operatorname{skew}X] &= \mathbb{C}_e \operatorname{sym}X, \\ \operatorname{skew}[\mathbb{C}_e \operatorname{sym}X + \mathbb{C}_c \operatorname{skew}X] &= \mathbb{C}_c \operatorname{skew}X. \end{aligned} \quad (\text{III.20})$$

We recall that the elastic stress of the relaxed micromorphic model is:

$$\tilde{\sigma}(\nabla u, P) = \mathbb{C}_e \operatorname{sym}(\nabla u - P) + \mathbb{C}_c \operatorname{skew}(\nabla u - P), \quad (\text{III.21})$$

so that skew-symmetry of the elastic stress $\tilde{\sigma}$ is entirely controlled by the rotational coupling tensor \mathbb{C}_c since, relying on formulas (III.20), we have

$$\operatorname{skew} \tilde{\sigma} = \operatorname{skew}[\mathbb{C}_e \operatorname{sym}(\nabla u - P) + \mathbb{C}_c \operatorname{skew}(\nabla u - P)] = \mathbb{C}_c \operatorname{skew}(\nabla u - P). \quad (\text{III.22})$$

For a positive definite coupling tensor \mathbb{C}_c , we note that skew-symmetric stresses $\operatorname{skew} \tilde{\sigma} \neq 0$ occur if and only if $\operatorname{skew}(\nabla u - P) \neq 0$.

If $\mathbb{C}_c \equiv 0$, the elastic Cauchy stress $\tilde{\sigma}$ satisfies *Boltzmann's axiom of symmetry of force stresses*. In addition, for $\mathbb{C}_c \equiv 0$, the *elastic distortion* $e = \nabla u - P$ can be non-symmetric, while the elastic stress $\tilde{\sigma}$ remains symmetric.⁴

In [201] the authors have introduced the original and important notion of *non-redundant strain measures* in the micromorphic continuum. As it turns out, the relaxed micromorphic model with zero rotational coupling tensor $\mathbb{C}_c \equiv 0$ is a *non-redundant micromorphic formulation*. Conversely, the standard Mindlin-Eringen model remains *redundant*, as does the linear Cosserat model.

With Boltzmann's axiom, which is in sharp contrast to standard micromorphic models, the model would feature symmetric force-stress tensors. Such an assumption has been made, for example, by Teisseyre [222,223] in his model for the description of seismic wave propagation phenomena (for the use of micromorphic models for earthquake modeling see also the discussion in [164]).

1.4 Dynamic equilibrium equations

Considering the anisotropic strain energy (III.1) and the anisotropic kinetic energy (III.13), the dynamical equilibrium equations for the relaxed micromorphic model take the compact format:

$$\rho u_{,tt} - \rho \widehat{L}_c^2 \text{Div} [\mathbb{J}_{g0} \nabla u_{,tt}] = \text{Div} [\tilde{\sigma}], \quad \rho \widehat{L}_c^2 \mathbb{J}_{m0} P_{,tt} = \tilde{\sigma} - s - \text{Curl } m, \quad (\text{III.23})$$

with the associated natural and kinematical boundary conditions:

$$\begin{aligned} t := (\tilde{\sigma} + \mathcal{I}) \cdot n = t^{\text{ext}} & \quad \text{or} & \quad u = u_0, & \quad \forall x \in \partial\Omega, \\ \tau \cdot \nu_i := -m \cdot \epsilon \cdot n = \tau^{\text{ext}} & \quad \text{or} & \quad P \cdot \nu_i = p_i, & \quad i = 2, 3, \quad \forall x \in \partial\Omega, \end{aligned} \quad (\text{III.24})$$

where ϵ is the Levi-Civita third order tensor, n is the normal to the boundary, ν_1 and ν_2 are 2 orthogonal vectors tangent to the boundary, $u_0, p_2, p_3, t^{\text{ext}}, \tau^{\text{ext}}$ are assigned quantities and we have defined:

$$\begin{aligned} \tilde{\sigma} &= \mathbb{C}_e \text{sym} (\nabla u - P) + \mathbb{C}_c \text{skew} (\nabla u - P), & s &= \mathbb{C}_m \text{sym } P, \\ \mathcal{I} &= \rho \widehat{L}_c^2 \mathbb{J}_{g0} \nabla u_{,tt}, & m &= \mu L_c^2 \overline{\mathbb{L}}_{\text{aniso}} \text{Curl } P. \end{aligned} \quad (\text{III.25})$$

Hence, the dynamical equilibrium equations for the isotropic relaxed micromorphic model, obtained considering the isotropic strain energy (III.4) and the isotropic kinetic energy (III.16), take the form:

$$\rho u_{,tt} - \text{Div}[\mathcal{I}] = \text{Div}[\tilde{\sigma}], \quad \tilde{\mathcal{I}} = \tilde{\sigma} - s - \text{Curl } m, \quad \forall x \in \Omega, \quad (\text{III.26})$$

where

$$\begin{aligned} \mathcal{I} &= \bar{\eta}_1 \text{dev sym } \nabla u_{,tt} + \bar{\eta}_2 \text{skew } \nabla u_{,tt} + \frac{\bar{\eta}_3}{3} \text{tr} (\nabla u_{,tt}), \\ \tilde{\mathcal{I}} &= \eta_1 \text{dev sym } P_{,tt} + \eta_2 \text{skew } P_{,tt} + \frac{\eta_3}{3} \text{tr} (P_{,tt}), \\ \tilde{\sigma} &= 2\mu_e \text{sym} (\nabla u - P) + \lambda_e \text{tr} (\nabla u - P) \mathbb{1} + 2\mu_c \text{skew} (\nabla u - P), \\ s &= 2\mu_m \text{sym } P + \lambda_m \text{tr} (P) \mathbb{1}, \\ m &= \mu L_c^2 \text{Curl } P. \end{aligned} \quad (\text{III.27})$$

Of course, the associated natural and kinematical boundary conditions are also modified considering the new definition of the parameters.

⁴Using $\mathbb{C}_c = 0$ is similar to the Reuss-bound approach in homogenization theory (stress fields are taken constant but fluctuations in strain are allowed). Here, analogously, we would assume symmetric stresses $\tilde{\sigma}$ but non-symmetric distortion-fluctuations in $e = \nabla u - P$. Voigt (see [230, p.596]) already discussed non-symmetric states of distortion. However, we can supply some further support for using $\mathbb{C}_c \equiv 0$. Indeed as Kröner notes [114], “asymmetric stress tensors only come under consideration when a distribution of rotational moments acts upon the body externally, which is excluded here. The question of whether the (...) rotations produces stresses can also be answered. We must first exclude asymmetric stress tensors, since they contradict the laws of equilibrium in the theory of elasticity”. Furthermore, Kunin [115, p. 21] states the following theorem: in the nonlocal theory of a linear elastic medium of simple structure with finite action-at-a-distance, it is always possible to introduce a symmetric stress tensor and an energy density, which can be expressed in terms of stress and strain in the usual way.

The system of equations in P can be split into their dev sym, skew and tr parts obtaining (see [50]):

$$\begin{aligned}
\rho u_{,tt} - \text{Div}[\mathcal{T}] &= \text{Div} [2\mu_e \text{sym}(\nabla u - P) + \lambda_e \text{tr}(\nabla u - P) \mathbf{1} + 2\mu_c \text{skew}(\nabla u - P)], \\
\eta_1 \text{dev sym } P_{,tt} &= 2\mu_e \text{dev sym}(\nabla u - P) - 2\mu_m \text{dev sym } P - \mu L_c^2 \text{dev sym}(\text{Curl Curl } P), \\
\eta_2 \text{skew } P_{,tt} &= 2\mu_c \text{skew}(\nabla u - P) - \mu L_c^2 \text{skew}(\text{Curl Curl } P), \\
\frac{1}{3}\eta_3 \text{tr}(P_{,tt}) &= \left(\frac{2}{3}\mu_e + \lambda_e\right) \text{tr}(\nabla u - P) - \left(\frac{2}{3}\mu_m + \lambda_m\right) \text{tr}(P) - \frac{1}{3}\mu L_c^2 \text{tr}(\text{Curl Curl } P).
\end{aligned} \tag{III.28}$$

We note here that the presence of the $\text{Curl } P$ in the energy generates a non-local term $\text{Curl Curl } P$ in the equation of motion, while the possibility of band-gaps is still present, see [139]. The presence of the $\text{Curl } P$ term is essential to simultaneously allow for the description of non localities and band gap in an enriched continuum mechanics framework.

CHAPTER III.2

Analysis of the material symmetry classes

Now, we need to shortly discuss that such a reduced formulation is fully able to be treated in an invariant setting. Considering the displacement u and the micro-distortion field P , we apply the following coordinate transformation (generating the so-called Rayleigh-action on it [7]):

$$\begin{aligned} x &= Q^T \cdot \xi, & P^\#(\xi) &:= Q \cdot [P(Q^T \cdot \xi)] \cdot Q^T, \\ u^\#(\xi) &:= Q \cdot u(Q^T \cdot \xi), & \nabla_\xi u^\#(\xi) &= Q \cdot \nabla_x u(Q^T \cdot \xi) \cdot Q^T. \end{aligned} \quad (\text{III.29})$$

Thus, we require that P transforms as ∇u under simultaneous rotations of the reference and spatial configurations. With this definition, it can be shown [161] that:

$$\text{Curl}_\xi P^\#(\xi) = Q \cdot [\text{Curl}_x P(Q^T \cdot \xi)] \cdot Q^T. \quad (\text{III.30})$$

As explained in detail in [161], possessing a material symmetry is tantamount to requiring, under the transformation (III.29) with any $Q \in \mathcal{G}$ -symmetry group of the material, that both the strain energy density and the kinetic energy density are *form-invariant*, i.e.:

$$\begin{aligned} W(\nabla_\xi u^\#(\xi), P^\#(\xi), \text{Curl}_\xi P^\#(\xi)) &= W(\nabla_x u(x), P(x), \text{Curl}_x P(x)), \\ J(u^\#(\xi), \nabla_\xi u^\#(\xi), P^\#(\xi)) &= J(u(x), \nabla_x u(x), P(x)), \end{aligned} \quad (\text{III.31})$$

that is equivalent to saying that, $\forall Q \in \mathcal{G}$ -symmetry group of the material, we have:

$$\begin{aligned} W(\nabla u, P, \text{Curl} P) &= W(Q \cdot \nabla u \cdot Q^T, Q \cdot P \cdot Q^T, Q \cdot (\text{Curl} P) \cdot Q^T) \\ J(u, \nabla u, P) &= J(Q \cdot u, Q \cdot \nabla u \cdot Q^T, Q \cdot P \cdot Q^T). \end{aligned} \quad (\text{III.32})$$

The invariance condition depends on the set \mathcal{G} in which the transformation matrix Q lives. Depending on the symmetry properties of the group \mathcal{G} , we will be able to define different material classes. For instance in the case of full anisotropy the group \mathcal{G} corresponds to $\{-\mathbf{1}, \mathbf{1}\}$, while in the case of full isotropy we obtain \mathcal{G} is the entire rotation group $\text{SO}(3)$. Those are the two extreme cases, the classification of the linearly elastic materials according to their symmetry includes the classical eight classes of elastic symmetry [33, 45]. Symmetry groups for some classes of symmetry are contained within the symmetry group of other class as schematically shown in Fig. 35.

2.1 The strain energy density in the Mandel-Voigt vector notation

In this section, we consider an equivalent formulation of the relaxed micromorphic model obtained by using the Mandel-Voigt vector notation for the macro strain $\text{sym} \nabla u$ as well as for the micro strain $\text{sym} P$. This means that the second order tensors $\text{sym} \nabla u$ and $\text{sym} P$ are replaced by the vectors ε and β , in which the components of the original tensors are sorted column-wise by respecting a given order which is chosen “a priori”. This representation is more suitable if one wants to specify the anisotropy classes of the constitutive tensors in a format that is easily found in the literature.

We consider a linear mapping $\mathfrak{M}_{\alpha ij} : \text{Sym}(3) \rightarrow \mathbb{R}^6$ (as done in [143, 229, 230]) such that the independent components of $(\text{sym} \nabla u)_{ij}$ and $(\text{sym} P)_{ij}$ are isomorphically mapped in the corresponding vectors ε_α and β_α . The same analysis can be made for the symmetric parts of the curvature term and the kinetic energy obtaining analogous results. We obtain:

$$\varepsilon_\alpha = \mathfrak{M}_{\alpha ij} (\text{sym} \nabla u)_{ij}. \quad (\text{III.33})$$

$$\beta_\alpha = \mathfrak{M}_{\alpha ij} (\text{sym} P)_{ij}. \quad (\text{III.34})$$

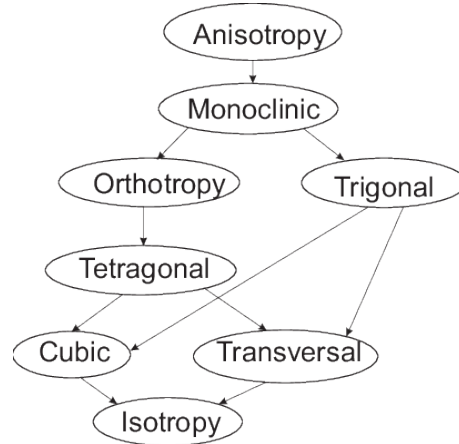


Figure 35: Material symmetry classes and their inclusions [113].

Considering the components of the mapping shown in the Appendix C.1, we have:

$$\beta = \begin{pmatrix} (\text{sym } P)_{11} \\ (\text{sym } P)_{22} \\ (\text{sym } P)_{33} \\ c (\text{sym } P)_{23} \\ c (\text{sym } P)_{13} \\ c (\text{sym } P)_{12} \end{pmatrix}, \quad \varepsilon = \begin{pmatrix} (\text{sym } \nabla u)_{11} \\ (\text{sym } \nabla u)_{22} \\ (\text{sym } \nabla u)_{33} \\ c (\text{sym } \nabla u)_{23} \\ c (\text{sym } \nabla u)_{13} \\ c (\text{sym } \nabla u)_{12} \end{pmatrix}. \quad (\text{III.35})$$

The coefficient c depends on the notation used (2 for Voigt notation [229, 230], $\sqrt{2}$ for Mandel notation [143]).

Let us consider an anisotropic energy term in $\nabla u - P$, namely:

$$\frac{1}{2} (\mathbb{C}_e)_{ijkl} (\text{sym}(\nabla u - P))_{ij} (\text{sym}(\nabla u - P))_{kl} \quad (\text{III.36})$$

Now, if we consider a quadratic energy in $\varepsilon - \beta$ we can always express it as:

$$\frac{1}{2} (\tilde{\mathbb{C}}_e)_{\alpha\beta} (\varepsilon_\alpha - \beta_\alpha) (\varepsilon_\beta - \beta_\beta) = \frac{1}{2} (\tilde{\mathbb{C}}_e)_{\alpha\beta} \mathfrak{M}_{\alpha ij} \mathfrak{M}_{\beta kl} (\text{sym}(\nabla u - P))_{ij} (\text{sym}(\nabla u - P))_{kl}. \quad (\text{III.37})$$

Here, $\tilde{\mathbb{C}}_e : \mathbb{R}^6 \rightarrow \mathbb{R}^6$ is a general second order symmetric tensor on $\mathbb{R}^{6 \times 6}$ (matrix), with 21 independent coefficients.

Comparing eq. (III.37) with (III.36), i.e.:

$$\begin{aligned} \frac{1}{2} (\mathbb{C}_e)_{ijkl} (\text{sym}(\nabla u - P))_{ij} (\text{sym}(\nabla u - P))_{kl} = \\ \frac{1}{2} (\tilde{\mathbb{C}}_e)_{\alpha\beta} \mathfrak{M}_{\alpha ij} \mathfrak{M}_{\beta kl} (\text{sym}(\nabla u - P))_{ij} (\text{sym}(\nabla u - P))_{kl}, \end{aligned} \quad (\text{III.38})$$

we must have:

$$(\mathbb{C}_e)_{ijkl} = \mathfrak{M}_{\alpha ij} (\tilde{\mathbb{C}}_e)_{\alpha\beta} \mathfrak{M}_{\beta kl}, \quad (\mathbb{C}_e)_{ijkl}^{-1} = \mathfrak{M}_{ij\alpha}^{-1} (\tilde{\mathbb{C}}_e)_{\alpha\beta}^{-1} \mathfrak{M}_{kl\beta}^{-1}. \quad (\text{III.39})$$

The second relation can be verified considering:

$$\begin{aligned} (\mathbb{C}_e)_{ijkl}^{-1} (\mathbb{C}_e)_{klmn} &= \mathfrak{M}_{\alpha ij}^{-1} (\tilde{\mathbb{C}}_e)_{\alpha\beta}^{-1} \mathfrak{M}_{\beta kl}^{-1} \mathfrak{M}_{kl\gamma} \mathfrak{M}_{\gamma\delta} (\tilde{\mathbb{C}}_e)_{\alpha\beta} \mathfrak{M}_{\alpha mn} = \mathfrak{M}_{\alpha ij}^{-1} (\tilde{\mathbb{C}}_e)_{\alpha\beta}^{-1} \tilde{\delta}_{\beta\gamma} (\tilde{\mathbb{C}}_e)_{\gamma\delta} \mathfrak{M}_{mn\delta} \\ &= \mathfrak{M}_{\alpha ij}^{-1} (\tilde{\mathbb{C}}_e)_{\alpha\beta}^{-1} (\tilde{\mathbb{C}}_e)_{\beta\delta} \mathfrak{M}_{mn\delta} = \mathfrak{M}_{\alpha ij}^{-1} \tilde{\delta}_{\alpha\delta} \mathfrak{M}_{mn\delta} = \mathfrak{M}_{\alpha ij}^{-1} \mathfrak{M}_{mn\alpha} = \mathbf{1}_{ijmn}. \end{aligned} \quad (\text{III.40})$$

On the other hand, the converse relations read:

$$(\tilde{\mathbb{C}}_e)_{\alpha\beta} = \mathfrak{M}_{ij\alpha}^{-1} (\mathbb{C}_e)_{ijkl} \mathfrak{M}_{kl\beta}^{-1}, \quad (\tilde{\mathbb{C}}_e)_{\alpha\beta}^{-1} = \mathfrak{M}_{\alpha ij} (\mathbb{C}_e)_{ijkl}^{-1} \mathfrak{M}_{\beta kl}. \quad (\text{III.41})$$

In the same fashion, we can obtain analogous equations for \mathbb{C}_m , \mathbb{L}_e , \mathbb{J}_g , \mathbb{J}_h and later \mathbb{C}_M .

With reference to (III.41) and recalling expression (C.5) (see Appendix C.1) for the components of \mathfrak{M}^{-1} , we see that the second order tensor $\tilde{\mathbb{C}}_e$ can be written as a function of the components of the fourth order tensor \mathbb{C}_e as:

$$\tilde{\mathbb{C}}_e = \begin{pmatrix} (\mathbb{C}_e)_{1111} & (\mathbb{C}_e)_{1122} & (\mathbb{C}_e)_{1133} & \frac{2}{c} (\mathbb{C}_e)_{1123} & \frac{2}{c} (\mathbb{C}_e)_{1113} & \frac{2}{c} (\mathbb{C}_e)_{1112} \\ (\mathbb{C}_e)_{2211} & (\mathbb{C}_e)_{2222} & (\mathbb{C}_e)_{2233} & \frac{2}{c} (\mathbb{C}_e)_{2223} & \frac{2}{c} (\mathbb{C}_e)_{2213} & \frac{2}{c} (\mathbb{C}_e)_{2212} \\ (\mathbb{C}_e)_{3311} & (\mathbb{C}_e)_{3322} & (\mathbb{C}_e)_{3333} & \frac{2}{c} (\mathbb{C}_e)_{3323} & \frac{2}{c} (\mathbb{C}_e)_{3313} & \frac{2}{c} (\mathbb{C}_e)_{3312} \\ \frac{2}{c} (\mathbb{C}_e)_{2311} & \frac{2}{c} (\mathbb{C}_e)_{2322} & \frac{2}{c} (\mathbb{C}_e)_{2333} & \frac{4}{c^2} (\mathbb{C}_e)_{2323} & \frac{4}{c^2} (\mathbb{C}_e)_{2313} & \frac{4}{c^2} (\mathbb{C}_e)_{2312} \\ \frac{2}{c} (\mathbb{C}_e)_{1311} & \frac{2}{c} (\mathbb{C}_e)_{1322} & \frac{2}{c} (\mathbb{C}_e)_{1333} & \frac{4}{c^2} (\mathbb{C}_e)_{1323} & \frac{4}{c^2} (\mathbb{C}_e)_{1313} & \frac{4}{c^2} (\mathbb{C}_e)_{1312} \\ \frac{2}{c} (\mathbb{C}_e)_{1211} & \frac{2}{c} (\mathbb{C}_e)_{1222} & \frac{2}{c} (\mathbb{C}_e)_{1233} & \frac{4}{c^2} (\mathbb{C}_e)_{1223} & \frac{4}{c^2} (\mathbb{C}_e)_{1213} & \frac{4}{c^2} (\mathbb{C}_e)_{1212} \end{pmatrix}, \quad (\text{III.42})$$

which is a symmetric 6×6 matrix due to the symmetries of \mathbb{C}_e according to which:

$$(\mathbb{C}_e)_{ijkl} = (\mathbb{C}_e)_{klij}. \quad (\text{III.43})$$

Now, we extend the reasoning for the elastic tensors acting on symmetric strain measure to the elastic tensors \mathbb{C}_c and \mathbb{L}_c which instead act on skew-symmetric strain measures and so provide the ‘‘rotational coupling’’ in the relaxed micromorphic model and the skew-symmetric part of the curvature, respectively.

To that end, we may always represent the 4th order tensor $\mathbb{C}_c : \mathfrak{so}(3) \rightarrow \mathfrak{so}(3)$ acting on skew-symmetric matrices by its version acting on axial vectors only, i.e. we write:

$$\langle \mathbb{C}_c \text{skew}(X), \text{skew}(X) \rangle_{\mathbb{R}^{3 \times 3}} = \langle \tilde{\mathbb{C}}_c \text{axl}(\text{skew}(X)), \text{axl}(\text{skew}(X)) \rangle_{\mathbb{R}^3}, \quad (\text{III.44})$$

where $\tilde{\mathbb{C}}_c : \mathbb{R}^3 \rightarrow \mathbb{R}^3$ is a symmetric second order tensor (since it appears in a quadratic form) and the operator axl defined in equation (INT.5). Therefore, $\tilde{\mathbb{C}}_c$ has only 6 independent coefficients and so does \mathbb{C}_c . Given a second order tensor X , it can be verified that:

$$\|\text{skew}(X)\|_{\mathbb{R}^{3 \times 3}}^2 = 2 \|\text{axl}(\text{skew}(X))\|_{\mathbb{R}^3}^2. \quad (\text{III.45})$$

2.2 Constitutive tensors for various anisotropy classes

In this section, we discuss the different anisotropy classes for \mathbb{C}_e , \mathbb{C}_m , \mathbb{C}_c , $\bar{\mathbb{L}}$, $\bar{\mathbb{J}}_g$ and $\bar{\mathbb{J}}_m$. In the case of \mathbb{C}_c it can be expressed more easily as $\tilde{\mathbb{C}}_c$. To respect the invariance relations given in (III.32), the constitutive tensors must be chosen such that, for every $Q \in \mathcal{G}$ -symmetry group of the material, we obtain:

$$\begin{aligned} (\mathbb{C}_e)_{ijkl} &= (\mathbb{C}_e)_{mnpq} Q_{im} Q_{jn} Q_{kp} Q_{lq}, & (\mathbb{C}_m)_{ijkl} &= (\mathbb{C}_m)_{mnpq} Q_{im} Q_{jn} Q_{kp} Q_{lq}, \\ (\tilde{\mathbb{C}}_c)_{ij} &= (\tilde{\mathbb{C}}_c)_{mn} Q_{im} Q_{jn}, & (\bar{\mathbb{L}})_{ijkl} &= (\bar{\mathbb{L}})_{mnpq} Q_{im} Q_{jn} Q_{kp} Q_{lq}, \\ (\bar{\mathbb{J}}_g)_{ijkl} &= (\bar{\mathbb{J}}_g)_{mnpq} Q_{im} Q_{jn} Q_{kp} Q_{lq}, & (\bar{\mathbb{J}}_m)_{ijkl} &= (\bar{\mathbb{J}}_m)_{mnpq} Q_{im} Q_{jn} Q_{kp} Q_{lq}. \end{aligned} \quad (\text{III.46})$$

In what follows, we will consider the split of the curvature term and the inertiae proposed in (III.4) and (III.15). Therefore, instead of the last three condition, we work with:

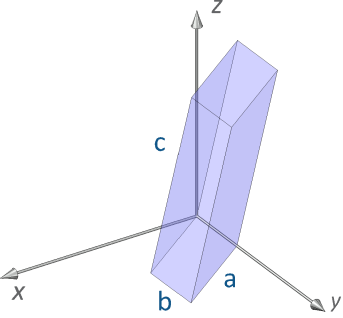
$$\begin{aligned} (\mathbb{L}_e)_{ijkl} &= (\mathbb{L}_e)_{mnpq} Q_{im} Q_{jn} Q_{kp} Q_{lq}, & (\tilde{\mathbb{L}}_c)_{ij} &= (\tilde{\mathbb{L}}_c)_{mn} Q_{im} Q_{jn}, \\ (\mathbb{J}_g)_{ijkl} &= (\mathbb{J}_g)_{mnpq} Q_{im} Q_{jn} Q_{kp} Q_{lq}, & (\tilde{\mathbb{J}}_c)_{ij} &= (\tilde{\mathbb{J}}_c)_{mn} Q_{im} Q_{jn}, \\ (\mathbb{J}_m)_{ijkl} &= (\mathbb{J}_m)_{mnpq} Q_{im} Q_{jn} Q_{kp} Q_{lq}, & (\tilde{\mathbb{J}}_d)_{ij} &= (\tilde{\mathbb{J}}_d)_{mn} Q_{im} Q_{jn}. \end{aligned} \quad (\text{III.47})$$

From these definitions, we can derive the structure of the constitutive tensors for every possible symmetry.

In what follows, we will present some of the main material symmetries and the associated crystal lattices, giving the form of the resulting constitutive tensors $\tilde{\mathbb{E}}$ and $\tilde{\mathbb{K}}$. Indeed, the constitutive tensors $\tilde{\mathbb{C}}_e$, $\tilde{\mathbb{C}}_m$, $\tilde{\mathbb{L}}_e$, $\bar{\mathbb{J}}_g$ and $\bar{\mathbb{J}}_m$ acting on vectors in \mathbb{R}^6 (equivalent to symmetric matrices) must have the form $\tilde{\mathbb{E}}$, while $\tilde{\mathbb{C}}_c$, $\tilde{\mathbb{L}}_c$, $\tilde{\mathbb{J}}_c$ and $\tilde{\mathbb{J}}_d$ that act on vectors in \mathbb{R}^3 (equivalent to skew-symmetric matrices), must have the form $\tilde{\mathbb{K}}$. In particular, we consider here the following material symmetries:

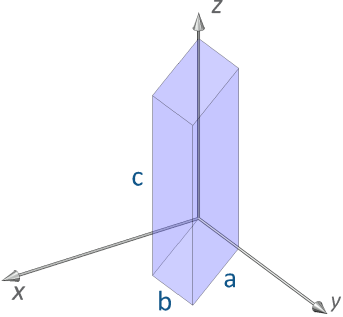
- anisotropic;
- monoclinic;
- orthotropic;
- tetragonal;
- transversely isotropic;
- cubic;
- isotropic.

Anisotropic (Triclinic): As far as elastic material symmetry is concerned, the symmetry of the triclinic crystal system is the same as the absence of symmetry. Triclinic crystal systems do have some symmetry, but they do not have enough symmetry to restrict the form of the constitutive tensors.

$$\begin{aligned} \tilde{\mathbb{E}}^{\text{tric}} &= \begin{pmatrix} \tilde{\mathbb{E}}_{11} & \tilde{\mathbb{E}}_{12} & \tilde{\mathbb{E}}_{13} & \tilde{\mathbb{E}}_{14} & \tilde{\mathbb{E}}_{15} & \tilde{\mathbb{E}}_{16} \\ & \tilde{\mathbb{E}}_{22} & \tilde{\mathbb{E}}_{23} & \tilde{\mathbb{E}}_{24} & \tilde{\mathbb{E}}_{25} & \tilde{\mathbb{E}}_{26} \\ & & \tilde{\mathbb{E}}_{33} & \tilde{\mathbb{E}}_{34} & \tilde{\mathbb{E}}_{35} & \tilde{\mathbb{E}}_{36} \\ & & & \tilde{\mathbb{E}}_{44} & \tilde{\mathbb{E}}_{45} & \tilde{\mathbb{E}}_{46} \\ & \text{sym} & & & \tilde{\mathbb{E}}_{55} & \tilde{\mathbb{E}}_{56} \\ & & & & & \tilde{\mathbb{E}}_{66} \end{pmatrix}, \\ \tilde{\mathbb{K}}^{\text{tric}} &= \begin{pmatrix} \tilde{\mathbb{K}}_{11} & \tilde{\mathbb{K}}_{21} & \tilde{\mathbb{K}}_{31} \\ & \tilde{\mathbb{K}}_{22} & \tilde{\mathbb{K}}_{23} \\ & \text{sym} & \tilde{\mathbb{K}}_{33} \end{pmatrix}. \end{aligned} \quad (\text{III.48})$$


21+6 independent coefficients, no symmetry transformations.

Monoclinic: The monoclinic crystal system has exactly one plane of reflective symmetry. The normal to the plane of mirror symmetry is taken here to be in the e_3 direction.

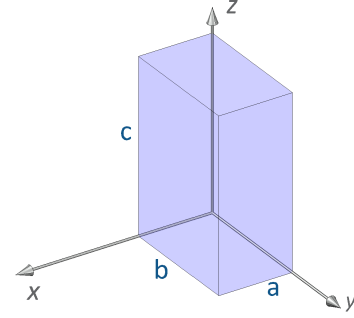
$$\begin{aligned} \tilde{\mathbb{E}}^{\text{mon}} &= \begin{pmatrix} \tilde{\mathbb{E}}_{11} & \tilde{\mathbb{E}}_{12} & \tilde{\mathbb{E}}_{13} & 0 & 0 & \tilde{\mathbb{E}}_{16} \\ & \tilde{\mathbb{E}}_{22} & \tilde{\mathbb{E}}_{23} & 0 & 0 & \tilde{\mathbb{E}}_{26} \\ & & \tilde{\mathbb{E}}_{33} & 0 & 0 & \tilde{\mathbb{E}}_{36} \\ & & & \tilde{\mathbb{E}}_{44} & \tilde{\mathbb{E}}_{45} & 0 \\ & \text{sym} & & & \tilde{\mathbb{E}}_{55} & 0 \\ & & & & & \tilde{\mathbb{E}}_{66} \end{pmatrix}, \\ \tilde{\mathbb{K}}^{\text{mon}} &= \begin{pmatrix} \tilde{\mathbb{K}}_{11} & 0 & \tilde{\mathbb{K}}_{31} \\ & \tilde{\mathbb{K}}_{22} & 0 \\ & \text{sym} & \tilde{\mathbb{K}}_{33} \end{pmatrix}. \end{aligned} \quad (\text{III.49})$$


13+4 independent coefficients, one symmetry xy-plane.

Orthotropic (orthorhombic): This crystal system is known by two names, rhombic and orthorhombic. When the same symmetry is applied to textured materials it is generally called orthotropy. The crystal has three mutually orthogonal planes of reflection symmetry.

$$\begin{aligned} \tilde{\mathbb{E}}^{\text{orth}} &= \begin{pmatrix} \tilde{\mathbb{E}}_{11} & \tilde{\mathbb{E}}_{12} & \tilde{\mathbb{E}}_{13} & 0 & 0 & 0 \\ & \tilde{\mathbb{E}}_{22} & \tilde{\mathbb{E}}_{23} & 0 & 0 & 0 \\ & & \tilde{\mathbb{E}}_{33} & 0 & 0 & 0 \\ & & & \tilde{\mathbb{E}}_{44} & 0 & 0 \\ & \text{sym} & & & \tilde{\mathbb{E}}_{55} & 0 \\ & & & & & \tilde{\mathbb{E}}_{66} \end{pmatrix}, \\ \tilde{\mathbb{K}}^{\text{orth}} &= \begin{pmatrix} \tilde{\mathbb{K}}_{11} & 0 & 0 \\ & \tilde{\mathbb{K}}_{22} & 0 \\ & & \tilde{\mathbb{K}}_{33} \end{pmatrix}, \end{aligned} \quad (\text{III.50})$$

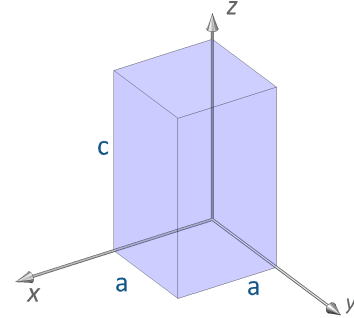
9+3 independent coefficients, three symmetry planes (xy , xz , yz).



Tetragonal: The tetragonal crystal has a unit cell with the shape of a rectangular prism with a square basis. Therefore, the material symmetry includes three mutually orthogonal planes of reflection symmetry plus 90° rotation symmetry with respect to one of those planes.

$$\begin{aligned} \tilde{\mathbb{E}}^{\text{tetr}} &= \begin{pmatrix} 2\mu_e + \lambda_e & \lambda_e & \lambda_e^* & 0 & 0 & 0 \\ & 2\mu_e + \lambda_e & \lambda_e^* & 0 & 0 & 0 \\ & & \nu_e & 0 & 0 & 0 \\ & & & \mu_e^* & 0 & 0 \\ & \text{sym} & & & \mu_e^* & 0 \\ & & & & & \mu_e^{**} \end{pmatrix}, \\ \tilde{\mathbb{K}}^{\text{tetr}} &= \frac{1}{2} \begin{pmatrix} \mu_c^* & 0 & 0 \\ & \mu_c^* & 0 \\ & & \mu_c \end{pmatrix}, \end{aligned} \quad (\text{III.51})$$

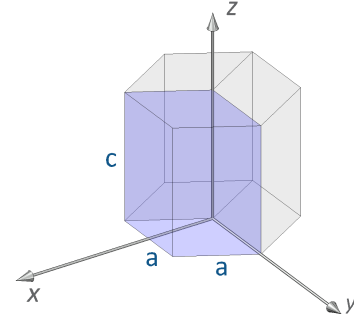
6+2 independent coefficients, three symmetry planes (xy , xz , yz) and 90° rotations in the xy -plane.



Transversely isotropic (Hexagonal): Considering elastic materials, the symmetry of the hexagonal crystal system is the same as the transverse isotropy. The properties are symmetric with respect to a plane of isotropy (xy -plane). In the crystal, there are three orthogonal planes of reflection symmetry and one axial symmetry.

$$\begin{aligned} \tilde{\mathbb{E}}^{\text{trans}} &= \begin{pmatrix} 2\mu_e + \lambda_e & \lambda_e & \lambda_e^* & 0 & 0 & 0 \\ & 2\mu_e + \lambda_e & \lambda_e^* & 0 & 0 & 0 \\ & & \nu_e & 0 & 0 & 0 \\ & & & \mu_e^* & 0 & 0 \\ & \text{sym} & & & \mu_e^* & 0 \\ & & & & & \mu_e \end{pmatrix}, \\ \tilde{\mathbb{K}}^{\text{trans}} &= \frac{1}{2} \begin{pmatrix} \mu_c^* & 0 & 0 \\ & \mu_c^* & 0 \\ & & \mu_c \end{pmatrix}, \end{aligned} \quad (\text{III.52})$$

5+2 independent coefficients, three symmetry planes (xy , xz , yz) and every possible rotation in the xy -plane.

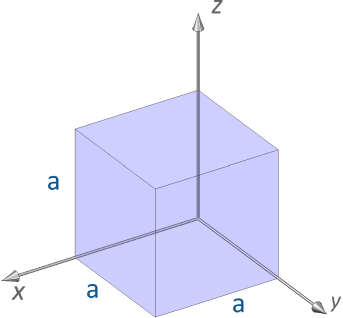


Cubic: The cubic (or isometric) crystal has a unit cell with the the shape of a cube. Therefore, the material symmetry includes three mutually orthogonal planes of reflection symmetry plus 90° rotation symmetry with respect to those planes.

$$\tilde{\mathbb{E}}^{\text{cubic}} = \begin{pmatrix} 2\mu_e + \lambda_e & \lambda_e & \lambda_e & 0 & 0 & 0 \\ & 2\mu_e + \lambda_e & \lambda_e & 0 & 0 & 0 \\ & & 2\mu_e + \lambda_e & 0 & 0 & 0 \\ & & & \mu_e^* & 0 & 0 \\ & \text{sym} & & & \mu_e^* & 0 \\ & & & & & \mu_e^* \end{pmatrix}, \quad (III.53)$$

$$\tilde{\mathbb{K}}^{\text{cubic}} = \frac{\mu_c}{2} \mathbf{1}.$$

3+1 independent coefficients, 90° rotations in the three symmetry planes (xy, xz, yz).



Isotropic: Isotropy means that the material properties do not depend on the direction. The representative shape would have to be a sphere. Therefore, the properties are invariant with respect to every possible rotation.

$$\tilde{\mathbb{E}}^{\text{iso}} = \begin{pmatrix} 2\mu_e + \lambda_e & \lambda_e & \lambda_e & 0 & 0 & 0 \\ \lambda_e & 2\mu_e + \lambda_e & \lambda_e & 0 & 0 & 0 \\ \lambda_e & \lambda_e & 2\mu_e + \lambda_e & 0 & 0 & 0 \\ 0 & 0 & 0 & \mu_e & 0 & 0 \\ 0 & 0 & 0 & 0 & \mu_e & 0 \\ 0 & 0 & 0 & 0 & 0 & \mu_e \end{pmatrix}, \quad \tilde{\mathbb{K}}^{\text{iso}} = \frac{\mu_c}{2} \mathbf{1}. \quad (III.54)$$

2+1 independent coefficients, every possible rotation and symmetry.

After considering the representation (III.53) and (III.54), we appreciate the fact that there is no difference between the cubic and isotropic rotational coupling. Both reduce $\tilde{\mathbb{C}}_c$ to be a spherical tensor $\tilde{\mathbb{C}}_c = \frac{\mu_c}{2} \mathbf{1}$, with $\mu_c \geq 0$. We believe that it is very difficult to make statements about the anisotropic rotational coupling (see footnote 4), therefore we study the reduction of any given anisotropic rotational coupling to the isotropic case in Appendix C.3.

Indeed, the first applications of the relaxed micromorphic model to real band-gap metamaterials show that an isotropic version of the tensor $\tilde{\mathbb{C}}_c$ is sufficient to trigger band-gap behaviors. We provide here the general framework to treat any possible degree of anisotropy for the rotational coupling. Nevertheless, if there is no evidence of the need of anisotropic rotational coupling based on experimental observations, an isotropic coupling given by the Cosserat couple modulus μ_c alone should always be preferred. Therefore, it is possible to consider a reduction of a given anisotropic rotational coupling to the isotropic case as analyzed in Appendix C.3.

CHAPTER III.3

The macroscopic limit of the relaxed model – macroscopic consistency conditions

The question of parameter identification has already been treated in the general anisotropic micromorphic model initially proposed by Mindlin-Eringen [69]. However, the resulting interpretation of the material constants, as well as their connection to the classical anisotropy formulation of linear elasticity, is still not settled satisfactorily and is presumably impossible. As already seen, in our relaxed model the complexity of the general micromorphic model has been decisively reduced, featuring basically only symmetric strain-like variables and the Curl of the micro-distortion P . However, the relaxed model is still general enough to include the full micro-stretch as well as the full Cosserat micro-polar model, see [176]. Furthermore, well-posedness results for the static and dynamic cases have been provided in [176] making decisive use of recently established coercive inequalities, generalizing Korn's inequality to incompatible tensor fields [15,167,181–183].

In this section, we propose the derivation of the macroscopic consistency condition that is of primary importance for an effective application of the relaxed micromorphic model to cases of real interest. The basic idea is that of considering a sample of a specific microstructured material which is large enough to consider the effect of the underlying microstructure negligible. On this large sample, standard mechanical tests can be performed allowing for the unique determination of the elastic coefficients \mathbb{C}_M . The existence of our formula relating \mathbb{C}_M (which is well known) to \mathbb{C}_e and \mathbb{C}_m (which are still unknown), allows to further reduce the number of coefficients that need to be determined to unequivocally characterize the mechanical behavior of microstructured materials. This unique feature of our relaxed model gives again more credibility to the relaxed approach by opening the way to a clear experimental campaign to determine some of the new micromorphic elastic constants.

Thanks to our previous considerations, we are able to establish equivalent relationships between the second order tensors $\tilde{\mathbb{C}}_M$, $\tilde{\mathbb{C}}_e$ and $\tilde{\mathbb{C}}_m$. The results that we show in this section have the following advantages which allow us to expectedly proceed towards well-conceived applications on real metamaterials:

- the consistency condition that we derive here relates the macro moduli in \mathbb{C}_M to the micro moduli in \mathbb{C}_e and \mathbb{C}_m . We claim that, given a specific metamaterial, the moduli in \mathbb{C}_M can be determined on the basis of very simple mechanical tests. The idea is to consider a specimen which is big enough that the effect of the microstructure can be considered negligible. Once the tensor \mathbb{C}_M is known, then \mathbb{C}_e and \mathbb{C}_m can be directly related via the consistency condition that we present here. This drastically reduces the number of unknown coefficients that have to be determined, thus providing an effective tool towards manageable applications.
- the way towards application is made even easier by the introduction of the second order tensors $\tilde{\mathbb{C}}_M$, $\tilde{\mathbb{C}}_e$ and $\tilde{\mathbb{C}}_m$ whose form can be easily found in the literature once the class of anisotropy of the medium is fixed, see chapter III.2.

3.1 Some considerations on the isotropic macroscopic consistency condition

In this section, we want to recall some results concerning the *macroscopic consistency condition* for the relaxed micromorphic model in the isotropic case [168,174]. It is of fundamental importance to catch the power that the introduced homogenization formulas may have for an effective application of the relaxed micromorphic model. In section III.3.3, we will present a generalization of such homogenization formulas to the fully anisotropic framework so opening the way for the effective mechanical characterization of a huge class of mechanical metamaterials.

The main idea behind the determination of our homogenized formulas is to consider a very large sample of a given microstructured material. This sample must be large enough that the effect of the microstructure on the macroscopic behavior of the sample can be considered to be negligible. Under this hypothesis, we can introduce a macroscopic elasticity tensor $\mathbb{C}_M : \text{Sym}(3) \rightarrow \text{Sym}(3)$ which best fits the macroscopic behavior of the sample and we can suppose that the material behavior can be described by classical linear elasticity with energy:

$$W = \frac{1}{2} \langle \mathbb{C}_M \text{sym} \nabla u, \text{sym} \nabla u \rangle. \quad (\text{III.55})$$

The corresponding classical symmetric Cauchy stress is clearly defined as:

$$\sigma_M(\text{sym} \nabla u) = \mathbb{C}_M \text{sym} \nabla u. \quad (\text{III.56})$$

For very large sample sizes, however, a scaling argument easily shows that the *relative* characteristic length scale L_c of the micromorphic model must vanish. Therefore, we have a way of comparing the classical formulation (III.55) to the relaxed micromorphic formulation (III.1) and to offer an *a priori relation* between \mathbb{C}_e , \mathbb{C}_m on the one hand and \mathbb{C}_M on the other.

In [168, 174], the authors obtained the *macroscopic consistency conditions for the isotropic case*:

$$(2\mu_M + 3\lambda_M) = \frac{(2\mu_e + 3\lambda_e)(2\mu_m + 3\lambda_m)}{(2\mu_e + 3\lambda_e) + (2\mu_m + 3\lambda_m)}, \quad (\text{III.57})$$

$$\mu_M = \frac{\mu_e \mu_m}{\mu_e + \mu_m} = \mu_e (\mu_e + \mu_m)^{-1} \mu_m.$$

Or, analogously:

$$(2\mu_e + 3\lambda_e) = \frac{(2\mu_M + 3\lambda_M)(2\mu_m + 3\lambda_m)}{(2\mu_m + 3\lambda_m) - (2\mu_M + 3\lambda_M)}, \quad (\text{III.58})$$

$$\mu_e = \frac{\mu_M \mu_m}{\mu_m - \mu_M} = \mu_M (\mu_m - \mu_M)^{-1} \mu_m.$$

Note that these formulas determine μ_M and κ_M (i.e. the elastic bulk modulus $\kappa_M = \frac{2\mu_M + 3\lambda_M}{3}$) to be one half of the harmonic mean of μ_e , μ_m , and κ_e , κ_m respectively.

As a matter of fact, the *harmonic mean* $\mathcal{H}(\mu_e, \mu_m)$ defined for real numbers is:

$$\mathcal{H}(\mu_e, \mu_m) = \left[\frac{1}{2} \left(\frac{1}{\mu_e} + \frac{1}{\mu_m} \right) \right]^{-1} = \frac{2\mu_e \mu_m}{\mu_e + \mu_m}. \quad (\text{III.59})$$

In the isotropic case, upon inspection of equation (III.58), we see that the “macroscopic” elastic response, embodied by μ_M and λ_M , cannot be equal or stiffer than the microscopic response, embodied by μ_m and λ_m . This is certainly physically sound and expresses in short that “*smaller is stiffer*”. Moreover, $\mu_m = \mu_M$ is tantamount to “micro = macro” and formally equivalent to $\mu_e \rightarrow \infty$.

The fundamental importance of the equation (III.58) has already been proven in [132], where it is shown that the macroscopic stiffnesses provides the slopes of the acoustic curves for band-gap metamaterials. This will be even clearer in further applications where static test will be conceived to evaluate “a priori” λ_M and μ_M .

Therefore, we have a way of comparing a classical first gradient formulation with the relaxed micromorphic model and to offer an a priori relation between the microscopic parameters $\lambda_e, \lambda_m, \mu_e, \mu_m$ on the one side and the resulting macroscopic parameters λ_M, μ_M on the other side [12, 168, 174]:

$$\kappa_M = \frac{\kappa_e \kappa_m}{\kappa_e + \kappa_m}, \quad \mu_M = \frac{\mu_e \mu_m}{\mu_e + \mu_m}, \quad (\text{III.60})$$

Furthermore, if strict positive-definiteness (III.11) holds, we have:

$$\begin{aligned} \kappa_e + \kappa_m > 0, \quad \mu_e + \mu_m > 0, \quad \kappa_e > \kappa_M, \quad \kappa_m > \kappa_M, \quad \mu_e > \mu_M, \\ \mu_m > \mu_M, \end{aligned} \quad (\text{III.61})$$

and, therefore, the following inverse relations stand:

$$\kappa_e = \frac{\kappa_m \kappa_M}{\kappa_m - \kappa_M}, \quad \kappa_m = \frac{\kappa_e \kappa_M}{\kappa_e - \kappa_M}, \quad \mu_e = \frac{\mu_m \mu_M}{\mu_m - \mu_M}, \quad \mu_m = \frac{\mu_e \mu_M}{\mu_e - \mu_M}. \quad (\text{III.62})$$

3.2 The static macroscopic limit and the dynamic long wavelength limit

The governing equations for the anisotropic relaxed micromorphic model in the dynamic case take the form given in (III.23), namely:

$$\rho u_{,tt} - \rho \widehat{L}_c^2 \text{Div} [\overline{\mathbb{J}}_{g0} \nabla u_{,tt}] = \text{Div} [\tilde{\sigma}], \quad \rho \widehat{L}_c^2 \overline{\mathbb{J}}_{m0} P_{,tt} = \tilde{\sigma} - s - \mu L_c^2 \text{Curl} (\overline{\mathbb{L}}_{\text{aniso}} \text{Curl} P), \quad (\text{III.63})$$

The classical continuum theory is the *long wavelength limit*, corresponding to large length and time scales, and it predicts properties independent of specimen size. The long wavelength limit is given by letting $\widehat{L}_c, L_c \rightarrow 0$ simultaneously. In this case, the system (III.63) formally reduces to:

$$\begin{aligned} \rho u_{,tt} &= \text{Div} [\mathbb{C}_e \text{sym}(\nabla u - P) + \mathbb{C}_c \text{skew}(\nabla u - P)], \\ 0 &= \mathbb{C}_e \text{sym}(\nabla u - P) + \mathbb{C}_c \text{skew}(\nabla u - P) - \mathbb{C}_m \text{sym} P. \end{aligned} \quad (\text{III.64})$$

Furthermore, considering a static problem for very large sample sizes a scaling argument easily shows that the *relative* characteristic length scale L_c of the micromorphic model must vanish and no inertia must be considered. Therefore, equation (III.63) reduces further to:

$$\begin{aligned} \text{Div} [\mathbb{C}_e \text{sym}(\nabla u - P) + \mathbb{C}_c \text{skew}(\nabla u - P)] &= 0, \\ \mathbb{C}_e \text{sym}(\nabla u - P) + \mathbb{C}_c \text{skew}(\nabla u - P) - \mathbb{C}_m \text{sym} P &= 0. \end{aligned} \quad (\text{III.65})$$

All the calculations made in the following are made in the macroscopic static case for simplicity. It must be noted that the presence of the macroscopic inertia term $\rho u_{,tt}$ does not influence the calculations and all the results obtained are still valid as a long wavelength limit in the dynamical case.

3.3 The general relaxed anisotropic case in the limit $L_c \rightarrow 0$

We will show that our relaxed micromorphic model defined by the energy (III.1), or equivalently by the equations of motion (III.63), can be reduced to a sort of equivalent “macroscopic model” when letting $L_c \rightarrow 0$. Indeed, when $L_c = 0$ equation (III.63) reduces to (III.65). In particular, (III.65)₂ gives a direct relation between P and ∇u which, when inserted in (III.65)₁, allows us to rewrite the energy in terms of ∇u . Hence, we can introduce an equivalent macroscopic stress tensor $\sigma_M(\text{sym} \nabla u)$ which is the limit of $\tilde{\sigma}(\nabla u, P)$ for $L_c \rightarrow 0$. In symbols:

$$\sigma_M(\text{sym} \nabla u) = \lim_{L_c \rightarrow 0} \tilde{\sigma}(\nabla u, P). \quad (\text{III.66})$$

In the linear-elastic case the tensor $\sigma_M(\text{sym} \nabla u)$ can be written as:

$$\sigma_M(\text{sym} \nabla u) = \mathbb{C}_M \text{sym} \nabla u, \quad (\text{III.67})$$

assuming that it is the Cauchy stress tensor of a classical first gradient continuum.

In view of applications, considering very large samples of the anisotropic medium is equivalent to letting L_c , the characteristic length, tend to zero. As a consequence of $L_c = 0$, the second equilibrium equation in (III.63) loses the $\text{Curl} \text{Curl} P$ -term and turns into an algebraic side condition connecting P and ∇u (equation (III.65)₂). This equation can be decoupled (by the assumed special mapping symmetry properties

of the elasticity tensors, see equations (III.20)) into two equations for the symmetric and skew-symmetric part, respectively, yielding:

$$\mathbb{C}_e \operatorname{sym}(\nabla u - P) = \mathbb{C}_m \operatorname{sym} P, \quad \mathbb{C}_c \operatorname{skew}(\nabla u - P) = 0. \quad (\text{III.68})$$

This uncoupling is true since \mathbb{C}_e and \mathbb{C}_m map symmetric matrices to symmetric matrices and $\mathbb{C}_c \operatorname{skew}(\nabla u - P)$ is skew-symmetric by assumption (see subsection III.1.3 for more details). From the second equation in (III.68), we can easily derive that:

$$\mathbb{C}_c \operatorname{skew} \nabla u = \mathbb{C}_c \operatorname{skew} P. \quad (\text{III.69})$$

On the other hand, solving (III.68)₁ for $\operatorname{sym} P$ gives¹:

$$\begin{aligned} (\mathbb{C}_m + \mathbb{C}_e) \operatorname{sym} P &= \mathbb{C}_e \operatorname{sym} \nabla u, \\ \iff \operatorname{sym} P &= (\mathbb{C}_m + \mathbb{C}_e)^{-1} (\mathbb{C}_e \operatorname{sym} \nabla u). \end{aligned} \quad (\text{III.70})$$

This is an identity between the micro-distortion P and the gradient of the displacement ∇u which proves how, in the macroscopic limiting case, the model is transparent with respect to the micro-distortion, i.e. only macroscopic deformations involving $\operatorname{sym} \nabla u$ are allowed. We insert (III.68)₁, (III.69) and (III.70) into (III.65)₁ and considering the uncoupling between symmetric and skew symmetric parts of the involved tensors, we get:

$$\operatorname{Div} [\mathbb{C}_m \operatorname{sym} P] = 0 \iff \operatorname{Div} \left[\mathbb{C}_m (\mathbb{C}_m + \mathbb{C}_e)^{-1} \mathbb{C}_e \operatorname{sym} \nabla u \right] = 0. \quad (\text{III.71})$$

On the other hand, the classical balance equation for the linear elastic macroscopic response is:

$$\operatorname{Div} [\mathbb{C}_M \operatorname{sym} \nabla u] = 0. \quad (\text{III.72})$$

Comparing the macroscopic balance equation (III.72) with the one derived from our relaxed model when letting $L_c = 0$ ((III.71)₁), we obtain the following *a priori relation* between the macroscopic elasticity tensor \mathbb{C}_M and the microscopic tensor \mathbb{C}_m as well as the mesoscopic (relative) elasticity tensor \mathbb{C}_e :

$$\boxed{\mathbb{C}_M := \mathbb{C}_m (\mathbb{C}_m + \mathbb{C}_e)^{-1} \mathbb{C}_e,} \quad (\text{III.73})$$

which is a generalization of (III.57) when considering our anisotropic setting. Given the positive definiteness of \mathbb{C}_m and \mathbb{C}_e , the resulting macroscopic constitutive tensor \mathbb{C}_M is *symmetric* and *positive definite*, as it is proven in Appendix C.4. From equation (III.73), we get by simple inversion²:

$$\mathbb{C}_M^{-1} = \mathbb{C}_m^{-1} (\mathbb{C}_m + \mathbb{C}_e) \quad \mathbb{C}_e^{-1} = \mathbb{C}_e^{-1} + \mathbb{C}_m^{-1}. \quad (\text{III.74})$$

Therefore, we note, surprisingly at first glance, that \mathbb{C}_M is the “parallel sum” of \mathbb{C}_e and \mathbb{C}_m ³, that is equal to one half of the *harmonic mean operator* on positive definite symmetric matrices (see [17, p. 103]), defined as:

$$\mathcal{H}(\mathbb{C}_e, \mathbb{C}_m) := \left[\frac{1}{2} (\mathbb{C}_e^{-1} + \mathbb{C}_m^{-1}) \right]^{-1} = 2 \mathbb{C}_m (\mathbb{C}_e + \mathbb{C}_m)^{-1} \mathbb{C}_e = 2 \mathbb{C}_M. \quad (\text{III.75})$$

We can obtain the inverse relation with algebraic operations. First, from equation (III.74) it is immediate that:

$$\mathbb{C}_e^{-1} = \mathbb{C}_M^{-1} - \mathbb{C}_m^{-1}, \quad (\text{III.76})$$

¹We note here that the inverse of an elastic stiffness tensor, like $(\mathbb{C}_m + \mathbb{C}_e)$ has the same symmetry group structure as $\mathbb{C}_m + \mathbb{C}_e$ itself. This can be shown easily by directly looking at its definition of groups.

²It can be checked that, given fourth order invertible tensors A , B and C , the following identity holds: $(A \cdot B \cdot C)^{-1} = C^{-1} \cdot B^{-1} \cdot A^{-1}$

³The parallel sum of two tensors A and B is defined as $(A^{-1} + B^{-1})^{-1}$.

and, considering that $A^{-1} B^{-1} C^{-1} = (C B A)^{-1}$, we obtain:

$$\begin{aligned}
 \mathbb{C}_e &= (\mathbb{C}_M^{-1} - \mathbb{C}_m^{-1})^{-1} = \mathbb{1} (\mathbb{C}_M^{-1} - \mathbb{C}_m^{-1})^{-1} \mathbb{1} = \mathbb{C}_m \underbrace{\left[\mathbb{C}_m^{-1} (\mathbb{C}_M^{-1} - \mathbb{C}_m^{-1})^{-1} \mathbb{C}_M^{-1} \right]}_{A^{-1} B^{-1} C^{-1}} \mathbb{C}_M \\
 &= \mathbb{C}_m \underbrace{\left[\mathbb{C}_M (\mathbb{C}_M^{-1} - \mathbb{C}_m^{-1}) \mathbb{C}_m \right]^{-1}}_{(C B A)^{-1}} \mathbb{C}_M = \mathbb{C}_m \left[(\mathbb{1} - \mathbb{C}_M \mathbb{C}_m^{-1}) \mathbb{C}_m \right]^{-1} \mathbb{C}_M \\
 &= \mathbb{C}_m \left[\mathbb{C}_m - \mathbb{C}_M \right]^{-1} \mathbb{C}_M.
 \end{aligned} \tag{III.77}$$

So finally, we have the further compact relation:

$$\boxed{\mathbb{C}_e = \mathbb{C}_m (\mathbb{C}_m - \mathbb{C}_M)^{-1} \mathbb{C}_M.} \tag{III.78}$$

Note that these results are true without assuming that the tensors \mathbb{C}_m , \mathbb{C}_e and \mathbb{C}_M commute (and, in fact, they do not).

3.4 Particularization for specific anisotropy classes

To show how equation (III.73) particularizes for some of the anisotropy classes presented in III.2.2, we use the vectorial notation defined in subsection III.2.1. Considering (III.39), we can rewrite equation (III.73) as:

$$\begin{aligned}
 \left(\tilde{\mathbb{C}}_M \right)_{\alpha\beta} \mathfrak{M}_{\alpha ij} \mathfrak{M}_{\beta kl} &= \left(\tilde{\mathbb{C}}_m \right)_{\alpha\gamma} \mathfrak{M}_{\alpha ij} \mathfrak{M}_{\gamma mn} \left(\tilde{\mathbb{C}}_m + \tilde{\mathbb{C}}_e \right)_{\delta\epsilon}^{-1} \mathfrak{M}_{mn\delta}^{-1} \mathfrak{M}_{pq\epsilon}^{-1} \left(\tilde{\mathbb{C}}_e \right)_{\zeta\beta} \mathfrak{M}_{\zeta pq} \mathfrak{M}_{\beta kl} \\
 &= \left(\tilde{\mathbb{C}}_m \right)_{\alpha\gamma} \tilde{\delta}_{\gamma\delta} \tilde{\delta}_{\delta\epsilon} \left(\tilde{\mathbb{C}}_m + \tilde{\mathbb{C}}_e \right)_{\delta\epsilon}^{-1} \left(\tilde{\mathbb{C}}_e \right)_{\zeta\beta} \mathfrak{M}_{\alpha ij} \mathfrak{M}_{\beta kl} \\
 &= \left(\tilde{\mathbb{C}}_m \right)_{\alpha\gamma} \left(\tilde{\mathbb{C}}_m + \tilde{\mathbb{C}}_e \right)_{\gamma\zeta}^{-1} \left(\tilde{\mathbb{C}}_e \right)_{\zeta\beta} \mathfrak{M}_{\alpha ij} \mathfrak{M}_{\beta kl}.
 \end{aligned} \tag{III.79}$$

From this last equation we easily notice that:

$$\boxed{\tilde{\mathbb{C}}_M = \tilde{\mathbb{C}}_m \cdot \left(\tilde{\mathbb{C}}_m + \tilde{\mathbb{C}}_e \right)^{-1} \cdot \tilde{\mathbb{C}}_e.} \tag{III.80}$$

This formula for second-order elasticity tensors is completely analogous to (III.73), which was obtained for 4th order tensors and allows to pass from micro to macro coefficients just by specifying the special forms of the 6×6 matrices $\tilde{\mathbb{C}}_M$, $\tilde{\mathbb{C}}_m$, $\tilde{\mathbb{C}}_e$. Using algebraic arguments analogous to those for the 4th order tensors case, we obtain the inverse relation:

$$\boxed{\tilde{\mathbb{C}}_e = \tilde{\mathbb{C}}_m \cdot \left(\tilde{\mathbb{C}}_m - \tilde{\mathbb{C}}_M \right)^{-1} \cdot \tilde{\mathbb{C}}_M.} \tag{III.81}$$

These expressions may be of use when the elastic properties $\tilde{\mathbb{C}}_m$ of a unit elementary cell of the considered metamaterial and the macroscopic properties $\tilde{\mathbb{C}}_M$ of the metamaterial considered as a macroscopic block are known. Therefore, the elastic coupling tensor $\tilde{\mathbb{C}}_e$ is easily computable and is, in fact uniquely determined. In the following subsections, we will particularize equations (III.80) and (III.81) to specific symmetries, thus dealing with isotropic, cubic, orthotropic and generally anisotropic materials, as intended in our relaxed micromorphic framework. For deriving such particular cases, we make the implicit assumption that \mathbb{C}_e , \mathbb{C}_m and \mathbb{C}_M have the same symmetries, which is indeed a sensible ansatz.

3.4.1 The isotropic case

In this subsection, we show how the fundamental formula (III.80) can be particularized to the isotropic case so retrieving the homogenization formulas for the Lamé parameters proposed in [168, 174].

In subsection III.2.2, the structure of the isotropic constitutive elastic tensors $\tilde{\mathbb{C}}_e^{\text{iso}}$ and $\tilde{\mathbb{C}}_m^{\text{iso}}$ was shown, see (III.54). Defining the bulk moduli $\kappa_e = \frac{1}{3}(2\mu_e + 3\lambda_e)$, $\kappa_m = \frac{1}{3}(2\mu_m + 3\lambda_m)$, $\kappa_M = \frac{1}{3}(2\mu_M + 3\lambda_M)$, and

using the consistency condition in equation (III.80) and simplifying, we find:

$$\tilde{\mathbb{C}}_{\text{M}}^{\text{iso}} = \begin{pmatrix} \kappa_{\text{M}} + 4/3 \mu_{\text{M}} & \kappa_{\text{M}} - 2/3 \mu_{\text{M}} & \kappa_{\text{M}} - 2/3 \mu_{\text{M}} & 0 & 0 & 0 \\ \kappa_{\text{M}} - 2/3 \mu_{\text{M}} & \kappa_{\text{M}} + 4/3 \mu_{\text{M}} & \kappa_{\text{M}} - 2/3 \mu_{\text{M}} & 0 & 0 & 0 \\ \kappa_{\text{M}} - 2/3 \mu_{\text{M}} & \kappa_{\text{M}} - 2/3 \mu_{\text{M}} & \kappa_{\text{M}} + 4/3 \mu_{\text{M}} & 0 & 0 & 0 \\ 0 & 0 & 0 & \mu_{\text{M}} & 0 & 0 \\ 0 & 0 & 0 & 0 & \mu_{\text{M}} & 0 \\ 0 & 0 & 0 & 0 & 0 & \mu_{\text{M}} \end{pmatrix}, \quad (\text{III.82})$$

where we set:

$$\kappa_{\text{M}} = \frac{\kappa_e \kappa_{\text{m}}}{\kappa_e + \kappa_{\text{m}}}, \quad \mu_{\text{M}} = \frac{\mu_e \mu_{\text{m}}}{\mu_e + \mu_{\text{m}}}. \quad (\text{III.83})$$

The relation for κ_{M} can also be expressed as a function of μ_{M} and λ_{M} :

$$(2\mu_{\text{M}} + 3\lambda_{\text{M}}) = \frac{(2\mu_{\text{m}} + 3\lambda_{\text{m}})(2\mu_e + 3\lambda_e)}{(2(\mu_e + \mu_{\text{m}}) + 3(\lambda_e + \lambda_{\text{m}}))}. \quad (\text{III.84})$$

Equations (III.83) can also be inverted:

$$\begin{aligned} \kappa_e &= \frac{\kappa_{\text{M}} \kappa_{\text{m}}}{\kappa_{\text{m}} - \kappa_{\text{M}}} = \kappa_{\text{M}} (\kappa_{\text{m}} - \kappa_{\text{M}})^{-1} \kappa_{\text{m}}, \\ \mu_e &= \frac{\mu_{\text{M}} \mu_{\text{m}}}{\mu_{\text{m}} - \mu_{\text{M}}} = \mu_{\text{M}} (\mu_{\text{m}} - \mu_{\text{M}})^{-1} \mu_{\text{m}}. \end{aligned} \quad (\text{III.85})$$

The first equation in (III.85) can be analogously rewritten in terms of λ_e and μ_e as:

$$(2\mu_e + 3\lambda_e) = \frac{(2\mu_{\text{M}} + 3\lambda_{\text{M}})(2\mu_{\text{m}} + 3\lambda_{\text{m}})}{(2\mu_{\text{m}} + 3\lambda_{\text{m}}) - (2\mu_{\text{M}} + 3\lambda_{\text{M}})}. \quad (\text{III.86})$$

3.4.2 The cubic symmetry case

In this subsection, we start investigating the interest that the homogenization formula (III.80) may have in the case of simple anisotropies, as in the cubic case. In a forthcoming work [49], this formula for the cubic case will be applied to show how it is fundamental for the mechanical characterization of real metamaterials.

In subsection III.2.2, the structure of the cubic constitutive elastic tensors $\tilde{\mathbb{C}}_e^{\text{cub}}$ and $\tilde{\mathbb{C}}_{\text{m}}^{\text{cub}}$ was shown, see (III.53).

Via the bulk moduli and the consistency condition in equation (III.80), we obtain:

$$\tilde{\mathbb{C}}_{\text{M}}^{\text{cub}} = \begin{pmatrix} \kappa_{\text{M}} + 4/3 \mu_{\text{M}} & \kappa_{\text{M}} - 2/3 \mu_{\text{M}} & \kappa_{\text{M}} - 2/3 \mu_{\text{M}} & 0 & 0 & 0 \\ \kappa_{\text{M}} - 2/3 \mu_{\text{M}} & \kappa_{\text{M}} + 4/3 \mu_{\text{M}} & \kappa_{\text{M}} - 2/3 \mu_{\text{M}} & 0 & 0 & 0 \\ \kappa_{\text{M}} - 2/3 \mu_{\text{M}} & \kappa_{\text{M}} - 2/3 \mu_{\text{M}} & \kappa_{\text{M}} + 4/3 \mu_{\text{M}} & 0 & 0 & 0 \\ 0 & 0 & 0 & \mu_{\text{M}}^* & 0 & 0 \\ 0 & 0 & 0 & 0 & \mu_{\text{M}}^* & 0 \\ 0 & 0 & 0 & 0 & 0 & \mu_{\text{M}}^* \end{pmatrix}. \quad (\text{III.87})$$

where:

$$\kappa_{\text{M}} = \frac{\kappa_e \kappa_{\text{m}}}{\kappa_e + \kappa_{\text{m}}}, \quad \mu_{\text{M}} = \frac{\mu_e \mu_{\text{m}}}{\mu_e + \mu_{\text{m}}}, \quad \mu_{\text{M}}^* = \frac{\mu_e^* \mu_{\text{m}}^*}{\mu_e^* + \mu_{\text{m}}^*}. \quad (\text{III.88})$$

The relation for κ_{M} can also be expressed as a function of μ_{M} and λ_{M} :

$$(2\mu_{\text{M}} + 3\lambda_{\text{M}}) = \frac{(2\mu_{\text{m}} + 3\lambda_{\text{m}})(2\mu_e + 3\lambda_e)}{(2(\mu_e + \mu_{\text{m}}) + 3(\lambda_e + \lambda_{\text{m}}))}. \quad (\text{III.89})$$

Equations (III.88) can also be inverted:

$$\begin{aligned}
\kappa_e &= \frac{\kappa_M \kappa_m}{\kappa_m - \kappa_M} = \kappa_M (\kappa_m - \kappa_M)^{-1} \kappa_m, \\
\mu_e &= \frac{\mu_M \mu_m}{\mu_m - \mu_M} = \mu_M (\mu_m - \mu_M)^{-1} \mu_m, \\
\mu_e^* &= \frac{\mu_M^* \mu_m^*}{\mu_m^* - \mu_M^*} = \mu_M^* (\mu_m^* - \mu_M^*)^{-1} \mu_m^*.
\end{aligned} \tag{III.90}$$

The first equation in (III.90) can be analogously rewritten in terms of λ_e and μ_e as:

$$(2\mu_e + 3\lambda_e) = \frac{(2\mu_M + 3\lambda_M)(2\mu_m + 3\lambda_m)}{(2\mu_m + 3\lambda_m) - (2\mu_M + 3\lambda_M)}. \tag{III.91}$$

3.4.3 The orthotropic case

In subsection III.2.2, the structure of the cubic constitutive elastic tensors $\tilde{\mathbb{C}}_e^{\text{orth}}$ and $\tilde{\mathbb{C}}_m^{\text{orth}}$ was shown, see (III.50).

We define the sub-blocks $\tilde{\mathbb{C}}_e^{\text{a}}$, $\tilde{\mathbb{C}}_m^{\text{a}}$ and $\tilde{\mathbb{C}}_M^{\text{a}}$ as:

$$\begin{aligned}
\tilde{\mathbb{C}}_e^{\text{a}} &= \begin{pmatrix} \left(\begin{smallmatrix} \tilde{\mathbb{C}}_e \\ \tilde{\mathbb{C}}_e \\ \tilde{\mathbb{C}}_e \end{smallmatrix} \right)_{11} & \left(\begin{smallmatrix} \tilde{\mathbb{C}}_e \\ \tilde{\mathbb{C}}_e \\ \tilde{\mathbb{C}}_e \end{smallmatrix} \right)_{12} & \left(\begin{smallmatrix} \tilde{\mathbb{C}}_e \\ \tilde{\mathbb{C}}_e \\ \tilde{\mathbb{C}}_e \end{smallmatrix} \right)_{13} \\ \left(\begin{smallmatrix} \tilde{\mathbb{C}}_e \\ \tilde{\mathbb{C}}_e \\ \tilde{\mathbb{C}}_e \end{smallmatrix} \right)_{12} & \left(\begin{smallmatrix} \tilde{\mathbb{C}}_e \\ \tilde{\mathbb{C}}_e \\ \tilde{\mathbb{C}}_e \end{smallmatrix} \right)_{22} & \left(\begin{smallmatrix} \tilde{\mathbb{C}}_e \\ \tilde{\mathbb{C}}_e \\ \tilde{\mathbb{C}}_e \end{smallmatrix} \right)_{23} \\ \left(\begin{smallmatrix} \tilde{\mathbb{C}}_e \\ \tilde{\mathbb{C}}_e \\ \tilde{\mathbb{C}}_e \end{smallmatrix} \right)_{13} & \left(\begin{smallmatrix} \tilde{\mathbb{C}}_e \\ \tilde{\mathbb{C}}_e \\ \tilde{\mathbb{C}}_e \end{smallmatrix} \right)_{23} & \left(\begin{smallmatrix} \tilde{\mathbb{C}}_e \\ \tilde{\mathbb{C}}_e \\ \tilde{\mathbb{C}}_e \end{smallmatrix} \right)_{33} \end{pmatrix}, & \tilde{\mathbb{C}}_m^{\text{a}} &= \begin{pmatrix} \left(\begin{smallmatrix} \tilde{\mathbb{C}}_m \\ \tilde{\mathbb{C}}_m \\ \tilde{\mathbb{C}}_m \end{smallmatrix} \right)_{11} & \left(\begin{smallmatrix} \tilde{\mathbb{C}}_m \\ \tilde{\mathbb{C}}_m \\ \tilde{\mathbb{C}}_m \end{smallmatrix} \right)_{12} & \left(\begin{smallmatrix} \tilde{\mathbb{C}}_m \\ \tilde{\mathbb{C}}_m \\ \tilde{\mathbb{C}}_m \end{smallmatrix} \right)_{13} \\ \left(\begin{smallmatrix} \tilde{\mathbb{C}}_m \\ \tilde{\mathbb{C}}_m \\ \tilde{\mathbb{C}}_m \end{smallmatrix} \right)_{12} & \left(\begin{smallmatrix} \tilde{\mathbb{C}}_m \\ \tilde{\mathbb{C}}_m \\ \tilde{\mathbb{C}}_m \end{smallmatrix} \right)_{22} & \left(\begin{smallmatrix} \tilde{\mathbb{C}}_m \\ \tilde{\mathbb{C}}_m \\ \tilde{\mathbb{C}}_m \end{smallmatrix} \right)_{23} \\ \left(\begin{smallmatrix} \tilde{\mathbb{C}}_m \\ \tilde{\mathbb{C}}_m \\ \tilde{\mathbb{C}}_m \end{smallmatrix} \right)_{13} & \left(\begin{smallmatrix} \tilde{\mathbb{C}}_m \\ \tilde{\mathbb{C}}_m \\ \tilde{\mathbb{C}}_m \end{smallmatrix} \right)_{23} & \left(\begin{smallmatrix} \tilde{\mathbb{C}}_m \\ \tilde{\mathbb{C}}_m \\ \tilde{\mathbb{C}}_m \end{smallmatrix} \right)_{33} \end{pmatrix}, \\
\tilde{\mathbb{C}}_M^{\text{a}} &= \begin{pmatrix} \left(\begin{smallmatrix} \tilde{\mathbb{C}}_M \\ \tilde{\mathbb{C}}_M \\ \tilde{\mathbb{C}}_M \end{smallmatrix} \right)_{11} & \left(\begin{smallmatrix} \tilde{\mathbb{C}}_M \\ \tilde{\mathbb{C}}_M \\ \tilde{\mathbb{C}}_M \end{smallmatrix} \right)_{12} & \left(\begin{smallmatrix} \tilde{\mathbb{C}}_M \\ \tilde{\mathbb{C}}_M \\ \tilde{\mathbb{C}}_M \end{smallmatrix} \right)_{13} \\ \left(\begin{smallmatrix} \tilde{\mathbb{C}}_M \\ \tilde{\mathbb{C}}_M \\ \tilde{\mathbb{C}}_M \end{smallmatrix} \right)_{12} & \left(\begin{smallmatrix} \tilde{\mathbb{C}}_M \\ \tilde{\mathbb{C}}_M \\ \tilde{\mathbb{C}}_M \end{smallmatrix} \right)_{22} & \left(\begin{smallmatrix} \tilde{\mathbb{C}}_M \\ \tilde{\mathbb{C}}_M \\ \tilde{\mathbb{C}}_M \end{smallmatrix} \right)_{23} \\ \left(\begin{smallmatrix} \tilde{\mathbb{C}}_M \\ \tilde{\mathbb{C}}_M \\ \tilde{\mathbb{C}}_M \end{smallmatrix} \right)_{13} & \left(\begin{smallmatrix} \tilde{\mathbb{C}}_M \\ \tilde{\mathbb{C}}_M \\ \tilde{\mathbb{C}}_M \end{smallmatrix} \right)_{23} & \left(\begin{smallmatrix} \tilde{\mathbb{C}}_M \\ \tilde{\mathbb{C}}_M \\ \tilde{\mathbb{C}}_M \end{smallmatrix} \right)_{33} \end{pmatrix}.
\end{aligned} \tag{III.92}$$

The macroscopic constitutive tensor $\tilde{\mathbb{C}}_M^{\text{orth}}$ keeps the orthotropic structure of the two $\tilde{\mathbb{C}}_e^{\text{orth}}$ and $\tilde{\mathbb{C}}_m^{\text{orth}}$. Considering $p = 4, 5, 6$ without the sum over repeated indices and using the consistency condition in equation (III.80), we obtain:

$$\tilde{\mathbb{C}}_M^{\text{a}} = \tilde{\mathbb{C}}_e^{\text{a}} \cdot (\tilde{\mathbb{C}}_e^{\text{a}} + \tilde{\mathbb{C}}_m^{\text{a}})^{-1} \cdot \tilde{\mathbb{C}}_m^{\text{a}}, \quad \left(\tilde{\mathbb{C}}_M \right)_{pp} = \frac{\left(\tilde{\mathbb{C}}_e \right)_{pp} \left(\tilde{\mathbb{C}}_m \right)_{pp}}{\left(\tilde{\mathbb{C}}_e + \tilde{\mathbb{C}}_m \right)_{pp}}. \tag{III.93}$$

The formulas in equation (III.93) can also be inverted as:

$$\tilde{\mathbb{C}}_e^{\text{a}} = \tilde{\mathbb{C}}_M^{\text{a}} \cdot (\tilde{\mathbb{C}}_m^{\text{a}} - \tilde{\mathbb{C}}_M^{\text{a}})^{-1} \cdot \tilde{\mathbb{C}}_m^{\text{a}}, \quad \left(\tilde{\mathbb{C}}_e \right)_{pp} = \frac{\left(\tilde{\mathbb{C}}_M \right)_{pp} \left(\tilde{\mathbb{C}}_m \right)_{pp}}{\left(\tilde{\mathbb{C}}_m - \tilde{\mathbb{C}}_M \right)_{pp}}. \tag{III.94}$$

Conclusion

In this part, we have obtained that for zero characteristic length scale $L_c = 0$ (which corresponds to a long wavelength limit or to a specimen of arbitrarily large size), we can identify both the symmetric and the skew-symmetric part of the micro-distortion P as a function of to the gradient of the displacement ∇u :

$$\begin{aligned} (\mathbb{C}_m + \mathbb{C}_e) \operatorname{sym} P &= \mathbb{C}_e \operatorname{sym} \nabla u , \\ \mathbb{C}_c \operatorname{skew} P &= \mathbb{C}_c \operatorname{skew} \nabla u . \end{aligned} \quad (\text{III.95})$$

From this result, we obtain that the experimentally observable macroscopic stiffness for an energy-equivalent linear elastic medium has the stiffness tensor:

$$\mathbb{C}_M = \frac{1}{2} \mathcal{H}(\mathbb{C}_e, \mathbb{C}_m) = (\mathbb{C}_m^{-1} + \mathbb{C}_e^{-1})^{-1} = \mathbb{C}_e (\mathbb{C}_m + \mathbb{C}_e)^{-1} \mathbb{C}_m. \quad (\text{III.96})$$

Here, \mathcal{H} is the harmonic mean of the elastic (relative) stiffness tensor \mathbb{C}_e and the microscopic stiffness tensor \mathbb{C}_m of the relaxed micromorphic model. Inversion of expression (III.96) yields:

$$\mathbb{C}_e = \mathbb{C}_m (\mathbb{C}_m - \mathbb{C}_M)^{-1} \mathbb{C}_M = (\mathbb{C}_M^{-1} - \mathbb{C}_m^{-1})^{-1} . \quad (\text{III.97})$$

In (III.97), the tensor \mathbb{C}_e is uniquely determined and positive definite, provided that $\mathbb{C}_m - \mathbb{C}_M$ is positive definite. No similar simple expression exists for the standard anisotropic Mindlin-Eringen model.

We remark that the rotational coupling tensor \mathbb{C}_c is in no way related to either the macroscopic or the microscopic measurable quantities, in sharp contrast to $\mathbb{C}_m, \mathbb{C}_M, \mathbb{C}_e$.

Moreover, our presented model allows full use of the well-known Voigt-representation for classical elasticity tensors. Thus, we do not need to investigate the anisotropy classes based on 6th-order tensors [7], neither for the local energy contribution nor for the curvature expression. This makes the presented framework by far more attractive, due to the transparent comparison to classical linear, anisotropic elasticity.

Our a priori novel macroscopic consistency condition (III.96) drastically reduces the burden of determining constitutive coefficients. Indeed, the fundamental importance of formula (III.96) will be soon provided in a forthcoming paper in which a ‘‘cubic’’ band-gap metamaterial will be investigated. The macroscopic coefficients \mathbb{C}_M will be determined on the basis of classical static tests on samples of the considered metamaterial. This will allow to drastically reduce the constitutive parameters to be determined. Such remaining parameters together with the micro-inertiae and, eventually, the characteristic length L_c , will be determined on the basis of dynamical tests, following what was done in [132] for the isotropic case.

Part IV

Modeling phononic band-gaps via the relaxed micromorphic model

Contents of Part IV

Introduction	95
1 Bulk wave propagation in the relaxed micromorphic model	97
1.1 Solution of the dynamic problem	97
1.2 Necessary and sufficient conditions for real wave propagation	101
1.3 Dispersion curves for the relaxed micromorphic model	105
1.3.1 Longitudinal waves	105
1.3.2 Transverse waves	106
1.3.3 Uncoupled waves	108
2 Dispersion curves and band-gaps in other enriched continuum models	109
2.1 The classical Cauchy medium	110
2.2 The Cosserat micromorphic model	111
2.3 The internal variable model	112
2.4 The standard Mindlin-Eringen model	113
2.5 The relaxed micromorphic model with curvature $\ \text{Div } P\ ^2$	114
3 Reflection and transmission of waves at a Cauchy/relaxed micromorphic interface	115
3.1 Conservation of the total energy	115
3.1.1 The classical Cauchy medium	115
3.1.2 The relaxed micromorphic continuum	115
3.2 Interface jump conditions at a Cauchy/relaxed-micromorphic interface	116
3.2.1 Decomposition of the incident, transmitted and reflected waves	117
3.2.2 The case of purely longitudinal incident waves	118
3.3 Reflection and transmission coefficients at a Cauchy/relaxed-micromorphic interface	120
3.3.1 The degenerate limit case $L_c = 0$ (internal variable model)	120
4 Modeling real two dimensional phononic crystals	122
4.1 The steel plate with cross-shaped holes	122
4.1.1 Microstructure and FEM analysis of a phononic metamaterial	122
4.1.2 Identification of the material parameters	124
4.1.3 Validation of the relaxed micromorphic model via the transmission spectra	127
4.2 The steel plate with liquid-filled round holes	127
4.2.1 Experiments of wave transmission at a Cauchy/phononic-crystal interface	128
4.2.2 Identification of the parameters	129
Conclusion	133

Introduction

Mechanical band-gap metamaterials are suitably engineered microstructured materials which are able to inhibit elastic wave propagation in specific frequency ranges due to the presence of their underlying microstructure. These frequency intervals in which wave inhibition takes place are known as frequency band-gaps and their intrinsic characteristics (characteristic values of the gap frequency, extension of the band-gap, etc.) strongly depend on the metamaterial microstructure. Such unorthodox dynamical behavior can be related to two main physical phenomena occurring at the micro-level:

- local resonance phenomena (Mie resonance): the micro-structural components, excited at particular frequencies, start oscillating independently of the matrix thus capturing the energy of the propagating wave which remains confined at the level of the microstructure;
- micro-diffusion phenomena (Bragg scattering): when the propagating wave has wavelengths which are small enough to start interacting with the microstructure of the material, reflection and transmission phenomena occur at the micro-level.

Such resonance and micro-diffusion mechanisms (usually a mix of the two) are at the basis of both electromagnetic and elastic band-gaps (see e.g. [5, 127]) and they are manifestly related to the particular microstructural topologies of the considered metamaterials. In fact, it is well known (see e.g. [5, 123, 142, 213, 221]) that the characteristics of the microstructures strongly influence the macroscopic band-gap behavior.

In recent works [139, 140], the *relaxed micromorphic model* was suggested to account for the onset of microstructure-related frequency band-gaps [139, 140] while remaining in the macroscopic framework of continuum mechanics. In [141], a comprehensive study of jump conditions for surfaces of discontinuity of the material properties in relaxed micromorphic media was presented, thus establishing a strong basis for the systematic study of reflection and transmission phenomena in real band-gap metamaterials. In this part, we will show that the particular constraint introduced in [141] that we called “*macro internal clamp with free microstructure*” is indeed able to reproduce real situations in which a Cauchy material (e.g. steel) is connected to a phononic crystal (e.g. a steel plate with fluid-filled holes).

The relaxed micromorphic model is, by its own nature, a “macroscopic” model, in the sense that all the constitutive parameters introduced take into account the presence of the micro-structure in an “averaged” sense. Nevertheless, it is interesting to validate the estimate of the parameters of the relaxed micromorphic model performed here against more “homogenization-oriented” methods of the type presented in [8, 217]. The present part is organized according to the following structure:

- In chapter IV.1, we derive the bulk governing equations and the associated boundary conditions for the relaxed micromorphic model [80, 139, 140, 176]. The hypothesis of plane wave is introduced and a discussion concerning the behavior of the dispersion relations obtained by means of our relaxed micromorphic model is performed. A derivation of the necessary and sufficient conditions for real wave propagation is also presented.
- In chapter IV.2, we make a review of some of the available isotropic, linear-elastic, enriched continuum models for the description of the dynamical behavior of metamaterials. We show that the relaxed micromorphic model is the only non-local enriched model which is able to describe band-gaps when considering a kinetic energy independently accounting for micro and macro motions.
- In chapter IV.3, we present some results rigorously derived in [141] concerning the conservation of total energy in relaxed micromorphic media. The explicit form of the energy fluxes is presented both in the general case and when using the plane wave ansatz. For completeness, the conservation of total energy

is recalled also for classical Cauchy continua. Furthermore, a particular connection between a Cauchy medium and a relaxed micromorphic medium, called “*macro internal clamp with free microstructure*”, is introduced. This connection allows continuity of macroscopic displacement at the considered interface together with free motions of the microstructure on the side of the interface occupied by the relaxed micromorphic medium. The procedure for the determination of the reflection and transmission coefficients at a Cauchy/relaxed-micromorphic interface is also presented.

- In chapter IV.4, the cases of two real phononic crystals are presented. For the first phononic crystal, the parameters of the relaxed micromorphic model are determined via the fitting of the dispersion curves and the the profile of the reflection coefficient is obtained and compared with a FE model. In the second case, the maximum possible number of constitutive elastic parameters are instead fitted, by inverse approach, directly on the reflection spectrum based on real experiments on a specific phononic crystals (see [127]). Furthermore, a first evidence of non-local effects in band-gap metamaterials is given, by quantifying them through the determination of the characteristic length L_c for the phononic crystal experimentally studied in [127].

CHAPTER IV.1

Bulk wave propagation in the relaxed micromorphic model

We recall here the strain and kinetic energy densities for the relaxed micromorphic model that will be used to study the dynamic problem and to model the band gap behavior for specific phononic crystals. The elastic energy density reads

$$W = \mu_e \|\operatorname{sym}(\nabla u - P)\|^2 + \frac{\lambda_e}{2} (\operatorname{tr}(\nabla u - P))^2 + \mu_c \|\operatorname{skew}(\nabla u - P)\|^2 \quad (\text{IV.1})$$

$$+ \mu_m \|\operatorname{sym} P\|^2 + \frac{\lambda_m}{2} (\operatorname{tr} P)^2 + \frac{\mu L_c^2}{2} \|\operatorname{Curl} P\|^2,$$

where the parameters and the elastic stress are analogous to the standard Mindlin-Eringen micromorphic model.

For the kinetic energy, we consider:

$$J = \frac{1}{2} \rho u_{,t}^2 + \frac{1}{2} \eta_1 \|\operatorname{dev} \operatorname{sym} P_{,t}\|^2 + \frac{1}{2} \eta_2 \|\operatorname{skew} P_{,t}\|^2 + \frac{1}{6} \eta_3 \operatorname{tr}(P_{,t})^2 + \frac{1}{2} \bar{\eta}_1 \|\operatorname{dev} \operatorname{sym} \nabla u_{,t}\|^2 \quad (\text{IV.2})$$

$$+ \frac{1}{2} \bar{\eta}_2 \|\operatorname{skew} \nabla u_{,t}\|^2 + \frac{1}{6} \bar{\eta}_3 \operatorname{tr}(\nabla u_{,t})^2.$$

1.1 Solution of the dynamic problem

Isotropic equation of motion and plane wave ansatz The dynamical formulation is the one given in Equation (III.26):

$$\rho u_{,tt} - \operatorname{Div}[Z] = \operatorname{Div}[\tilde{\sigma}], \quad \tilde{Z} = \tilde{\sigma} - s - \operatorname{Curl} m, \quad \forall x \in \Omega, \quad (\text{IV.3})$$

where

$$\begin{aligned} Z &= \bar{\eta}_1 \operatorname{dev} \operatorname{sym} \nabla u_{,tt} + \bar{\eta}_2 \operatorname{skew} \nabla u_{,tt} + \frac{\bar{\eta}_3}{3} \operatorname{tr}(\nabla u_{,tt}), \\ \tilde{Z} &= \eta_1 \operatorname{dev} \operatorname{sym} P_{,tt} + \eta_2 \operatorname{skew} P_{,tt} + \frac{\eta_3}{3} \operatorname{tr}(P_{,tt}), \\ \tilde{\sigma} &= 2\mu_e \operatorname{sym}(\nabla u - P) + \lambda_e \operatorname{tr}(\nabla u - P) \mathbb{1} + 2\mu_c \operatorname{skew}(\nabla u - P), \\ s &= 2\mu_m \operatorname{sym} P + \lambda_m \operatorname{tr}(P) \mathbb{1}, \\ m &= \mu L_c^2 \operatorname{Curl} P. \end{aligned} \quad (\text{IV.4})$$

Sufficiently far from a source, dynamic wave solutions may be treated as plane waves. Therefore, we suppose that the space dependence of all introduced kinematic fields are limited to a direction defined by a unit vector $\tilde{\xi} \in \mathbb{R}^3$, which is the direction of propagation of the wave and which is assumed given. Hence, we look for solutions of (IV.3) in the form:

$$u = u(X, t), \quad P = P(X, t), \quad (\text{IV.5})$$

where $X = \langle \tilde{\xi}, x \rangle_{\mathbb{R}^3}$ is the direction of propagation of the wave. Since our formulation is isotropic, we can, without loss of generality, specify the propagation direction $\tilde{\xi} = e_1$. Then $X = \langle e_1, x \rangle_{\mathbb{R}^3} = x_1$, and we obtain that the space dependence of all introduced kinematic fields are limited to the component x_1 ¹.

¹In an isotropic model, it is clear that there is no direction dependence. More specifically, let $\tilde{\xi} \in \mathbb{R}^3$ be an arbitrary direction and $Q \in \operatorname{SO}(3)$ an orthogonal spatial coordinate change such that $Q \cdot e_1 = \tilde{\xi}$. In the rotated variables, the ensuing system of PDE's (IV.3) is form-invariant, see [161].

The uncoupled plane wave propagation systems To express the system (IV.3) in a decomposed form, we define the following variables:

$$\begin{aligned} P^S &:= \frac{1}{3} \operatorname{tr}(P), & P^D &:= P_{11} - P^S, & P^V &:= P_{22} - P_{33}, \\ P_{[ij]} &:= (\operatorname{skew} P)_{ij} = \frac{1}{2} (P_{ij} - P_{ji}), & P_{(ij)} &:= (\operatorname{sym} P)_{ij} = \frac{1}{2} (P_{ij} + P_{ji}). \end{aligned} \quad (\text{IV.6})$$

Since the dependency is only on the space variables x_1 and the time t , the system (IV.3) can be rewritten with the help of the newly introduced variable, as:

- a set of three equations involving only longitudinal quantities:

$$\begin{aligned} \rho \ddot{u}_1 - \frac{2\bar{\eta}_1 + \bar{\eta}_3}{3} \ddot{u}_{1,11} &= (2\mu_e + \lambda_e) u_{1,11} - 2\mu_e P_{,1}^D - (2\mu_e + 3\lambda_e) P_{,1}^S, \\ \eta_1 \ddot{P}^D &= \frac{4}{3} \mu_e u_{1,1} + \frac{1}{3} \mu L_c^2 P_{,11}^D - \frac{2}{3} \mu L_c^2 P_{,11}^S - 2(\mu_e + \mu_m) P^D, \\ \eta_3 \ddot{P}^S &= \frac{2\mu_e + 3\lambda_e}{3} u_{1,1} - \frac{1}{3} \mu L_c^2 P_{,11}^D + \frac{2}{3} \mu L_c^2 P_{,11}^S \\ &\quad - (2\mu_e + 3\lambda_e + 2\mu_m + 3\lambda_m) P^S, \end{aligned} \quad (\text{IV.7})$$

- two sets of three equations involving only transverse quantities in the ξ -th direction, with $\xi = 2, 3$:

$$\begin{aligned} \rho \ddot{u}_\xi - \frac{\bar{\eta}_1 + \bar{\eta}_2}{2} \ddot{u}_{\xi,11} &= (\mu_e + \mu_c) u_{\xi,11} - 2\mu_e P_{(1\xi),1} + 2\mu_c P_{[1\xi],1}, \\ \eta_1 \ddot{P}_{(1\xi)} &= \mu_e u_{\xi,1} + \frac{1}{2} \mu L_c^2 P_{(1\xi),11} + \frac{1}{2} \mu L_c^2 P_{[1\xi],11} \\ &\quad - 2(\mu_e + \mu_m) P_{(1\xi)}, \\ \eta_2 \ddot{P}_{[1\xi]} &= -\mu_c u_{\xi,1} + \frac{1}{2} \mu L_c^2 P_{(1\xi),11} + \frac{1}{2} \mu L_c^2 P_{[1\xi],11} - 2\mu_c P_{[1\xi]}, \end{aligned} \quad (\text{IV.8})$$

- one equation involving only the variable $P_{(23)}$:

$$\eta_1 \ddot{P}_{(23)} = -2(\mu_e + \mu_m) P_{(23)} + \mu L_c^2 P_{(23),11}, \quad (\text{IV.9})$$

- one equation involving only the variable $P_{[23]}$:

$$\eta_2 \ddot{P}_{[23]} = -2\mu_c P_{[23]} + \mu L_c^2 P_{[23],11}, \quad (\text{IV.10})$$

- one equation involving only the variable P^V :

$$\eta_1 \ddot{P}^V = -2(\mu_e + \mu_m) P^V + \mu L_c^2 P_{,11}^V, \quad (\text{IV.11})$$

Harmonic solutions for the plane wave problem We now want to study harmonic solutions traveling in an infinite domain of the differential systems (IV.7) involving only longitudinal quantities, the two systems in (IV.8) involving only transverse quantities and the one composed by the uncoupled equations (IV.9), (IV.10) and (IV.11). Therefore, we define four unknown vectors that reflect the coupling of the variables in the equations of motion (see [50, 131, 132, 136–141]):

$$\underbrace{v_1 = (u_1, P^D, P^S)}_{\text{longitudinal}}, \quad \underbrace{v_\tau = (u_\tau, P_{(1\tau)}, P_{[1\tau]})}_{\text{transversal}}, \quad \tau = 2, 3, \quad \underbrace{v_4 = (P_{(23)}, P_{[23]}, P^V)}_{\text{uncoupled}}. \quad (\text{IV.12})$$

Since we want to find harmonic waves, we look for solutions of the form:

$$v_1 = \beta^1 e^{i(kX - \omega t)}, \quad v_\tau = \beta^\tau e^{i(kX - \omega t)}, \quad \tau = 2, 3, \quad v_4 = \beta^4 e^{i(kX - \omega t)}, \quad (\text{IV.13})$$

where $\beta^1 = (\beta_1^1, \beta_2^1, \beta_3^1)^T \in \mathbb{C}^3$, $\beta^\tau = (\beta_1^\tau, \beta_2^\tau, \beta_3^\tau)^T \in \mathbb{C}^3$ and $\beta^4 = (\beta_1^4, \beta_2^4, \beta_3^4)^T \in \mathbb{C}^3$ are the unknown amplitudes of the considered waves², k is the wavenumber and ω is the angular frequency.

Replacing these expressions in equations (IV.3), we can express the system (see [139, 140, 179]) as:

$$A_1 \cdot \beta^1 = 0, \quad A_\tau \cdot \beta^\tau = 0, \quad \tau = 2, 3, \quad A_4 \cdot \beta^4 = 0, \quad (\text{IV.14})$$

with

$$A_1(\omega, k) = \begin{pmatrix} -\omega^2 \left(1 + k^2 \frac{2\bar{\eta}_1 + \bar{\eta}_3}{3\rho}\right) + c_p^2 k^2 & i k 2 \mu_e / \rho & i k (2 \mu_e + 3 \lambda_e) / \rho \\ -i k \frac{4}{3} \mu_e / \eta_1 & -\omega^2 + \frac{1}{3} c_{m1}^2 k^2 + \omega_s^2 & -\frac{2}{3} c_{m1}^2 k^2 \\ -\frac{1}{3} i k (2 \mu_e + 3 \lambda_e) / \eta_3 & -\frac{1}{3} c_{m3}^2 k^2 & -\omega^2 + \frac{2}{3} c_{m3}^2 k^2 + \omega_p^2 \end{pmatrix},$$

$$A_2(\omega, k) = A_3(\omega, k) = \begin{pmatrix} -\omega^2 \left(1 + k^2 \frac{\bar{\eta}_1 + \bar{\eta}_2}{2\rho}\right) + c_s^2 k^2 & i k 2 \mu_e / \rho & -i k 2 \mu_c / \rho \\ -i k \mu_e / \eta_1 & -\omega^2 + \frac{1}{2} c_{m1}^2 k^2 + \omega_s^2 & \frac{1}{2} c_{m1}^2 k^2 \\ i k \mu_c / \eta_2 & \frac{1}{2} c_{m2}^2 k^2 & -\omega^2 + \frac{1}{2} c_{m2}^2 k^2 + \omega_r^2 \end{pmatrix}, \quad (\text{IV.15})$$

$$A_4(\omega, k) = \begin{pmatrix} -\omega^2 + c_{m1}^2 k^2 + \omega_s^2 & 0 & 0 \\ & -\omega^2 + c_{m2}^2 k^2 + \omega_r^2 & 0 \\ \text{sym} & & -\omega^2 + c_{m1}^2 k^2 + \omega_s^2 \end{pmatrix},$$

where the following characteristic quantities have also been introduced:

$$\boxed{\begin{aligned} c_{m1} &= \sqrt{\frac{\mu_e L_c^2}{\eta_1}}, & c_{m2} &= \sqrt{\frac{\mu_e L_c^2}{\eta_2}}, & c_{m3} &= \sqrt{\frac{\mu_e L_c^2}{\eta_3}}, & c_p &= \sqrt{\frac{\lambda_e + 2\mu_e}{\rho}}, & c_s &= \sqrt{\frac{\mu_e + \mu_c}{\rho}}, \\ \omega_p &= \sqrt{\frac{(3\lambda_e + 2\mu_e) + (3\lambda_m + 2\mu_m)}{\eta_3}}, & \omega_r &= \sqrt{\frac{2\mu_c}{\eta_2}}, & \omega_s &= \sqrt{\frac{2(\mu_e + \mu_m)}{\eta_1}}. \end{aligned}}$$

We remark here that, considering the form of the resulting tensors, we can always take the gradient micro-inertia $\bar{\eta}_1 = 0$ and redefine $\bar{\eta}_2^* = \bar{\eta}_1 + \bar{\eta}_2$ and $\bar{\eta}_3^* = 2\bar{\eta}_1 + \bar{\eta}_3$ to obtain an equivalent form.

Now, we want to express the system (IV.14) equivalently featuring only symmetric matrices with real entries. To do so, we define the diagonal matrix:

$$\text{diag}_1 = \begin{pmatrix} \sqrt{\rho} & 0 & 0 \\ 0 & i \frac{\sqrt{6\eta_1}}{2} & 0 \\ 0 & 0 & i\sqrt{3\eta_3} \end{pmatrix}. \quad (\text{IV.16})$$

Setting $\gamma = \text{diag}_1 \cdot \beta$ and the matrix $\bar{A}_1(\omega, k) = \text{diag}_1 \cdot A_1(\omega, k) \cdot \text{diag}_1^{-1}$, the problem (IV.14) can be formulated equivalently as³:

²Here, \mathbb{C}^3 is the space of complex constant three-dimensional vectors and we understand that having found the (in general, complex) solutions of (IV.13) only the real or imaginary parts separately constitute actual wave solutions which can be observed in reality.

³We can face the problem in two more equivalent ways. The first one is to assume from the start that the amplitudes of the micro-distortion field are multiplied by the imaginary unit i , i.e. $\beta = (\beta_1, i\beta_2, i\beta_3)^T \in \mathbb{C}^3$, as done in [155, p. 24, eq. 8.6]. Doing so, we obtain a real matrix that can be symmetrized with a real diagonal matrix $\text{diag}_1 = (\sqrt{\rho}, \frac{\sqrt{6\eta_1}}{2}$ and $\sqrt{3\eta_3}$ on the diagonal). On the other hand, it is also possible to consider from the beginning $\beta = (\sqrt{\rho}\beta_1, i\frac{\sqrt{6\eta_1}}{2}\beta_2, i\sqrt{3\eta_3}\beta_3)^T \in \mathbb{C}^3$ obtaining directly a real symmetric matrix.

$$\bar{A}_1 \cdot \gamma = \begin{pmatrix} -\omega^2 \left(1 + k^2 \frac{2\bar{\eta}_1 + \bar{\eta}_3}{3\rho}\right) + c_p^2 k^2 & \frac{2\sqrt{6}}{3} k \mu_e / \sqrt{\rho\eta_1} & \frac{\sqrt{3}}{3} k (2\mu_e + 3\lambda_e) / \sqrt{\rho\eta_3} \\ & -\omega^2 + \frac{1}{3} c_{m1}^2 k^2 + \omega_s^2 & -\frac{\sqrt{2}}{3} c_{m1} c_{m3} k^2 \\ \text{sym} & & -\omega^2 + \frac{2}{3} c_{m3}^2 k^2 + \omega_p^2 \end{pmatrix} \begin{pmatrix} \gamma_1 \\ \gamma_2 \\ \gamma_3 \end{pmatrix} = 0. \quad (\text{IV.17})$$

Analogously considering

$$\text{diag}_2 = \begin{pmatrix} \sqrt{\rho} & 0 & 0 \\ 0 & i\sqrt{2\eta_1} & 0 \\ 0 & 0 & i\sqrt{2\eta_2} \end{pmatrix}, \quad (\text{IV.18})$$

we obtain $\bar{A}_2(\omega, k) = \bar{A}_3(\omega, k) = \text{diag}_2 \cdot A_2(\omega, k) \cdot \text{diag}_2^{-1}$

$$\bar{A}_2(\omega, k) = \bar{A}_3(\omega, k) = \begin{pmatrix} -\omega^2 \left(1 + k^2 \frac{\bar{\eta}_1 + \bar{\eta}_2}{2\rho}\right) + c_s^2 k^2 & k \sqrt{2} \mu_e / \sqrt{\rho\eta_1} & -k \sqrt{2} \mu_c / \sqrt{\rho\eta_2}, \\ & -\omega^2 + \frac{1}{2} c_{m1}^2 k^2 + \omega_s^2 & \frac{1}{2} c_{m1} c_{m2} k^2 \\ \text{sym} & & -\omega^2 + \frac{1}{2} c_{m2}^2 k^2 + \omega_r^2 \end{pmatrix}. \quad (\text{IV.19})$$

In order to have non-trivial solutions of the algebraic systems (IV.14), one must impose that

$$\det \bar{A}_1(\omega, k) = 0, \quad \det \bar{A}_2(\omega, k) = \det \bar{A}_3(\omega, k) = 0, \quad \det A_4(\omega, k) = 0, \quad (\text{IV.20})$$

the solution of which allows to determine the so-called dispersion relations $\omega = \omega(k)$ for longitudinal and transverse waves in the relaxed micromorphic continuum, see Section IV.1.3. The solutions of the eigenvalue problem obtained via the proposed decomposition are the same as the ones obtained via the standard formulation shown in the Appendix D.4 with the full 12×12 matrix, for more details see [50]. For estimates on the isotropic moduli, we refer to [131, 132] and, for a comparison with other micromorphic models, to [137, 138].

For solutions $\omega = \omega(k)$ of (IV.20) we define the

$$\text{phase velocity: } v = \frac{\omega}{k}, \quad \text{group velocity: } c = \frac{d\omega(k)}{dk}. \quad (\text{IV.21})$$

Real wave numbers $k \in \mathbb{R}$ correspond to propagating waves, while complex values of k are associated with waves whose amplitude either grows or decays along the coordinate X . In linear elasticity, phase velocity and group velocity coincide since there is no dispersion and both are real, see Appendix D.1.

Generalization for the full anisotropic case In the case of anisotropy, the equation of motion is (III.23) (instead of Equation (III.26)):

$$\rho u_{,tt} - \rho \widehat{L}_c^2 \text{Div} [\mathbb{J}_{g0} \nabla u_{,tt}] = \text{Div} [\tilde{\sigma}], \quad \rho \widehat{L}_c^2 \mathbb{J}_{m0} P_{,tt} = \tilde{\sigma} - s - \text{Curl } m, \quad (\text{IV.22})$$

where

$$\begin{aligned} \tilde{\sigma} &= \mathbb{C}_e \text{sym}(\nabla u - P) + \mathbb{C}_c \text{skew}(\nabla u - P), & s &= \mathbb{C}_m \text{sym } P, \\ m &= \mu L_c^2 \bar{\mathbb{L}}_{\text{aniso}} \text{Curl } P. \end{aligned} \quad (\text{IV.23})$$

Assuming again plane harmonic waves, we have:

$$\begin{aligned} u(x, t) &= \widehat{u} e^{i(k\langle \xi, x \rangle_{\mathbb{R}^3} - \omega t)}, & \widehat{u} &\in \mathbb{C}^3, & \|\xi\|^2 &= 1, \\ P(x, t) &= \widehat{P} e^{i(k\langle \xi, x \rangle_{\mathbb{R}^3} - \omega t)}, & \widehat{P} &\in \mathbb{C}^{3 \times 3}, \end{aligned} \quad (\text{IV.24})$$

where \hat{u} is the polarization vector and \hat{P} is the polarization matrix. In the anisotropic case, the vector ξ cannot be specified without losing generality and the dispersion curves will, therefore, depend on the direction defined via the vector ξ . With this hypothesis, the system (IV.22) can be written as a linear system in $\hat{\beta} := (\hat{u}, \hat{P}) \in \mathbb{C}^{12}$ as:

$$\hat{A}(\xi, \omega, k) \cdot \hat{\beta} = 0., \quad (\text{IV.25})$$

where \hat{A} is a 12×12 tensor. To have non-trivial solutions of the algebraic systems (IV.25), one must impose that

$$\det \hat{A}(\xi, \omega, k) = 0. \quad (\text{IV.26})$$

This is the generalization of conditions (IV.20) for the anisotropic case. The various solutions of this equation give the branches of the dispersion curves. It must be noted that a decomposition of \hat{A} in sub-matrices is obtainable only for particular energies and/or directions ξ .

1.2 Necessary and sufficient conditions for real wave propagation

Investigations of real wave propagation and ellipticity are not new in principle. Indeed, it is textbook knowledge for linear elasticity that positive definiteness of the elastic energy implies real wave velocities (phase velocities) $v = \omega/k$ where ω [rad/s] is the angular frequency and k [rad/m] $\in \mathbb{R}$ is the wavenumber of planar propagating waves. In classical elasticity, having real wave velocities is equivalent to rank-one convexity (strong ellipticity or Legendre-Hadamard ellipticity). Moreover, ellipticity is equivalent to the positive definiteness of the acoustic tensor. For anisotropic linear elasticity we mention [41], while for anisotropic nonlinear elasticity we refer the reader to [10, 152, 205, 207].

The same question of ellipticity and real wave velocities in enriched continuum mechanics has been discussed for micropolar models, e.g. in [211] and for elastic materials with voids in [42]. For the isotropic micromorphic model results can be found with respect to positive definite energy and/or real wave velocity [185, 212], Mindlin [155, 156] and Eringen's book [67, pp. 277-280]. These latter results present conditions which are neither easily verifiable nor are truly transparent. This is due to the very high number of material coefficients of the Eringen-Mindlin theory that are strongly reduced in the relaxed micromorphic model [150]. Indeed, the implication that positive definiteness of the energy always implies real wave velocities is not directly established and demonstrated. In this chapter, we investigate the relaxed micromorphic model in terms of conditions for real wave velocities for plane waves and establish a necessary and sufficient condition for this to happen.

We present a set of necessary and sufficient conditions for real wave-velocities in the relaxed micromorphic model which is weaker than positivity of the energy, as the strong ellipticity condition is with respect to positive definiteness of the energy in the case of linear elasticity.

Since we are only interested in real k (outside the band gap region), the wave velocity (phase velocity) is real if and only if ω is real.

In what follows, we will consider the isotropic case with vanishing gradient micro-inertia. The case with non-vanishing micro-inertia could be readily obtained considering that the "effective" macroscopic inertiae $\rho_l = \rho \left(1 + k^2 \frac{2\bar{\eta}_1 + \bar{\eta}_3}{3\rho}\right)$ and $\rho_t = \rho \left(1 + k^2 \frac{\bar{\eta}_1 + \bar{\eta}_2}{2\rho}\right)$ replace the macroscopic inertia ρ in the matrices and the parameters' definition for longitudinal and transverse waves, respectively. These "effective" inertiae are positive for every k and are always bigger than ρ ; therefore, all the obtained results are to be considered general. However, considering the vanishing gradient micro-inertia, the matrices become:

$$\bar{A}_1(\omega, k) = \begin{pmatrix} -\omega^2 + c_p^2 k^2 & \frac{2\sqrt{6}}{3} k \mu_e / \sqrt{\rho\eta_1} & \frac{\sqrt{3}}{3} k (2\mu_e + 3\lambda_e) / \sqrt{\rho\eta_3} \\ & -\omega^2 + \frac{1}{3} c_{m1}^2 k^2 + \omega_s^2 & -\frac{\sqrt{2}}{3} k^2 c_{m1} c_{m3} \\ \text{sym} & & -\omega^2 + \frac{2}{3} k^2 c_{m3}^2 + \omega_p^2 \end{pmatrix}, \quad (\text{IV.27})$$

$$\bar{A}_2(\omega, k) = \bar{A}_3(\omega, k) = \begin{pmatrix} -\omega^2 + c_s^2 k^2 & k \sqrt{2} \mu_e / \sqrt{\rho \eta_1} & -k \sqrt{2} \mu_c / \sqrt{\rho \eta_2}, \\ & -\omega^2 + \frac{1}{2} c_{m1}^2 k^2 + \omega_s^2 & \frac{1}{2} k^2 c_{m1} c_{m2} \\ \text{sym} & & -\omega^2 + \frac{1}{2} c_{m2}^2 k^2 + \omega_r^2 \end{pmatrix}. \quad (\text{IV.28})$$

Since ω^2 appears on the diagonal only, the problem (IV.20) can be analogously expressed as an eigenvalue-problem:

$$\begin{aligned} \det (B_1(k) - \omega^2 \mathbf{1}) &= 0, & \det (B_2(k) - \omega^2 \mathbf{1}) &= 0, \\ \det (B_3(k) - \omega^2 \mathbf{1}) &= 0, & \det (B_4(k) - \omega^2 \mathbf{1}) &= 0, \end{aligned} \quad (\text{IV.29})$$

where

$$B_1(k) = \begin{pmatrix} c_p^2 k^2 & \frac{2\sqrt{6}}{3} k \mu_e / \sqrt{\rho \eta_1} & \frac{\sqrt{3}}{3} k (2 \mu_e + 3 \lambda_e) / \sqrt{\rho \eta_3} \\ & \frac{1}{3} c_{m1}^2 k^2 + \omega_s^2 & -\frac{\sqrt{2}}{3} k^2 c_{m1} c_{m3} \\ \text{sym} & & \frac{2}{3} k^2 c_{m3}^2 + \omega_p^2 \end{pmatrix}, \quad (\text{IV.30})$$

$$B_2(k) = B_3(k) = \begin{pmatrix} c_s^2 k^2 & k \sqrt{2} \mu_e / \sqrt{\rho \eta_1} & -k \sqrt{2} \mu_c / \sqrt{\rho \eta_2}, \\ & \frac{1}{2} c_{m1}^2 k^2 + \omega_s^2 & \frac{1}{2} k^2 c_{m1} c_{m2} \\ \text{sym} & & \frac{1}{2} c_{m2}^2 k^2 + \omega_r^2 \end{pmatrix}, \quad (\text{IV.31})$$

$$B_4(k) = \begin{pmatrix} c_{m1}^2 k^2 + \omega_s^2 & 0 & 0 \\ & c_{m2}^2 k^2 + \omega_r^2 & 0 \\ \text{sym} & & c_{m1}^2 k^2 + \omega_s^2 \end{pmatrix}. \quad (\text{IV.32})$$

Note that $B_1(k)$, $B_2(k)$, $B_3(k)$ and $B_4(k)$ are real symmetric matrices and, therefore, the resulting eigenvalues ω^2 are real. Obtaining real wave velocities is tantamount to having $\omega^2 \geq 0$ for all solutions of (IV.29).

Since it is useful in what follows we explicitly remark that:

$$2 \mu_e + \lambda_e = \frac{4}{3} \mu_e + \frac{2 \mu_e + 3 \lambda_e}{3} = \frac{4}{3} \mu_e + \kappa_e = \frac{4 \mu_e + 3 \kappa_e}{3}, \quad 2 \mu_m + \lambda_m = \frac{4 \mu_m + 3 \kappa_m}{3}. \quad (\text{IV.33})$$

With these relations, it is easy to show how $\mu_e > 0$ and $\kappa_e > 0$ imply $2 \mu_e + \lambda_e > 0$. Moreover, as shown in the appendix (equations (D.48) and (D.49)), we note here that if only $\mu_e + \mu_m > 0$ and $\kappa_e + \kappa_m > 0$, then the macroscopic parameters are less or equal than respective microscopic parameters, namely:

$$\kappa_e \geq \kappa_M, \quad \kappa_m \geq \kappa_M, \quad \mu_e \geq \mu_M, \quad \mu_m \geq \mu_M, \quad (\text{IV.34})$$

and, moreover, the following inequalities are satisfied:

$$2 \mu_e + \lambda_e \geq 2 \mu_M + \lambda_M, \quad 2 \mu_m + \lambda_m \geq 2 \mu_M + \lambda_M, \quad \frac{4 \mu_M + 3 \kappa_e}{3} \geq 2 \mu_M + \lambda_M. \quad (\text{IV.35})$$

Note that the Cosserat couple modulus μ_c [170] does not appear in the introduced scale between micro and macro.

We will show next that all the eigenvalues ω^2 of $B_1(k)$, $B_2(k)$ and $B_3(k)$ are real and positive for every $k \neq 0$ and non-negative for $k = 0$ provided certain conditions on the material coefficients are satisfied.

Sufficient conditions for real longitudinal wave propagation ($k \neq 0$): Sylvester's criterion states that a Hermitian matrix M is positive-definite if and only if the leading principal minors are positive [81]. For the matrix B_1 the three principal minors are:

$$(B_1)_{11} = \frac{2\mu_e + \lambda_e}{\rho}, \quad (IV.36)$$

$$\begin{aligned} (\text{Cof } (B_1))_{33} &= \frac{k^2}{3\eta_1 \rho} [6(2\mu_e + \lambda_e)\mu_m + 6\mu_e \kappa_e + (2\mu_e + \lambda_e)\mu L_c^2 k^2] \\ &= \frac{k^2}{3\eta_1 \rho} [2(4\mu_M + 3\kappa_e)(\mu_e + \mu_m) + (2\mu_e + \lambda_e)\mu L_c^2 k^2], \end{aligned} \quad (IV.37)$$

$$\begin{aligned} \det(B_1) &= \frac{k^2}{\eta_1 \eta_3 \rho} \left[6\kappa_e \kappa_m (\mu_e + \mu_m) + 8\mu_e \mu_m (\kappa_e + \kappa_m) + (2\mu_e + \lambda_e)(2\mu_m + \lambda_m)\mu L_c^2 k^2 \right] \\ &= \frac{k^2}{\eta_1 \eta_3 \rho} \left[6(\kappa_e + \kappa_m)(\mu_e + \mu_m)(2\mu_M + \lambda_M) + (2\mu_e + \lambda_e)(2\mu_m + \lambda_m)\mu L_c^2 k^2 \right]. \end{aligned} \quad (IV.38)$$

The three principal minors of B_1 are clearly positive for $k \neq 0$ if⁴:

$$\begin{aligned} \mu_e > 0, & \quad \mu_m > 0, & \quad \kappa_e + \kappa_m > 0, & \quad 2\mu_M + \lambda_M > 0, \\ 4\mu_M + 3\kappa_e > 0, & \quad 2\mu_e + \lambda_e > 0, & \quad 2\mu_m + \lambda_m > 0. \end{aligned} \quad (IV.39)$$

Sufficient conditions for transverse wave propagation ($k \neq 0$): Similarly, for the matrix $B_2(k) = B_3(k)$ the three principal minors are:

$$(B_2)_{11} = \frac{\mu_e + \mu_c}{\rho}, \quad (IV.40)$$

$$(\text{Cof } (B_2))_{33} = \frac{k^2}{2\eta_1 \rho} \left[4(\mu_e \mu_c + \mu_m(\mu_e + \mu_c) + (\mu_e + \mu_c)\mu L_c^2 k^2) \right]. \quad (IV.41)$$

$$\det(B_2) = \frac{k^2}{\eta_1 \eta_2 \rho} \left[4\mu_m \mu_c \mu_e + (\mu_e + \mu_c)\mu_m \mu L_c^2 k^2 \right]. \quad (IV.42)$$

Considering positive η , ρ and separating terms in the brackets by looking at large and small values of k , we can state *necessary* and *sufficient* conditions for strict positive-definiteness of $B_2(k)$ at arbitrary $k \neq 0$:

$$\mu_e > 0, \quad \mu_m > 0, \quad \mu_c \geq 0. \quad (IV.43)$$

Sufficient conditions for real uncoupled wave propagation ($k \neq 0$): Since $B_4(k)$ is diagonal, it is easy to show that positive definiteness is tantamount to the set of *necessary* and *sufficient* conditions for $k \neq 0$:

$$\mu_e > 0, \quad \mu_e + \mu_m > 0, \quad \mu_c \geq 0. \quad (IV.44)$$

Sufficient conditions for real wave propagation ($k = 0$): Considering the case $k = 0$, we see that the matrices reduce to:

$$B_1(0) = \begin{pmatrix} 0 & 0 & 0 \\ 0 & \omega_s^2 & 0 \\ 0 & 0 & \omega_p^2 \end{pmatrix}, \quad B_2(0) = B_3(0) = \begin{pmatrix} 0 & 0 & 0 \\ 0 & \omega_s^2 & 0 \\ 0 & 0 & \omega_r^2 \end{pmatrix}, \quad B_4(0) = \begin{pmatrix} \omega_s^2 & 0 & 0 \\ 0 & \omega_r^2 & 0 \\ 0 & 0 & \omega_s^2 \end{pmatrix}. \quad (IV.45)$$

Since the matrices are diagonal for $k = 0$, we can show that positive semi-definiteness is tantamount to the set of *necessary* and *sufficient* conditions :

$$\mu_e \geq 0, \quad \mu_e + \mu_m \geq 0, \quad \mu_c \geq 0, \quad \kappa_e + \kappa_m \geq 0. \quad (IV.46)$$

⁴We note here that $4\mu_M + 3\kappa_e > 0 \iff 2\mu_e + \lambda_e > \frac{4}{3}(\mu_e - \mu_M) \iff 2\mu_M + \lambda_M > \kappa_M - \kappa_e$. Furthermore, if $\mu_e + \mu_m > 0$ and $\kappa_e + \kappa_m > 0$, we have $3(2\mu_e + \lambda_e) \geq 4\mu_M + 3\kappa_e \geq \frac{4}{3}(2\mu_M + \lambda_M)$, see Appendix.

Sufficient conditions for real wave propagation: Considering all the conditions found until now, we can state a simple *sufficient* condition for real wave velocities for all real k :

$$\begin{aligned} \mu_e > 0, & \quad \mu_m > 0, & \quad \kappa_e + \kappa_m > 0, & \quad 2\mu_M + \lambda_M > 0, & \quad (IV.47) \\ 4\mu_M + 3\kappa_e > 0, & \quad 2\mu_e + \lambda_e > 0, & \quad 2\mu_m + \lambda_m > 0. \end{aligned}$$

Necessary conditions for real wave propagation: In order to see a set of global necessary conditions for positivity at arbitrary $k \neq 0$ we consider first large and small values of $k \neq 0$ separately. For $k \rightarrow +\infty$ we must have:

$$2\mu_e + \lambda_e > 0, \quad (2\mu_e + \lambda_e)\mu L_c^2 > 0, \quad (2\mu_e + \lambda_e)(2\mu_m + \lambda_m)\mu L_c^2 > 0, \quad (IV.48)$$

or analogously:

$$2\mu_e + \lambda_e > 0, \quad \mu L_c^2 > 0, \quad 2\mu_m + \lambda_m > 0, \quad (IV.49)$$

while for $k \rightarrow 0$ we must have:

$$2\mu_e + \lambda_e > 0, \quad (4\mu_M + 3\kappa_e)(\mu_e + \mu_m) > 0, \quad (\kappa_e + \kappa_m)(\mu_e + \mu_m)(2\mu_M + \lambda_M) > 0. \quad (IV.50)$$

Since from (IV.43) we have necessarily $\mu_e > 0$, $\mu_m > 0$, and from (IV.46) we get $\kappa_e + \kappa_m \geq 0$ and considering together the two limits for k we obtain the necessary condition:

$$\begin{aligned} 2\mu_e + \lambda_e > 0, & \quad 2\mu_m + \lambda_m > 0, & \quad 4\mu_M + 3\kappa_e > 0, & \quad \kappa_e + \kappa_m > 0, & \quad (IV.51) \\ \mu_e > 0, & \quad \mu_m > 0, & \quad \mu_c \geq 0, & \quad 2\mu_M + \lambda_M > 0. \end{aligned}$$

Inspection shows that (IV.51) is our proposed sufficient condition (IV.39). From $\mu_e > 0$ and $\mu_m > 0$, it follows that $\mu_M > 0$. Therefore condition (IV.51) is *necessary* and *sufficient*. We have shown our main proposition:

Proposition (real wave velocities). *The dynamic relaxed micromorphic model (eq. (IV.3)) admits real plane waves if and only if*

$$\begin{aligned} \mu_c \geq 0, & \quad \mu_e > 0, & \quad 2\mu_e + \lambda_e > 0, & \quad (IV.52) \\ & \quad \mu_m > 0, & \quad 2\mu_m + \lambda_m > 0, \\ & \quad (\mu_M > 0), & \quad 2\mu_M + \lambda_M > 0, \\ & \quad \kappa_e + \kappa_m > 0, & \quad 4\mu_M + 3\kappa_e > 0. \quad \blacksquare \end{aligned}$$

In (IV.52) the requirement $\mu_M > 0$ is redundant, since it is already assumed that $\mu_e, \mu_m > 0$. It is clear that positive definiteness of the elastic energy (III.9) implies (IV.52). We remark that, as shown in the Appendix D.3, the set of inequalities (IV.52) is already implied by:

$$\boxed{\mu_e > 0, \quad \mu_m > 0, \quad \mu_c \geq 0, \quad \kappa_e + \kappa_m > 0, \quad 2\mu_M + \lambda_M > 0.} \quad (IV.53)$$

Finally, letting $\mu_m \rightarrow +\infty$ and $\kappa_m \rightarrow +\infty$ (or $\mu_m \rightarrow +\infty$ and $\lambda_m > \text{const.}$) generates the limit condition for real wave velocities ($\mu_e \rightarrow \mu_M$)

$$\mu_M > 0, \quad \mu_c \geq 0, \quad 2\mu_M + \lambda_M > 0. \quad (IV.54)$$

which coincides, up to μ_c , with the strong ellipticity condition in isotropic linear elasticity, see Appendix D.1, and it coincides fully with the condition for real wave velocities in micropolar elasticity, see Appendix D.2. A condition similar to (IV.54) can be found in [155, eq. 8.14 p. 26] where Mindlin requires that $\mu_M > 0$, $2\mu_M + \lambda_M > 0^5$ (in our notation) which are obtained from the requirement of positive *group velocity* at $k = 0$

$$\frac{d\omega_{\text{acoustic, long}}(0)}{dk} > 0, \quad \frac{d\omega_{\text{acoustic, trans}}(0)}{dk} > 0. \quad (IV.55)$$

Let us emphasize that our method is not easily generalized to the anisotropic setting [12]. In this case, the block-structure of the problem will be lost and one has to deal with the full 12×12 case, see equation (D.69) in the Appendix D.4. Nonetheless, we expect positive-definiteness to always imply real wave propagation.

⁵Mindlin explains that such parameters “are less than those that would be calculated from the strain-stiffnesses [of the unit cell]. This phenomenon is due to the compliance of the unit cell and has been found in a theory of crystal lattices by Gazis and Wallis [77]”.

1.3 Dispersion curves for the relaxed micromorphic model

It is clear that the study of dispersion relations for the relaxed micromorphic continuum is intrinsically more complicated than in the case of classical Cauchy continuum due to its enriched kinematics. For the relaxed micromorphic model, the formal limit $\eta \rightarrow +\infty$ shows no dispersion at all giving two pseudo-acoustic linear curves, longitudinal and transverse with slopes $c_p = \sqrt{(2\mu_e + \lambda_e)/\rho}$ and $c_s = \sqrt{(\mu_e + \mu_c)/\rho}$, respectively.

As far as longitudinal and transverse waves are concerned, the expressions for the wave-numbers k which allow for non-trivial solutions are by far more complicated. We refer to [141] for the complete set-up of the eigenvalue problems which must be solved to find the explicit expressions for the wave-numbers, limiting ourselves here to denote them by $\pm k_1^1, \pm k_1^2$ for longitudinal waves and $\pm k_\alpha^1, \pm k_\alpha^2, \alpha = 2, 3$ for transverse waves. Of course, the computed expressions for $k_1^1, k_1^2, k_\alpha^1, k_\alpha^2$ depend on the elastic constitutive parameters of the relaxed micromorphic model appearing in (IV.1) and on the frequency ω .

1.3.1 Longitudinal waves

We present the longitudinal *dispersion relations* obtained with both vanishing and non-vanishing gradient micro-inertia (Figure 36). The dispersion curves for longitudinal waves consist in one acoustic branch LA and two optic branches LO₁-LO₂. This is made clear after considering the corresponding cut-off frequencies⁶:

$$\omega_{\text{LA}}(0) = 0, \quad \omega_{\text{LO}_1}(0) = \omega_p = \sqrt{\frac{(3\lambda_e + 2\mu_e) + (3\lambda_m + 2\mu_m)}{\eta_3}}, \quad \omega_{\text{LO}_2}(0) = \omega_s = \sqrt{\frac{2(\mu_e + \mu_m)}{\eta_1}}. \quad (\text{IV.56})$$

The case $k = 0$ corresponds to the long wave-length limit. As proven in general in chapter III.3, in the long wave-length limit the relaxed micromorphic model tends to a Cauchy material with constitutive tensor \mathbb{C}_M . This is confirmed by the group velocity $c_{\text{LA}} = \partial\omega_{\text{LA}}/\partial k$ in $k = 0$ of the acoustic branch of the longitudinal dispersion curves that, as in the Cauchy model, is⁷:

$$c_{\text{LA}}(0) = \sqrt{\frac{2\mu_M + \lambda_M}{\rho}}. \quad (\text{IV.57})$$

To study the asymptotic behavior of the dispersion curves, it is better to consider first the case with vanishing gradient micro-inertia ($\bar{\eta}_1 = \bar{\eta}_2 = \bar{\eta}_3 = 0$). In this case the longitudinal acoustic branch has a horizontal

⁶The cut-off frequencies for longitudinal waves can easily be obtained by solving the problem for $k = 0$, i.e. $\det \bar{A}_1(\omega, 0) = 0$. Analogously, the problem $\det \bar{A}_2(\omega, 0) = 0$ must be considered for transverse waves.

⁷The group velocity c_{LA} of the acoustic longitudinal curve for $k = 0$ can be derived via the equation $\frac{\partial^2}{\partial^2 k} (\det \bar{A}_1(\omega(k), k))|_{k=0} = 0$, as made in [50]. Analogously, the equation $\frac{\partial^2}{\partial^2 k} (\det \bar{A}_2(\omega(k), k))|_{k=0} = 0$ must be solved in the transverse case.

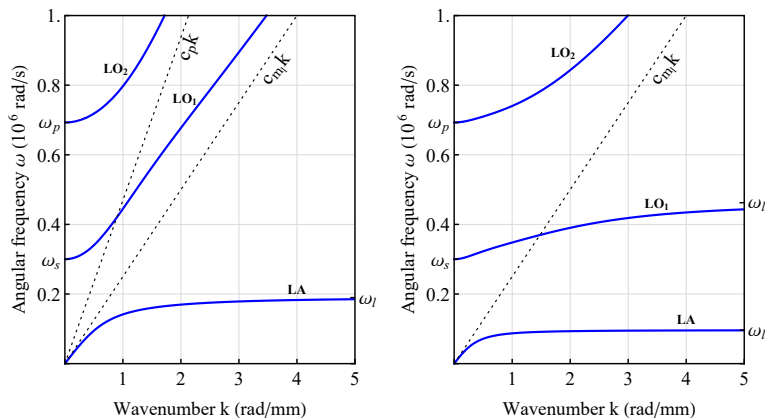


Figure 36: Dispersion relations for longitudinal waves in the *relaxed micromorphic model* with vanishing micro-inertia (left) and non-vanishing micro-inertia (right).

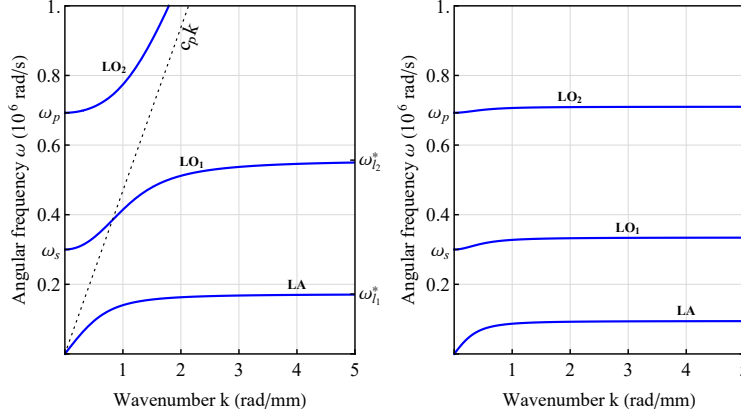


Figure 37: Dispersion relations for longitudinal waves in the *internal variable model* with vanishing micro-inertia (left) and non-vanishing micro-inertia (right).

asymptote, while both the optic branches have an oblique asymptote for $k \rightarrow +\infty$:

$$\omega_{LA} \sim \omega_l = \sqrt{\frac{3(2\mu_m + \lambda_m)}{2\eta_1 + \eta_3}}, \quad \omega_{LO_1} \sim c_{m1} k = \sqrt{\frac{c_{m1}^2 + 2c_{m3}^2}{3}} k, \quad \omega_{LO_2} \sim c_p k. \quad (\text{IV.58})$$

On the other hand, if the gradient micro-inertia is present, the second optic branch keeps its oblique asymptote, while the acoustic and the first optic branch have coupled horizontal asymptotes for $k \rightarrow +\infty$:

$$\omega_{LA} \sim \omega_{l_1} = \sqrt{\frac{\omega_l^2 + \omega_v^2 - \sqrt{(\omega_l^2 + \omega_v^2)^2 - 4\omega_l^2 \omega_l^2}}{2}}, \quad \omega_{LO_1} \sim \omega_{l_2} = \sqrt{\frac{\omega_l^2 + \omega_v^2 + \sqrt{(\omega_l^2 + \omega_v^2)^2 - 4\omega_l^2 \omega_l^2}}{2}}, \quad (\text{IV.59})$$

$$\omega_{LO_2} \sim c_{m1} k.$$

where we have:

$$\omega_l = \sqrt{\frac{3(2\mu_m + \lambda_m)}{2\eta_1 + \eta_3}}, \quad \omega_{\bar{l}} = \sqrt{\frac{3(2\mu_e + \lambda_e)}{2\bar{\eta}_1 + \bar{\eta}_3}}, \quad \omega_v = \sqrt{\frac{3(2\mu_e + \lambda_e) + 3(2\mu_m + \lambda_m)}{2\eta_1 + \eta_3}}. \quad (\text{IV.60})$$

The limiting case of the internal variable model Considering the limiting case in which the length scale L_c vanishes, the relaxed micromorphic model reduces to an internal variable model. Considering a vanishing gradient micro-inertia we obtain one more horizontal asymptote with respect to the relaxed micromorphic model leading to the asymptotic behavior:

$$\omega_{LA} \sim \omega_{l_1}^* = \sqrt{a_l - \sqrt{a_l^2 - b_l^2}}, \quad \omega_{LO_1} \sim \omega_{l_2}^* = \sqrt{a_l + \sqrt{a_l^2 - b_l^2}}, \quad \omega_{LO_2} \sim c_p k, \quad (\text{IV.61})$$

in which:

$$a_l = \frac{2\mu_e}{\eta_1} \frac{3\kappa_e}{\eta_3} \frac{2\eta_1 + \eta_3}{3(\lambda_e + 2\mu_e)} + \frac{\mu_m}{\eta_1} + \frac{3\kappa_m}{2\eta_3}, \quad b_l^2 = \frac{2\mu_e}{\eta_1} \frac{3\kappa_e}{\eta_3} \frac{\lambda_m + 2\mu_m}{\lambda_e + 2\mu_e} + 4 \frac{\mu_m}{\eta_1} \frac{3\kappa_m}{2\eta_3}. \quad (\text{IV.62})$$

The internal variable model with non-vanishing gradient micro-inertia has three horizontal asymptotes whose analytic expressions are too complex to be written.

1.3.2 Transverse waves

The dispersion curves for transverse waves consist of one acoustic branch TA and two optic branches TO₁-TO₂ (see Figure 38). The corresponding cut-off frequencies are:

$$\omega_{TA}(0) = 0, \quad \omega_{TO_1}(0) = \omega_r = \sqrt{\frac{2\mu_c}{\eta_2}}, \quad \omega_{TO_2}(0) = \omega_s = \sqrt{\frac{2(\mu_e + \mu_m)}{\eta_1}}. \quad (\text{IV.63})$$

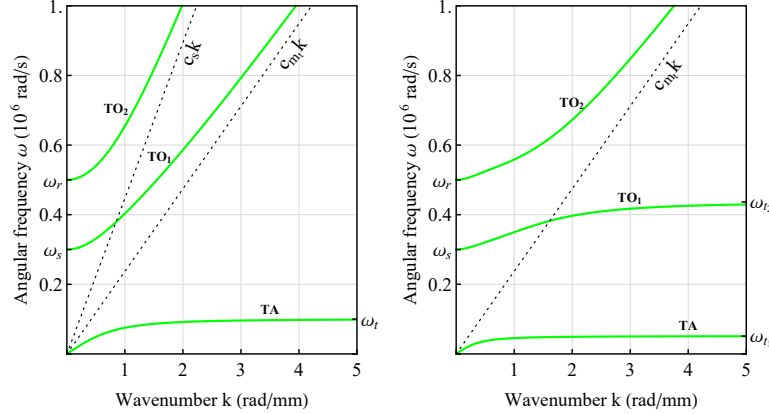


Figure 38: Dispersion relations for transverse waves in the *relaxed micromorphic model* with vanishing micro-inertia (left) and non-vanishing micro-inertia (right).

Once again the case $k = 0$ corresponds to the long wave-length limit. The group velocity $c_{TA} = \partial\omega_{TA}/\partial k$ in $k = 0$ of the acoustic branch of the transverse dispersion curves is equivalent to the Cauchy model (see footnote 7):

$$c_{TA}(0) = \sqrt{\frac{\mu_M}{\rho}}. \quad (\text{IV.64})$$

To study the asymptotic behavior of the dispersion curves, it is better to consider first the case with vanishing gradient micro-inertia ($\bar{\eta}_1 = \bar{\eta}_2 = \bar{\eta}_3 = 0$). In this case the transverse acoustic branch has a horizontal asymptote, while both optic branches have an oblique asymptote for $k \rightarrow +\infty$:

$$\omega_{TA} \sim \omega_t = \sqrt{\frac{2\mu_m}{\eta_1 + \eta_2}}, \quad \omega_{TO_1} \sim c_{mt} k = \sqrt{\frac{c_{m1}^2 + c_{m2}^2}{2}} k, \quad \omega_{TO_2} \sim c_s k. \quad (\text{IV.65})$$

On the other hand, if the gradient micro-inertia is present, the second optic branch keeps its oblique asymptote, while the acoustic and the first optic branch have coupled horizontal asymptotes for $k \rightarrow +\infty$:

$$\omega_{TA} \sim \omega_{t_1} = \sqrt{\frac{\omega_t^2 + \omega_q^2 - \sqrt{(\omega_t^2 + \omega_q^2)^2 - 4\omega_t^2 \omega_q^2}}{2}}, \quad \omega_{TO_1} \sim \omega_{t_2} = \sqrt{\frac{\omega_t^2 + \omega_q^2 + \sqrt{(\omega_t^2 + \omega_q^2)^2 - 4\omega_t^2 \omega_q^2}}{2}}, \quad (\text{IV.66})$$

$$\omega_{TO_2} \sim c_{m_t} k,$$

where:

$$\omega_t = \sqrt{\frac{2\mu_m}{\eta_1 + \eta_2}}, \quad \omega_{\bar{t}} = \sqrt{\frac{2(\mu_c + \mu_e)}{\bar{\eta}_1 + \bar{\eta}_2}}, \quad \omega_q = \sqrt{\frac{2(\mu_e + \mu_m + \mu_c)}{\eta_1 + \eta_2}}. \quad (\text{IV.67})$$

The limiting case of the internal variable model Considering the limiting case in which the length scale L_c vanishes, the relaxed micromorphic model reduces to an internal variable model. Assuming a vanishing gradient micro-inertia, we obtain one more horizontal asymptote with respect to the relaxed micromorphic model leading to the asymptotic behavior:

$$\omega_{LA} \sim \omega_{t_1}^* = \sqrt{a_t - \sqrt{a_t^2 - b_t^2}}, \quad \omega_{TO_1} \sim \omega_{t_2}^* = \sqrt{a_t + \sqrt{a_t^2 - b_t^2}}, \quad \omega_{TO_2} \sim c_s k, \quad (\text{IV.68})$$

in which:

$$a_t = \frac{\mu_c \mu_e + \mu_c \mu_m + \mu_e \mu_m}{\eta_1 (\mu_c + \mu_e)} + \frac{\mu_c \mu_e}{\eta_2 (\mu_c + \mu_e)}, \quad b_t^2 = \frac{4\mu_c \mu_e \mu_m}{\eta_1 \eta_2 (\mu_c + \mu_e)}. \quad (\text{IV.69})$$

The internal variable model with non-vanishing gradient micro-inertia shows three horizontal asymptotes whose analytical expressions are too complex to be written.

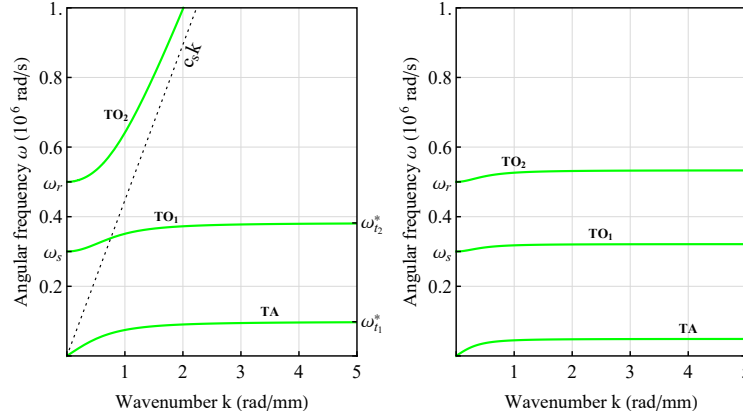


Figure 39: Dispersion relations for transverse waves in the *internal variable model* with vanishing micro-inertia (left) and non-vanishing micro-inertia (right).

1.3.3 Uncoupled waves

Considering the solutions of the uncoupled equations, we obtain three dispersion curves: the transverse rotational optic TRO, the transverse shear optic TSO and the transverse constant-volume optic TCVO. In the papers [139–141], it was explicitly pointed out that the frequency ω for uncoupled waves in relaxed micromorphic continua can be calculated as a function of the wave-numbers k . These relations can be easily inverted to find ω as a function of k , finding that they do not depend on the presence or lack of a gradient micro-inertia. Indeed, we obtain:

$$\begin{aligned} \omega_{\text{TSO}} &= \sqrt{\omega_s^2 + c_{m1}^2 k^2}, & \omega_{\text{TRO}} &= \sqrt{\omega_r^2 + c_{m2}^2 k^2}, & \omega_{\text{TCVO}} &= \sqrt{\omega_s^2 + c_{m1}^2 k^2}, & (\text{IV.70}) \\ k &= \frac{1}{c_{m1}} \sqrt{\omega^2 - \omega_s^2}, & k &= \frac{1}{c_{m2}} \sqrt{\omega^2 - \omega_r^2}, & k &= \frac{1}{c_{m1}} \sqrt{\omega^2 - \omega_s^2}. \end{aligned}$$

In the limiting case of the internal variable model, the velocities c_{m1} and c_{m2} are zero leading to constant frequencies for every k :

$$\omega_{\text{TSO}} = \omega_s, \quad \omega_{\text{TRO}} = \omega_r, \quad \omega_{\text{TCVO}} = \omega_s. \quad (\text{IV.71})$$

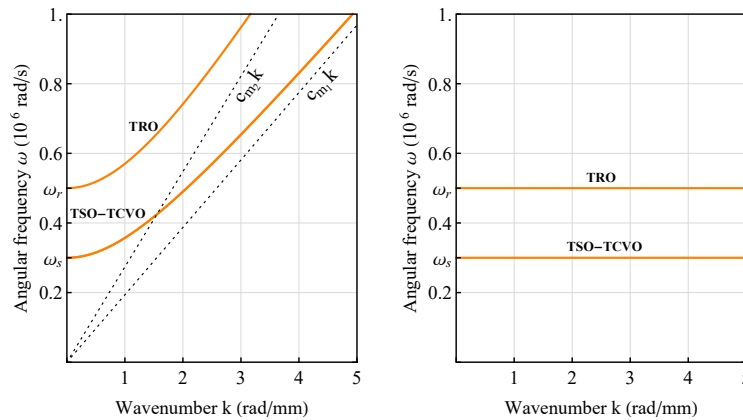


Figure 40: Dispersion relations for the uncoupled waves in the *relaxed micromorphic model* (left) and in the *internal variable model* (right).

CHAPTER IV.2

Dispersion curves and band-gaps in other enriched continuum models

Classical Cauchy continuum theories are not always well adapted to cover the wealth of experimental evidences on the dynamical behavior of real materials. As a first point, in fact, real materials commonly show dispersive behaviors, which means that the speed of propagation of the traveling wave changes with the wavelength. Such a phenomenon is not astonishing if one thinks that the structure of matter changes when observing it at smaller scales: at the scale of crystals or molecules there is always some heterogeneity of matter. For this reason, considering wavelengths small enough to interact with the microstructure, the waves will propagate at a different speed than other waves with higher wavelengths. Cauchy continuum theories are not able to account for dispersive phenomena and are a good approximation of reality only for those materials which do not exhibit their heterogeneity at the scale of interest. Therefore, Cauchy continuum theories are not adapted to model dispersive behaviors and more refined models need to be introduced. One possibility is second or higher order theories that allow for the description of dispersion for the acoustic modes (see e.g. [55,197]). On the one hand, second gradient theories describe some dispersive behaviors but, on the other hand, they are often insufficient for microstructures that have vibrational modes independent of the motion of the unit cell. To describe the complex dynamical behavior of such metamaterials in a continuum framework, the introduction of enriched kinematics (as in the relaxed micromorphic models in Figure 41) is a mandatory requirement [67,138–140,155]. Continuum models of the micromorphic type, in fact, allow for the description of microstructure-related vibrational modes via degrees of freedom additional to the displacement field.

The curvature contribution in the micromorphic model conceptually determines how the substructure interacts with itself and the associated characteristic length is a measure of the range of action of such microstructure related deformation modes. In this sense, we call the full-gradient contribution $\|\nabla P\|^2$ (or any other curvature term essentially controlling ∇P) of *strong interaction* type: neighboring substructures feel the presence of each other or, equivalently, the generated moment stresses depend on ∇P . On the contrary, the corresponding moment stresses depend only on $\text{Curl} P$ in the relaxed micromorphic model, connecting neighboring cells only via tangent micro-interactions. Certain substructure deformations are energetically free (in fact all compatible parts $\nabla\vartheta$ in P are not taken into account) while the model remains reversibly elastic and energy-conservative. We call this a *weak interaction*. As a matter of fact, the wording *relaxed* is motivated by this observation.

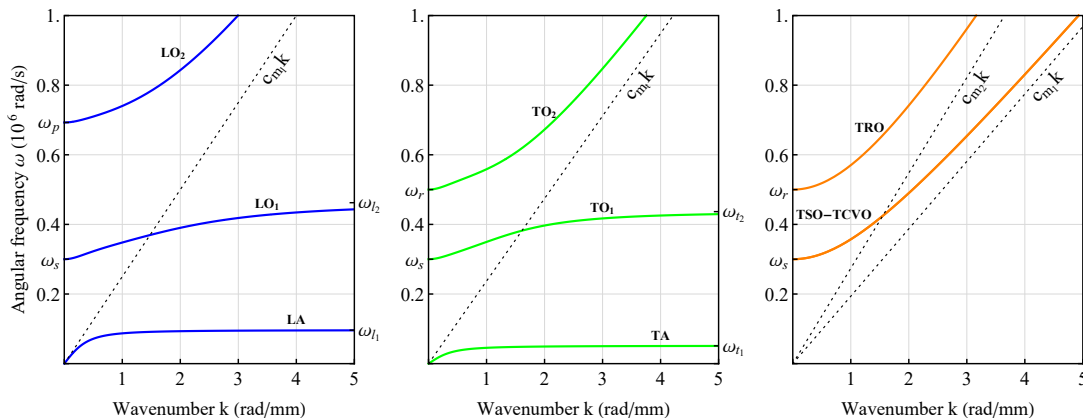


Figure 41: Dispersion relations for the *relaxed micromorphic model* with non-vanishing gradient micro-inertia, longitudinal (left), transverse (center) and uncoupled (right) waves.

The insufficiency of Cauchy continuum theories becomes even more evident when considering more complex metamaterials which are able to inhibit wave propagation, i.e. so called band-gap metamaterials. In what follows, we will show that the relaxed micromorphic model, whose dispersion curves are shown in Figure 41, is the only non-local continuum model of the micromorphic type which is able to account for band-gaps with a simple uncoupled kinetic energy [138–141]. Moreover, we show here, following what done in [136], that the addition of kinetic energy terms which couple the motions of the microstructure to the macro-motions of the unit cells may have a deep impact on the ability of describing band-gaps behaviors.

2.1 The classical Cauchy medium

The first model to analyze is the classical Cauchy medium. As already mentioned before, this model predicts neither dispersive behavior nor optic modes. However, we will show how to describe some dispersive behavior adding an inertia term on the gradient of the displacement ∇u . In Figure 42, the dispersion curves for the longitudinal acoustic wave LA and the transverse acoustic TA are shown and compared to the corresponding acoustic branches of the relaxed micromorphic model (LA_{REL} and TA_{REL}). In [50], it was shown that the tangents c_l and c_t of the acoustic branches in $k = 0$ in the classical linear elastic dispersion curves, considering Lamé constants μ_M and λ_M , coincide with the ones obtained for the relaxed micromorphic model, see Figure 42. The energies considered are:

$$W = \mu_M \|\text{sym}(\nabla u)\|^2 + \frac{\lambda_M}{2} (\text{tr} \nabla u)^2, \quad (\text{IV.72})$$

$$J = \frac{1}{2} \rho \|u_{,t}\|^2 + \frac{1}{2} \bar{\eta}_1 \|\text{dev sym} \nabla u_{,t}\|^2 + \frac{1}{2} \bar{\eta}_2 \|\text{skew} \nabla u_{,t}\|^2 + \frac{1}{6} \bar{\eta}_3 (\text{tr} \nabla u_{,t})^2.$$

From this energy, we can derive the dynamical equilibrium equations:

$$\rho u_{,tt} + \text{Div}[\mathcal{I}] = \text{Div}[\sigma], \quad (\text{IV.73})$$

where

$$\mathcal{I} = \bar{\eta}_1 \text{dev sym} \nabla u_{,tt} + \bar{\eta}_2 \text{skew} \nabla u_{,tt} + \frac{1}{3} \bar{\eta}_3 \text{tr}(\nabla u_{,tt}), \quad \sigma = 2\mu_M \text{sym}(\nabla u) + \lambda_M \text{tr}(\nabla u) \mathbf{1}.$$

The dispersion curves obtained in the plane wave case are:

$$\omega_{\text{LA}} = \frac{c_l k}{\sqrt{1 + k^2 \frac{2\bar{\eta}_1 + \bar{\eta}_3}{3\rho}}}, \quad \omega_{\text{TA}} = \frac{c_t k}{\sqrt{1 + k^2 \frac{\bar{\eta}_1 + \bar{\eta}_2}{2\rho}}}.$$

where

$$c_l = \frac{d\omega_{\text{acoustic, long}}(0)}{dk} = \sqrt{\frac{2\mu_M + \lambda_M}{\rho}}, \quad c_t = \frac{d\omega_{\text{acoustic, trans}}(0)}{dk} = \sqrt{\frac{\mu_M}{\rho}}. \quad (\text{IV.74})$$

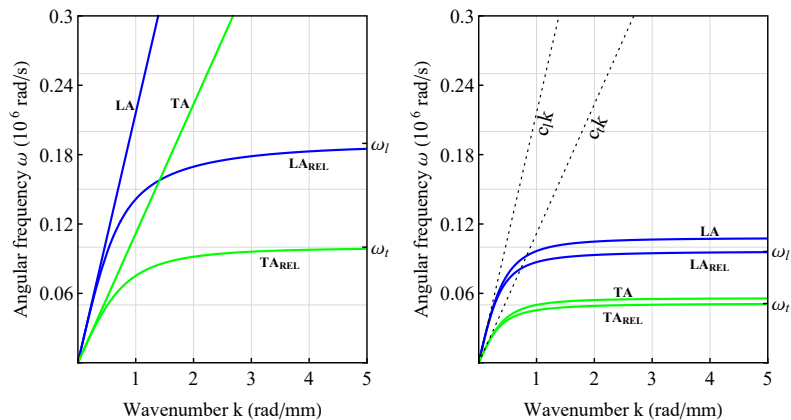


Figure 42: Dispersion relations for the *classical Cauchy medium* compared to the acoustic branches of the relaxed micromorphic model with vanishing (left) and non-vanishing gradient micro-inertia (right).

The non-linearity of the dispersion curves is due to the gradient micro-inertia. These relations are a generalization of the classical relations (that can be obtained for vanishing gradient micro-inertia):

$$\omega_{LA} = c_l k, \quad \omega_{TA} = c_t k.$$

2.2 The Cosserat micromorphic model

We present the *dispersion relations* obtained with a Cosserat micromorphic model with both vanishing and non-vanishing gradient micro-inertia in figure 43. The number of branches in the dispersion relations is reduced in comparison to the relaxed micromorphic model. This fact is due to the presence of a skew symmetric micromorphic tensor $A \in \mathfrak{so}(3)$ with only three independent variables. The case with vanishing gradient micro-inertia does not allow for band-gaps while, on the other hand, a complete band-gap can be obtained adding a gradient micro-inertia term.

In the isotropic case, the elastic energy density and the kinetic energy density of the Cosserat model read:

$$\begin{aligned} W &= \mu_M \|\text{sym } \nabla u\|^2 + \frac{\lambda_M}{2} (\text{tr } (\nabla u))^2 + \mu_c \|\text{skew } (\nabla u - A)\|^2 + \frac{\mu L_c^2}{2} \|\text{Curl } A\|^2, \\ J &= \frac{\rho}{2} \|u_{,t}\|^2 + \frac{\eta_2}{2} \|A_{,t}\|^2 + \frac{1}{2} \bar{\eta}_1 \|\text{dev sym } \nabla u_{,t}\|^2 + \frac{1}{2} \bar{\eta}_2 \|\text{skew } \nabla u_{,t}\|^2 + \frac{1}{6} \bar{\eta}_3 (\text{tr } \nabla u_{,t})^2. \end{aligned} \quad (\text{IV.75})$$

where $A \in \mathfrak{so}(3)$. The dynamical formulation is obtained defining a joint Hamiltonian and assuming stationary action finding:

$$\begin{aligned} \rho u_{,tt} &= \text{Div} [2\mu_M \text{sym } (\nabla u - A) + 2\mu_c \text{skew } (\nabla u - A) + \lambda_M \text{tr } (\nabla u - A) \mathbf{1}], \\ \eta A_{,tt} &= -\mu L_c^2 \text{skew } (\text{Curl } \text{Curl } A) + 2\mu_c \text{skew } (\nabla u - A), \end{aligned} \quad (\text{IV.76})$$

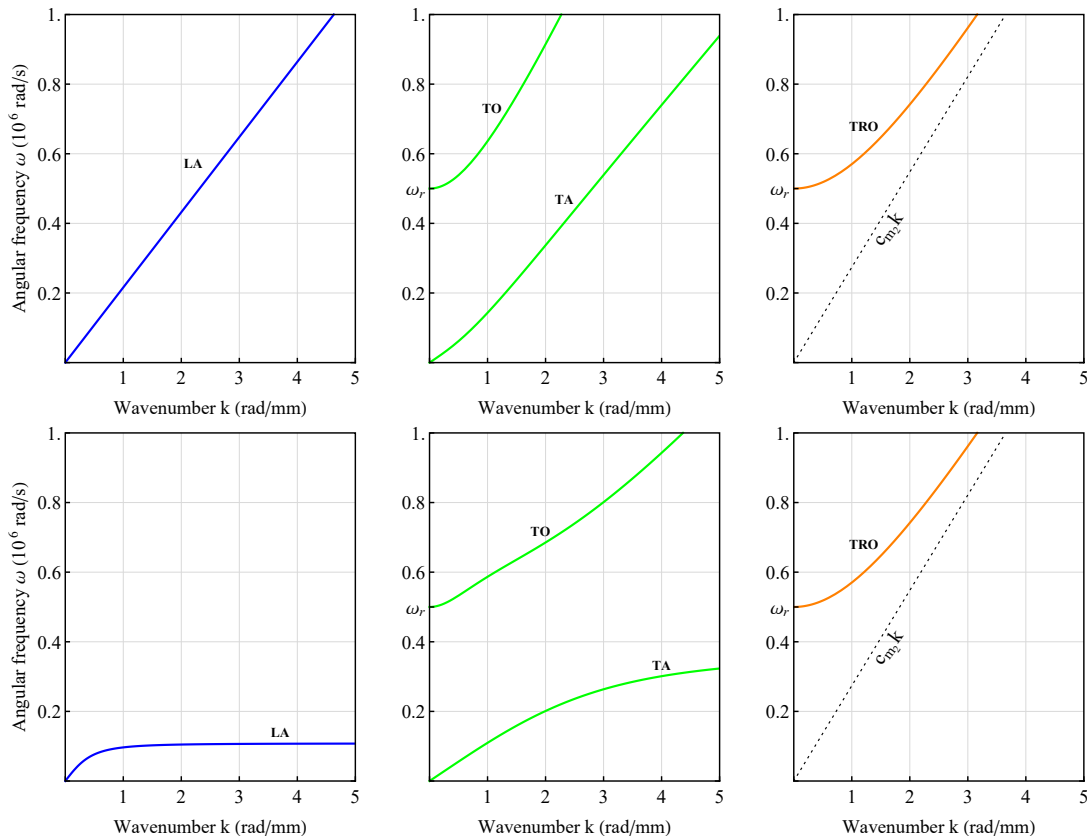


Figure 43: Longitudinal (left), transverse (center) and uncoupled (right) dispersion relations for the *Cosserat model* with vanishing (top) and non-vanishing (bottom) micro-inertia.

2.3 The internal variable model

We present the dispersion relations obtained for the internal variable model for a vanishing and a non-vanishing gradient inertia (Figure 44). We notice in Figure 44 that the internal variable model with vanishing gradient micro-inertia allows for the description of two separate band-gaps for both longitudinal and transverse waves (for higher values of μ_c and therefore ω_r , it would allow for two complete band-gaps). Moreover, by direct observation of Figure 44, we notice that, when switching the gradient micro-inertia on and suitably choosing the relative position of ω_r and ω_p , the internal variable model allows to account for 3 band gaps. We thus have an extra band-gap with respect to the case with vanishing gradient inertia and to the analogous case for the relaxed micromorphic model, but we are not able to capture non-local effects. The fact of excluding the possibility of describing non-local effects in metamaterials can sometimes be too restrictive.

The case of the internal variable model is obtained from a micromorphic model by neglecting the curvature term. We recall (see [176]) that the energy for the internal variable model does not include higher space derivatives of the micro-distortion tensor P and, in the isotropic case, takes the form:

$$W = \mu_e \|\text{sym}(\nabla u - P)\|^2 + \frac{\lambda_e}{2} (\text{tr}(\nabla u - P))^2 + \mu_c \|\text{skew}(\nabla u - P)\|^2 \quad (\text{IV.77})$$

$$+ \mu_m \|\text{sym} P\|^2 + \frac{\lambda_m}{2} (\text{tr} P)^2,$$

The dynamical equilibrium equations are:

$$\rho u_{,tt} + \text{Div}[\mathcal{I}] = \text{Div}[\tilde{\sigma}], \quad \eta P_{,tt} = \tilde{\sigma} - s, \quad (\text{IV.78})$$

where

$$\mathcal{I} = \bar{\eta}_1 \text{dev sym } \nabla u_{,tt} + \bar{\eta}_2 \text{skew } \nabla u_{,tt} + \frac{1}{3} \bar{\eta}_3 \text{tr}(\nabla u_{,tt}), \quad (\text{IV.79})$$

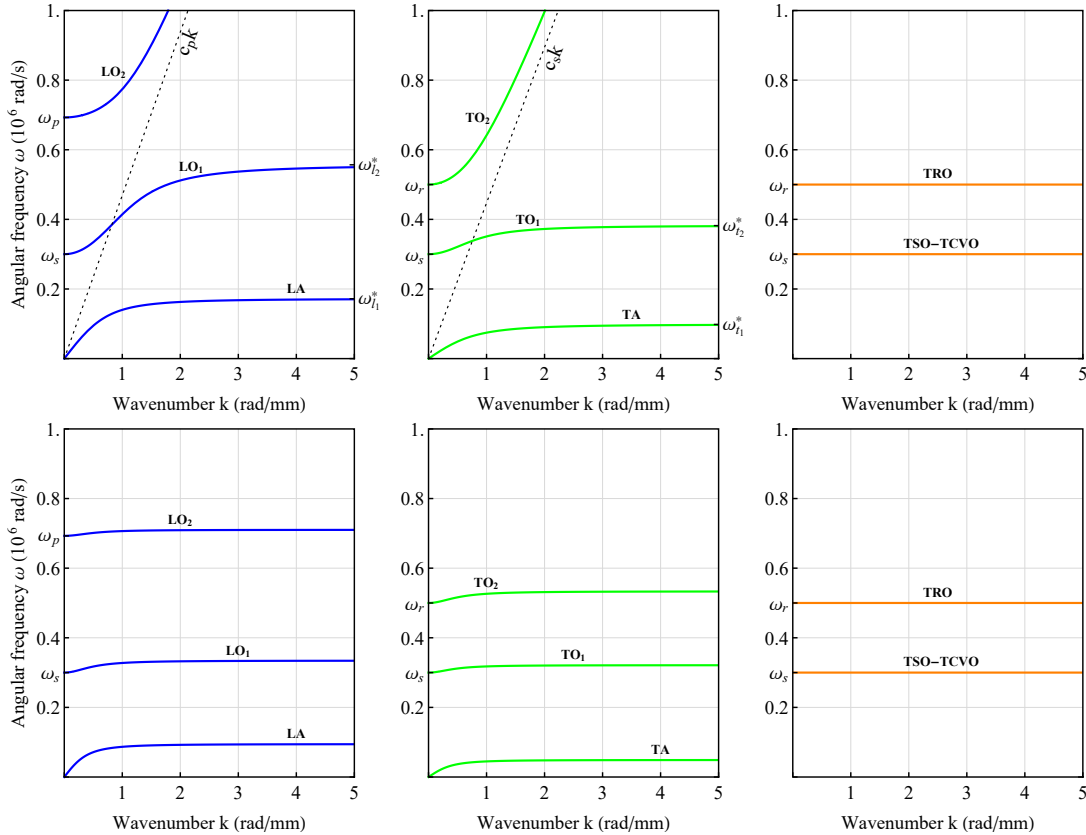


Figure 44: Dispersion relations for the *internal variable model* with vanishing (top) and non-vanishing (bottom) gradient micro-inertia, longitudinal (left), transverse (center) and uncoupled (right) waves.

$$\begin{aligned}\tilde{\sigma} &= 2\mu_e \operatorname{sym}(\nabla u - P) + \lambda_e \operatorname{tr}(\nabla u - P) \mathbf{1} + 2\mu_c \operatorname{skew}(\nabla u - P), \\ s &= 2\mu_m \operatorname{sym} P + \lambda_m \operatorname{tr}(P) \mathbf{1}.\end{aligned}\quad (\text{IV.80})$$

2.4 The standard Mindlin-Eringen model

We present the *dispersion relations* obtained with both vanishing and non-vanishing gradient micro-inertia with the standard Mindlin-Eringen model in Figure 45. We conclude that when considering the model with standard Mindlin-Eringen micromorphic model with vanishing gradient micro-inertia, there always exist waves which propagate inside the considered medium. The only possible effect is to obtain a partial band gap for the uncoupled waves. On the other hand, the gradient micro-inertia allows for the description of one complete band-gap. The elastic energy of the isotropic micromorphic model in the sense of Mindlin-Eringen (see [156] and [67, p. 270, eq. 7.1.4]) is:

$$\begin{aligned}W &= \mu_e \|\operatorname{sym}(\nabla u - P)\|^2 + \frac{\lambda_e}{2} (\operatorname{tr}(\nabla u - P))^2 + \mu_c \|\operatorname{skew}(\nabla u - P)\|^2 \\ &+ \mu_m \|\operatorname{sym} P\|^2 + \frac{\lambda_m}{2} (\operatorname{tr} P)^2 + \frac{\mu L_c^2}{2} \|\nabla P\|^2.\end{aligned}\quad (\text{IV.81})$$

The dynamical equilibrium equations are:

$$\begin{aligned}\rho u_{,tt} &= \operatorname{Div} \sigma = \operatorname{Div} [2\mu_e \operatorname{sym}(\nabla u - P) + 2\mu_c \operatorname{skew}(\nabla u - P) + \lambda_e \operatorname{tr}(\nabla u - P) \mathbf{1}], \\ \eta P_{,tt} &= 2\mu_e \operatorname{sym}(\nabla u - P) + 2\mu_c \operatorname{skew}(\nabla u - P) + \lambda_e \operatorname{tr}(\nabla u - P) \mathbf{1} \\ &- [2\mu_m \operatorname{sym} P + \lambda_m \operatorname{tr}(P) \mathbf{1}] + \mu L_c^2 \operatorname{Div} \nabla P.\end{aligned}\quad (\text{IV.82})$$

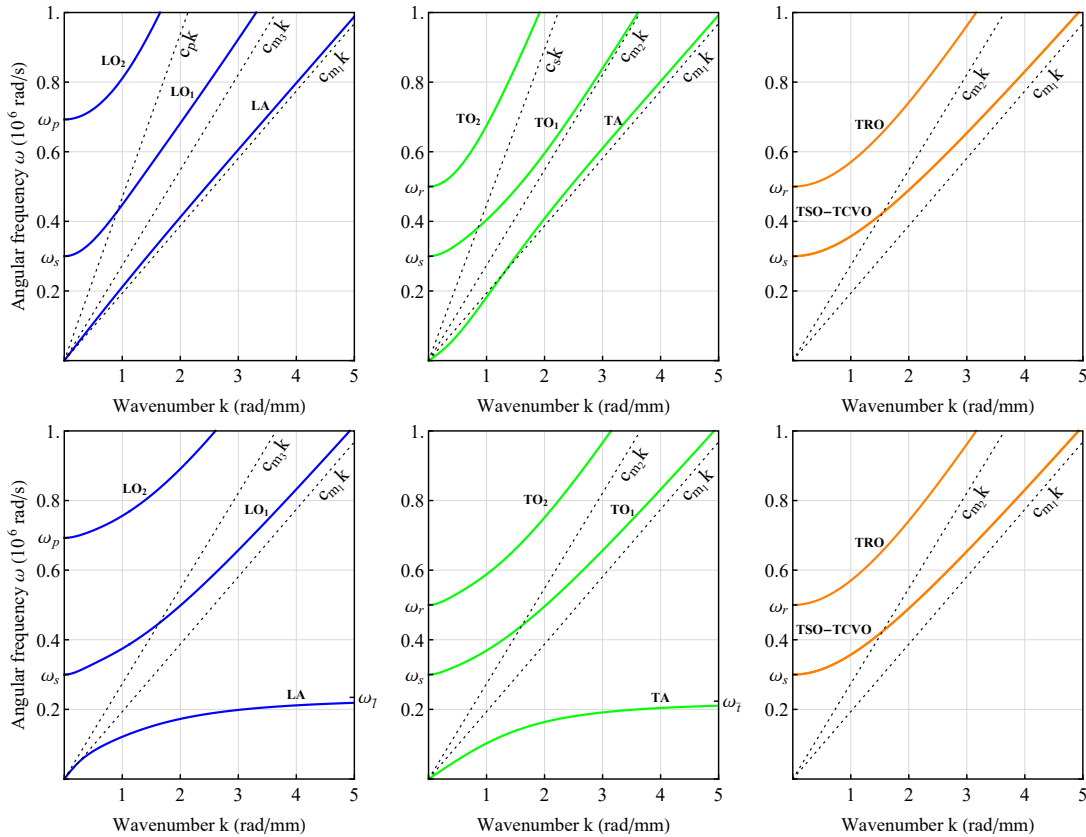


Figure 45: Longitudinal (left), transverse (center) and uncoupled (right) dispersion relations for the *standard micromorphic model with $\|\nabla P\|^2$* with vanishing (top) and non-vanishing (bottom) gradient micro-inertia.

2.5 The relaxed micromorphic model with curvature $\|\text{Div } P\|^2$

The Div-model is obtained from the relaxed micromorphic model by replacing $\|\text{Curl } P\|^2$ with $\|\text{Div } P\|^2$. In the Div-model, a weak interaction similar to the relaxed micromorphic model appears since the corresponding moment stresses depend only on $\text{Div } P$ and, therefore, substructure deformations of the type $P = \text{Curl } \zeta + \nabla \vartheta$, where $\zeta : \mathbb{R}^{3 \times 3} \rightarrow \mathbb{R}^{3 \times 3}$ is arbitrary and $\vartheta : \mathbb{R}^3 \rightarrow \mathbb{R}^3$ satisfies $\Delta \vartheta \equiv 0$, are energetically free. We present the *dispersion relations* obtained with both vanishing and non-vanishing gradient micro-inertia in Figure 46. No *band gap* on the longitudinal and transverse waves can be modeled and the uncoupled waves have fixed frequencies (Figure 46). We can conclude that, when considering the micromorphic model with only $\|\text{Div } P\|^2$ for every value of μ_c , there always exist waves which propagate inside the considered medium independently of the value of the frequency. The uncoupled waves assume a peculiar behavior in which the frequency is independent of the wavenumber k . The energy of this model is:

$$W = \mu_e \|\text{sym}(\nabla u - P)\|^2 + \frac{\lambda_e}{2} (\text{tr}(\nabla u - P))^2 + \mu_c \|\text{skew}(\nabla u - P)\|^2 \quad (\text{IV.83})$$

$$+ \mu_m \|\text{sym } P\|^2 + \frac{\lambda_m}{2} (\text{tr } P)^2 + \frac{\mu L_d^2}{2} \|\text{Div } P\|^2.$$

The dynamical equilibrium equations are:

$$\begin{aligned} \rho u_{,tt} &= \text{Div } \sigma = \text{Div} [2\mu_e \text{sym}(\nabla u - P) + 2\mu_c \text{skew}(\nabla u - P) + \lambda_e \text{tr}(\nabla u - P) \mathbf{1}], \\ \eta P_{,tt} &= 2\mu_e \text{sym}(\nabla u - P) + 2\mu_c \text{skew}(\nabla u - P) + \lambda_e \text{tr}(\nabla u - P) \mathbf{1} \\ &\quad - [2\mu_m \text{sym } P + \lambda_m \text{tr}(P) \mathbf{1}] + \mu L_d^2 \nabla(\text{Div } P). \end{aligned} \quad (\text{IV.84})$$

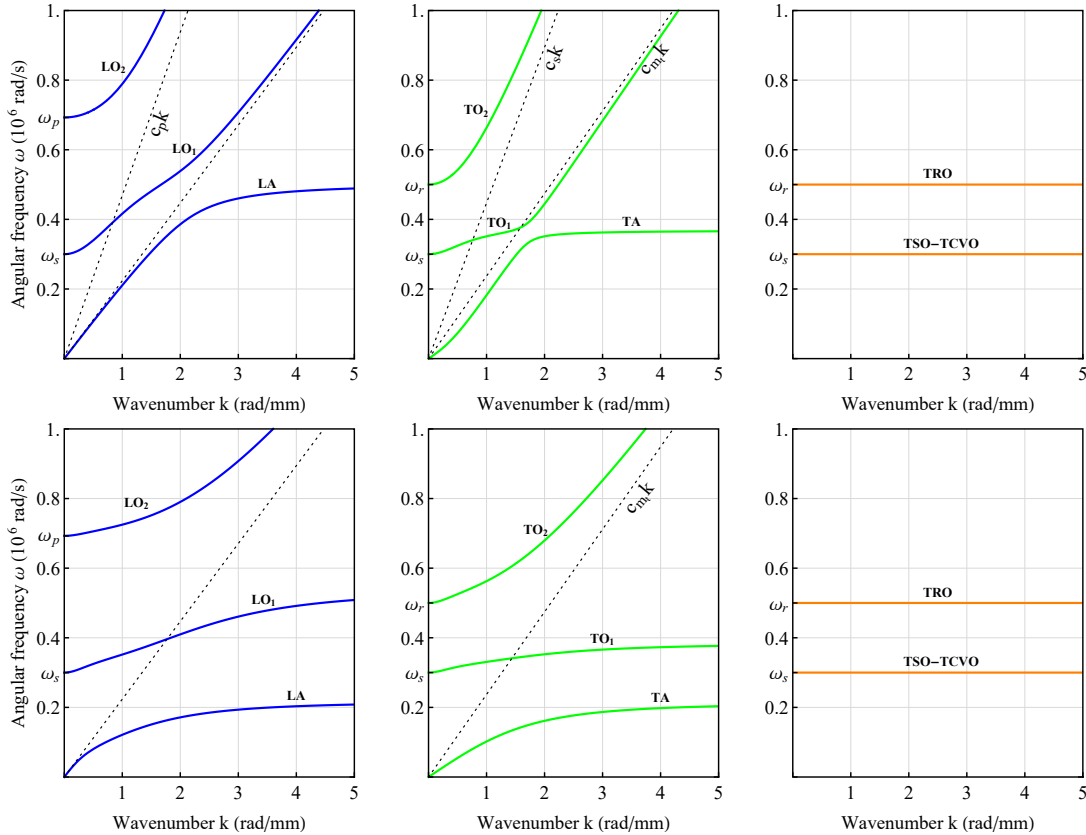


Figure 46: Longitudinal (left), transverse (center) and uncoupled (right) dispersion relations for the *micromorphic model with $\|\text{Div } P\|^2$* with vanishing (top) and non-vanishing (bottom) gradient micro-inertia.

CHAPTER IV.3

Reflection and transmission of waves at a Cauchy/relaxed micromorphic interface

3.1 Conservation of the total energy

Considering conservative mechanical systems, like in the present manuscript, the conservation of total energy must be verified in the form

$$\frac{dE}{dt} + \operatorname{div} H = 0, \quad (\text{IV.85})$$

where $E = T + W$ is the total energy of the considered system and H is the energy flux vector. It is clear that the explicit expressions for the total energy and for the energy flux are different depending on whether one considers a classical Cauchy model or a relaxed micromorphic one. If the expression of the total energy E is straightforward for the two mentioned cases (it suffices to look at the given expressions of T and W), the explicit expression of the energy flux H is more complicated to be obtained. The explicit expression of the energy fluxes for the Cauchy and relaxed micromorphic media have been deduced in [141], to which we refer for additional details on this subject.

3.1.1 The classical Cauchy medium

In classical Cauchy continua the energy flux vector H can be written as

$$H = -\sigma_M \cdot u_{,t}, \quad (\text{IV.86})$$

where the symmetric Cauchy stress tensor σ_M has been defined in the Appendix D.1 (equation (D.3)) in terms of the displacement field. The first component of the energy flux vector given in equation (IV.86), simplifies in the 1D case into

$$H_1 = -\dot{u}_1 [(\lambda + 2\mu) u_{1,1}] - \dot{u}_2 [\mu u_{2,1}] - \dot{u}_3 [\mu u_{3,1}]. \quad (\text{IV.87})$$

3.1.2 The relaxed micromorphic continuum

In relaxed micromorphic media, the energy flux vector \tilde{H} is defined as (see [141])

$$\tilde{H} = -[\tilde{\sigma} + \mathcal{I}]^T \cdot u_{,t} - (m^T \cdot P_{,t}) \epsilon, \quad (\text{IV.88})$$

where the stress tensor $\tilde{\sigma}$ and the hyper-stress tensor m have been defined in equation (IV.4) in terms of the basic kinematical fields and ϵ is the Levi-Civita tensor.

When considering conservation of total energy, it can be checked that the first component of the energy flux (IV.88) can be rewritten in terms of the new variables as

$$\tilde{H}_1 = H_1^1 + H_1^2 + H_1^3 + H_1^4 + H_1^5 + H_1^6 \quad (\text{IV.89})$$

with

$$\begin{aligned}
 H_1^1 &= v_{1,t} \cdot \left[\begin{pmatrix} -2\mu_e - \lambda_e & 0 & 0 \\ 0 & -\frac{\mu L_c^2}{2} & \mu L_c^2 \\ 0 & \mu L_c^2 & -2\mu L_c^2 \end{pmatrix} \cdot v_1' + \begin{pmatrix} -\frac{2\bar{\eta}_1 + \bar{\eta}_3}{3} & 0 & 0 \\ 0 & 0 & 0 \\ 0 & 0 & 0 \end{pmatrix} \cdot v_{1,tt}' + \begin{pmatrix} 0 & 2\mu_e & 2\mu_e + 3\lambda_e \\ 0 & 0 & 0 \\ 0 & 0 & 0 \end{pmatrix} \cdot v_1 \right], \\
 H_1^2 &= v_{2,t} \cdot \left[\begin{pmatrix} -(\mu_e + \mu_c) & 0 & 0 \\ 0 & -\mu L_c^2 & -\mu L_c^2 \\ 0 & -\mu L_c^2 & -\mu L_c^2 \end{pmatrix} \cdot v_2' + \begin{pmatrix} -\frac{\bar{\eta}_1 + \bar{\eta}_2}{2} & 0 & 0 \\ 0 & 0 & 0 \\ 0 & 0 & 0 \end{pmatrix} \cdot v_{2,tt}' + \begin{pmatrix} 0 & 2\mu_e & -2\mu_c \\ 0 & 0 & 0 \\ 0 & 0 & 0 \end{pmatrix} \cdot v_2 \right], \\
 H_1^3 &= v_{3,t} \cdot \left[\begin{pmatrix} -(\mu_e + \mu_c) & 0 & 0 \\ 0 & -\mu L_c^2 & -\mu L_c^2 \\ 0 & -\mu L_c^2 & -\mu L_c^2 \end{pmatrix} \cdot v_3' + \begin{pmatrix} -\frac{\bar{\eta}_1 + \bar{\eta}_2}{2} & 0 & 0 \\ 0 & 0 & 0 \\ 0 & 0 & 0 \end{pmatrix} \cdot v_{3,tt}' + \begin{pmatrix} 0 & 2\mu_e & -2\mu_c \\ 0 & 0 & 0 \\ 0 & 0 & 0 \end{pmatrix} \cdot v_3 \right], \\
 H_1^4 &= -2\mu L_c^2 (v_4)_{,1} v_{4,t}, \quad H_1^5 = -2\mu L_c^2 (v_5)_{,1} v_{5,t}, \quad H_1^6 = -\frac{\mu L_c^2}{2} (v_6)_{,1} v_{6,t}.
 \end{aligned} \tag{IV.90}$$

3.2 Interface jump conditions at a Cauchy/relaxed-micromorphic interface

In this section we present a possible choice of boundary conditions to impose between a Cauchy medium and a relaxed micromorphic medium. Such set of boundary conditions has been derived in [141] and allows to describe free vibrations of the microstructure at the considered interface. We will show in the remainder of this part how this particular choice of boundary conditions is capable to describe phenomena of wave transmission in real mechanical metamaterials. For the full presentation of the complete sets of possible connections that can be established at Cauchy/relaxed, relaxed/relaxed, Cauchy/Mindlin, Mindlin/Mindlin interfaces we refer to [141].

When considering connections between a Cauchy and a relaxed micromorphic medium one can impose more kinematical boundary conditions than in the case of connections between Cauchy continua. More precisely, one can act on the displacement field u (on both sides of the interface) and also on the tangential micro-distortion P (on the side of the interface occupied by the relaxed micromorphic continuum). In what follows, we consider the “-” region occupied by the Cauchy continuum and the “+” region occupied by the micromorphic continuum, so that, accordingly, we use the following notations:

$$f = \sigma^- \cdot n^-, \quad t = (\tilde{\sigma}^+ + \mathcal{I}^+) \cdot n^+, \quad \tau = \mu L_c^2 (\text{Curl } P^+) \cdot \epsilon \cdot n^+. \tag{IV.91}$$

It is easy to see that when the normal is $n = (1, 0, 0)$, the normal components τ_{11}, τ_{21} and τ_{31} of the double force are identically zero. Therefore, the number of independent conditions that one can impose on the micro-distortions is 6 when considering a relaxed micromorphic model.

Here, we focus our attention on one particular type of connection between a classical Cauchy continuum and a relaxed micromorphic one, which is sensible to reproduce the real situation in which the microstructure of the band-gap metamaterial is free to vibrate independently of the macroscopic matrix. Such particular connection guarantees continuity of the macroscopic displacement and free motion of the microstructure (which means vanishing double force) at the interface:

$$[[u]] = 0, \quad t - f = 0, \quad \tau \cdot \nu_1 = \tau \cdot \nu_2 = 0. \tag{IV.92}$$

We explicitly remark that continuity of displacement implies continuity of internal forces and that the conditions on the arbitrariness of micro-motions are assured by imposing that the tangent part of the double force is vanishing.

Introducing the tangent vectors $\nu_1 = (0, 1, 0)$ and $\nu_2 = (0, 0, 1)$ and considering the new variables presented in (IV.6) and (IV.12), the boundary conditions on the jump of displacement read:

$$v_1^+ \cdot n - u_1^- = 0, \quad v_2^+ \cdot n - u_2^- = 0, \quad v_3^+ \cdot n - u_3^- = 0, \tag{IV.93}$$

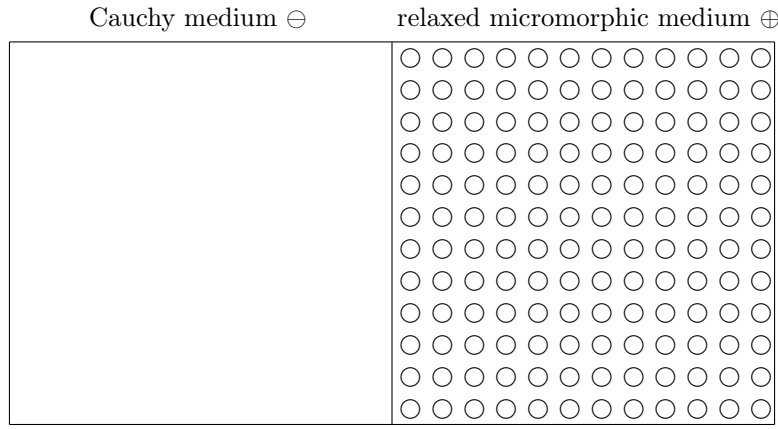


Figure 47: Schematics of a macro internal clamp with free microstructure at a Cauchy/relaxed-micromorphic interface.

while the conditions on the internal forces become (see also [141]):

$$\begin{aligned} \begin{pmatrix} \lambda_e + 2\mu_e \\ 0 \\ 0 \end{pmatrix} \cdot (v_1^+)' + \begin{pmatrix} \frac{2\bar{\eta}_1 + \bar{\eta}_3}{3} \\ 0 \\ 0 \end{pmatrix} \cdot (v_{1,tt}^+)' + \begin{pmatrix} 0 \\ -2\mu_e \\ -(3\lambda_e + 2\mu_e) \end{pmatrix} \cdot v_1^+ &= (\lambda + 2\mu) (u_1^-)', \\ \begin{pmatrix} \mu_e + \mu_c \\ 0 \\ 0 \end{pmatrix} \cdot (v_2^+)' + \begin{pmatrix} \frac{\bar{\eta}_1 + \bar{\eta}_2}{2} \\ 0 \\ 0 \end{pmatrix} \cdot (v_{2,tt}^+)' + \begin{pmatrix} 0 \\ -2\mu_e \\ 2\mu_c \end{pmatrix} \cdot v_2^+ &= \mu (u_2^-)', \\ \begin{pmatrix} \mu_e + \mu_c \\ 0 \\ 0 \end{pmatrix} \cdot (v_3^+)' + \begin{pmatrix} \frac{\bar{\eta}_1 + \bar{\eta}_2}{2} \\ 0 \\ 0 \end{pmatrix} \cdot (v_{3,tt}^+)' + \begin{pmatrix} 0 \\ -2\mu_e \\ 2\mu_c \end{pmatrix} \cdot v_3^+ &= \mu (u_3^-)'. \end{aligned} \quad (\text{IV.94})$$

The conditions on the tangent part of the double force τ can be written as

$$\begin{aligned} \tau_{22} &= \begin{pmatrix} 0 \\ -\mu L_c^2/2 \\ \mu L_c^2 \end{pmatrix} \cdot (v_1^+)' + \frac{\mu L_c^2}{2} (v_6^+)' = 0, & \tau_{33} &= \begin{pmatrix} 0 \\ -\mu L_c^2/2 \\ \mu L_c^2 \end{pmatrix} \cdot (v_1^+)' - \frac{\mu L_c^2}{2} (v_6^+)' = 0, \\ \tau_{12} &= \begin{pmatrix} 0 \\ \mu L_c^2 \\ \mu L_c^2 \end{pmatrix} \cdot (v_2^+)' = 0, & \tau_{13} &= \begin{pmatrix} 0 \\ \mu L_c^2 \\ \mu L_c^2 \end{pmatrix} \cdot (v_3^+)' = 0, \\ \tau_{23} &= \mu L_c^2 \left((v_4^+)' + (v_5^+)' \right) = 0, & \tau_{32} &= \mu L_c^2 \left((v_4^+)' - (v_5^+)' \right) = 0, \end{aligned} \quad (\text{IV.95})$$

while we recall once again that the normal part of the double force is vanishing, i.e.:

$$\tau_{11} = 0, \quad \tau_{21} = 0, \quad \tau_{31} = 0. \quad (\text{IV.96})$$

3.2.1 Decomposition of the incident, transmitted and reflected waves

When studying the reflection and transmission of a plane wave at a Cauchy/relaxed-micromorphic interface, we assume that an incident wave traveling in the Cauchy medium impacts the interface. Two waves are then generated, namely one wave reflected in the Cauchy medium and one transmitted in the relaxed micromorphic medium. We explicitly remark that the reflected wave contains the longitudinal and transverse parts of the

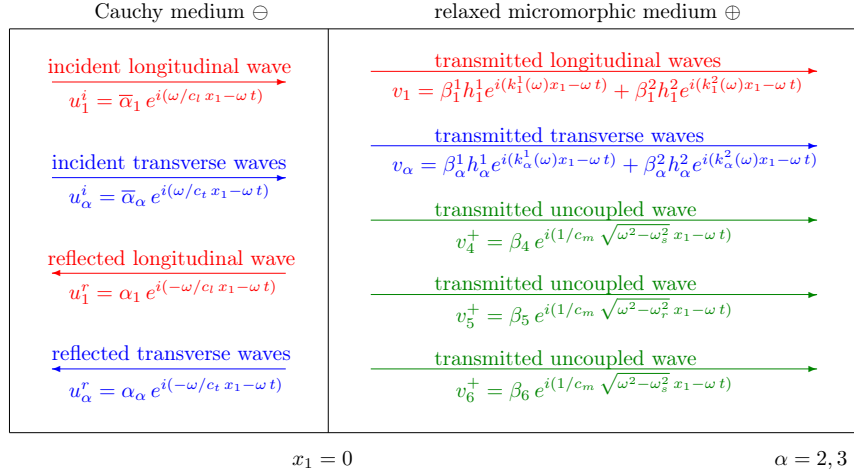


Figure 48: Incident, reflected and transmitted waves at a Cauchy/relaxed-micromorphic interface.

displacement field, while the transmitted wave contains a longitudinal part on the field v_1 , two transverse parts on v_α ($\alpha = 2, 3$) and the three uncoupled fields v_4 , v_5 and v_6 ¹ (see also Figure 48.).

Considering the plane wave ansatz and both the incident and reflected wave, the displacement field in the Cauchy medium can be written as:

$$\begin{aligned}
 u_1^- &= \bar{\alpha}_1 e^{i(\omega/c_l x_1 - \omega t)} + \alpha_1 e^{i(-\omega/c_l x_1 - \omega t)}, \\
 u_2^- &= \bar{\alpha}_2 e^{i(\omega/c_t x_1 - \omega t)} + \alpha_2 e^{i(-\omega/c_t x_1 - \omega t)}, \\
 u_3^- &= \bar{\alpha}_3 e^{i(\omega/c_t x_1 - \omega t)} + \alpha_3 e^{i(-\omega/c_t x_1 - \omega t)}
 \end{aligned} \tag{IV.97}$$

and we assume the wave forms (IV.13) for the unknown fields v_1^+ , v_α^+ , v_4^+ , v_5^+ and v_6^+ in the relaxed micromorphic medium, i.e.:

$$\begin{aligned}
 v_1^+ &= \beta_1^1 h_1^1 e^{i(k_1^1(\omega)x_1 - \omega t)} + \beta_1^2 h_1^2 e^{i(k_1^2(\omega)x_1 - \omega t)}, & v_\alpha^+ &= \beta_\alpha^1 h_\alpha^1 e^{i(k_\alpha^1(\omega)x_1 - \omega t)} + \beta_\alpha^2 h_\alpha^2 e^{i(k_\alpha^2(\omega)x_1 - \omega t)}, & \alpha &= 2, 3, \\
 v_4^+ &= \beta_4 e^{i(1/c_m \sqrt{\omega^2 - \omega_s^2} x_1 - \omega t)}, & v_5^+ &= \beta_5 e^{i(1/c_m \sqrt{\omega^2 - \omega_r^2} x_1 - \omega t)}, & v_6^+ &= \beta_6 e^{i(1/c_m \sqrt{\omega^2 - \omega_s^2} x_1 - \omega t)}.
 \end{aligned} \tag{IV.98}$$

Here $\bar{\alpha}_1, \bar{\alpha}_2, \bar{\alpha}_3 \in \mathbb{R}$ are the amplitudes of the incident (longitudinal and transverse) waves traveling in the Cauchy continuum that are assumed to be known, while $\alpha_1, \alpha_2, \alpha_3 \in \mathbb{R}$ are the amplitudes of the longitudinal and transverse reflected waves. Analogously, $\beta_1^1, \beta_1^2 \in \mathbb{R}$ are the amplitudes associated to the longitudinal wave transmitted in the relaxed medium, while $h_1^1, h_1^2 \in \mathbb{R}^3$ and $k_1^1, k_1^2 \in \mathbb{R}$ are the eigenvectors and eigenvalues associated to the eigenvalue problem for longitudinal waves (see [141]). Similarly, $\beta_\alpha^1, \beta_\alpha^2 \in \mathbb{R}$, $h_\alpha^1, h_\alpha^2 \in \mathbb{R}^3$, $k_\alpha^1, k_\alpha^2 \in \mathbb{R}$ ($\alpha = 2, 3$) are defined for transverse waves transmitted in the relaxed medium (see [141] for details). Finally $\beta_4, \beta_5, \beta_6 \in \mathbb{R}$ are the amplitudes of the uncoupled waves transmitted in the relaxed medium.

Assuming that the amplitudes of the incident waves are known, we can count the 12 unknown amplitudes $\alpha_1, \alpha_2, \alpha_3, \beta_1^1, \beta_1^2, \beta_\alpha^1, \beta_\alpha^2$ ($\alpha = 2, 3$), $\beta_4, \beta_5, \beta_6$ which can be calculated by imposing the 12 scalar jump condition (IV.93), (IV.94) and (IV.95).

3.2.2 The case of purely longitudinal incident waves

In the remainder of this manuscript, we are interested in a first calibration of the constitutive parameters of our relaxed micromorphic model on a real experiment of wave transmission in a band gap metamaterial.

To do so, we focus on the experiment proposed in [127] in which only longitudinal waves are considered. We hence consider here the solution of our relaxed problem only for what concerns the longitudinal part.

¹ v_4, v_5 and v_6 correspond to the components of v_4 defined in Equation (IV.12)

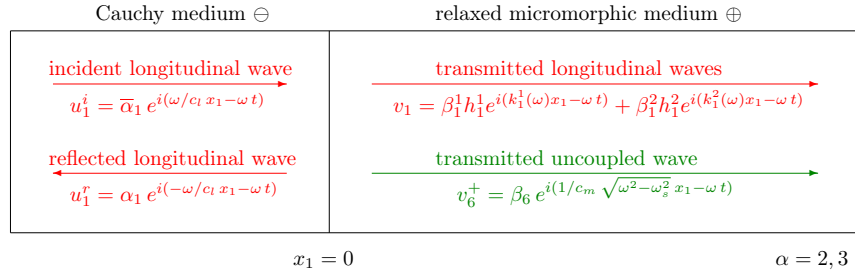


Figure 49: Incident, reflected and transmitted longitudinal waves at a Cauchy/relaxed-micromorphic interface.

In other words, we are only considering the longitudinal fields v_1 and u_1 together with the field v_6 which is coupled to v_1 through the boundary conditions (IV.95).

In summary, the *boundary value problem* for longitudinal waves can be written as (see equations (IV.3), (IV.93), (IV.94), (IV.95) and (D.4))

$$\begin{aligned}
 u_{1,tt}^- &= c_l^2 (u_1^-)'' , \\
 v_{1,tt}^+ &= A_1^R \cdot (v_1^+)' + B_1^R \cdot (v_1^+)' + C_1^R \cdot v_1^+ , \\
 v_{6,tt}^+ &= A_6^R (v_6^+)'' + C_6^R v_6^+ ,
 \end{aligned} \tag{IV.99}$$

together with the boundary conditions:

$$\begin{aligned}
 v_1^+ \cdot n - u_1^- &= 0, \\
 \begin{pmatrix} \lambda_e + 2\mu_e \\ 0 \\ 0 \end{pmatrix} \cdot (v_1^+)' + \begin{pmatrix} 0 \\ -2\mu_e \\ -(3\lambda_e + 2\mu_e) \end{pmatrix} \cdot v_1^+ &= (\lambda + 2\mu) (u_1^-)' \\
 \begin{pmatrix} 0 \\ -\mu L_c^2/2 \\ \mu L_c^2 \end{pmatrix} \cdot (v_1^+)' &= 0, \quad (v_6^+)' = 0.
 \end{aligned} \tag{IV.100}$$

The wave form solution for purely longitudinal fields is given by (see also equations (IV.97), (IV.98) and Figure 49):

$$\begin{aligned}
 u_1^- &= \bar{\alpha}_1 e^{i(\omega/c_l x_1 - \omega t)} + \alpha_1 e^{i(-\omega/c_l x_1 - \omega t)} , \\
 v_1^+ &= \beta_1^1 h_1^1 e^{i(k_1^1(\omega)x_1 - \omega t)} + \beta_1^2 h_1^2 e^{i(k_1^2(\omega)x_1 - \omega t)} , \\
 v_6^+ &= \beta_6 e^{i(1/c_m \sqrt{\omega^2 - \omega_s^2} x_1 - \omega t)} .
 \end{aligned} \tag{IV.101}$$

Replacing the wave solution (IV.101) in the 4 scalar jump conditions (IV.100) and setting $x_1 = 0$ (position of the interface) we can calculate the 4 unknown amplitudes α_1 , β_1^1 , β_1^2 and β_6 .

From the condition $(v_6^+)' = 0$, it is straightforward to prove that $\beta_6 = 0$, so that finally $v_6^+ = 0 \forall x_1$ and $\forall t$. As for the other amplitudes, they have more complicated expressions which we do not explicitly show here since it does not add any fundamental information to the reasoning.

3.3 Reflection and transmission coefficients at a Cauchy/relaxed-micromorphic interface

We now want to define the reflection and transmission coefficients for the considered Cauchy/relaxed-micromorphic interface. To that end, we introduce the quantities

$$J_i = \int_0^\Pi H_i(0, t) dt, \quad J_r = \int_0^\Pi H_r(0, t) dt, \quad J_t = \int_0^\Pi H_t(0, t) dt,$$

where Π is the period of the traveling plane wave and H_i , H_r and H_t are the energy fluxes of the incident, reflected and transmitted energies, respectively. The reflection and transmission coefficients can hence be defined as

$$R = \frac{J_r}{J_i}, \quad T = \frac{J_t}{J_i}. \quad (\text{IV.102})$$

Since the considered system is conservative, one must have $R + T = 1$.

In the particular case of reflection and transmission of longitudinal plane waves at a Cauchy/relaxed micromorphic interface, recalling equations (IV.87) and (IV.89) together with the solutions (IV.101) for the unknown fields we have:

$$H_i = \dot{u}_1^i(\lambda + 2\mu)u_{1,1}^i, \quad H_r = \dot{u}_1^r(\lambda + 2\mu)u_{1,1}^r, \quad H_t = H_1^1 + H_1^6, \quad (\text{IV.103})$$

where we set $u_1^i = \bar{\alpha}_1 e^{i(\omega/c_1 x_1 - \omega t)}$ and $u_1^r = \alpha_1 e^{i(-\omega/c_1 x_1 - \omega t)}$. We explicitly remark that the fluxes H_1^1 and H_1^6 defined in equation (IV.90) must be calculated with the solutions v_1^+ and v_6^+ obtained for the considered constraint and given in equation (IV.101).

Since in this particular case we have shown that v_6^+ is zero, then H_1^6 does not contribute to the evaluation of the transmitted energy. Once the expressions for the energy fluxes have been calculated for the considered constraint (macro internal clamp with free microstructure), the reflection and transmission coefficients can be computed by using equations (IV.102). We remark that R and T depend on the frequency ω of the traveling waves.

3.3.1 The degenerate limit case $L_c = 0$ (internal variable model)

We show here that at the interface between a Cauchy continuum and a relaxed micromorphic one it is possible to model, as a degenerate limit case, the onset of two band gaps whose bounds are $[\omega_l^1, \omega_s]$ and $[\omega_l^2, \omega_p]$ (see [141] and equations IV.61 and IV.62), where:

$$\begin{aligned} \omega_l^1 &= \sqrt{a_l - \sqrt{a_l^2 - b_l^2}}, & \omega_s &= \sqrt{\frac{2(\mu_e + \mu_m)}{\eta}}, \\ \omega_l^2 &= \sqrt{a_l + \sqrt{a_l^2 - b_l^2}}, & \omega_p &= \sqrt{\frac{2(\mu_e + \mu_m) + 3(\lambda_e + \lambda_m)}{\eta}}, \end{aligned} \quad (\text{IV.104})$$

where we have defined:

$$a_l = \frac{2\mu_e}{\eta_1} \frac{3\kappa_e}{\eta_3} \frac{2\eta_1 + \eta_3}{3(\lambda_e + 2\mu_e)} + \frac{\mu_m}{\eta_1} + \frac{3\kappa_m}{2\eta_3}, \quad b_l^2 = \frac{2\mu_e}{\eta_1} \frac{3\kappa_e}{\eta_3} \frac{\lambda_m + 2\mu_m}{\lambda_e + 2\mu_e} + 4 \frac{\mu_m}{\eta_1} \frac{3\kappa_m}{2\eta_3}. \quad (\text{IV.105})$$

In Figure 50, we show a characteristic pattern of the transmission coefficient at a Cauchy/relaxed-micromorphic interface for a particular choice of the constitutive parameters and setting $L_c = 0$. The main characteristic feature of the relaxed micromorphic model with $L_c = 0$ (internal variable model) is that two separate band gaps can be determined and their bounds can be explicitly defined as functions of the constitutive parameters of the model according to equations (IV.104).

Switching on and slowly increasing the parameter L_c produces small changes on the reflection profile of Figure 50, which corresponds to the smoothening of the sharp corners that can be seen corresponding to the band-gap frequencies.

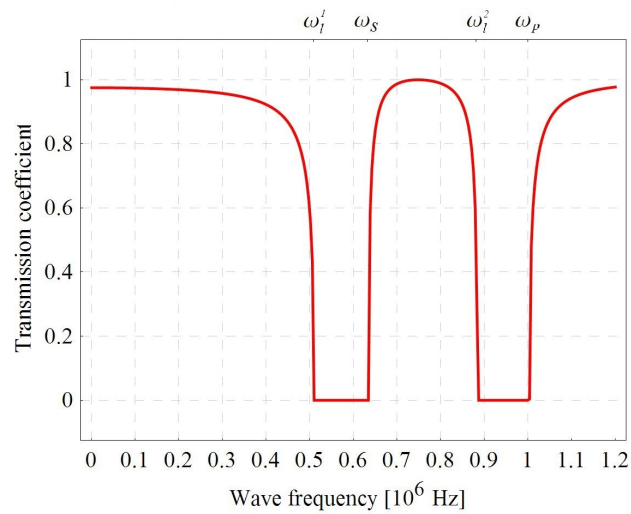


Figure 50: Transmission coefficient of the relaxed micromorphic model with $L_c = 0$ for $\lambda_e = \mu_e = \lambda_m = \mu_m = 100$ GPa and $\eta = 1$ kg/m.

CHAPTER IV.4

Modeling real two dimensional phononic crystals

In this chapter, we consider the application of the relaxed micromorphic model to two real phononic metamaterials, namely:

- a steel plate with cross-shaped holes;
- a steel plate with liquid-filled round holes.

The relaxed micromorphic model will be fitted using two different procedures and a validation of the model is presented, thus showing definitive proof of the applicability of our model to real engineering cases.

4.1 The steel plate with cross-shaped holes

In this section, we apply the results presented to describe the reflective behavior of the interface between an aluminum plate (modeled as a classical Cauchy continuum) and a metamaterial with specific microstructure (modeled via a relaxed micromorphic model). To show the validity of the enriched continuum modeling framework previously introduced we will compare it with direct FEM simulations performed with the software COMSOL Multiphysics[®].

4.1.1 Microstructure and FEM analysis of a phononic metamaterial

In a previous work [132], it was shown that the analysis of bulk wave propagation in a metamaterial with periodic cross-like holes (see Figure 51) can be achieved using the relaxed micromorphic model. More particularly, the parameters of the relaxed model are fit by superimposing the dispersion curves obtained via the relaxed model to those obtained via a Bloch wave analysis (Figure 52). The details of the Bloch wave analysis can be found in [132]; here we limit ourself saying that this study is based on the application of periodic conditions to the microstructure and a subsequent modal analysis.

The transmission spectra for a Cauchy-material/metamaterial interface are determined via FEM according to the model represented in Figure 53. An external excitation is applied on the left side by imposing a unitary harmonic displacement and an analysis for different frequencies is performed by using the structural package of COMSOL Multiphysics[®]. The incident wave propagates in the first part of the geometry which consists in

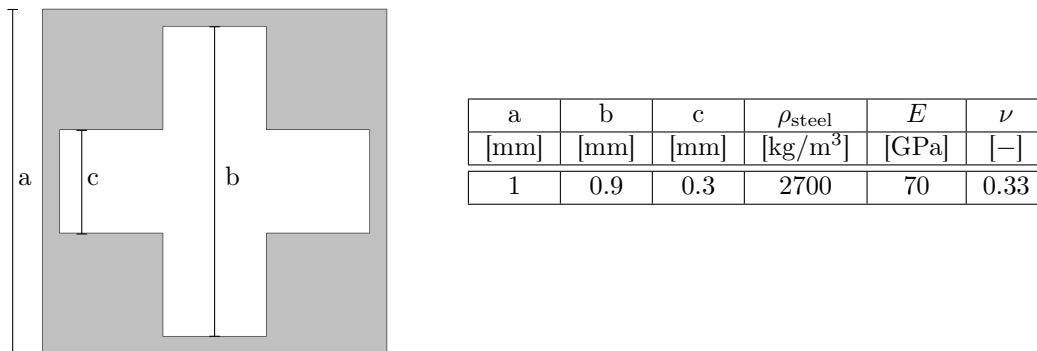


Figure 51: Microstructure of the considered metamaterial (left), values of the elastic parameters of the base material (aluminum) and geometric parameters relative to the unit cell (right).

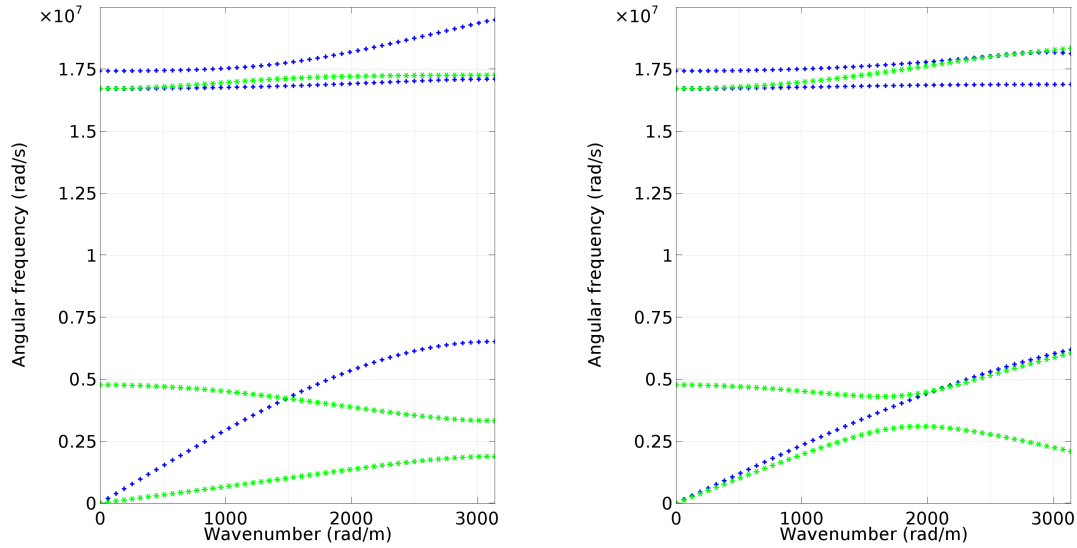


Figure 52: Dispersion curves for waves propagating at 0° (left) and 45° (right) obtained with a Bloch wave analysis of the cell shown in Figure 51.

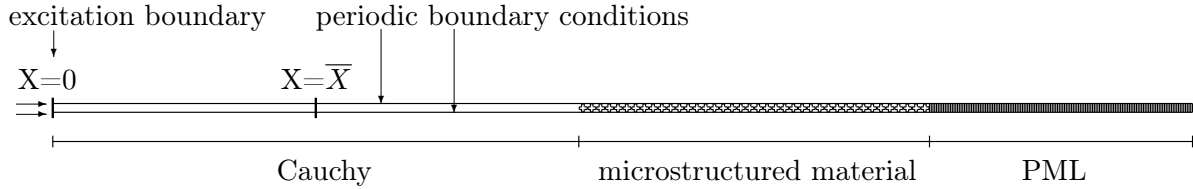


Figure 53: Schematic representation of the FEM model for the determination of the transmission spectrum, as implemented in COMSOL Multiphysics®.

a homogeneous strip of the Cauchy material. After a length of 0.6 m an array of 40 unit cells with cross-like holes of the type described in Figure 51 is added. When the wave arrives at the interface, it is partially reflected and partially transmitted. Finally, a Perfectly Matched Layer (PML) is added at the end of the strip to dissipate the transmitted wave and avoid spurious reflections in the metamaterial. On the upper and lower boundary, a periodic condition is applied to impose the propagation along the strip direction, thus reproducing the condition of plane wave propagation. The thickness of the strip is set to be equal to the height of the unit cell.

We are considering an interface between a classical Cauchy continuum on the $-$ side and a microstructured material on the $+$ side. The object is to see how much energy is transmitted through the interface. A priori, we have no information about the wave propagation in the microstructured material but the propagation in the homogeneous Cauchy continuum can be expected to be planar if the source is far enough from the interface. Therefore, we expect to find longitudinal waves propagating with wavenumbers $k_l = \pm \frac{\omega}{c_l}$ and transverse waves with $k_t = \pm \frac{\omega}{c_t}$, where $c_l = \sqrt{\frac{\lambda+2\mu}{\rho}}$ and $c_t = \sqrt{\frac{\mu}{\rho}}$. The plus or minus sign in the wavenumber is due to the possibility that the waves can travel in both directions. Thus, we have that the waveform solution in the Cauchy material can be written as:

$$u_1^-(X, t) = u_1^i(X, t) + u_1^r(X, t), \quad u_2^-(X, t) = u_2^i(X, t) + u_2^r(X, t), \quad u_3^-(X, t) = u_3^i(X, t) + u_3^r(X, t),$$

where, as before, we set:

$$\begin{aligned} u_1^i(X, t) &= \bar{\alpha}_1 e^{i(\frac{\omega}{c_l} X - \omega t)}, & u_1^r(X, t) &= \alpha_1 e^{i(-\frac{\omega}{c_l} X - \omega t)}, \\ u_2^i(X, t) &= \bar{\alpha}_2 e^{i(\frac{\omega}{c_t} X - \omega t)}, & u_2^r(X, t) &= \alpha_2 e^{i(-\frac{\omega}{c_t} X - \omega t)}, \\ u_3^i(X, t) &= \bar{\alpha}_3 e^{i(\frac{\omega}{c_t} X - \omega t)}, & u_3^r(X, t) &= \alpha_3 e^{i(-\frac{\omega}{c_t} X - \omega t)}. \end{aligned} \quad (\text{IV.106})$$

Given the frequency ω of the traveling wave, the solution is hence known except for the 6 amplitudes $\bar{\alpha}_i$ and α_i ($i = 1, 2, 3$).

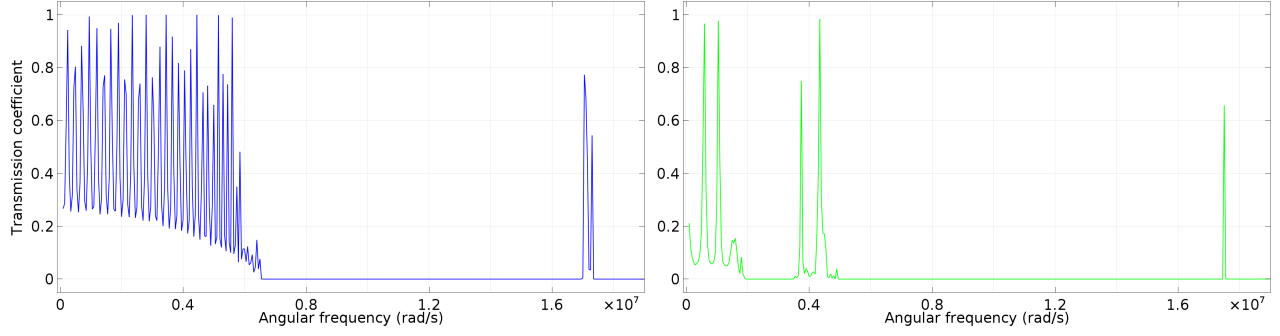


Figure 54: Transmission coefficient as function of frequency for an incident longitudinal (top) and transverse (bottom) wave for the FEM model.

To evaluate the unknown amplitudes in Equations (IV.106), we can use the direct solution obtained via the FEM simulation. In particular, the solution for the displacement field obtained via the FEM code can be interpreted as the solution at a given instant (e.g. $t = 0$) for every point of the domain. Considering the points $X = 0$ and $X = \bar{X}$ (see Figure 53) and the instant $t = 0$, we can set a system of equations to compute the unknown amplitudes; we write:

$$\begin{aligned} u_1^-(0, 0) &= \bar{\alpha}_1 + \alpha_1, & u_2^-(0, 0) &= \bar{\alpha}_2 + \alpha_2, & u_3^-(0, 0) &= \bar{\alpha}_3 + \alpha_3, & \text{(IV.107)} \\ u_1^-(\bar{X}, 0) &= \bar{\alpha}_1 e^{i \frac{\omega}{c_t} \bar{X}} + \alpha_1 e^{-i \frac{\omega}{c_t} \bar{X}}, & u_2^-(\bar{X}, 0) &= \bar{\alpha}_2 e^{i \frac{\omega}{c_t} \bar{X}} + \alpha_2 e^{-i \frac{\omega}{c_t} \bar{X}}, & u_3^-(\bar{X}, 0) &= \bar{\alpha}_3 e^{i \frac{\omega}{c_t} \bar{X}} + \alpha_3 e^{-i \frac{\omega}{c_t} \bar{X}}. \end{aligned}$$

where $u_i^-(0, 0)$ and $u_i^-(\bar{X}, 0)$ are known from the results of the FEM simulation.

From this system, we can evaluate the unknown amplitudes and, therefore, the incident and reflected flux by using equation (IV.87). Finally, the reflection and transmission coefficients can be computed as:

$$R = \frac{J_r}{J_i}, \quad T = 1 - R. \quad \text{(IV.108)}$$

We note that this semi-analytical procedure is valid only if the propagation of waves in the Cauchy material is planar in the FEM solution. It can happen, usually at high frequencies, that the resulting vibrational mode does not respect this assumption and, therefore, the transmission spectra obtained applying this method may not be completely correct. However, in the range of frequencies considered here, the solution is constant along the section and the waveform evaluated with the resulting amplitudes is perfectly described by the solution obtained using Equations (IV.106) and (IV.107), thus confirming the validity of the procedure.

Actually, the accuracy of the peaks' height in Figure 54 depends on the frequency step of the calculation and can be more effectively described by choosing smaller frequency-steps close to the point of interest.

4.1.2 Identification of the material parameters

Macroscopic parameters The first step towards the identification of the relaxed micromorphic model's parameter is to find the equivalent macroscopic first gradient material. The first relation that must be imposed is that the macroscopic material has a density which is the average of the considered metamaterial, namely:

$$\int_{\Omega} \rho d\Omega = \int_{\boxplus} \rho_{\text{steel}} dA \quad \Longrightarrow \quad \rho = \frac{1}{|\Omega|} \int_{\boxplus} \rho_{\text{steel}} dA. \quad \text{(IV.109)}$$

Afterwards, it is possible to determine the macroscopic elastic moduli μ_M and λ_M via the tangents in 0 to the acoustic branches that, in the relaxed micromorphic model, are known (see IV.1.3 and IV.2.1):

$$\frac{\partial \omega_{\text{TA}}}{\partial k}(0) = \sqrt{\frac{\mu_M}{\rho}} \quad \Longrightarrow \quad \mu_M = \rho \left(\frac{\partial \omega_{\text{TA}}}{\partial k}(0) \right)^2, \quad \text{(IV.110)}$$

$$\frac{\partial \omega_{\text{LA}}}{\partial k}(0) = \sqrt{\frac{2\mu_M + \lambda_M}{\rho}} \quad \Longrightarrow \quad \lambda_M = \rho \left(\frac{\partial \omega_{\text{LA}}}{\partial k}(0) \right)^2 - 2\mu_M, \quad \text{(IV.111)}$$

These parameters are enough to describe the metamaterial as a first gradient model. However, the approximation would be sensible only for a body which is large enough to assure that the effect of the underlying microstructure is negligible. Furthermore, neither dispersive behavior nor optic branches of the dispersion curves could be described.

Relations between the elastic moduli and the free micro-inertiae We can now use the known values of the macroscopic parameters, as well as those of the cut-offs, to compute the values of some elastic parameters of the relaxed micromorphic model, i.e.:

$$\left\{ \begin{array}{l} \omega_s = \sqrt{\frac{2(\mu_e + \mu_m)}{\eta_1}} \\ \mu_M = \frac{\mu_e \mu_m}{\mu_e + \mu_m} \end{array} \right. \Rightarrow \left\{ \begin{array}{l} \mu_e = \frac{\eta_1 \omega_s^2}{4} \left(1 \pm \sqrt{1 - \frac{8\mu_M}{\eta_1 \omega_s^2}} \right) \\ \mu_m = \frac{\eta_1 \omega_s^2}{4} \left(1 \mp \sqrt{1 - \frac{8\mu_M}{\eta_1 \omega_s^2}} \right) \\ \eta_1 > \frac{8\mu_M}{\omega_s^2} \end{array} \right. \quad (\text{IV.112})$$

$$\omega_r = \sqrt{\frac{2\mu_c}{\eta_2}} \Rightarrow \left\{ \begin{array}{l} \mu_c = \frac{\eta_2 \omega_r^2}{2} \\ \eta_2 > 0 \end{array} \right. \quad (\text{IV.113})$$

$$\left\{ \begin{array}{l} \omega_p = \sqrt{\frac{3(\kappa_e + \kappa_m)}{\eta_3}} \\ \kappa_M = \frac{\kappa_e \kappa_m}{\kappa_e + \kappa_m} \end{array} \right. \Rightarrow \left\{ \begin{array}{l} \kappa_e = \frac{\eta_3 \omega_p^2}{6} \left(1 \pm \sqrt{1 - \frac{12\kappa_M}{\eta_3 \omega_p^2}} \right) \\ \kappa_m = \frac{\eta_3 \omega_p^2}{6} \left(1 \pm \sqrt{1 - \frac{12\kappa_M}{\eta_3 \omega_p^2}} \right) \\ \eta_3 > \frac{12\kappa_M}{\omega_p^2} \end{array} \right. \quad (\text{IV.114})$$

With these derived relations, we have obtained the entire set of elastic moduli depending on the free micro-inertiae. Furthermore, assuming that the elastic moduli are real and positive we also obtain limiting values for η_1 , η_2 and η_3 to be used as a first step in the iterative process for their determination.

Determination of the micro-inertiae We have defined all the elastic parameters apart from the characteristic length L_c , the gradient and free micro-inertiae, leaving us with 7 free parameters left. The determination of the micro-inertiae should be made imposing the asymptotic behavior of the dispersion curves. In particular, considering the internal variable model with non-vanishing gradient micro-inertiae we find that the three limiting values of the longitudinal curves depend on $\eta_1, \eta_3, \bar{\eta}_1, \bar{\eta}_3$ while the transverse curves depend on $\eta_1, \eta_2, \bar{\eta}_1, \bar{\eta}_2$. As remarked while considering the form of the equations, we can always consider the gradient micro-inertia $\bar{\eta}_1 = 0$ ¹. Therefore, we obtain that the longitudinal curves depend on $\eta_1, \eta_3, \bar{\eta}_3$ while the transverse curves depend on $\eta_1, \eta_2, \bar{\eta}_2$.

The remaining parameters should be chosen imposing the asymptotic behavior of the dispersion curves. However, the analytical expression of the asymptotes is very complex, being the solution of a third order equation in ω^2 , therefore the procedure used for the fitting of the micro-inertiae is iterative. The first set of values considered for the free micro-inertiae is composed by the lower bounds $\eta_1 = \frac{8\mu_M}{\omega_s^2}$ and $\eta_3 = \frac{12\kappa_M}{\omega_p^2}$, and by $\eta_2 = \eta_1$. For the gradient micro-inertia, we assume at first $\bar{\eta}_2 = \eta_2$ and $\bar{\eta}_3 = \eta_3$. Furthermore, we start by setting $L_c = 0$, so assuming a negligible presence of non-local effects. As a matter of fact, the micro-structure studied in this section can be effectively described considering a vanishing characteristic length $L_c = 0$.

In [132], the material parameters of the relaxed micromorphic model were determined for the considered micro-structure following the proposed procedure. The values are shown in Table 4.1. The results of the fitting procedure proposed are shown in Figure 55 in which the dispersion curves obtained via the relaxed micromorphic model are compared to those issued via a Bloch wave analysis. In the same Figure, we

¹ Given any set of micro-inertiae $\bar{\eta}_1, \bar{\eta}_2$ and $\bar{\eta}_3$, the set $\bar{\eta}_1^* = 0, \bar{\eta}_2^* = \bar{\eta}_1 + \bar{\eta}_2$ and $\bar{\eta}_3^* = 2\bar{\eta}_1 + \bar{\eta}_3$ does not change the form of the equilibrium equations nor of the dispersion curves. Therefore, setting $\bar{\eta}_1 = 0$ does not preclude any possibility for the relaxed micromorphic model.

ρ	μ_c	λ_{micro}	μ_{micro}	λ_e	μ_e	L_c
[kg/m ³]	[GPa]	[GPa]	[GPa]	[GPa]	[GPa]	[m]
1323	0.272	19.8	0.737	17.7	3.857	0

η_1	η_2	η_3	$\bar{\eta}_1$	$\bar{\eta}_2$	$\bar{\eta}_3$	$\bar{\eta}_2$ from [132]	$\bar{\eta}_3$ from [132]
[kg/m]	[kg/m]	[kg/m]	[kg/m]	[kg/m]	[kg/m]	[kg/m]	[kg/m]
3.25×10^{-5}	3.25×10^{-5}	4×10^{-4}	0	2×10^{-4}	6×10^{-4}	0.3×10^{-4}	1.8×10^{-4}

Table 4.1: Values of the material parameters (top) and of the micro-inertia parameters (bottom) of the weighted relaxed micromorphic model. All parameters are the same as the ones measured in [132] except for $\bar{\eta}_2$ and $\bar{\eta}_3$.

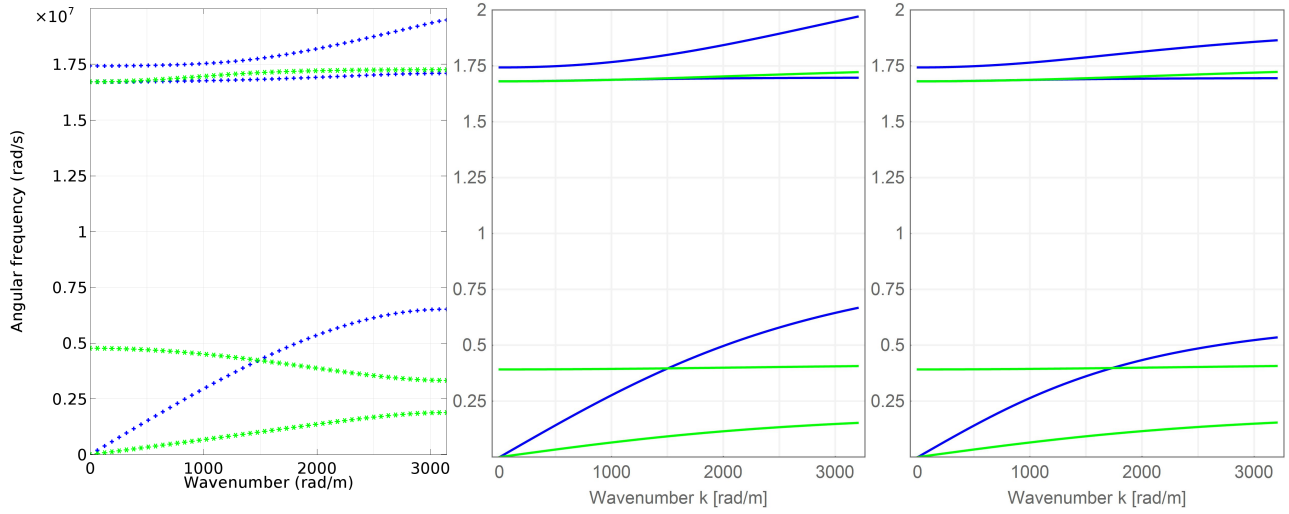


Figure 55: Comparison between the dispersion curves obtained with a Bloch wave analysis of the cell shown in Figure 51 (left) and dispersion curves for the relaxed micromorphic model with the parameters measured in [132] (center) and with the slightly modified set of the relaxed parameters value proposed in Table 4.1 (right). Longitudinal branches are in blue while the transverse ones are in green.

also propose a slight variation of the parameters fitted in [132] which may provide a more precise result when considering the transmission spectra. Indeed, the fitting given in [132] is the best one possible when considering a finite interval of wavenumbers. In order to fit at best the reflection and transmission spectrum, the fitting of the dispersion curves alone may not be sufficient, since the horizontal asymptotes are approached for bigger wavenumbers (smaller wavelengths). The third graph in Figure 55 provides the most precise results for the band gap interval as well as for the reflection/transmission spectra. All the material parameters considered are given in Table 4.1. The objective here is to show that the parameters derived in [132] using the bulk dispersion curves alone are true material constants that allow to describe the mechanical behavior of the considered metamaterial even when considering a complex (meta-) structure of the type presented in Figure 51. In particular, we will show that such parameters properly describe the mechanical behavior of the chosen metamaterial so well that the behavior of that metamaterial can be successfully described in more complex situations as the reflection and transmission at discontinuity interfaces of the material properties. The interest of using the relaxed micromorphic model resides in the unique possibility it offers to exploit only few material parameters for the description of the mechanical behavior of an otherwise rather complicated system.

For a comprehensive description of Figure 55, we refer the reader to [132]. Here, we limit ourselves to point out the very good description of the band-gap and of the general behavior. The only difference between the two approaches is given by the absence of a decreasing behavior in the first transverse optic mode. However, the average behavior of that vibrational mode is still well described. As a matter of fact, a decreasing behavior of the dispersion curves can be also obtained when considering the non-local behavior of the relaxed micromorphic model (L_c different from zero). The numerical investigation of the fully non-local case deserves extra attention and will be considered in a forthcoming paper. Indeed, in order to unveil

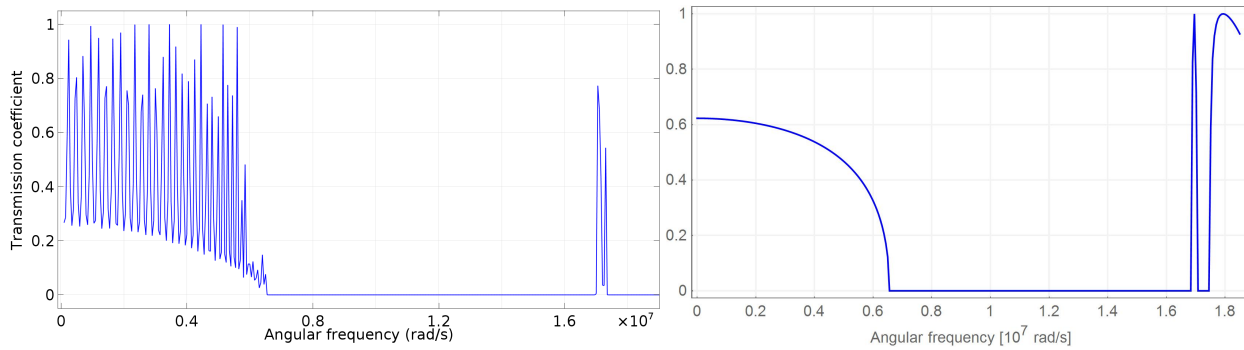


Figure 56: Transmission coefficient as function of frequency for an incident longitudinal wave for the FEM model (left) and for the relaxed micromorphic model (right).

the full effect of non-locality of the relaxed micromorphic model the characteristic length L_c plays a crucial role, together with the conjoint introduction of an extra micro-inertia term associated to the time derivative of $\text{Curl}P$. We will treat such a delicate extended case in a subsequent work which will finally show the full potentiality of the relaxed micromorphic model that is representative of the behavior of the considered microstructures medium for wavelengths spanning in a very large range up to arriving to small wavelengths comparable to the size of the unit cell.

4.1.3 Validation of the relaxed micromorphic model via the transmission spectra

In this subsection, we compare the resulting transmission spectra for both the FEM model, as computed with the semi-analytical method proposed in section IV.4.1.1, and the relaxed micromorphic one. In Figure 56, we show the spectra obtained considering a longitudinal traveling wave arriving at the interface for the FEM model and for the relaxed micromorphic continuum.

The average description of the transmission spectrum at the interface between a homogeneous material and a microstructured one is very accurate. The transmission coefficient starts around 0.6 and becomes zero at around 0.7×10^7 rad/s in both the models and the first peak, even if higher in the relaxed micromorphic model, is comparable. For higher frequencies, the relaxed micromorphic model shows a second peak, while the FEM does not seem to allow any transmission. It is also useful to point out that, in the FEM model, the propagation of the wave through the interface is somehow present but the amplitude of the wave decreases inside the microstructured metamaterial becoming zero after approximately 7 unit cells, see Figure 57 (left). On the other hand, for the range of frequencies of the central band gap the amplitude of the displacements becomes zero near the interface and the reflection can be entirely attributed to the presence of the interface (see Figure 57 (right)). This difference seems to indicate that there is transmission at the interface for the second optic mode, but the wave continues to reflect inside the microstructured material.

As a matter of fact, for the frequencies considered in Figure 57(left), the corresponding wavelengths of the incident wave start to become very small with respect to the size of the cell, so that Bragg scattering is sensible to take place. This fact is somehow captured by the FEM model, but cannot be captured by the relaxed model which is intrinsically a continuum model. In this case the frequency is too high in order to ensure the hypothesis of continuum model is still completely representative of reality.

The same analysis can be done for transverse waves, as shown in Figure 58. In this case, the approximation given by the continuous model is even better because no extra peak can be found for higher frequencies. The two transmission peaks are fully described even if the value of the transmission coefficient is not exactly analogous. As before, the height of the peaks is better caught by the FEM model when adding more frequency points. Also, the width of the peaks is comparable, only with the exception of the second one.

4.2 The steel plate with liquid-filled round holes

In this section we are interested in the modeling of the mechanical behavior of a particular metamaterial (phononic crystal) which has been known to inhibit elastic wave propagation on an experimental basis (see [127]).

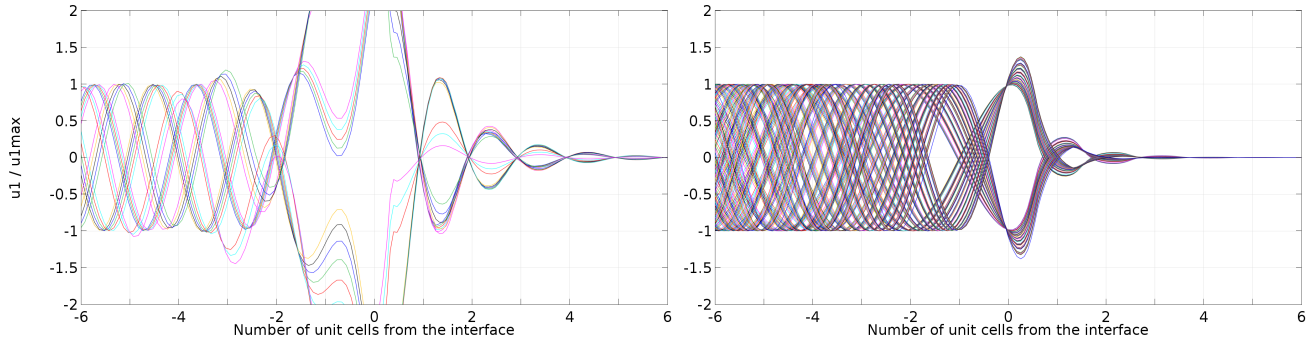


Figure 57: Dimensionless displacement on the bottom edge for the vibrating modes in the range of angular frequencies 1.75×10^7 – 1.9×10^7 rad/s (left) and 0.80×10^7 – 1.5×10^7 (right) (FEM simulations).

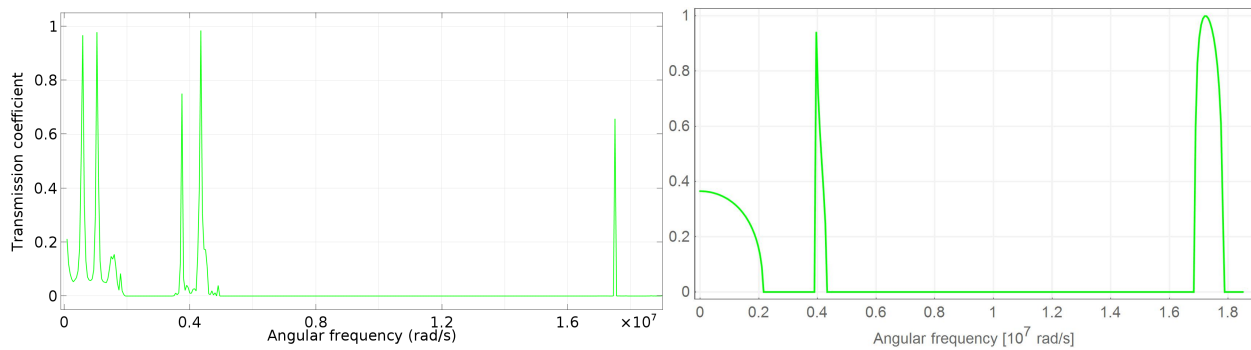


Figure 58: Transmission coefficient as function of frequency for an incident transverse wave for the FEM model (left) and for the relaxed micromorphic model (right).

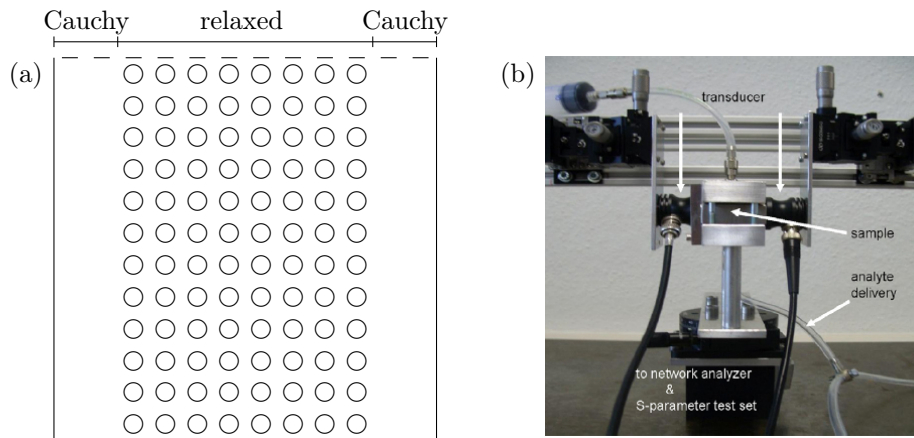


Figure 59: Schematics of the sample structure (a) and the experimental setup (b) ([127, Figure 1(b)]).

The structure presented, which is schematically shown in Figure 59(a) consists of a steel plate with liquid-filled holes in square array. The lattice constant, denoted by a , is 3.0 mm, the thickness t of the plate is 15 mm, the diameter d of the hole is 1.8 mm and the width of the cavity, w , is 1.5 mm.

4.2.1 Experiments of wave transmission at a Cauchy/phononic-crystal interface

We show in Figure 60 the obtained experimental transmission spectrum of the considered phononic crystal, i.e. with 8 rows of liquid-filled holes (see Figure 59(a)) as a function of the frequency of the traveling wave. Given the geometry of the specimen shown in Figure 59, a longitudinal wave is sent in the Cauchy medium on the left side and the transmission coefficient is evaluated when the wave leaves the metamaterial on the

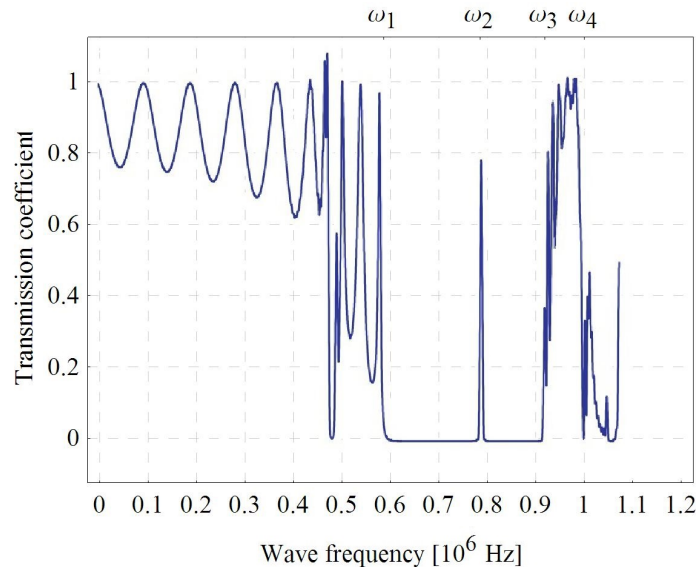


Figure 60: Transmission spectrum of the phononic crystal presented in Figure 59a, with liquid-filled holes [127, Figure 2b].

opposite side. The transmission spectrum is shown in Figure 60. With liquid filled holes the band gap edge crosses the -3 dB-level at $\omega_1 = 586 \text{ kHz}$. Transmission of acoustic waves is suppressed until the upper edge at $\omega_3 = 918 \text{ kHz}$ but a single peak arises at $\omega_2 = 793 \text{ kHz}$, which can be attributed to the resonance of the liquid-filled holes. The periodic variation of transmission at lower frequencies is caused by Bragg resonances. The second transmission band extends to about $\omega_4 \simeq 1 \text{ MHz}$.

4.2.2 Identification of the parameters

In this subsection we present the procedure that we used in order to fit in the best possible way the maximum possible number of parameters of our relaxed micromorphic model on the available data based on a real phononic crystal. To start with, we assume the macroscopic mass density to be known as the averaged density of steel with fluid-filled holes. In particular we choose $\rho = 5000 \text{ kg/m}^3$. Nevertheless, we verify a posteriori that the value of ρ indeed does not sensibly affect the profile of the reflection coefficient for frequencies between 0 and 1 MHz. This fact is sensible if, in accordance to [140, 141] and to Figure 41, we notice that the parameter ρ only intervenes in the definition of the oblique asymptote $c_p = \sqrt{\frac{\lambda_e + 2\mu_e}{\rho}}$ for longitudinal waves. Such asymptote governs the slope of the optic wave LO1 which starts playing a significant role for frequencies higher than ω_p . In the considered example, ω_p will be set to be equal to ω_3 which is experimentally found to be close to 1 MHz. For frequencies higher than 1 MHz variations of ρ could eventually produce more tangible changes in the profile of the reflection coefficient.

To perform the fitting of the remaining parameters, we started by imposing the following identities:

$$\begin{aligned} \omega_l^1(\mu_e, \mu_m, \lambda_e, \lambda_m, \eta) &= \omega_1, & \omega_p(\mu_e, \mu_m, \lambda_e, \lambda_m, \eta) &= \omega_3, \\ \omega_l^2(\mu_e, \mu_m, \lambda_e, \lambda_m, \eta) &= \omega_2, & \omega_s(\mu_e, \mu_m, \eta) &= \omega_2 - 8 \text{ kHz}. \end{aligned} \quad (\text{IV.115})$$

where we recall that the explicit expressions of ω_l^1 , ω_s , ω_l^2 , ω_p as functions of the elastic parameters of the relaxed micromorphic model are given in equations (IV.104). We hence have 4 conditions to determine the 5 elastic parameters $\mu_e, \mu_m, \lambda_e, \lambda_m, \eta$ setting in a first instance $L_c = 0$. If analogous experiments as the one proposed in [127] for longitudinal waves would be reproduced on the same metamaterial but for transverse waves, extra conditions on the parameters of the relaxed micromorphic model would be available that would permit a more accurate fitting.

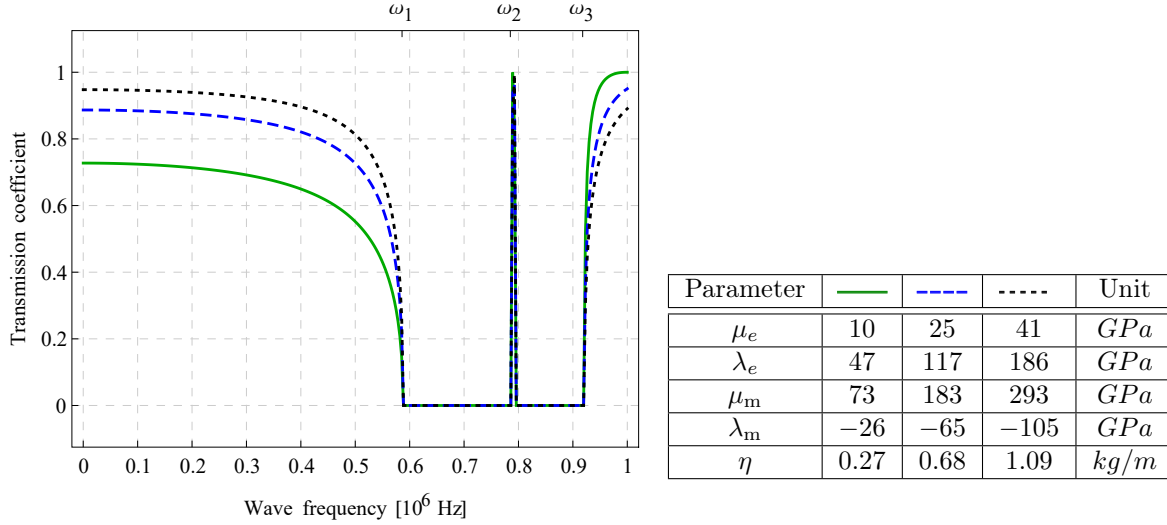


Figure 61: Profiles of the transmission coefficients obtained for different arbitrary values of the parameter μ_e (left).

Table 4.2: Values of the constitutive parameters obtained via the solution (IV.116) for arbitrary values of the parameter μ_e (right).

(a)

Condition	Value	Unit
$\omega_l^1 = \omega_1$	586	<i>kHz</i>
$\omega_s = \omega_2 - 8 \text{ kHz}$	785	<i>kHz</i>
$\omega_l^2 = \omega_2$	793	<i>kHz</i>
$\omega_p = \omega_3$	918	<i>kHz</i>

(b)

Parameter	Value	Unit
μ_e	25	<i>GPa</i>
λ_e	117	<i>GPa</i>
μ_m	183	<i>GPa</i>
λ_m	-65	<i>GPa</i>
η	0.68	<i>kg/m</i>

Table 4.3: Conditions used for the parameters identification (a) and corresponding values of the obtained elastic parameters of the relaxed micromorphic model (b).

We start by numerically solving the system of four equations (IV.115) with respect to the parameters $\lambda_e, \mu_m, \lambda_m$ and η leaving free the parameter μ_e . The obtained solution is²

$$\lambda_e = 4.58 \mu_e, \quad \mu_m = 7.21 \mu_e, \quad \lambda_m = -2.57 \mu_e, \quad \eta = 2.66 \cdot 10^{-11} \mu_e. \quad (\text{IV.116})$$

The free parameter μ_e is then varied in order to evaluate its influence on the reflection coefficient. A parametric study on the free coefficient μ_e is performed giving rise to the profiles of the transmission coefficients shown in Figure 61 with the parameters shown in Table 4.2.

At this point, we are able to choose the value of the parameter μ_e which respects conditions (IV.116) and which fits at best the profile of Figure 60. We conclude that, based on the described fitting procedure, the values of the parameters that best fits the profile associated to the real phononic crystal are those presented in Table 4.3b. Figure 62 shows the comparison between the profile of the transmission coefficient obtained in [127] for a real phononic crystal and the one obtained with our relaxed micromorphic model when setting $L_c = 0$.

We see a very good fitting can be obtained up to frequencies of the order of 1 *MHz*. In particular, the oscillatory behavior observed for lower frequencies and which, according to the authors of [127], is due to Bragg scattering phenomena is caught by our model in an “averaged” sense.

The fitting for higher frequencies is almost perfect up to reaching 1 *MHz*, while for frequencies higher

²We explicitly mention that, additionally to the solution (IV.116) we obtain a second solution which, nevertheless must be excluded since it violates the positive definiteness of the strain energy density W . Solution (IV.116) is then the only possible solution which can be used to fit the profile of the transmission coefficient. We checked that it is possible to leave free any other parameter rather than μ_e to perform the desired fitting of the transmission coefficient and that it yields comparable results for the obtained values of the constitutive parameters.

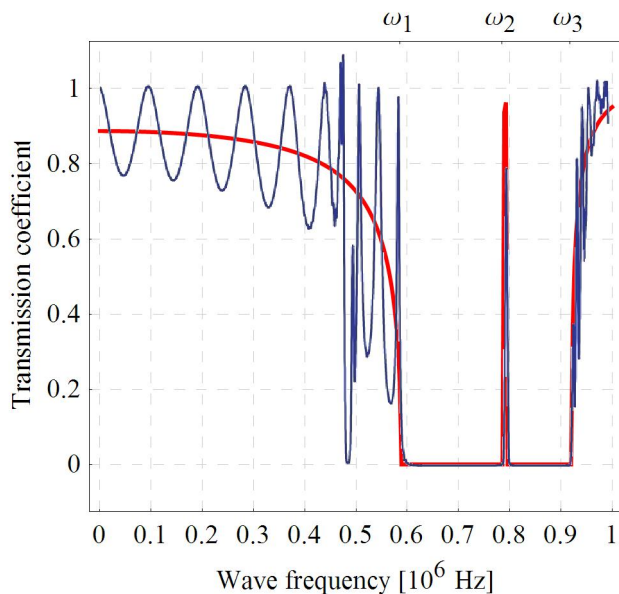


Figure 62: Comparison of the profile obtained in [127] based on a real metamaterial and the one obtained with the relaxed micromorphic model with the values given in Table 4.3 and $L_c = 0$.

than 1 *MHz* the relaxed micromorphic model loses its predictivity due to the fact that the corresponding wavelengths are so small that the continuum hypothesis is sensible to become inaccurate.

We need to explicitly remark that the peak of reflection, which is obtained around the frequency ω_2 and that is experimentally related to a resonant behavior of the fluid inside the walls is slightly overestimated by the simulation via the relaxed micromorphic model with respect to the one observed in [127]. This peak magnification can be related to the fact that no dissipation is accounted for in our model, while the fluid viscosity may perhaps play here a non-negligible role.

In what follows, we will show that we can estimate the characteristic length L_c of the metamaterial experimentally tested in [127] to be comparable to the order of magnitude of the diameter of the embedded microstructure. We will also show that, even if the estimated value of L_c is non-negligible with respect to the characteristic size of the embedded microstructure, its effect on the amount of energy which is transmitted in the considered metamaterial is very small. This means that the error which is introduced if one uses an internal variable model instead of a relaxed micromorphic one is energetically small. On the other hand, non-locality is a fundamental feature of metamaterials with heterogeneous microstructure and as such it should always be included in their modeling. As a matter of fact, non-local effects are sensible to become more and more important when the contrast in the mechanical properties between adjacent unitary cells at the microscopic level becomes more pronounced.

As a general rule, we claim that the degenerate limit case $L_c = 0$ can be used for a first rough fitting of the elastic parameters of the relaxed micromorphic model. After that, the characteristic length L_c must be switched on in order to achieve a more accurate fitting of the experimental results. This last operation will allow for the estimate of non-local effects in real metamaterials.

The relaxed micromorphic model allows for the possibility of including non-local effects in band-gap metamaterials. In the next section we will have the twofold task of:

- fitting at best our constitutive parameters on a real metamaterial,
- estimate the order of magnitude of non-localities in such metamaterial.

We now come back to the point where we set $L_c = 0$ in order to start fitting our constitutive parameters (see subsection IV.3.3.1). This fact allowed us to obtain here the values of the elastic parameters of our model by a first fitting with the profile of the transmission coefficient (see Table 4.3).

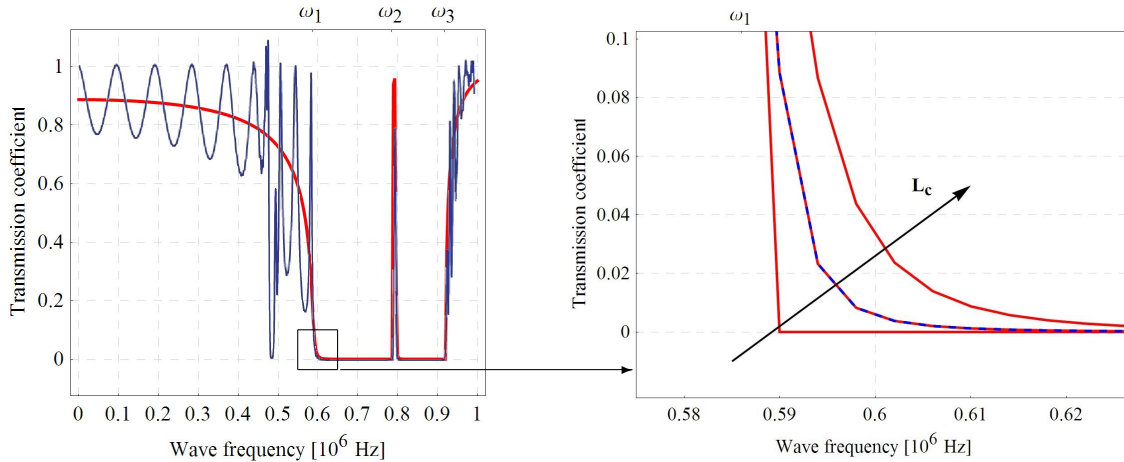


Figure 63: Fitting of the parameter L_c on the experimental profile of the transmission coefficients.

On the other hand, as expected, switching on the characteristic length L_c allows an even better fitting as shown in Figure 63.

Indeed, we notice from Figure 63 that the degenerate limit case $L_c = 0$ lets the calculated transmission coefficient slightly deviate from the experimental one (sharp corners). Small variations of the numerical profile can be perceived as far as $L_c \in [0, 0.5 \text{ mm})$. On the other hand, as far as $L_c = 0.5 \text{ mm}$ an almost perfect fitting is achieved (dashed line in Figure 63 on the right)). This means that we have been able to estimate the non-locality of the considered metamaterial to be of the order of 0.5 mm , i.e. $\sim 1/3$ of the diameter of the holes.

We need to explicitly say that the value of the macroscopic density ρ might slightly affect the variation of the transmission coefficient as a function of L_c . Nevertheless, we need to consider a density of 1 order of magnitude higher ($50\,000 \text{ kg/m}^3$) in order to appreciate a sensible deviation of the profiles shown in Figure 63. We leave to a subsequent work the aim of determining also the macroscopic mass density ρ by using extra conditions provided by the fact of considering also measurements on transverse waves.

The determination of the parameter L_c completes the fitting of the elastic parameters of our relaxed micromorphic model on the band-gap metamaterial experimentally tested in [127] (see also Table 4.3). The Cosserat couple modulus parameter μ_c cannot be measured as far as only longitudinal waves are considered and, thus, it remains to be determined. We have to explicitly remark that if an analogous fitting procedure would have been possible for transverse waves, having access to the related transmission spectrum.

The main scope of the present part, that we think to have successfully achieved, is threefold:

- we give the very first estimation of the maximum possible number of constitutive parameters of the relaxed micromorphic model based on a simple measurement of transmission of longitudinal waves at a Cauchy/band-gap-metamaterial interface
- we give the very first evidence of the non-locality in band-gap metamaterials based upon real experiments
- we elucidate the physical meaning of the constraint which has been introduced in [141] and that we called “*internal clamp with free microstructure*”: such constraint allows for the description of continuity of displacement in the solid phase at the Cauchy/metamaterial interface, while the fluid in the embedded microstructure is free to vibrate. It is exactly the freedom which is left to the micro-motions that allows for the description of the local resonant peak around the frequency ω_2 which is indeed not possible for other types of constraints (see [141]).

Conclusion

Metamaterials are artifacts composed by microstructural elements assembled in periodic or quasi-periodic patterns, giving rise to materials with unorthodox properties. For some of these metamaterials, the presence of a microstructure allows for macroscopic wave-inhibition. More particularly, this means that, given the topology of the microstructure, when the material is solicited at frequencies that fall in the band-gap region, any of the possible micro-motions is activated at such frequencies. Hence, this results in the impossibility of waves to travel in the considered metamaterial. The structure of the relaxed micromorphic model allows to describe complete frequency band-gaps with the simplest possible micro-inertia and without losing the non-locality of the model. It is decisive to use $\text{Curl } P$ instead of the full micro-distortion gradient ∇P and to take a positive Cosserat couple modulus $\mu_c > 0$. Considering that non-locality is an intrinsic characteristic feature of micro-structured materials, especially when high contrasts of the mechanical properties occur at the micro-level, models that allow for its description are a necessary requirement.

In this part, we analyzed the behavior of the relaxed micromorphic model in the case of plane wave propagation. Furthermore, we derived the set of necessary and sufficient conditions that have to be imposed on the constitutive parameters of the relaxed micromorphic model in order to guarantee

- positive definiteness;
- real wave velocity;
- Legendre–Hadamard strong ellipticity condition.

We showed that, on the one hand, definite positiveness implies real wave propagation, while on the other hand, real wave propagation is not guaranteed by the strong ellipticity condition. We conclude that in strong contrast to the case of classical isotropic linear elasticity, where the three concepts are known to be equivalent, in the case of the relaxed micromorphic continua only definite positiveness of the strain energy density can be considered to be a good criterion to guarantee real wave speeds in the considered media. The proposed considerations can be extended to all enriched continua where the equivalence between the three notions is far from being straightforward.

Furthermore, we made a review of some of the available isotropic, linear-elastic, enriched continuum models for the description of the dynamical behavior of metamaterials. We show that the relaxed micromorphic model is the only non-local enriched model which is able to describe band-gaps when considering a kinetic energy independently accounting for micro and macro motions. Considering an inertia term which couples the micro-motions to the macroscopic motions, also other non-local models exhibit the possibility of describing band-gap behaviors. Nevertheless, the relaxed micromorphic model is still the more effective one to describe (multiple) band-gaps and non-local effects in a realistic way. In fact, even with the addition of the new micro-inertia term, the relaxed model is able to account for the description of two band-gaps, in contrast to the single band-gap allowed by the Mindlin-Eringen model. Finally, the internal variable model with the new kinetic energy terms allows for the description of up to three band gaps. Nevertheless, the overall trends shown by the dispersion curves turn to be quite unrealistic due to the fact that all the branches of the dispersion curves show very low or no dispersion at all.

Afterwards, we consider the application of the relaxed micromorphic model to two real phononic metamaterials, namely:

- a steel plate with cross-shaped holes;
- a steel plate with liquid-filled round holes.

For the first metamaterial, we provide a validation of the material parameters of the relaxed micromorphic model derived in [132] by means of the study of the transmission properties of a rather simplified meta-structure made up of 40 unit cells of a metamaterial made of periodic cross-like holes [132]. In particular, the interface between a homogeneous solid and this meta-structure is considered and the reflection and transmission coefficients are derived as a function of the frequency. The transmission spectra are computed both via a direct FEM simulation and via a direct implementation of the relaxed model with the material constants derived in [132]. The obtained results show an excellent agreement and the relaxed model revealed to be more than 10 times faster in terms of computational time with respect to the FEM implementation of the same problem.

Considering the steel plate with liquid-filled round holes, we give the very first estimate of the resulting elastic coefficients of the relaxed micromorphic model based upon the experimentally-based transmission spectra presented in [127] which concern the measurement of the transmitted energy as a function of the frequency of the traveling wave for this particular band-gap metamaterial. Restricting our attention to the problem of studying reflection and transmission of longitudinal waves at a Cauchy/relaxed-micromorphic interface, we are able to reproduce the main characteristic features which are observed in [127] for a phononic crystal obtained by means of an aluminum plate with small fluid-filled holes (diameter $\sim 1.8\text{ mm}$). Suitably choosing the values of the parameters of our relaxed micromorphic model, we are able to fit the profile of the transmission coefficient proposed in [127] as a function of the frequency of the traveling waves. Two band-gaps which almost collapse to form a unique band-gap can be observed both in [127] and as a result of the simulations based upon our relaxed micromorphic model.

We conclude recalling the finding that we believe to be the most important to be pointed out. Indeed, we showed by direct comparison of our relaxed micromorphic model with available evidences that non-local effects are an intrinsic feature of band-gap metamaterials. A characteristic length $L_c = 0.5\text{ mm}$ has been estimated for the real phononic crystal studied in [127] which is almost $1/3$ of the diameter of the holes in the embedded microstructure. Even if the energetic contribution associated to the underlying non-locality is very small (only small changes in the transmission coefficient can be appreciated when increasing L_c from 0 to 0.5 mm), such non-locality is intrinsically present in any microstructured material and as such it should be always accounted for when modeling their mechanical behavior. The macroscopic effects of non-localities are sensible to become more and more energetically significant when considering stronger contrasts in the mechanical properties at the microscopic level (e.g. unitary cells with very different stiffnesses). The relaxed micromorphic model should be always used when one wants to model band-gap metamaterials that show non-localities.

On the basis of the results presented here, we can claim that the relaxed micromorphic model is the only macroscopic continuum model known to date which is simultaneously able to account for

- prediction of complete band-gaps in mechanical metamaterials;
- non-local effects (via the introduction of higher order derivatives of the micro distortion tensor in the strain energy density).

The present part represents the first step towards the use of the relaxed micromorphic model for the characterization of the mechanical behavior of metamaterials and for their use in view of meta-structural design in the simplified framework of enriched continuum mechanics. Furthermore, the results presented in this part allow to give the first physical interpretation of the boundary conditions which can be imposed at a Cauchy/relaxed-micromorphic interface based upon a real experiment. Work in progress is focused on the generalization of the results presented here to the anisotropic framework [49] in order to be able to characterize a wider class of metamaterials, thus increasing the interest of using enriched continuum models for realistic meta-structural design.

General conclusion and perspectives

General conclusion and perspectives

For centuries, continuum theories have been used successfully for the description of the mechanical behavior of materials at the macroscopic scale. The idea, which is at the basis of such theories, is that the discrete nature of matter can somehow be neglected when considering sufficiently large pieces of a given material, which can thereby be regarded as a continuum. This fundamental assumption has been used continuously since the 19th century, when Cauchy showed how such “averaged” theories are a powerful tool for determining the mechanical behavior of large-scale engineering structures. Indeed, the advantage of considering a body as a large-scale object, as opposed to viewing each of its atoms separately, is considered nowadays evident.

However, the systematic use of Cauchy theories may sometimes represent a too drastic simplification of reality, since some essential characteristics related to the heterogeneity of their microstructure are implicitly neglected. When considering a scale which is small enough, every material is actually heterogeneous, but this does not affect the mechanical behavior at the engineering scale, in most cases. Therefore, a Cauchy continuum theory is a suitable choice for modeling the macroscopic mechanical behavior of the considered materials in the simplest and most effective way. On the other hand, some materials are heterogeneous even at relatively large scales and, as a consequence, one cannot neglect the effect of their microstructure on the overall mechanical behavior. In such cases, a Cauchy continuum theory may not be sufficient to fully describe the considered material, especially for particular loading and/or boundary conditions. The resulting structure may possess some microstructure-related behaviors; for example in this manuscript we studied the case of:

- fibrous composite reinforcement and the macroscopic effects due to the bending of the yarns at the mesoscopic scale;
- metamaterials and band-gaps due to local resonances.

For those cases we proved that a more complex framework than classical Cauchy continuum theory is needed: Enriched Continuum Theories.

The fibrous composite reinforcements have been thoroughly studied in light of the broad set of engineering applications. This lightweight material possesses very high specific stiffness and it deforms to adapt to complex shapes. The forming process is particularly difficult to describe because, especially before the addition of the resin, the material is strongly inhomogeneous and local effects characterize its macroscopic behavior. The modeling of the forming process, however, could lead to a higher quality product and also to a better cost-efficiency. We showed in this manuscript how a second gradient energy can be used to describe such phenomena. However, the model presented is still not ready for a complex implementation in real engineering applications. Even if we proved how the second gradient model can capture the effects due to the mesoscopic bending of the yarns, a thorough experimental testing is due to define both a non-linear first gradient energy and the parameters in the second gradient energy. The main perspective of the work is to set up an experimental procedure to fully characterize the complex behavior of these materials.

The second example of a macroscopic property due to a microscopic heterogeneity is found in some metamaterials that show an unorthodox behavior with respect to wave propagation. In particular, some of these metamaterials can inhibit wave propagation for certain frequency ranges, usually referred to as “frequency band-gaps”. Conceived by assembling small components and arranging them into periodic or quasi-periodic patterns, these materials are attracting an ever-growing attention both for what concerns its modeling and the relative experiments. Numerous efforts are currently being made to reliably account for the observed band-gaps in the simulation of such metamaterials. The most common models are intrinsically microscopic and based on the use of Bloch’s theorem for periodic microstructures or on numerical homogenization techniques. Nevertheless, a systematic treatment of band-gap modeling based on the spirit of Enriched Continuum Mechanics is still lacking and deserves attention. In this work, we showed how a relaxed micromorphic model

can account for some microscopic-related modes of vibration while remaining in a continuous framework. Furthermore, the needed mathematical tools for the relaxed micromorphic model were derived both in the isotropic and the anisotropic cases for which the needed existence and uniqueness result can be found in the literature.

Only in the framework of enriched continuum theories, we can obtain a simplified modeling and a more effective conception of real large-scale civil engineering “metastructures”, made up of metamaterials as building blocks, that resist vibrations and shocks in a large range of frequencies. Furthermore, based on the abundant literature concerning this subject, we believe possible to identify and describe a wide class of periodic and quasi-periodic band-gap microstructures via the relaxed micromorphic model that can be used as basis for the design of such metastructures. Considering these remarks and the results presented in this manuscript, we believe that the relaxed micromorphic model is a suitable choice for the description of the behavior of band-gap metamaterials in view of the conception of large-scale civil engineering metastructures.

Work in progress is focused on the generalization of the results presented here to the anisotropic framework [49] in order to be able to characterize a wider class of metamaterials, so increasing the interest of using enriched continuum models for realistic meta-structural design. The main perspective for the relaxed micromorphic model is its numerical implementation in a Finite Element code for the conception of complex band-gap metastructures. The fact of using a continuum relaxed micromorphic model could be an incredibly powerful tool for the design of complex metastructures which are constituted by metamaterials with already known mechanical properties. Indeed, the fact of dealing with few macroscopic elastic coefficients should make the finite element implementation of the model rather easy, thus allowing for numerically efficient models for the design of complex structures. Once the material parameters of the considered metamaterials have been estimated by inverse approach, standard finite element codes could be used in order to design structures with extended sizes and complex geometries. This will allow us to eventually design some prototype structures which are able to absorb elastic waves in precise frequency ranges (for example by means of 3D printing).

A possible further extension of the relaxed micromorphic model is the insertion of additional micromorphic degrees of freedom to account for even more microstructure-related effects. We dubbed this possible extension the “relaxed multimorphic model”. When the full setting-up of the anisotropic relaxed multimorphic model will be concluded (for which advanced techniques of functional analysis and calculus of variations are required), we will be able to use the a continuous model to perform numerical simulations for specific metamaterials in even greater detail.

End matter

Bibliography

1. Jan D. Achenbach. *Wave propagation in elastic solids*. North-Holland Publishing Company, Amsterdam, The Netherlands, 1973.
2. Yamina Aimène, Emmanuelle Vidal-Sallé, Benjamin Hagège, François Sidoroff, and Philippe Boisse. A hyperelastic approach for composite reinforcement large deformation analysis. *Journal of Composite Materials*, 44(1):5–26, 2010.
3. Jean-Jacques Alibert, Pierre Seppecher, and Francesco dell’Isola. Truss modular beams with deformation energy depending on higher displacement gradients. *Mathematics and Mechanics of Solids*, 8(1):51–73, 2003.
4. Holm Altenbach, Victor A. Eremeyev, Leonid P. Lebedev, and Leonardo A. Rendón. Acceleration waves and ellipticity in thermoelastic micropolar media. *Archive of Applied Mechanics*, 80(3):217–227, 2010.
5. Mario N. Armenise, Carlo E. Campanella, Caterina Ciminelli, Francesco Dell’Olio, and Vittorio M. N. Passaro. Phononic and photonic band gap structures: Modelling and applications. *Physics Procedia*, 3(1):357–364, 2010.
6. Ali Asghar Atai and David J. Steigmann. On the nonlinear mechanics of discrete networks. *Archive of Applied mechanics*, 67(5):303–319, 1997.
7. Nicolas Auffray. On the algebraic structure of isotropic generalized elasticity theories. *Mathematics and Mechanics of Solids*, 20(5):565–581, 2015.
8. Andrés I. Ávila, Georges Griso, Bernadette Miara, and Eduard Rohan. Multiscale Modeling of Elastic Waves: Theoretical Justification and Numerical Simulation of Band Gaps. *Multiscale Modeling and Simulation*, 7(1):1–21, 2008.
9. Pierre Badel, Emmanuelle Vidal-Sallé, and Philippe Boisse. Large deformation analysis of fibrous materials using rate constitutive equations. *Comput. Struct.*, 86(11-12):1164–1175, 2008.
10. Daniel Balzani, Patrizio Neff, Jörg Schröder, and Gerhard A. Holzapfel. A polyconvex framework for soft biological tissues. Adjustment to experimental data. *International Journal of Solids and Structures*, 43(20):6052–6070, 2006.
11. Gabriele Barbagallo, Angela Madeo, Ismael Azehaf, Ivan Giorgio, Fabrice Morestin, and Philippe Boisse. Bias extension test on an unbalanced woven composite reinforcement: Experiments and modeling via a second-gradient continuum approach. *Journal of Composite Materials*, 51(2):153–170, 2017.
12. Gabriele Barbagallo, Angela Madeo, Marco Valerio d’Agostino, Rafael Abreu, Ionel-Dumitrel Ghiba, and Patrizio Neff. Transparent anisotropy for the relaxed micromorphic model: macroscopic consistency conditions and long wave length asymptotics. *International Journal of Solids and Structures*, 120:7–30, 2017.
13. Gabriele Barbagallo, Angela Madeo, Fabrice Morestin, and Philippe Boisse. Modelling the deep drawing of a 3D woven fabric with a second gradient model. *Mathematics and Mechanics of Solids*, Preprint, 2016.
14. Jose Baruchel, Jean-Yves Buffiere, Eric Maire, Paul Merle, and Gilles Peix. *X-Ray Tomography in Material Science*. Hermès Science Publications, Paris, 2000.
15. Sebastian Bauer, Patrizio Neff, Dirk Pauly, and Gerhard Starke. New Poincaré-type inequalities. *Comptes Rendus Mathématique*, 352(2):163–166, 2014.
16. Arkadi Berezovski, Jüri Engelbrecht, and Mihhail Berezovski. Waves in microstructured solids: a unified viewpoint of modeling. *Acta Mechanica*, 220(1-4):349–363, 2011.
17. Rajendra Bhatia. *Positive definite matrices*. Princeton University Press, 2009.
18. Simon Bickerton, Pavel Šimáček, Sarah E. Guglielmi, and Suresh G. Advani. Investigation of draping and its effects on the mold filling process during manufacturing of a compound curved composite part. *Composites Part A: Applied Science and Manufacturing*, 28(9-10):801–816, 1997.
19. David Bigaud, Loïc Dréano, and Patrice Hamelin. Models of interactions between process, microstructure and mechanical properties of composite materials – a study of the interlock layer-to-layer braiding technique. *Composite Structures*, 67(1):99–114, 2005.
20. Davide Bigoni and Panos A. Gougiotis. Folding and faulting of an elastic continuum. *Proceedings of the Royal Society A: Mathematical, Physical and Engineering Sciences*, 472(2187):20160018, 2016.
21. Jeffrey L. Bleustein. A note on the boundary conditions of Toupin’s strain-gradient theory. *International Journal of Solids and Structures*, 3(6):1053–1057, 1967.
22. Jean-Paul Boehler. Lois de comportement anisotrope des milieux continus. *Journal de Mécanique*, 17(153):70, 1978.
23. Jean-Paul Boehler. Introduction to the invariant formulation of anisotropic constitutive equations. In *Applications of Tensor Functions in Solid Mechanics*, pages 13–30. Springer Vienna, Vienna, 1987.

24. Thomas Böhlke and Albrecht Bertram. A minimum problem defining effective isotropic elastic properties. *Zeitschrift für Angewandte Mathematik und Mechanik*, 80(S2):419–420, 2000.
25. Philippe Boisse, Karine Buet, Alain Gasser, and Jean Launay. Meso/macro-mechanical behaviour of textile reinforcements for thin composites. *Composites Science and Technology*, 61(3):395–401, 2001.
26. Philippe Boisse, A. Hakim Cherouat, Jean Claude Gelin, and Hamid Sabhi. Experimental study and finite element simulation of a glass fiber fabric shaping process. *Polymer composites*, 16(1):83–95, 1995.
27. Philippe Boisse, Nahiène Hamila, F. Helenon, Benjamin Hagège, and Jian Cao. Different approaches for woven composite reinforcement forming simulation. *International Journal of Material Forming*, 1(1):21–29, 2008.
28. Philippe Boisse, Nahiène Hamila, Emmanuelle Vidal-Sallé, and François Dumont. Simulation of wrinkling during textile composite reinforcement forming. Influence of tensile, in-plane shear and bending stiffnesses. *Composites Science and Technology*, 71(5):683–692, 2011.
29. Philippe Boisse, Bassem Zouari, and Jean-Luc Daniel. Importance of in-plane shear rigidity in finite element analyses of woven fabric composite preforming. *Composites Part A: Applied Science and Manufacturing*, 37(12):2201–2212, 2006.
30. Philippe Boisse, Bassem Zouari, and Alain Gasser. A mesoscopic approach for the simulation of woven fibre composite forming. *Composites Science and Technology*, 65(3-4):429–436, 2005.
31. Jian Cao, Remko Akkerman, Philippe Boisse, Julie Chen, H.S. Cheng, E.F. de Graaf, J.L. Gorczyca, Philip Harrison, Gilles Hivet, Jérôme Launay, Wonoh Lee, L. Liu, Stepan V. Lomov, Andrew C. Long, Emmanuel de Luycker, Fabrice Morestin, J. Padvoiskis, Xiongqi Peng, James Sherwood, T. Stoilova, Xiaoming M. Tao, Ignaas Verpoest, A. Willems, Joram Wiggers, T. X. Yu, and Bo Zhu. Characterization of mechanical behavior of woven fabrics: Experimental methods and benchmark results. *Composites Part A: Applied Science and Manufacturing*, 39(6):1037–1053, 2008.
32. Augustin-Louis Cauchy. Sur les équations qui expriment les conditions d'équilibre, ou les lois du mouvement intérieur d'un corps solide, élastique ou non élastique (1828). In *Œuvres complètes*, volume 2(8) of *Cambridge Library Collection - Mathematics*, pages 195–226. Cambridge University Press, Cambridge, 2009.
33. Peter Chadwick, Maurizio Vianello, and Stephen C. Cowin. A new proof that the number of linear elastic symmetries is eight. *Journal of the Mechanics and Physics of Solids*, 49(11):2471–2492, 2001.
34. Adrien Charmetant. *Approches hyperélastiques pour la modélisation du comportement mécanique de préformes tissées de composites*. PhD thesis, INSA Lyon, 2011.
35. Adrien Charmetant, Jean Guillaume Orliac, Emmanuelle Vidal-Sallé, and Philippe Boisse. Hyperelastic model for large deformation analyses of 3D interlock composite preforms. *Composites Science and Technology*, 72(12):1352–1360, 2012.
36. Adrien Charmetant, Emmanuelle Vidal-Sallé, and Philippe Boisse. Hyperelastic modelling for mesoscopic analyses of composite reinforcements. *Composites Science and Technology*, 71(14):1623–1631, 2011.
37. Youping Chen and James D. Lee. Connecting molecular dynamics to micromorphic theory. (I). Instantaneous and averaged mechanical variables. *Physica A: Statistical Mechanics and its Applications*, 322:359–376, 2003.
38. Youping Chen and James D. Lee. Determining material constants in micromorphic theory through phonon dispersion relations. *International Journal of Engineering Science*, 41(8):871–886, 2003.
39. Youping Chen, James D. Lee, and Azim Eskandarian. Atomistic viewpoint of the applicability of microcontinuum theories. *International Journal of Solids and Structures*, 41(8):2085–2097, 2004.
40. Abdelhakim Cherouat and Jean Louis Billoët. Mechanical and numerical modelling of composite manufacturing processes deep-drawing and laying-up of thin pre-impregnated woven fabrics. *Journal of Materials Processing Technology*, 118(1-3):460–471, 2001.
41. Stan Chiriță, Alexandru Danescu, and Michele Ciarletta. On the strong ellipticity of the anisotropic linearly elastic materials. *Journal of Elasticity*, 87(1):1–27, 2007.
42. Stan Chiriță and Ionel-Dumitrel Ghiba. Strong ellipticity and progressive waves in elastic materials with voids. *Proceedings of the Royal Society A: Mathematical, Physical and Engineering Sciences*, 466(2114):439–458, 2009.
43. William D. Claus Jr. and Ahmed Cemal Eringen. Dislocation dispersion of elastic waves. *International Journal of Engineering Science*, 9(7):605–610, 1971.
44. Eugène Cosserat and François Cosserat. *Théorie des corps déformables (engl. translation by D. Delphenich 2007, pdf available at http://www.uni-due.de/~7ehm0014/Cosserat_files/Cosserat09_eng.pdf)*. A. Hermann et Fils, Paris, 1909.
45. Stephen C. Cowin and Morteza M. Mehrabadi. Anisotropic Symmetries of Linear Elasticity. *Applied Mechanics Reviews*, 48(5):247, 1995.
46. Stephen C. Cowin and Jace W. Nunziato. Linear elastic materials with voids. *Journal of Elasticity*, 13(2):125–147, 1983.
47. Gavin Creech and Anthony K. Pickett. Meso-modelling of Non-crimp Fabric composites for coupled drape and failure analysis. *Journal of Materials Science*, 41(20):6725–6736, 2006.
48. G. J. Curtiss, J. M. Milne, and W. N. Reynolds. Non-Hookean Behaviour of Strong Carbon Fibres. *Nature*, 220(5171):1024–1025, 1968.
49. Marco Valerio d'Agostino, Gabriele Barbagallo, Ionel-Dumitrel Ghiba, Bernhard Eidel, Patrizio Neff, and Angela Madeo. Efficient description of anisotropic wave dispersion in mechanical metamaterials via the relaxed micromorphic model. *Submitted*, 2017.
50. Marco Valerio d'Agostino, Gabriele Barbagallo, Ionel-Dumitrel Ghiba, Angela Madeo, and Patrizio Neff. A panorama of dispersion curves for the weighted isotropic relaxed micromorphic model. *Zeitschrift für Angewandte Mathematik und Mechanik*, 2017.

51. Pierre-Gilles de Gennes. Some effects of long range forces on interfacial phenomena. *Journal de Physique Lettres*, 42(16):377–379, 1981.
52. Emmanuel de Luycker, Fabrice Morestin, Philippe Boisse, and David Marsal. Simulation of 3D interlock composite preforming. *Composite Structures*, 88:615–623, 2009.
53. Emmanuel de Luycker, Jean Guillaume Orliac, Fabrice Morestin, Philippe Boisse, David Marsal, and Stephane Otin. Experimental and numerical analyses of 3D interlock composite preforming. *International Journal of Material Forming*, 3(1):719–722, 2010.
54. Francesco dell’Isola, Massimo Guarascio, and Kolumban Hutter. A variational approach for the deformation of a saturated porous solid. A second-gradient theory extending Terzaghi’s effective stress principle. *Archive Of Applied Mechanics*, 70(5):323–337, 2000.
55. Francesco dell’Isola, Angela Madeo, and Luca Placidi. Linear plane wave propagation and normal transmission and reflection at discontinuity surfaces in second gradient 3D continua. *Zeitschrift für Angewandte Mathematik und Mechanik*, 92(1):52–71, 2012.
56. Francesco dell’Isola and Giacomo Rotoli. Validity of Laplace formula and dependence of surface tension on curvature in second gradient fluids. *Mechanics Research Communications*, 22(5):485–490, 1995.
57. Francesco dell’Isola, Giulio Sciarra, and Stefano Vidoli. Generalized Hooke’s law for isotropic second gradient materials. *Proceedings of the Royal Society A: Mathematical, Physical and Engineering Sciences*, 465(2107):2177–2196, 2009.
58. Francesco dell’Isola and David J. Steigmann. A two-dimensional gradient-elasticity theory for woven fabrics. *Journal of Elasticity*, 118(1):113–125, 2015.
59. Frederik Desplentere, Stepan V. Lomov, D. L. Woerdeman, Ignaas Verpoest, M. Wevers, and A. Bogdanovich. Micro-CT characterization of variability in 3D textile architecture. *Composites Science and Technology*, 65(13):1920–1930, 2005.
60. Damien Durville. Numerical simulation of entangled materials mechanical properties. *Journal of Materials Science*, 40(22):5941–5948, 2005.
61. Damien Durville. Simulation of the mechanical behaviour of woven fabrics at the scale of fibers. *International Journal of Material Forming*, 3(S2):1241–1251, 2010.
62. François Ebobisse and Patrizio Neff. Existence and uniqueness for rate-independent infinitesimal gradient plasticity with isotropic hardening and plastic spin. *Mathematics and Mechanics of Solids*, 15(6):691–703, 2010.
63. François Ebobisse, Patrizio Neff, and Daya Reddy. Existence results in dislocation based rate-independent isotropic gradient plasticity with kinematical hardening and plastic spin: The case with symmetric local backstress. *Preprint ArXiv*, 1504.01973, 2015.
64. Victor A. Eremeyev. Acceleration waves in micropolar elastic media. *Doklady Physics*, 50(4):204–206, 2005.
65. Ahmed Cemal Eringen. Mechanics of micromorphic materials. In *Applied Mechanics*, pages 131–138. Springer Berlin Heidelberg, Berlin, Heidelberg, 1966.
66. Ahmed Cemal Eringen. Theory of thermo-microstretch elastic solids. *International Journal of Engineering Science*, 28(12):1291–1301, 1990.
67. Ahmed Cemal Eringen. *Microcontinuum field theories*. Springer-Verlag, New York, 1999.
68. Ahmed Cemal Eringen and William D. Claus Jr. A micromorphic approach to dislocation theory and its relation to several existing theories. In *Fundamental aspects of dislocation theory, Volume II. National Bureau of Standards Special. 317(2)*, pages 1023–1040. 1969.
69. Ahmed Cemal Eringen and Erdogan S. Suhubi. Nonlinear theory of simple micro-elastic solids – I. *International Journal of Engineering Science*, 2(2):189–203, 1964.
70. Manuel Ferretti, Angela Madeo, Francesco dell’Isola, and Philippe Boisse. Modeling the onset of shear boundary layers in fibrous composite reinforcements by second-gradient theory. *Zeitschrift für Angewandte Mathematik und Physik*, 65(3):587–612, 2014.
71. Samuel Forest. Mechanics of generalized continua: construction by homogenization. *Le Journal de Physique IV*, 08(4):39–48, 1998.
72. Samuel Forest. Homogenization methods and mechanics of generalized continua - part 2. *Theoretical and Applied Mechanics*, 28-29(28-29):113–144, 2002.
73. Samuel Forest. Micromorphic approach for gradient elasticity, viscoplasticity, and damage. *Journal of Engineering Mechanics*, 135(3):117–131, 2009.
74. Samuel Forest and Rainer Sievert. Nonlinear microstrain theories. *International Journal of Solids and Structures*, 43(24):7224–7245, 2006.
75. Samuel Forest and Duy Khanh Trinh. Generalized continua and non-homogeneous boundary conditions in homogenisation methods. *Zeitschrift für Angewandte Mathematik und Mechanik*, 91(2):90–109, 2011.
76. Sébastien Gatouillat, Andrea Breggi, Emmanuelle Vidal-Sallé, and Philippe Boisse. Meso modelling for composite preform shaping - Simulation of the loss of cohesion of the woven fibre network. *Composites Part A: Applied Science and Manufacturing*, 54:135–144, 2013.
77. Denos C. Gazis and Richard F. Wallis. Extensional waves in cubic crystals plates. In *Proceedings of the 4th U.S. National Congress in Applied Mechanics*, pages 161–168, 1962.

78. Paul Germain. The method of virtual power in continuum mechanics. Part 2: Microstructure. *SIAM Journal on Applied Mathematics*, 25(3):556–575, 1973.
79. Ionel-Dumitrel Ghiba, Patrizio Neff, Angela Madeo, and Ingo Münch. A variant of the linear isotropic indeterminate couple-stress model with symmetric local force-stress, symmetric nonlocal force-stress, symmetric couple-stresses and orthogonal boundary conditions. *Mathematics and Mechanics of Solids*, 22(6):1221–1266, 2017.
80. Ionel-Dumitrel Ghiba, Patrizio Neff, Angela Madeo, Luca Placidi, and Giuseppe Rosi. The relaxed linear micromorphic continuum: Existence, uniqueness and continuous dependence in dynamics. *Mathematics and Mechanics of Solids*, 20(10):1171–1197, 2015.
81. George T. Gilbert. Positive definite matrices and Sylvester’s criterion. *The American Mathematical Monthly*, 98(1):44–46, 1991.
82. Panos A. Gougiotis and Davide Bigoni. Stress channelling in extreme couple-stress materials Part I: Strong ellipticity, wave propagation, ellipticity, and discontinuity relations. *Journal of the Mechanics and Physics of Solids*, 88:150–168, 2016.
83. Paschalis Grammenoudis and Charalampos Tsakmakis. Micromorphic continuum Part I: Strain and stress tensors and their associated rates. *International Journal of Non-Linear Mechanics*, 44(9):943–956, 2009.
84. Leopoldo Greco and Massimo Cuomo. B-Spline interpolation of Kirchhoff-Love space rods. *Computer Methods in Applied Mechanics and Engineering*, 256:251–269, 2013.
85. Leopoldo Greco and Massimo Cuomo. An implicit G1 multi patch B-spline interpolation for Kirchhoff-Love space rod. *Computer Methods in Applied Mechanics and Engineering*, 269:173–197, 2014.
86. A.E. Green and Ronald S. Rivlin. Multipolar continuum mechanics. *Archive for Rational Mechanics and Analysis*, 17(2):113–147, 1964.
87. George Green. An essay on the application of mathematical analysis to the theories of electricity and magnetism (originally published as book in Nottingham, 1828). *Journal für die reine und angewandte Mathematik (Crelles Journal)*, 1852(44):356–374, jan 1852.
88. Elena F. Grekova and Gérard A. Maugin. Modelling of complex elastic crystals by means of multi-spin micromorphic media. *International Journal of Engineering Science*, 43(5):494–519, 2005.
89. Mica Grujicic, K. M. Chittajallu, and Shawn Walsh. Effect of shear, compaction and nesting on permeability of the orthogonal plain-weave fabric preforms. *Materials Chemistry and Physics*, 86(2-3):358–369, 2004.
90. Nahiène Hamila and Philippe Boisse. A meso-macro three node finite element for draping of textile composite preforms. *Applied Composite Materials*, 14(4):235–250, 2007.
91. Nahiène Hamila and Philippe Boisse. Simulations of textile composite reinforcement draping using a new semi-discrete three node finite element. *Composites Part B: Engineering*, 39(6):999–1010, 2008.
92. Philip Harrison, Michael J. Clifford, and Andrew C. Long. Shear characterisation of viscous woven textile composites: A comparison between picture frame and bias extension experiments. *Composites Science and Technology*, 64(10-11):1453–1465, 2004.
93. Philip Harrison, Joram Wiggers, and Andrew C. Long. Normalization of Shear Test Data for Rate-independent Compressible Fabrics. *Journal of Composite Materials*, 42(1):1–30, 2008.
94. Eliza M. Haseganu and David J. Steigmann. Equilibrium analysis of finitely deformed elastic networks. *Computational Mechanics*, 17(6):359–373, 1996.
95. Gabor T. Herman. *Fundamentals of Computerized Tomography*. Advances in Pattern Recognition. Academic Press, New York, 1980.
96. Claudia Britta Hirschberger, Ellen Kuhl, and Paul Steinmann. On deformational and configurational mechanics of micromorphic hyperelasticity—theory and computation. *Computer Methods in Applied Mechanics and Engineering*, 196(41):4027–4044, 2007.
97. Gerhard A. Holzapfel, Thomas C. Gasser, and Ray W. Ogden. A new constitutive framework for arterial wall mechanics and a comparative study of material models. *Journal of Elasticity*, 61(1-3):1–48, 2000.
98. J.D.H. Hughes. Strength and modulus of current carbon fibres. *Carbon*, 24(5):551–556, 1986.
99. Dorin Ieşan. A theory of thermoelastic materials with voids. *Acta Mechanica*, 60:67–89, 1986.
100. Dorin Ieşan and Ludovico Nappa. Extremum principles and existence results in micromorphic elasticity. *International Journal of Engineering Science*, 39(18):2051–2070, 2001.
101. Mikhail Itskov. On the theory of fourth-order tensors and their applications in computational mechanics. *Computer Methods in Applied Mechanics and Engineering*, 189(2):419–438, 2000.
102. Mikhail Itskov and Nuri Aksel. A class of orthotropic and transversely isotropic hyperelastic constitutive models based on a polyconvex strain energy function. *International Journal of Solids and Structures*, 41(14):3833–3848, 2004.
103. Ralf Jänicke, Stefan Diebels, Hans-Georg Sehlhorst, and Alexander Düster. Two-scale modelling of micromorphic continua. *Continuum Mechanics and Thermodynamics*, 21(4):297–315, 2009.
104. Jena Jeong and Patrizio Neff. Existence, uniqueness and stability in linear Cosserat elasticity for weakest curvature conditions. *Mathematics and Mechanics of Solids*, 15(1):78–95, 2010.
105. Jena Jeong, Hamidrēza Ramézani, Ingo Münch, and Patrizio Neff. A numerical study for linear isotropic Cosserat elasticity with conformally invariant curvature. *Zeitschrift für Angewandte Mathematik und Mechanik*, 89(7):552–569, 2009.

106. Wen-Guang Jiang, M.S. Yao, and John M. Walton. A concise finite element model for simple straight wire rope strand. *International Journal of Mechanical Sciences*, 41(2):143–161, 1999.
107. S. Kawabata, Masako Niwa, and H. Kawai. The finite-deformation theory of plain-weave fabrics. Part I: the biaxial-deformation theory. *The Journal of The Textile Institute*, 64(1):21–46, jan 1973.
108. S. Kawabata, Masako Niwa, and H. Kawai. The finite-deformation theory of plain-weave fabrics. Part II: the uniaxial-deformation theory. *The Journal of The Textile Institute*, 64(2):47–61, 1973.
109. M. Aurangzeb Khan, Tarek Mabrouki, Emmanuelle Vidal-Sallé, and Philippe Boisse. Numerical and experimental analyses of woven composite reinforcement forming using a hypoelastic behaviour. Application to the double dome benchmark. *Journal of Materials Processing Technology*, 210(2):378–388, 2010.
110. Kin-Wai Sze, Kin-Man Lam, and Guoping Qiu. A new key frame representation for video segment retrieval. *IEEE Transactions on Circuits and Systems for Video Technology*, 15(9):1148–1155, sep 2005.
111. Nina Kirchner and Paul Steinmann. A unifying treatise on variational principles for gradient and micromorphic continua. *Philosophical Magazine*, 85(33-35):3875–3895, 2005.
112. Severino L. Koh. A special theory of microelasticity. *International Journal of Engineering Science*, 8(7):583–593, 1970.
113. Katarzyna Kowalczyk-Gajewska and Janina Ostrowska-Maciejewska. Review on spectral decomposition of Hooke’s tensor for all symmetry groups of linear elastic material. *Engineering transactions*, 57(3-4):145–183, 2009.
114. Ekkehart Kröner. Der fundamentale Zusammenhang zwischen Versetzungsdichte und Spannungsfunktionen. *Zeitschrift für Physik*, 142(4):463–475, 1955.
115. Isaak Abramovich Kunin. *Elastic media with microstructure II: three-dimensional models*. Springer Series in Solid-State Sciences. Springer Berlin, Heidelberg, 2012.
116. Roderic S. Lakes. Size effects and micromechanics of a porous solid. *Journal of Materials Science*, 18(9):2572–2580, 1983.
117. Roderic S. Lakes. Experimental micro mechanics methods for conventional and negative Poisson’s ratio cellular solids as Cosserat continua. *Journal of Engineering Materials and Technology*, 113(1):148–155, 1991.
118. Johannes Lankeit, Patrizio Neff, and Frank Osterbrink. Integrability conditions between the first and second Cosserat deformation tensor in geometrically nonlinear micropolar models and existence of minimizers. *Zeitschrift für Angewandte Mathematik und Physik*, 68(1):11, 2017.
119. Pierre Latil, Laurent Orgéas, Christian Geindreau, Pierre J. J. Dumont, and Sabine Rolland du Roscoat. Towards the 3D in situ characterisation of deformation micro-mechanisms within a compressed bundle of fibres. *Composites Science and Technology*, 71(4):480–488, 2011.
120. Jean Launay, Gilles Hivet, Ahn V. Duong, and Philippe Boisse. Experimental analysis of the influence of tensions on in plane shear behaviour of woven composite reinforcements. *Composites Science and Technology*, 68(2):506–515, 2008.
121. Markus Lazar. On conservation and balance laws in micromorphic elastodynamics. *Journal of Elasticity*, 88(1):63–78, 2007.
122. Wonoh Lee, J. Padvoiskis, Jian Cao, Emmanuel de Luycker, Philippe Boisse, Fabrice Morestin, Jinhui Chen, and James Sherwood. Bias-extension of woven composite fabrics. *International Journal of Material Forming*, 1(SUPPL. 1):895–898, 2008.
123. Zhengyou Liu, Xixiang Zhang, Yiwei Mao, Yirong Zhu, Zhiyu Yang, Che Ting Chan, and Ping Sheng. Locally resonant sonic materials. *Science*, 289(5485):1734–1736, 2000.
124. Stepan V. Lomov, A. V. Gusakov, Gert Huysmans, Andreas G. Prodromou, and I. Verpoest. Textile geometry preprocessor for meso-mechanical models of woven composites. *Composites Science and Technology*, 60(11):2083–2095, 2000.
125. Stepan V. Lomov and Ignaas Verpoest. Model of shear of woven fabric and parametric description of shear resistance of glass woven reinforcements. *Composites Science and Technology*, 66(7-8):919–933, 2006.
126. Augustus Edward Hough Love. *A treatise on the mathematical theory of elasticity*. Dover Publications, Inc, New York, 1944.
127. Ralf Lucklum, Manzhou Ke, and Mikhail Zubtsov. Two-dimensional phononic crystal sensor based on a cavity mode. *Sensors and Actuators, B: Chemical*, 171-172:271–277, 2012.
128. C. Mack and H. M. Taylor. The Fitting of Woven Cloth to Surfaces. *Journal of the Textile Institute Transactions*, 47(9):T477–T488, 1956.
129. Angela Madeo, Gabriele Barbagallo, Manuel Collet, Marco Valerio d’Agostino, Marco Miniaci, and Patrizio Neff. Relaxed micromorphic modeling of the interface between a homogeneous solid and a band-gap metamaterial: New perspectives towards metastructural design. *Mathematics and Mechanics of Solids*, Preprint, 2017.
130. Angela Madeo, Gabriele Barbagallo, Marco Valerio d’Agostino, and Philippe Boisse. Continuum and discrete models for unbalanced woven fabrics. *International Journal of Solids and Structures*, 94-95:263–284, 2016.
131. Angela Madeo, Gabriele Barbagallo, Marco Valerio d’Agostino, Luca Placidi, and Patrizio Neff. First evidence of non-locality in real band-gap metamaterials: determining parameters in the relaxed micromorphic model. *Proceedings of the Royal Society A: Mathematical, Physical and Engineering Sciences*, 472(2190):20160169, 2016.
132. Angela Madeo, Manuel Collet, Marco Miniaci, Kévin Billon, Morvan Ouisse, and Patrizio Neff. Modeling phononic crystals via the weighted relaxed micromorphic model with free and gradient micro-inertia. *Journal of Elasticity*, 2017.

133. Angela Madeo, Francesco dell'Isola, Nicoletta Ianiro, and Giulio Sciarra. A variational deduction of second gradient poroelasticity II: An application to the consolidation problem. *Journal of Mechanics of Materials and Structures*, 3(4):607–625, 2008.
134. Angela Madeo, Manuel Ferretti, Francesco dell'Isola, and Philippe Boisse. Thick fibrous composite reinforcements behave as special second-gradient materials: three-point bending of 3D interlocks. *Zeitschrift für Angewandte Mathematik und Mechanik*, 66(4):2041–2060, 2015.
135. Angela Madeo, Ionel-Dumitrel Ghiba, Patrizio Neff, and Ingo Münch. A new view on boundary conditions in the Grioli–Koiter–Mindlin–Toupin indeterminate couple stress model. *European Journal of Mechanics - A/Solids*, 59:294–322, 2016.
136. Angela Madeo, Patrizio Neff, Elias C. Aifantis, Gabriele Barbagallo, and Marco Valerio d'Agostino. On the role of micro-inertia in enriched continuum mechanics. *Proceedings of the Royal Society A: Mathematical, Physical and Engineering Science*, 473(2198):20160722, 2017.
137. Angela Madeo, Patrizio Neff, Gabriele Barbagallo, Marco Valerio d'Agostino, and Ionel-Dumitrel Ghiba. A review on wave propagation modeling in band-gap metamaterials via enriched continuum models. In Francesco dell'Isola, Mircea Sofonea, and David J. Steigmann, editors, *Mathematical Modelling in Solid Mechanics*, Advanced Structured Materials, pages 89–105. Springer, Singapore, 2017.
138. Angela Madeo, Patrizio Neff, Marco Valerio d'Agostino, and Gabriele Barbagallo. Complete band gaps including non-local effects occur only in the relaxed micromorphic model. *Comptes Rendus Mécanique*, 344(11-12):784–796, 2016.
139. Angela Madeo, Patrizio Neff, Ionel-Dumitrel Ghiba, Luca Placidi, and Giuseppe Rosi. Band gaps in the relaxed linear micromorphic continuum. *Zeitschrift für Angewandte Mathematik und Mechanik*, 95(9):880–887, 2014.
140. Angela Madeo, Patrizio Neff, Ionel-Dumitrel Ghiba, Luca Placidi, and Giuseppe Rosi. Wave propagation in relaxed micromorphic continua: modeling metamaterials with frequency band-gaps. *Continuum Mechanics and Thermodynamics*, 27(4-5):551–570, 2015.
141. Angela Madeo, Patrizio Neff, Ionel-Dumitrel Ghiba, and Giuseppe Rosi. Reflection and transmission of elastic waves in non-local band-gap metamaterials: a comprehensive study via the relaxed micromorphic model. *Journal of the Mechanics and Physics of Solids*, 95:441–479, 2016.
142. Weining Man, Marian Florescu, Kazue Matsuyama, Polin Yadak, Geev Nahal, Seyed Hashemizad, Eric Williamson, Paul J. Steinhardt, Salvatore Torquato, and Paul Chaikin. Photonic band gap in isotropic hyperuniform disordered solids with low dielectric contrast. *Optics Express*, 21(17):19972–81, 2013.
143. Jean Mandel. Plastic waves in an infinite three dimensional medium. *Journal de Mécanique*, 1:3–30, 1962.
144. Paolo Maria Mariano and Giuseppe Modica. Ground states in complex bodies. *ESAIM: Control, Optimisation and Calculus of Variations*, 15(02):377–402, 2009.
145. Paolo Maria Mariano and Furio Lorenzo Stazi. Computational aspects of the mechanics of complex materials. *Archives of Computational Methods in Engineering*, 12(4):391–478, 2005.
146. Sylvain Mathieu. *Modélisation du comportement mécanique lors du procédé de mise en forme et pyrolyse des interlocks CMC*. PhD thesis, INSA Lyon, 2014.
147. Sylvain Mathieu, Philippe Boisse, Nahiène Hamila, and Florent Bouillon. Locking and stability of 3D woven composite reinforcements. *Key Engineering Materials*, 611-612:292–299, may 2014.
148. Sylvain Mathieu, Nahiène Hamila, F. Dupé, C. Descamps, and Philippe Boisse. Stability of 3D Textile Composite Reinforcement Simulations: Solutions to Spurious Transverse Modes. *Applied Composite Materials*, 23(4):739–760, 2016.
149. Gérard A. Maugin. *Continuum mechanics through the eighteenth and nineteenth centuries*, volume 214 of *Solid Mechanics and Its Applications*. Springer International Publishing, 2014.
150. Gérard A. Maugin. *Non-Classical Continuum Mechanics*, volume 51. Springer, 2016.
151. Johannes Meenen, Holm Altenbach, Victor A. Eremeyev, and Konstantin Naumenko. A variationally consistent derivation of microcontinuum theories. In *Shell-like Structures*, pages 571–584. Springer, 2011.
152. Jose Merodio and Patrizio Neff. A note on tensile instabilities and loss of ellipticity for a fiber-reinforced nonlinearly elastic solid. *Archives of Mechanics*, 58(3):293–303, 2006.
153. Amin Mikdam, Ahmed Makradi, Said Ahzi, Hamid Garmestani, Dongsheng S. Li, and Yves Remond. Effective conductivity in isotropic heterogeneous media using a strong-contrast statistical continuum theory. *Journal of the Mechanics and Physics of Solids*, 57(1):76–86, 2009.
154. Amin Mikdam, Ahmed Makradi, Said Ahzi, Hamid Garmestani, Dongsheng S. Li, and Yves Remond. Statistical continuum theory for the effective conductivity of fiber filled polymer composites: Effect of orientation distribution and aspect ratio. *Composites Science and Technology*, 70(3):510–517, 2010.
155. Raymond David Mindlin. Microstructure in linear elasticity. Technical report, Office of Naval Research, 1963.
156. Raymond David Mindlin. Micro-structure in linear elasticity. *Archive for Rational Mechanics and Analysis*, 16(1):51–78, 1964.
157. Raymond David Mindlin and N. N. Eshel. On first strain-gradient theories in linear elasticity. *International Journal of Solids and Structures*, 4(1):109–124, 1968.
158. Anil Misra and Payam Poorsolhjoui. Granular micromechanics based micromorphic model predicts frequency band gaps. *Continuum Mechanics and Thermodynamics*, 28(1):1–20, 2015.

159. Maher Moakher and Andrew N. Norris. The closest elastic tensor of arbitrary symmetry to an elasticity tensor of lower symmetry. *Journal of Elasticity*, 85(3):215–263, 2006.
160. Vincent Monchiet and Guy Bonnet. On the inversion of non symmetric sixth-order isotropic tensors and conditions of positiveness of third-order tensor valued quadratic functions. *Mechanics Research Communications*, 38(4):326–329, 2011.
161. Ingo Münch and Patrizio Neff. Rotational invariance conditions in elasticity, gradient elasticity and its connection to isotropy. *Mathematics and Mechanics of Solids*, Preprint, 2016.
162. Ingo Münch, Patrizio Neff, Angela Madeo, and Ionel-Dumitrel Ghiba. The modified indeterminate couple stress model: Why Yang et al.’s arguments motivating a symmetric couple stress tensor contain a gap and why the couple stress tensor may be chosen symmetric nevertheless. *to appear in Zeitschrift für Angewandte Mathematik und Mechanik*, 2016.
163. Ben Nadler, Panayiotis Papadopoulos, and David J. Steigmann. Multiscale constitutive modeling and numerical simulation of fabric material. *International Journal of Solids and Structures*, 43(2):206–221, 2006.
164. Hiroyuki Nagahama and Roman Teisseyre. Micromorphic continuum and fractal fracturing in the lithosphere. In *Fractals and Dynamic Systems in Geoscience*, pages 559–574. Springer, 2000.
165. N. Naouar, Emmanuelle Vidal-Sallé, J. Schneider, E. Maire, and Philippe Boisse. Meso-scale FE analyses of textile composite reinforcement deformation based on X-ray computed tomography. *Composite Structures*, 116(1):165–176, 2014.
166. Anne Nawrocki and Michel Labrosse. A finite element model for simple straight wire rope strands. *Computers & Structures*, 77(4):345–359, 2000.
167. Patrizio Neff. On Korn’s first inequality with non-constant coefficients. *Proceedings of the Royal Society of Edinburgh: Section A Mathematics*, 132(1):221–243, 2002.
168. Patrizio Neff. On material constants for micromorphic continua. In *Trends in Applications of Mathematics to Mechanics, STAMM Proceedings, Seeheim*, pages 337–348. Shaker-Verlag, 2004.
169. Patrizio Neff. Existence of minimizers for a finite-strain micromorphic elastic solid. *Proceedings of the Royal Society of Edinburgh: Section A Mathematics*, 136(05):997–1012, 2006.
170. Patrizio Neff. The Cosserat couple modulus for continuous solids is zero viz the linearized Cauchy-stress tensor is symmetric. *Zeitschrift für Angewandte Mathematik und Mechanik*, 86(11):892–912, 2006.
171. Patrizio Neff. Relations of constants for isotropic linear Cosserat elasticity. Technical report, Fachbereich Mathematik, Technische Universität Darmstadt (http://www.uni-due.de/%7ehm0014/Cosserat_files/web_coss_relations.pdf, typos in equations 2.8,2.9,2.10), Darmstadt, Germany, 2008.
172. Patrizio Neff. Existence of minimizers in nonlinear elastostatics of micromorphic solids. In *Encyclopedia of Thermal Stresses*, pages 1475–1485. Springer, 2014.
173. Patrizio Neff, Mircea Birsan, and Frank Osterbrink. Existence theorem for geometrically nonlinear Cosserat micropolar model under uniform convexity requirements. *Journal of Elasticity*, 121(1):1–23, 2015.
174. Patrizio Neff and Samuel Forest. A geometrically exact micromorphic model for elastic metallic foams accounting for affine microstructure. Modelling, existence of minimizers, identification of moduli and computational results. *Journal of Elasticity*, 87(2-3):239–276, 2007.
175. Patrizio Neff, Ionel-Dumitrel Ghiba, Markus Lazar, and Angela Madeo. The relaxed linear micromorphic continuum: well-posedness of the static problem and relations to the gauge theory of dislocations. *The Quarterly Journal of Mechanics and Applied Mathematics*, 68(1):53–84, 2015.
176. Patrizio Neff, Ionel-Dumitrel Ghiba, Angela Madeo, Luca Placidi, and Giuseppe Rosi. A unifying perspective: the relaxed linear micromorphic continuum. *Continuum Mechanics and Thermodynamics*, 26(5):639–681, 2014.
177. Patrizio Neff and Jena Jeong. A new paradigm: the linear isotropic Cosserat model with conformally invariant curvature energy. *Zeitschrift für Angewandte Mathematik und Mechanik*, 89(2):107–122, 2009.
178. Patrizio Neff, Jena Jeong, and Andreas Fischle. Stable identification of linear isotropic Cosserat parameters: bounded stiffness in bending and torsion implies conformal invariance of curvature. *Acta Mechanica*, 211(3-4):237–249, 2010.
179. Patrizio Neff, Angela Madeo, Gabriele Barbagallo, Marco Valerio d’Agostino, Rafael Abreu, and Ionel-Dumitrel Ghiba. Real wave propagation in the isotropic-relaxed micromorphic model. *Proceedings of the Royal Society A: Mathematical, Physical and Engineering Sciences*, 473(2197):20160790, 2017.
180. Patrizio Neff and Ingo Münch. Curl bounds Grad on SO(3). *ESAIM: Control, Optimisation and Calculus of Variations*, 14(1):148–159, 2008.
181. Patrizio Neff, Dirk Pauly, and Karl-Josef Witsch. A canonical extension of Korn’s first inequality to H(Curl) motivated by gradient plasticity with plastic spin. *Comptes Rendus Mathématique*, 349(23):1251–1254, 2011.
182. Patrizio Neff, Dirk Pauly, and Karl-Josef Witsch. Maxwell meets Korn: A new coercive inequality for tensor fields in $R^{n \times n}$ with square-integrable exterior derivative. *Mathematical Methods in the Applied Sciences*, 35(1):65–71, 2012.
183. Patrizio Neff, Dirk Pauly, and Karl-Josef Witsch. Poincaré meets Korn via Maxwell: extending Korn’s first inequality to incompatible tensor fields. *Journal of Differential Equations*, 258(4):1267–1302, 2015.
184. Farbod Nosrat-Nezami, Thomas Gereke, Christian Eberdt, and Chokri Cherif. Characterisation of the shear-tension coupling of carbon-fibre fabric under controlled membrane tensions for precise simulative predictions of industrial preforming processes. *Composites Part A: Applied Science and Manufacturing*, 67:131–139, 2014.
185. Witold Nowacki. *Theory of Asymmetric Elasticity*. Pergamon Press, 1985.

186. Jace W. Nunziato and Stephen C. Cowin. A nonlinear theory of elastic materials with voids. *Archive for Rational Mechanics and Analysis*, 72(2):175–201, 1979.
187. Ray W. Ogden. *Non-linear elastic deformations*, volume 1. Dover Publications, Inc, Mineola, NY, 1984.
188. Ray W. Ogden. Nonlinear Elasticity, Anisotropy, Material Stability and Residual Stresses in Soft Tissue. In *Biomechanics of Soft Tissue in Cardiovascular Systems*, volume 108, pages 65–108. Springer-Verlag, Vienna, 2003.
189. Victor G. Oshmyan, Stanislav A. Patlazhan, and Yves Remond. Principles of structural-mechanical modeling of polymers and composites. *Polymer Science Series A*, 48(9):1004–1013, 2006.
190. S. Parameshwaran and Severino L. Koh. Wave propagation in a micro-isotropic, micro-elastic solid. *International Journal of Engineering Science*, 11(1):95–107, 1973.
191. Richard S. Parnas. *Liquid Composite Molding*. Carl Hanser Verlag GmbH & Co. KG, München, 2000.
192. Juan Pazmino, Sylvain Mathieu, Valter Carvelli, Philippe Boisse, and Stepan V. Lomov. Numerical modelling of forming of a non-crimp 3D orthogonal weave E-glass composite reinforcement. *Composites Part A: Applied Science and Manufacturing*, 72:207–218, 2015.
193. Xiongqi Peng and Jian Cao. A continuum mechanics-based non-orthogonal constitutive model for woven composite fabrics. *Composites Part A: Applied Science and Manufacturing*, 36(6):859–874, 2005.
194. Xiongqi Peng, Jian Cao, Jinhui Chen, P. Xue, D. S. Lussier, and L. Liu. Experimental and numerical analysis on normalization of picture frame tests for composite materials. *Composites Science and Technology*, 64(1):11–21, 2004.
195. Catherine Pideri and Pierre Seppecher. A second gradient material resulting from the homogenization of an heterogeneous linear elastic medium. *Continuum Mechanics and Thermodynamics*, 9(5):241–257, 1997.
196. Gabrio Piola. Intorno alle equazioni fondamentali del movimento di corpi qualsivogliono, considerati secondo la naturale loro forma e costituzione (1846). In Francesco Dell’Isola, Ugo Andreaus, Luca Placidi, and Daria Scerrato, editors, *The complete works of Gabrio Piola*, volume I of *Advanced Structured Materials*, pages 1–370. Springer International Publishing, 2014.
197. Luca Placidi, Giuseppe Rosi, Ivan Giorgio, and Angela Madeo. Reflection and transmission of plane waves at surfaces carrying material properties and embedded in second-gradient materials. *Mathematics and Mechanics of Solids*, 19(5):555–578, 2014.
198. Kevin D. Potter. The early history of the resin transfer moulding process for aerospace applications. *Composites Part A: Applied Science and Manufacturing*, 30(5):619–621, may 1999.
199. Kevin D. Potter. Bias extension measurements on cross-plyed unidirectional prepreg. *Composites - Part A: Applied Science and Manufacturing*, 33(1):63–73, 2002.
200. Annie Raoult. Symmetry groups in nonlinear elasticity: an exercise in vintage mathematics. *Communications on Pure and Applied Analysis*, 8(1):435–456, 2008.
201. Giovanni Romano, Raffaele Barretta, and Marina Diaco. Micromorphic continua: non-redundant formulations. *Continuum Mechanics and Thermodynamics*, 28(6):1659–1670, 2016.
202. Chris D. Rudd, Andrew C. Long, K. N. Kendall, and C. Mangin. *Liquid moulding technologies: Resin transfer moulding, structural reaction injection moulding and related processing techniques*. Woodhead Publishing Limited, Cambridge, England, 1997.
203. Carlo Sansour. A unified concept of elastic-viscoplastic Cosserat and micromorphic continua. *Le Journal de Physique IV*, 8(8):341–348, 1998.
204. Carlo Sansour, Sebastian Skatulla, and Hussein M. Zbib. A formulation for the micromorphic continuum at finite inelastic strains. *International Journal of Solids and Structures*, 47(11):1546–1554, 2010.
205. Jörg Schröder and Patrizio Neff. Application of polyconvex anisotropic free energies to soft tissues. *5th World Congress on Computational Mechanics*, 2002.
206. Jörg Schröder, Patrizio Neff, and Daniel Balzani. A variational approach for materially stable anisotropic hyperelasticity. *International Journal of Solids and Structures*, 42(15):4352–4371, 2005.
207. Jörg Schröder, Patrizio Neff, and Vera Ebbing. Anisotropic polyconvex energies on the basis of crystallographic motivated structural tensors. *Journal of the Mechanics and Physics of Solids*, 56(12):3486–3506, 2008.
208. Giulio Sciarra, Francesco dell’Isola, Nicoletta Ianiro, and Angela Madeo. A variational deduction of second gradient poroelasticity I: general theory. *Journal of Mechanics of Materials and Structures*, 3(3):507–526, may 2008.
209. Pierre Seppecher, Jean-Jacques Alibert, and Francesco dell’Isola. Linear elastic trusses leading to continua with exotic mechanical interactions. *Journal of Physics: Conference Series*, 319(1):012018, 2011.
210. S. B. Sharma and M. P F Sutcliffe. A simplified finite element model for draping of woven material. *Composites Part A: Applied Science and Manufacturing*, 35(6):637–643, 2004.
211. A.C. Smith. Waves in micropolar elastic solids. *International Journal of Engineering Science*, 5(10):741–746, 1967.
212. A.C. Smith. Inequalities between the constants of a linear micro-elastic solid. *International Journal of Engineering Science*, 6(2):65–74, 1968.
213. Alessandro Spadoni, Massimo Ruzzene, Stefano Gonella, and Fabrizio Scarpa. Phononic properties of hexagonal chiral lattices. *Wave Motion*, 46(7):435–450, 2009.
214. Anthony James Merrill Spencer. Theory of Invariants. In *Mathematics*, volume 1, pages 239–353. Elsevier, 1971.

215. Anthony James Merrill Spencer. *Deformations of fibre-reinforced materials*. U.C.D. Library, Oxford, 1972.
216. Anthony James Merrill Spencer. Constitutive theory for strongly anisotropic solids. In Anthony James Merrill Spencer, editor, *Continuum Theory of the Mechanics of Fibre-Reinforced Composites*, pages 1–32. Springer-Verlag, Vienna, 1984.
217. Ashwin Sridhar, Varvara G. Kouznetsova, and Marc G. D. Geers. Homogenization of locally resonant acoustic metamaterials towards an emergent enriched continuum. *Computational Mechanics*, 57(3):423–435, 2016.
218. David J. Steigmann. Equilibrium of prestressed networks. *IMA Journal of Applied Mathematics*, 48(2):195–215, 1992.
219. David J. Steigmann. Invariants of the stretch tensors and their application to finite elasticity theory. *Mathematics and Mechanics of Solids*, 7(4):393–404, 2002.
220. David J. Steigmann. Frame-invariant polyconvex strain-energy functions for some anisotropic solids. *Mathematics and Mechanics of Solids*, 8(5):497–506, 2003.
221. Walter Steurer and Daniel Sutter-Widmer. Photonic and phononic quasicrystals. *Journal of Physics D: Applied Physics*, 40(13):229–247, 2007.
222. Roman Teisseyre. Earthquake processes in a micromorphic continuum. *Pure and Applied Geophysics PAGEOPH*, 102(1):15–28, 1973.
223. Roman Teisseyre. Symmetric micromorphic continuum: wave propagation, point source solutions and some applications to earthquake processes. In *Continuum Mechanics Aspects of Geodynamics and Rock Fracture Mechanics*, pages 201–244. Springer Netherlands, Dordrecht, 1974.
224. R. H W ten Thije, R. Akkerman, and J. Huétink. Large deformation simulation of anisotropic material using an updated Lagrangian finite element method. *Computer Methods in Applied Mechanics and Engineering*, 196(33-34):3141–3150, 2007.
225. Richard A. Toupin. Theories of elasticity with couple-stress. *Archive for Rational Mechanics and Analysis*, 17(2):85–112, 1964.
226. Clifford Truesdell and Richard A. Toupin. The classical field theories. In Siegfried Flügge, editor, *Principles of Classical Mechanics and Field Theory / Prinzipien der Klassischen Mechanik und Feldtheorie*, pages 226–858. Springer, Berlin, Heidelberg, 1960.
227. Franck J. Vernerey, Wing Kam Liu, and Brian Moran. Multi-scale micromorphic theory for hierarchical materials. *Journal of the Mechanics and Physics of Solids*, 55(12):2603–2651, 2007.
228. Franck J. Vernerey, Wing Kam Liub, Brian Moran, and Gregory Olsonc. A micromorphic model for the multiple scale failure of heterogeneous materials. *Journal of the Mechanics and Physics of Solids*, 56(4):1320–1347, 2008.
229. Woldemar Voigt. Ueber die Beziehung zwischen den beiden Elasticitätsconstanten isotroper Körper. *Annalen der Physik*, 274(12):573–587, 1889.
230. Woldemar Voigt. *Lehrbuch der Kristallphysik*. Vieweg+Teubner Verlag, Wiesbaden, 1966 edition, 1909.
231. Jinling Wang, John R. Page, and Rowan Paton. Experimental investigation of the draping properties of reinforcement fabrics. *Composites Science and Technology*, 58(2):229–237, 1998.
232. Peng Wang, Xavier Legrand, Philippe Boisse, Nahiène Hamila, and Damien Soulat. Experimental and numerical analyses of manufacturing process of a composite square box part: Comparison between textile reinforcement forming and surface 3D weaving. *Composites Part B: Engineering*, 78:26–34, 2015.
233. Alexander Ženišek. Polynomial approximation on tetrahedrons in the finite element method. *Journal of Approximation Theory*, 7(4):334–351, 1973.
234. Shangyou Zhang. A family of 3D continuously differentiable finite elements on tetrahedral grids. *Applied Numerical Mathematics*, 59(1):219–233, 2009.
235. Yifan Zhang, Fei Sun, Yanjie Wang, Li Chen, and Ning Pan. Study on intra/inter-ply shear deformation of three dimensional woven preforms for composite materials. *Materials and Design*, 49(August 2013):151–159, 2013.
236. Guangming Zhou, Xuekun Sun, and Youqi Wang. Multi-chain digital element analysis in textile mechanics. *Composites Science and Technology*, 64(2):239–244, 2004.
237. Olgierd C. Zienkiewicz and Robert L. Taylor. *The finite element method Volume 1: The basis*. Butterworth-Heinmann, 5th edition, 2000.
238. Bassem Zouari, Jean-Luc Daniel, and Philippe Boisse. A woven reinforcement forming simulation method. Influence of the shear stiffness. *Computers & Structures*, 84(5-6):351–363, 2006.

APPENDIX A

Appendix to part I

A.1 Micromorphic models as limiting cases of the relaxed micromorphic continuum

In this section, we show certain limiting cases of the anisotropic relaxed micromorphic continuum model. Since we assume $\mathbb{C}_m, \mathbb{C}_e$ to be positive definite and \mathbb{C}_c positive semi-definite, there exist three positive constants $c_{\text{dev}}^+, c_{\text{tr}}^+, c_e^+ > 0$ and $c_c^+ \geq 0$ such that:

$$\begin{aligned} \langle \mathbb{C}_e \text{sym}(\nabla u - P), \text{sym}(\nabla u - P) \rangle_{\mathbb{R}^{3 \times 3}} &\geq c_e^+ \|\text{sym}(\nabla u - P)\|_{\mathbb{R}^{3 \times 3}}^2, \\ \langle \mathbb{C}_m \text{sym} P, \text{sym} P \rangle_{\mathbb{R}^{3 \times 3}} &\geq c_{\text{dev}}^+ \|\text{dev sym } P\|_{\mathbb{R}^{3 \times 3}}^2 + c_{\text{tr}}^+ (\text{tr}(P))^2, \\ \langle \mathbb{C}_c \text{skew}(\nabla u - P), \text{skew}(\nabla u - P) \rangle_{\mathbb{R}^{3 \times 3}} &\geq c_c^+ \|\text{skew}(\nabla u - P)\|_{\mathbb{R}^{3 \times 3}}^2. \end{aligned} \quad (\text{A.1})$$

Cosserat model or micropolar model: Let us first consider:

$$\mathbb{C}_m \rightarrow \infty, \quad \mathbb{C}_e > 0, \quad \mathbb{C}_c \geq 0, \quad P \in \mathbb{R}^{3 \times 3}, \quad (\text{A.2})$$

which is the case if we assume $c_{\text{dev}}^+, c_{\text{tr}}^+ \rightarrow \infty$. In this case, the fact that the energy is bounded implies $\|\text{sym } P\|^2 = 0$ formally and, therefore, that $P \in \mathfrak{so}(3)$. This resulting model is equivalent to the *Cosserat model or micropolar model* (section I.2.2). The appearance of only $\text{Curl } P$ in the curvature is consistent with the classical Cosserat or micropolar model, since for skew-symmetric $P(x) = A(x) \in \mathfrak{so}(3)$ it holds that $\text{Curl } A$ is isomorphic to ∇A , see [180].

Micro-voids theory: On the other hand, we may consider:

$$\text{dev sym } \mathbb{C}_m \rightarrow \infty, \quad \mathbb{C}_e > 0, \quad \mathbb{C}_c = 0, \quad P \in \text{Sym}(3), \quad (\text{A.3})$$

where we assume that $c_{\text{dev}}^+ \rightarrow \infty$ and $\text{skew } P = 0$. In this case, we obtain that $\|\text{dev sym } P\|^2 = 0$ and, therefore, we can infer that $P = \mathbb{R} \cdot \mathbb{1}$. This model is called *micro-voids theory* (see [176] and section I.2.4) and again, the presence of $\text{Curl } P$ is fully consistent with the general micro-voids theory.

Micro-incompressible micromorphic model: One more case is:

$$\text{tr } \mathbb{C}_m \rightarrow \infty, \quad \mathbb{C}_e > 0, \quad \mathbb{C}_c \geq 0, \quad P \in \mathbb{R}^{3 \times 3}, \quad (\text{A.4})$$

where we assume that $c_{\text{tr}}^+ \rightarrow \infty$ and, therefore, $\text{tr } P = 0$. In this case we obtain that $P \in \mathfrak{sl}(3)$. This model is the *micro-incompressible micromorphic model* (section I.2.6).

Micro-stretch theory: Analogously, we may consider:

$$\text{dev sym } \mathbb{C}_m \rightarrow \infty, \quad \mathbb{C}_e > 0, \quad \mathbb{C}_c \geq 0, \quad P \in \mathbb{R}^{3 \times 3}, \quad (\text{A.5})$$

where we assume that $c_{\text{dev}}^+ \rightarrow \infty$. In this case we obtain only that $\|\text{dev sym } P\|^2 = 0$ and therefore that $P = \mathbb{R} \cdot \mathbb{1} + \mathfrak{so}(3)$. This set of models is called *micro-stretch theory* (see [176] and section I.2.3).

Micro-strain model: Instead, if we just consider:

$$\mathbb{C}_m > 0, \quad \mathbb{C}_e > 0, \quad \mathbb{C}_c = 0, \quad P \in \text{Sym}(3), \quad (\text{A.6})$$

which means constraining P in such a way that skew $P = 0$, then this resulting model is equivalent to Forest's *micro-strain model*, (see [74] and section I.2.5).

A.2 One-dimensional standard Mindlin-Eringen model versus new relaxed micromorphic model

We let $u : [0, 1] \rightarrow \mathbb{R}$ denote the displacement and $\hat{p} : [0, 1] \rightarrow \mathbb{R}$ the micro-distortion (we note that u corresponds to the first component of the displacement and \hat{p} corresponds to P_{11}).

Considering a one-dimensional model, we can reduce the energy of the Mindlin-Eringen model to:

$$\mu_e |u'(t) - \hat{p}(t)|^2 + \mu_c \underbrace{|\text{skew}(\cdot)|^2}_0 + \mu_m |\hat{p}(t)|^2 + \frac{\mu L_c^2}{2} |\hat{p}'(t)|^2. \quad (\text{A.7})$$

Therefore, in a purely one-dimensional setting, the μ_c -term does not appear. Furthermore, if $\mu_e \rightarrow \infty$ formally, the energy reads:

$$\mu_m |u'(t)|^2 + \frac{\mu L_c^2}{2} |u''(t)|^2, \quad (\text{A.8})$$

which is a second gradient elastic energy. The equilibrium equations read:

$$2\mu_e (u'(t) - \hat{p}(t)) \delta u'(t) = 0, \quad \forall \delta u \in C_0^\infty([0, 1], \mathbb{R}), \quad (\text{A.9})$$

$$[-2\mu_e (u'(t) - \hat{p}(t)) + 2\mu_m \hat{p}] \delta \hat{p}(t) + \mu L_c^2 \hat{p}' \delta \hat{p}' = 0. \quad \forall \delta \hat{p} \in C_0^\infty([0, 1], \mathbb{R}),$$

from which we obtain:

$$\frac{d}{dx} [2\mu_e (u'(t) - \hat{p}(t))] = 0, \quad -2\mu_e (u'(t) - \hat{p}(t)) + 2\mu_m \hat{p} + \mu L_c^2 \hat{p}'' = 0. \quad (\text{A.10})$$

If we consider $L_c \rightarrow 0$ we obtain:

$$\frac{d}{dx} [2\mu_e (u'(t) - \hat{p}(t))] = 0, \quad -2\mu_e (u'(t) - \hat{p}(t)) + 2\mu_m \hat{p} = 0. \quad (\text{A.11})$$

This can be reduced to:

$$\frac{d}{dx} \left[2 \frac{\mu_e \mu_m}{\mu_e + \mu_m} u'(t) \right] = 0, \quad \hat{p} = \frac{\mu_e}{\mu_e + \mu_m} u'(t). \quad (\text{A.12})$$

Therefore, this is equivalent to a classical elasticity model with energy:

$$\mu_M |u'(t)|^2, \quad \text{where } \mu_M = \frac{\mu_e \mu_m}{\mu_e + \mu_m}. \quad (\text{A.13})$$

Thus, in the one-dimensional setting, the Mindlin-Eringen format obeys our homogenization format as well.

For the relaxed micromorphic model we have instead:

$$\mu_e |u'(t) - \hat{p}(t)|^2 + \mu_c \underbrace{|\text{skew}(\cdot)|^2}_{=0} + \mu_m |\hat{p}(t)|^2 + \frac{\mu L_c^2}{2} \underbrace{\| \text{Curl} \begin{pmatrix} \hat{p} & 0 & 0 \\ 0 & 0 & 0 \\ 0 & 0 & 0 \end{pmatrix} \|^2}_{=0}. \quad (\text{A.14})$$

Therefore, there are no terms with L_c and the equilibrium equations read:

$$\frac{d}{dx} [2\mu_e (u'(t) - \hat{p}(t))] = 0, \quad -2\mu_e (u'(t) - \hat{p}(t)) + 2\mu_m \hat{p} = 0. \quad (\text{A.15})$$

This is the the same format as the Mindlin-Eringen model with $L_c \rightarrow 0$.

Here, it must be noted that when $\mu_e \rightarrow \infty$, we obtain formally only a first gradient elasticity model with energy:

$$\mu_m |u'(t)|^2. \quad (\text{A.16})$$

This is equivalent to a classical linear elasticity model with $\mu_M = \mu_m$, contrary to (A.8).

Here, one of the differences of the standard Mindlin-Eringen format, in comparison to the new relaxed formulation, clearly appears: the relaxed format does not reduce to a higher gradient elasticity model when specifying certain parameters.

APPENDIX B

Appendix to part II

B.1 Representation Theorems for Hyperelastic Materials

Various hyperelastic constitutive equations for an isotropic strain energy density which are suitable to describe the mechanical behavior of isotropic materials even at finite strains (see e.g. [187,219]) have been proposed in the literature. Generalized constitutive laws are also available for linear elastic isotropic second gradient media (see [57]). The main issue when defining a constitutive law is the choice of the deformation descriptors. In the literature, we find different theorems that ensure the minimum number of parameters needed to correctly represent the functional dependence of W on C . All of these results define a minimum number of invariants for any specific symmetry in the considered medium. For what follows the unitary vector along the preferred directions, namely the fiber directions in the case of the fabrics, will be denoted by m_1 and m_2 and the unitary vector m_3 is defined as $m_3 := m_1 \wedge m_2$. The invariants considered in the following and a brief description of their meaning are listed in the table B.1.

We must note that the invariants listed in table B.1 are not all independent. Indeed, it can be shown (see [200]) that these invariants can be written as functions of only six invariants as:

$$\begin{cases} i_2 = i_4 i_6 + (i_4 + i_6) (i_1 - (i_4 + i_6)) - i_8^2 - i_9^2 - i_{10}^2 \\ i_3 = (i_4 i_6 - i_8^2) (i_1 - (i_4 + i_6)) + 2 i_8 i_9 i_{10} - i_6 i_9^2 - i_4 i_{10}^2 \\ i_5 = i_4^2 + i_8^2 + i_9^2 \\ i_7 = i_6^2 + i_8^2 + i_{10}^2 \\ i_1 = i_4 + i_6 + i_{11}^* \end{cases} \quad (\text{B.1})$$

Invariant	Expression	Meaning in Terms of Deformation
i_1	$\text{tr}(C)$	Changes of length
i_2	$\text{tr}(\det(C) C^{-T})$	Changes of area
i_3	$\det(C)$	Changes of volume
$i_4 = i_{11}$	$m_1 \cdot C \cdot m_1$	Local stretch in the direction m_1
i_5	$m_1 \cdot C^2 \cdot m_1$	Shear and stretch strain in m_1
$i_6 = i_{22}$	$m_2 \cdot C \cdot m_2$	Local stretch in the direction m_2
i_7	$m_2 \cdot C^2 \cdot m_2$	Shear and stretch strain in m_2
$i_8 = i_{12}$	$m_1 \cdot C \cdot m_2$	Shear strain between the directions (m_1, m_2)
$i_9 = i_{13}$	$m_1 \cdot C \cdot m_3$	Shear strain between the directions (m_1, m_3)
$i_{10} = i_{23}$	$m_2 \cdot C \cdot m_3$	Shear strain between the directions (m_2, m_3)
$i_{11}^* = i_{33}$	$m_3 \cdot C \cdot m_3$	Local stretch in the direction m_3

Table B.1: Invariants of Deformation

Representation Theorem for Isotropic Materials: Considering a hyperelastic isotropic material only three independent scalar invariants of the Cauchy-Green tensor C are sufficient to correctly represent the functional dependence of W^{iso} on C . In other words, for an isotropic material, it is sufficient to consider an energy of the type:

$$W^{iso}(C) = W(i_1, i_2, i_3) \quad (\text{B.2})$$

Proofs of this theorem can be easily find in the literature (see [97, 188]).

Representation Theorem for Transversely Isotropic Materials: Considering a hyperelastic transversely isotropic material only five independent scalar invariants of the Cauchy-Green tensor C are sufficient to correctly represent the functional dependence of W^{tran} on C . In other words, for a transversely isotropic material (i.e. a material with a unique preferential direction), it is sufficient to consider an energy such as:

$$W^{tran}(C) = W(i_1, i_2, i_3, i_4, i_5) \quad (\text{B.3})$$

Constitutive equations for transversely isotropic materials are also well assessed in the literature (see e.g. [22, 23, 36, 101, 102, 188]).

Representation Theorem for Orthotropic Materials: As far as orthotropic materials are considered, clear and exploitable constitutive hyperelastic equations are harder to be found in the literature. Plenty of authors try to generalize the representation theorems valid for isotropic and transversely isotropic media, but often there is no apparent agreement between the different versions proposed for such a theorem.

The most diffused version of the representation theorem (see e.g. [97, 188, 216]) for the hyperelastic orthotropic materials states that only seven independent scalar invariants of the Cauchy-Green tensor C are sufficient to correctly represent the functional dependence of W^{orth} on C . In other words, for an orthotropic material, it is sufficient to consider an energy such as:

$$W^{orth}(C) = W(i_1, i_2, i_3, i_4, i_5, i_6, i_7) \quad (\text{B.4})$$

Nevertheless, it can be proved that only six independent scalar invariants are sufficient to completely describe the behavior of an orthotropic material (see the elegant proof given in [200]), so that, even if it is effectively possible to write the strain energy as function of seven scalar invariants, it must be kept in mind that not all of them are truly independent functions of C . In particular, following [200], we can introduce the set of six invariants $i_O := \{i_1, i_4, i_6, i_8, i_9, i_{10}\}$ to represent the functional dependence of W on C :

$$W^{orth}(C) = W(i_1, i_4, i_6, i_8, i_9, i_{10}) \quad (\text{B.5})$$

Indeed, all the other invariants can be expressed in terms of such six as recalled in equation B.1.

B.2 Alternative numerical implementation of the constrained micromorphic model: penalty method

In this subsection, we briefly mention a method that can be used in order to numerically implement a constrained micromorphic model as an alternative to the method of Lagrange multipliers. It is known as ‘‘penalty method’’ and consists in implementing a strain energy density which takes the form

$$W(i_4, i_6, i_8, \varphi, \nabla\varphi) = W_I(i_4, i_6, i_8) + W_{II}(\nabla\varphi) + W_{coupling}(i_8, \varphi), \quad (\text{B.6})$$

where W_I and W_{II} are given in Eqs. II.8 and II.9 respectively, while the coupling energy takes the form

$$W_{coupling}(i_8, \varphi) = \frac{K}{2}(\varphi - i_8)^2,$$

where K is a constant that may ideally tend to infinity. Indeed, in order to guarantee the boundedness of the strain energy density, it follows that φ must necessarily tend to i_8 . We numerically implemented such a penalty method in order to test the correct convergence of our equilibrium problem formulated with Lagrange multipliers. Since K is constant, the considered virtual variations are only δu and $\delta\varphi$ and, moreover, the

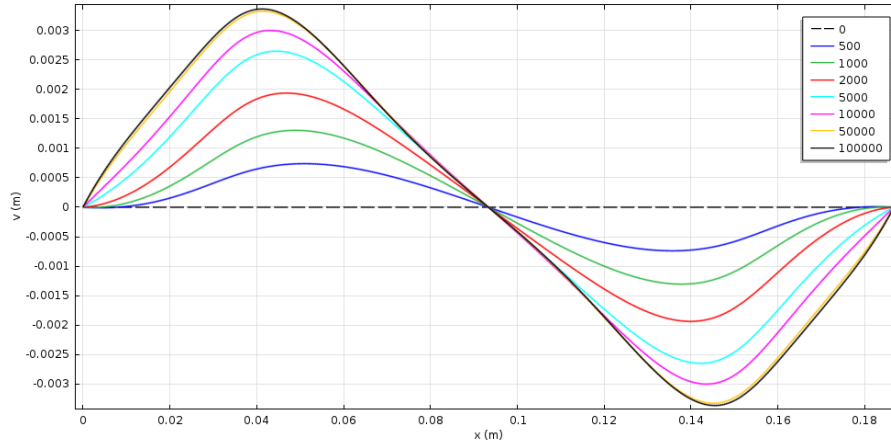


Figure 64: Vertical displacement of the mean axis for a displacement of 56 mm and different values of K

constant K must be chosen sufficiently large in order to guarantee numerical convergence of the solution. This last feature can be easily tested by controlling that the solution does not change when increasing the value of K (see Fig. 64). The constitutive parameters remain the same as the ones used in the numerical simulation with the Lagrange multiplier (see tables 3.1 and 3.2). We note that by suitably increasing the value of K , the model converges to the solution obtained with constrained micromorphic simulation with Lagrange multiplier. Therefore, this penalty method could be a useful tool for the easy implementation of constrained micromorphic models due to their high numerical stability.

B.3 Influence of cutting the corners on the onset of wrinkling for first and second gradient solutions

During experimental testing, it is a spread routine to cut the corners of the specimen as in the simulations shown in Figure 65, see [35]. This change in the geometry can have an influence on the onset of wrinkling during the deep drawing of the fabric. We notice that cutting the corner leads to a slightly reduced amount of wrinkling in the first gradient model, while for the second gradient model the wrinkling is already not relevant and therefore almost no influence is seen by the cutting of the corners. The considerations concerning the dependence of the solution from the size of the mesh remain the same as in the other cases both for the first and second gradient case.

APPENDIX C

Appendix to part III

C.1 Linear mapping for the Mandel-Voigt vector notation

The components of the defined mapping $\mathfrak{M}_{\alpha ij}$ can be represented as 3×3 matrices once fixing the index α :

$$\mathfrak{M}_{1ij} = \begin{pmatrix} 1 & 0 & 0 \\ 0 & 0 & 0 \\ 0 & 0 & 0 \end{pmatrix}, \quad \mathfrak{M}_{2ij} = \begin{pmatrix} 0 & 0 & 0 \\ 0 & 1 & 0 \\ 0 & 0 & 0 \end{pmatrix}, \quad \mathfrak{M}_{3ij} = \begin{pmatrix} 0 & 0 & 0 \\ 0 & 0 & 0 \\ 0 & 0 & 1 \end{pmatrix},$$

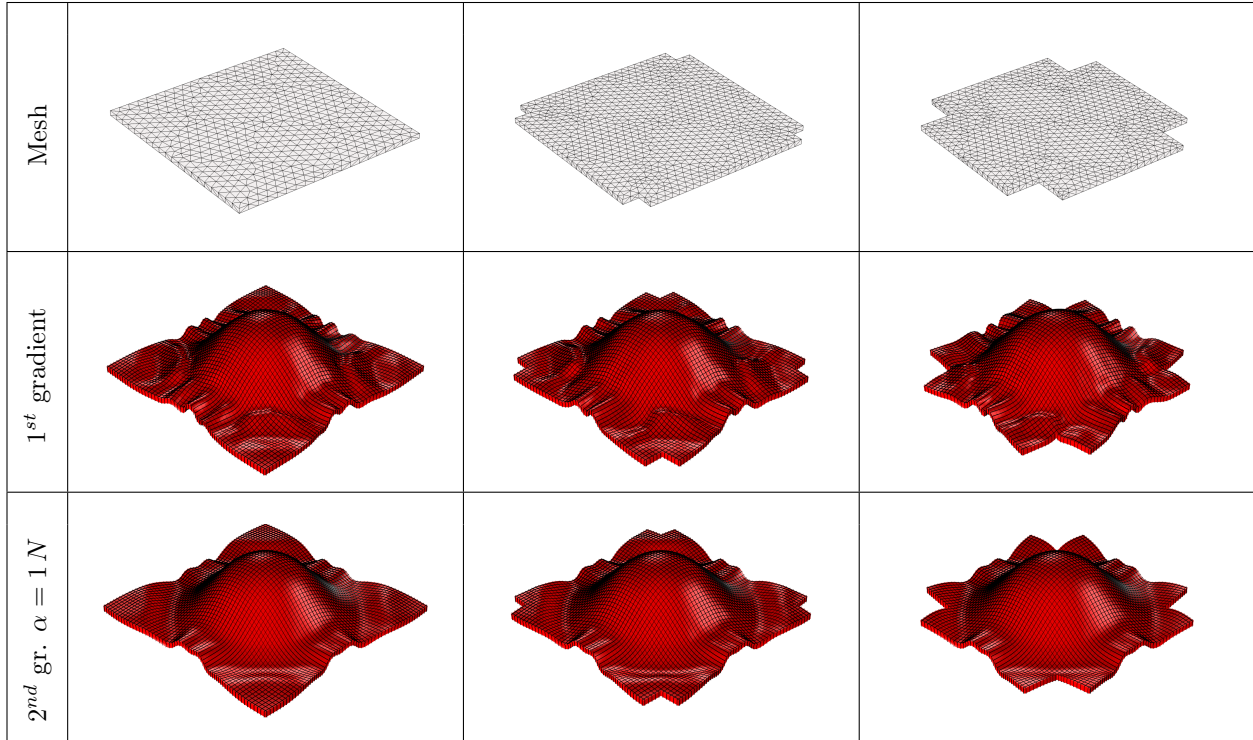


Figure 65: Influence of cutting the corners on the onset of wrinkling for the first and the second gradient model with shape functions with augmented continuity.

$$\mathfrak{M}_{4ij} = \begin{pmatrix} 0 & 0 & 0 \\ 0 & 0 & \frac{c}{2} \\ 0 & \frac{c}{2} & 0 \end{pmatrix}, \quad \mathfrak{M}_{5ij} = \begin{pmatrix} 0 & 0 & \frac{c}{2} \\ 0 & 0 & 0 \\ \frac{c}{2} & 0 & 0 \end{pmatrix}, \quad \mathfrak{M}_{6ij} = \begin{pmatrix} 0 & \frac{c}{2} & 0 \\ \frac{c}{2} & 0 & 0 \\ 0 & 0 & 0 \end{pmatrix}.$$

We define the inverse operator $\mathfrak{M}_{ij\alpha}^{-1} : \mathbb{R}^6 \rightarrow \text{Sym}(3)$ as:

$$(\text{sym } \nabla u)_{ij} = \mathfrak{M}_{ij\alpha}^{-1} \varepsilon_\alpha, \quad (\text{sym } P)_{ij} = \mathfrak{M}_{ij\alpha}^{-1} \beta_\alpha, \quad (\text{C.1})$$

with the following property:

$$\mathfrak{M}_{\alpha ij} \mathfrak{M}_{ij\beta}^{-1} = \tilde{\delta}_{\alpha\beta}, \quad (\text{C.2})$$

where $\tilde{\delta}$ is the Kronecker δ in $\mathbb{R}^6 \times \mathbb{R}^6$. We can to show that the components of the inverse operator are:

$$\begin{aligned} \mathfrak{M}_{ij1}^{-1} &= \begin{pmatrix} 1 & 0 & 0 \\ 0 & 0 & 0 \\ 0 & 0 & 0 \end{pmatrix}, & \mathfrak{M}_{ij2}^{-1} &= \begin{pmatrix} 0 & 0 & 0 \\ 0 & 1 & 0 \\ 0 & 0 & 0 \end{pmatrix}, & \mathfrak{M}_{ij3}^{-1} &= \begin{pmatrix} 0 & 0 & 0 \\ 0 & 0 & 0 \\ 0 & 0 & 1 \end{pmatrix}, \\ \mathfrak{M}_{ij4}^{-1} &= \begin{pmatrix} 0 & 0 & 0 \\ 0 & 0 & \frac{1}{c} \\ 0 & \frac{1}{c} & 0 \end{pmatrix}, & \mathfrak{M}_{ij5}^{-1} &= \begin{pmatrix} 0 & 0 & \frac{1}{c} \\ 0 & 0 & 0 \\ \frac{1}{c} & 0 & 0 \end{pmatrix}, & \mathfrak{M}_{ij6}^{-1} &= \begin{pmatrix} 0 & \frac{1}{c} & 0 \\ \frac{1}{c} & 0 & 0 \\ 0 & 0 & 0 \end{pmatrix}. \end{aligned} \quad (\text{C.3})$$

The mapping \mathfrak{M} has zeros everywhere except in the components $\{111, 222, 333, 423, 513, 612\}$. Therefore, we express it compactly as:

$$\begin{aligned} \mathfrak{M}_{\alpha ij} &= \tilde{\delta}_{\alpha 1} \delta_{i1} \delta_{j1} + \tilde{\delta}_{\alpha 2} \delta_{i2} \delta_{j2} + \tilde{\delta}_{\alpha 3} \delta_{i3} \delta_{j3} + \frac{c}{2} \left(\tilde{\delta}_{\alpha 4} (\delta_{i2} \delta_{j3} + \delta_{i3} \delta_{j2}) + \tilde{\delta}_{\alpha 5} (\delta_{i1} \delta_{j3} + \delta_{i3} \delta_{j1}) \right) \\ &\quad + \frac{c}{2} \tilde{\delta}_{\alpha 6} (\delta_{i1} \delta_{j2} + \delta_{i2} \delta_{j1}). \end{aligned} \quad (\text{C.4})$$

Analogously for the inverse \mathfrak{M}^{-1} :

$$\begin{aligned} \mathfrak{M}_{ij\alpha}^{-1} = & \tilde{\delta}_{\alpha 1} \delta_{i1} \delta_{j1} + \tilde{\delta}_{\alpha 2} \delta_{i2} \delta_{j2} + \tilde{\delta}_{\alpha 3} \delta_{i3} \delta_{j3} + \frac{1}{c} \left(\tilde{\delta}_{\alpha 4} (\delta_{i2} \delta_{j3} + \delta_{i3} \delta_{j2}) + \tilde{\delta}_{\alpha 5} (\delta_{i1} \delta_{j3} + \delta_{i3} \delta_{j1}) \right) \\ & + \frac{1}{c} \tilde{\delta}_{\alpha 6} (\delta_{i1} \delta_{j2} + \delta_{i2} \delta_{j1}). \end{aligned} \quad (\text{C.5})$$

We can check that the application of the linear mapping \mathfrak{M} to a symmetric second order tensor s_{ij} results in a vector in \mathbb{R}^6 whose first three components are the elements s_{11} , s_{22} and s_{33} , while its last three components are $c s_{23}$, $c s_{13}$ and $c s_{12}$ respectively. This is in accordance to classically used notation as in equation (III.35).

C.2 Non reduction for the standard Mindlin-Eringen model

In this section, we show that the considerations, which allowed the derivation of the macroscopic consistency conditions for the relaxed micromorphic model, cannot be repeated for the classical Mindlin Eringen model, which does not provide a transparent connection of the micro and meso elastic tensors to the macroscopic properties of the medium.

The elastic energy of the general anisotropic micromorphic model in the sense of Mindlin-Eringen is:

$$W = \underbrace{\frac{1}{2} \langle \bar{\mathbb{C}}_e (\nabla u - P), (\nabla u - P) \rangle}_{\text{anisotropic elastic - energy}} + \underbrace{\frac{1}{2} \langle \mathbb{C}_m \text{sym } P, \text{sym } P \rangle}_{\text{micro - self - energy}} + \underbrace{\frac{\mu L_c^2}{2} \|\nabla P\|^2}_{\text{curvature}}. \quad (\text{C.6})$$

The same expression in index notation is:

$$W = \frac{1}{2} (\bar{\mathbb{C}}_e)_{ijkl} (\nabla u - P)_{ij} (\nabla u - P)_{kl} + \frac{1}{2} (\mathbb{C}_m)_{ijkl} (\text{sym } P)_{ij} (\text{sym } P)_{kl} + \frac{\mu L_c^2}{2} P_{ij,k} P_{ij,k}. \quad (\text{C.7})$$

Here, we have discarded $\bar{\mathbb{E}}_{\text{cross}}$ for simplicity. Note that the coupling of skew-symmetric terms is now also contained in $\bar{\mathbb{C}}_e$ in some hidden way, instead of being explicitly present as in \mathbb{C}_c and our relaxed model. The static equilibrium equations are:

$$\begin{aligned} \text{Div} [\bar{\mathbb{C}}_e (\nabla u - P)] &= 0, \\ -\bar{\mathbb{C}}_e (\nabla u - P) + \mathbb{C}_m \text{sym } P + \mu L_c^2 \text{Div} [\nabla P] &= 0. \end{aligned} \quad (\text{C.8})$$

These can be equivalently written as:

$$\begin{aligned} \left((\bar{\mathbb{C}}_e)_{ijkl} (\nabla u - P)_{kl} \right)_{,j} &= 0, \\ -(\bar{\mathbb{C}}_e)_{ijkl} (\nabla u - P)_{kl} + (\mathbb{C}_m)_{ijkl} (\text{sym } P)_{kl} + \mu L_c^2 P_{ij,kk} &= 0. \end{aligned} \quad (\text{C.9})$$

Here we can define the elastic (relative) stress in such a way that it depends bijectively on the non-symmetric elastic distortion $e = \nabla u - P$ since $\bar{\mathbb{C}}_e$ is assumed to be uniformly positive definite:

$$\tilde{\sigma} (\nabla u, P) = \bar{\mathbb{C}}_e (\nabla u - P), \quad \tilde{\sigma}_{ij} (\nabla u, P) = (\bar{\mathbb{C}}_e)_{ijkl} (\nabla u - P)_{kl}. \quad (\text{C.10})$$

We can write in this model:

$$\nabla u - P = \bar{\mathbb{C}}_e^{-1} \tilde{\sigma}, \quad (\text{C.11})$$

where $\bar{\mathbb{C}}_e^{-1}$ is the Mindlin-Eringen elastic micromorphic compliance tensor.

In order to find the corresponding macroscopic tensor, we have to write the micromorphic elastic (relative) stress as a function of only ∇u .

Considering very large samples of the anisotropic structure amounts to letting L_c , the characteristic length, tend to zero. As a consequence of $L_c = 0$, the second equilibrium equation in (C.8) loses the $\text{Div} \nabla P$ -term and turns into an algebraic side-condition connecting P and ∇u via:

$$\bar{\mathbb{C}}_e (\nabla u - P) = \mathbb{C}_m \text{sym } P. \quad (\text{C.12})$$

Or, again in index notation:

$$(\overline{\mathbb{C}}_e)_{ijkl} (\nabla u - P)_{kl} = (\mathbb{C}_m)_{ijkl} (\text{sym } P)_{kl}. \quad (\text{C.13})$$

From this equation we obtain:

$$\begin{aligned} \mathbb{C}_m \text{sym } P &= \overline{\mathbb{C}}_e \text{sym} (\nabla u - P) + \overline{\mathbb{C}}_e \text{skew} (\nabla u - P) \\ &= \overline{\mathbb{C}}_e \text{sym } \nabla u - \overline{\mathbb{C}}_e \text{sym } P + \overline{\mathbb{C}}_e \text{skew} (\nabla u - P), \\ (\overline{\mathbb{C}}_e + \mathbb{C}_m) \text{sym } P &= \overline{\mathbb{C}}_e \text{sym } \nabla u + \overline{\mathbb{C}}_e \text{skew} (\nabla u - P) \\ \text{sym } P &= (\overline{\mathbb{C}}_e + \mathbb{C}_m)^{-1} \overline{\mathbb{C}}_e \text{sym } \nabla u + (\overline{\mathbb{C}}_e + \mathbb{C}_m)^{-1} \overline{\mathbb{C}}_e \text{skew} (\nabla u - P). \end{aligned} \quad (\text{C.14})$$

In index notation this becomes:

$$(\text{sym } P)_{ij} = (\overline{\mathbb{C}}_e + \mathbb{C}_m)_{ijkl}^{-1} (\overline{\mathbb{C}}_e)_{klmn} (\text{sym } \nabla u)_{mn} + (\overline{\mathbb{C}}_e + \mathbb{C}_m)_{ijkl}^{-1} (\overline{\mathbb{C}}_e)_{klmn} (\text{skew} (\nabla u - P))_{mn}. \quad (\text{C.15})$$

On the other hand, replacing (C.12) in (C.8)₁ yields:

$$\text{Div} [\mathbb{C}_m \text{sym } P] = 0. \quad (\text{C.16})$$

And again, by replacing this result in (C.14) we obtain:

$$\text{Div} \left[\mathbb{C}_m (\overline{\mathbb{C}}_e + \mathbb{C}_m)^{-1} \overline{\mathbb{C}}_e \text{sym } \nabla u + \mathbb{C}_m (\overline{\mathbb{C}}_e + \mathbb{C}_m)^{-1} \overline{\mathbb{C}}_e \text{skew} (\nabla u - P) \right] = 0. \quad (\text{C.17})$$

It is not possible to decouple this last equation due to the presence of the rotational coupling term $\text{skew} (\nabla u - P)$. Therefore, the only condition we can obtain is:

$$\mathbb{C}_m (\overline{\mathbb{C}}_e + \mathbb{C}_m)^{-1} \overline{\mathbb{C}}_e \text{sym } \nabla u + \mathbb{C}_m (\overline{\mathbb{C}}_e + \mathbb{C}_m)^{-1} \overline{\mathbb{C}}_e \text{skew} (\nabla u - P) = \mathbb{C}_M \text{sym } \nabla u, \quad (\text{C.18})$$

or, in index notation:

$$\begin{aligned} (\mathbb{C}_m)_{klmn} (\overline{\mathbb{C}}_e + \mathbb{C}_m)_{mnpq}^{-1} (\overline{\mathbb{C}}_e)_{pqij} (\text{sym } \nabla u)_{ij} + \\ + (\mathbb{C}_m)_{klmn} (\overline{\mathbb{C}}_e + \mathbb{C}_m)_{mnpq}^{-1} (\overline{\mathbb{C}}_e)_{pqij} (\text{skew} (\nabla u - P))_{ij} = (\mathbb{C}_M)_{klij} (\text{sym } \nabla u)_{ij}. \end{aligned} \quad (\text{C.19})$$

This has to hold for any $\text{sym } \nabla u$. Noting that $\mathbb{C}_M \text{sym } \nabla u \in \text{Sym}(3)$ and considering the symmetric part and the skew-symmetric part individually, we have

$$\left\{ \begin{array}{l} \text{sym} \left\{ \mathbb{C}_m (\overline{\mathbb{C}}_e + \mathbb{C}_m)^{-1} \overline{\mathbb{C}}_e \text{sym } \nabla u + \mathbb{C}_m (\overline{\mathbb{C}}_e + \mathbb{C}_m)^{-1} \overline{\mathbb{C}}_e \text{skew} (\nabla u - P) \right\} \\ \text{skew} \left\{ \mathbb{C}_m (\overline{\mathbb{C}}_e + \mathbb{C}_m)^{-1} \overline{\mathbb{C}}_e \text{sym } \nabla u + \mathbb{C}_m (\overline{\mathbb{C}}_e + \mathbb{C}_m)^{-1} \overline{\mathbb{C}}_e \text{skew} (\nabla u - P) \right\} = 0. \end{array} \right. = \mathbb{C}_M \text{sym } \nabla u, \quad (\text{C.20})$$

Similarly, in index notation we obtain:

$$\left\{ \begin{array}{l} \text{sym} \left\{ (\mathbb{C}_m)_{klmn} (\overline{\mathbb{C}}_e + \mathbb{C}_m)_{mnpq}^{-1} (\overline{\mathbb{C}}_e)_{pqij} \left((\text{sym } \nabla u)_{ij} + (\text{skew} (\nabla u - P))_{ij} \right) \right\} \\ \text{skew} \left\{ (\mathbb{C}_m)_{klmn} (\overline{\mathbb{C}}_e + \mathbb{C}_m)_{mnpq}^{-1} (\overline{\mathbb{C}}_e)_{pqij} \left((\text{sym } \nabla u)_{ij} + (\text{skew} (\nabla u - P))_{ij} \right) \right\} = 0. \end{array} \right. = (\mathbb{C}_M)_{klij} (\text{sym } \nabla u)_{ij}, \quad (\text{C.21})$$

A sufficient condition in order to obtain a decoupling of these equations (sym and skew) is exactly the reduced anisotropic format put forward in our relaxed model.

C.3 Some considerations about the anisotropic rotational coupling in the “relaxed micromorphic model”

Before understanding the general anisotropic character of the coupling tensor \mathbb{C}_c , we recall the transformation behavior of the energy expression in the isotropic case. An energy defined on second order tensors is isotropic if the transformation:

$$X \rightarrow Q^T \cdot X \cdot Q \quad \text{for } Q \in \text{SO}(3), \quad (\text{C.22})$$

does not affect the value of the energy. More precisely, we say that a local energy contribution acting on second order tensors is isotropic if

$$W(X) = W(Q^T \cdot X \cdot Q). \quad (\text{C.23})$$

Given a second order tensor which is subjected to the transformation (C.22), it is clear that its skew-symmetric part transforms as follows:

$$\text{skew}(X) \rightarrow \text{skew}(Q^T \cdot X \cdot Q) = Q^T \cdot \text{skew}(X) \cdot Q \quad \text{for } Q \in \text{SO}(3), \quad (\text{C.24})$$

and the corresponding axial vector of $\text{skew}(X)$ satisfies the transformation law:

$$\text{axl}(\text{skew}(X)) \rightarrow \text{axl}(\text{skew}(Q^T \cdot X \cdot Q)) = \text{axl}(Q^T \cdot \text{skew}(X) \cdot Q) = Q \cdot \text{axl}(\text{skew}(X)), \quad (\text{C.25})$$

see [161, 162]. Based on these transformation laws, we may investigate the anisotropy of the rotational coupling with the representation in terms of the second order tensor $\tilde{\mathbb{C}}_c$. Indeed, for the isotropy of an energy of the type $W(\text{skew}X)$ we require the invariance:

$$\forall Q \in \text{SO}(3): \quad \langle \mathbb{C}_c \text{skew}(X), \text{skew}(X) \rangle_{\mathbb{R}^{3 \times 3}} = \langle \mathbb{C}_c \text{skew}(Q^T \cdot X \cdot Q), \text{skew}(Q^T \cdot X \cdot Q) \rangle_{\mathbb{R}^{3 \times 3}}, \quad (\text{C.26})$$

which, using (III.44) and (C.25), is also equivalent to:

$$\begin{aligned} \forall Q \in \text{SO}(3): \quad & \langle \tilde{\mathbb{C}}_c \cdot \text{axl}(\text{skew}(X)), \text{axl}(\text{skew}(X)) \rangle_{\mathbb{R}^3} \\ & = \langle \tilde{\mathbb{C}}_c \cdot \text{axl}(\text{skew}(Q^T \cdot X \cdot Q)), \text{axl}(\text{skew}(Q^T \cdot X \cdot Q)) \rangle_{\mathbb{R}^3} \\ & = \langle \tilde{\mathbb{C}}_c \cdot Q \cdot \text{axl}(\text{skew}(X)), Q \cdot \text{axl}(\text{skew}(X)) \rangle_{\mathbb{R}^3}. \end{aligned} \quad (\text{C.27})$$

If we now set $\eta = \text{axl}(\text{skew}(X))$, the latter is equivalent to:

$$\forall Q \in \text{SO}(3): \quad \langle \tilde{\mathbb{C}}_c \cdot \eta, \eta \rangle_{\mathbb{R}^3} = \langle \tilde{\mathbb{C}}_c \cdot Q \cdot \eta, Q \cdot \eta \rangle_{\mathbb{R}^3} = \langle Q^T \cdot \tilde{\mathbb{C}}_c \cdot Q \cdot \eta, \eta \rangle_{\mathbb{R}^3}, \quad (\text{C.28})$$

where the transformation laws for the axl -operator given in (C.25) has been used. Since (C.28) must hold for all vectors $\eta \in \mathbb{R}^3$ we obtain:

$$\tilde{\mathbb{C}}_c = Q^T \cdot \tilde{\mathbb{C}}_c \cdot Q \quad \forall Q \in \text{SO}(3). \quad (\text{C.29})$$

Recalling that $Q \in \text{SO}(3)$ implies $Q^T = Q^{-1}$, it can be inferred that this last equation is satisfied if and only if:

$$\tilde{\mathbb{C}}_c = \frac{\mu_c}{2} \mathbf{1}, \quad \mu_c \geq 0, \quad (\text{C.30})$$

which is the expression of $\tilde{\mathbb{C}}_c$ for the isotropic case in which μ_c is called the *Cosserat couple modulus* [44]. Let us first state again that the relaxed micromorphic model is fully functional even without using \mathbb{C}_c at all. However, our experience in the isotropic case, in which \mathbb{C}_c reduces to the Cosserat couple modulus μ_c , has shown that in order to describe complete frequency band gaps, one should take $\mu_c > 0$. In the anisotropic case this would translate to requiring that \mathbb{C}_c is positive definite.

A method to reduce any given anisotropic rotational coupling to the isotropic case is, therefore, to simply project $\tilde{\mathbb{C}}_c^{\text{aniso}}$ to its isotropic part, given by the *arithmetic mean* of the eigenvalues of $\tilde{\mathbb{C}}_c^{\text{aniso}}$ (the Voigt bound):

$$\text{iso}_{\text{arithm}} \left(\tilde{\mathbb{C}}_c^{\text{aniso}} \right) := \frac{1}{3} \text{tr} \left(\tilde{\mathbb{C}}_c^{\text{aniso}} \right) \mathbf{1}. \quad (\text{C.31})$$

This defines a mapping $\text{iso}_{\text{arithm}} : \text{Sym}^+(3) \rightarrow \mathbb{R}^+ \mathbf{1}$. We note, however, that applying (C.31) has certain deficiencies, e.g. it is not stable under inversion:

$$\text{iso}_{\text{arithm}} \left(\left(\tilde{\mathbb{C}}_c^{\text{aniso}} \right)^{-1} \right) \neq \left[\text{iso}_{\text{arithm}} \left(\tilde{\mathbb{C}}_c^{\text{aniso}} \right) \right]^{-1}. \quad (\text{C.32})$$

Following the approach by Norris and Moakher [159], we can obtain the closest isotropic tensor to $\tilde{\mathbb{C}}_c^{\text{aniso}}$ with respect to a geodesic structure on $\text{Sym}^+(3)$. This will define a nonlinear operator $\text{iso}_{\text{geod}} : \text{Sym}^+(3) \rightarrow \mathbb{R}^+ \mathbf{1}$ such that:

$$\text{iso}_{\text{geod}} \left(\left(\tilde{\mathbb{C}}_c^{\text{aniso}} \right)^{-1} \right) = \left[\text{iso}_{\text{geod}} \left(\tilde{\mathbb{C}}_c^{\text{aniso}} \right) \right]^{-1}. \quad (\text{C.33})$$

This will be exemplified in a different contribution. In the meantime, we may alternatively propose a mapping $\text{iso}_{\text{log}} : \text{Sym}^+(3) \rightarrow \mathbb{R}^+ \mathbf{1}$ defined by:

$$\text{iso}_{\text{log}} \left(\tilde{\mathbb{C}}_c^{\text{aniso}} \right) := e^{\frac{1}{3} \text{tr}(\log(\tilde{\mathbb{C}}_c^{\text{aniso}}))} \mathbf{1} = e^{\frac{1}{3} \log(\det(\tilde{\mathbb{C}}_c^{\text{aniso}}))} \mathbf{1} = e^{\frac{1}{3} \log(\det(\tilde{\mathbb{C}}_c^{\text{aniso}}))} \mathbf{1} = \det \left(\tilde{\mathbb{C}}_c^{\text{aniso}} \right)^{\frac{1}{3}} \mathbf{1}. \quad (\text{C.34})$$

This is the *geometric mean* of the eigenvalues of $\tilde{\mathbb{C}}_c^{\text{aniso}}$. This mapping satisfies

$$\text{iso}_{\text{log}} \left(\left(\tilde{\mathbb{C}}_c^{\text{aniso}} \right)^{-1} \right) = \left[\text{iso}_{\text{log}} \left(\tilde{\mathbb{C}}_c^{\text{aniso}} \right) \right]^{-1}. \quad (\text{C.35})$$

There is also another possibility. We define the harmonic isotropy projector by:

$$\text{iso}_{\text{harm}} \left(\tilde{\mathbb{C}}_c^{\text{aniso}} \right) := \left[\text{iso}_{\text{arithm}} \left(\left(\tilde{\mathbb{C}}_c^{\text{aniso}} \right)^{-1} \right) \right]^{-1}. \quad (\text{C.36})$$

This is the *harmonic mean* of the eigenvalues of $\tilde{\mathbb{C}}_c^{\text{aniso}}$ (the Reuss-bound [24]). All introduced mappings satisfy the projection property:

$$\text{iso}_{\text{arithm}} (\gamma^+ \mathbf{1}) = \text{iso}_{\text{geod}} (\gamma^+ \mathbf{1}) = \text{iso}_{\text{log}} (\gamma^+ \mathbf{1}) = \text{iso}_{\text{harm}} (\gamma^+ \mathbf{1}) = \gamma^+ \mathbf{1}. \quad (\text{C.37})$$

Let us discuss the differences between $\text{iso}_{\text{arithm}}$ and iso_{log} . Consider a sequence of $\tilde{\mathbb{C}}_c^{\text{aniso},k} \rightarrow \tilde{\mathbb{C}}_c^{\text{aniso},\infty}$ for $k \rightarrow \infty$, where $\tilde{\mathbb{C}}_c^{\text{aniso},\infty}$ is *not* positive definite, i.e. some eigenvalue is zero (and $\det \left(\tilde{\mathbb{C}}_c^{\text{aniso},\infty} \right) = 0$). Then:

$$\text{iso}_{\text{arithm}} \left(\tilde{\mathbb{C}}_c^{\text{aniso},k} \right) = \frac{1}{3} \text{tr} \left(\tilde{\mathbb{C}}_c^{\text{aniso},k} \right) \mathbf{1} \rightarrow \frac{1}{3} \text{tr} \left(\tilde{\mathbb{C}}_c^{\text{aniso},\infty} \right) \mathbf{1}, \quad (\text{C.38})$$

is positive definite. The mapping property is such that $\text{iso}_{\text{arithm}} : \text{Sym}^+(3) \rightarrow \mathbb{R}^+ \mathbf{1}$. In contrast, we observe that:

$$\text{iso}_{\text{log}} \left(\tilde{\mathbb{C}}_c^{\text{aniso},k} \right) = \left(\det \left(\tilde{\mathbb{C}}_c^{\text{aniso},k} \right) \right)^{\frac{1}{3}} \mathbf{1} \rightarrow 0_{\mathbb{R}^3 \times 3}. \quad (\text{C.39})$$

Therefore, iso_{log} determines a zero isotropic coupling when eigenvalues of $\tilde{\mathbb{C}}_c^{\text{aniso}}$ vanish. For example,

$$\tilde{\mathbb{C}}_c^{\text{aniso}} = \begin{pmatrix} a_1 & 0 & 0 \\ 0 & 0 & 0 \\ 0 & 0 & 0 \end{pmatrix}, \quad \text{iso}_{\text{arithm}} \left(\tilde{\mathbb{C}}_c^{\text{aniso}} \right) = \frac{a_1}{3}, \quad \text{iso}_{\text{log}} \left(\tilde{\mathbb{C}}_c^{\text{aniso}} \right) = 0_{\mathbb{R}^3 \times 3}. \quad (\text{C.40})$$

At the present stage of understanding, however, we do not have extra arguments for using an anisotropic rotational coupling instead of an isotropic one. When possible, an isotropic rotational coupling given by the Cosserat couple modulus μ_c should be preferred.

C.4 Properties of the macroscopic constitutive tensors

C.4.1 Symmetry

Let us first consider the direct relation:

$$\mathbb{C}_M = \mathbb{C}_m (\mathbb{C}_m + \mathbb{C}_e)^{-1} \mathbb{C}_e. \quad (\text{C.41})$$

The constitutive tensor \mathbb{C}_M is the result of a product of the type:

$$\mathbb{C}_M = A(A+B)^{-1}B, \quad (\text{C.42})$$

where A , B and, as a consequence $(A+B)$ are symmetric. In order to show the symmetry of \mathbb{C}_M let us suppose that $(A+B)$ is invertible and write accordingly:

$$(A+B)(A+B)^{-1}B = B. \quad (\text{C.43})$$

We can decompose the product by using the distributive property of the matrix product with respect to the sum:

$$A(A+B)^{-1}B + B(A+B)^{-1}B = B. \quad (\text{C.44})$$

Therefore:

$$A(A+B)^{-1}B = B - B(A+B)^{-1}B. \quad (\text{C.45})$$

So we have that $\mathbb{C}_M = A(A+B)^{-1}B$ is the difference of two symmetric matrices, since $B(A+B)^{-1}B$ is also symmetric.¹ For the inverse relation, we consider:

$$\mathbb{C}_e = \mathbb{C}_m (\mathbb{C}_m - \mathbb{C}_M)^{-1} \mathbb{C}_M. \quad (\text{C.46})$$

Similarly, we can derive its symmetry (as long as $(\mathbb{C}_m - \mathbb{C}_M)_{kl}^{-1}$ exists):

$$A(A-B)^{-1}B = B + B(A-B)^{-1}B. \quad (\text{C.47})$$

C.4.2 Positive definiteness

Let us now investigate the positive-definiteness of

$$\mathbb{C}_M = \mathbb{C}_m (\mathbb{C}_m + \mathbb{C}_e)^{-1} \mathbb{C}_e. \quad (\text{C.48})$$

If we assume \mathbb{C}_m and \mathbb{C}_e to be positive definite, it follows from the properties of positive definiteness, that their sum as well as the inverse of the sum will be positive definite. Note first that a product AB of positive definite matrices A and B has real, positive eigenvalues. This can be seen by considering the characteristic equation:

$$\det(AB - \lambda \mathbf{1}) = 0 \iff \det(A^{-1/2}[AB - \lambda \mathbf{1}]A^{1/2}) = 0 \iff \det(A^{1/2}BA^{1/2} - \lambda \mathbf{1}) = 0. \quad (\text{C.49})$$

Now, $A^{1/2}BA^{1/2}$ is positive definite since, setting $\eta := A^{1/2}\xi$, we have:

$$\begin{aligned} \langle A^{1/2}BA^{1/2}\xi, \xi \rangle &= \langle BA^{1/2}\xi, A^{1/2}\xi \rangle = \langle B\eta, \eta \rangle \geq \lambda_{\min}(B)\|\eta\|^2 = \lambda_{\min}(B)\|A^{1/2}\xi\|^2 \\ &= \lambda_{\min}(B)\langle A^{1/2}\xi, A^{1/2}\xi \rangle = \lambda_{\min}(B)\langle A\xi, \xi \rangle \geq \lambda_{\min}(B)\lambda_{\min}(A)\|\xi\|^2. \end{aligned} \quad (\text{C.50})$$

Therefore, the eigenvalues of AB are real and positive. In general, however, the symmetry of the product AB will be lost. In our case, nonetheless, we proved in subsection C.4.1 that \mathbb{C}_M is symmetric and, therefore, positive definite.

¹We note again that the inverse of a positive definite tensor, like $A+B = \mathbb{C}_m + \mathbb{C}_e$ has the same symmetry group structure as $\mathbb{C}_m + \mathbb{C}_e$ itself. This can be easily shown by directly looking at the definition of groups.

For the inverse relationship, we consider:

$$\mathbb{C}_e = \mathbb{C}_m (\mathbb{C}_m - \mathbb{C}_M)^{-1} \mathbb{C}_M. \quad (\text{C.51})$$

In this case, in order to obtain the positive definiteness of \mathbb{C}_e it is not enough to assume that \mathbb{C}_m and \mathbb{C}_M are positive definite. However, one sufficient condition to impose is that $\mathbb{C}_m - \mathbb{C}_M$ is also positive definite. This property can be thought of as a generalization of the condition found in the isotropic case in which:

smaller is stiffer

the macroscopic elastic response cannot be equal or stiffer than the microscopic response

$$\mu_m > \mu_M, \quad (2\mu_m + 3\lambda_m) > (2\mu_M + 3\lambda_M).$$

APPENDIX D

Appendix to part IV

D.1 Bulk wave propagation for the classical Cauchy medium

In this subsection we recall that the strain energy density W and the kinetic energy T for a classical Cauchy medium in the isotropic setting take the form

$$W = \mu \|\text{sym } \nabla u\|^2 + \frac{\lambda}{2} (\text{tr}(\text{sym } \nabla u))^2, \quad T = \frac{1}{2} \rho \|u_{,t}\|^2, \quad (\text{D.1})$$

where λ and μ are the classical Lamé parameters and u denotes the classical macroscopic displacement field.

The associated bulk equations of motion in strong form, obtained by a classical least action principle, take the usual form:

$$\begin{aligned} \rho u_{,tt} &= \text{Div } \sigma_M, & \forall x \in \Omega, & \quad (\text{D.2}) \\ f := \sigma_M \cdot n &= 0 \quad \text{or} \quad u = u_0, & \forall x \in \partial\Omega, & \end{aligned}$$

where n is the normal to the boundary $\partial\Omega$, and σ_M is the symmetric elastic stress tensor defined as:

$$\sigma_M(\nabla u) = 2\mu \text{sym } \nabla u + \lambda \text{tr}(\nabla u) \mathbf{1}. \quad (\text{D.3})$$

Considering the case of *plane waves*, we suppose that the space dependence of all introduced kinematic fields are limited to the component x_1 of x which is the direction of propagation of the wave. With this hypothesis, see [141], the equations of motion (D.2)₁ become

$$\underbrace{u_{1,tt} = \frac{\lambda + 2\mu}{\rho} u_{1,11}}_{\text{longitudinal}}, \quad \underbrace{u_{2,tt} = \frac{\mu}{\rho} u_{2,11}}_{\text{transverse 2}}, \quad \underbrace{u_{3,tt} = \frac{\mu}{\rho} u_{3,11}}_{\text{transverse 3}}. \quad (\text{D.4})$$

We now look for solutions of the dynamic problem (D.4) of the form

$$u(x, t) = \alpha e^{i(kx_1 - \omega t)}, \quad \alpha \in \mathbb{R}^3. \quad (\text{D.5})$$

Considering a wave traveling in an *infinite domain* no conditions on the boundary are to be imposed and, replacing the wave form expression (D.5) in the bulk equation (D.2), we can find the standard dispersion relations for Cauchy media (see also [141]) obtaining

$$\underbrace{\omega^2 = c_l^2 k^2}_{\text{longitudinal}}, \quad \underbrace{\omega^2 = c_t^2 k^2}_{\text{transverse 2}}, \quad \underbrace{\omega^2 = c_t^2 k^2}_{\text{transverse 3}}, \quad (\text{D.6})$$

where

$$c_l = \sqrt{\frac{\lambda + 2\mu}{\rho}}, \quad c_t = \sqrt{\frac{\mu}{\rho}}, \quad (\text{D.7})$$

are the characteristic speeds in classical Cauchy media of longitudinal and transverse waves, respectively. The dispersion relations can be traced in the plane (ω, k) , giving rise to the standard non-dispersive behavior for a classical Cauchy continuum (see [1, 37–39, 141]). Indeed it is easily seen that for Cauchy continua the relations (D.6) can be inverted:

$$\underbrace{k = \pm \frac{1}{c_l} \omega}_{\text{longitudinal}}, \quad \underbrace{k = \pm \frac{1}{c_t} \omega}_{\text{transverse 2}}, \quad \underbrace{k = \pm \frac{1}{c_t} \omega}_{\text{transverse 3}}. \quad (\text{D.8})$$

For classical linear elasticity with isotropic energy density and kinetic energy density:

$$W(\nabla u) = \mu_M \|\text{sym } \nabla u\|^2 + \frac{\lambda_M}{2} (\text{tr}(\nabla u))^2, \quad J = \frac{\rho}{2} \|u_{,t}\|^2. \quad (\text{D.9})$$

The positive definiteness of the energy is equivalent to:

$$\mu_M > 0, \quad 2\mu_M + 3\lambda_M > 0. \quad (\text{D.10})$$

It is easy to see that our homogenization formula (III.57) implies (D.10) under the condition of positive definiteness of the relaxed micromorphic model.

The dynamical formulation is obtained by defining a joint Hamiltonian and assuming stationary action. The dynamical equilibrium equations are:

$$\rho u_{,tt} = \text{Div} [2\mu_M \text{sym}(\nabla u) + \lambda_M \text{tr}(\nabla u) \mathbf{1}]. \quad (\text{D.11})$$

As before, in our study of wave propagation in micromorphic media we limit ourselves to the case of plane waves traveling in an infinite domain. We suppose that the space dependence of all introduced kinematic fields are limited to a direction defined by a unit vector $\tilde{\xi} \in \mathbb{R}^3$ which is the direction of propagation of the wave. Therefore, we look for solutions of (D.11) in the form:

$$u(x, t) = \hat{u} e^{i(k\langle \tilde{\xi}, x \rangle_{\mathbb{R}^3} - \omega t)}, \quad \hat{u} \in \mathbb{C}^3, \quad \|\tilde{\xi}\|^2 = 1. \quad (\text{D.12})$$

Since our formulation is isotropic, we can, without loss of generality, specify the direction $\tilde{\xi} = e_1$. Then $X = \langle e_1, x \rangle_{\mathbb{R}^3} = x_1$, and we obtain:

$$u(x, t) = \hat{u} e^{i(kX - \omega t)}, \quad \hat{u} \in \mathbb{C}^3. \quad (\text{D.13})$$

With this ansatz, we can write (D.11) as:

$$A_5(e_1, \omega, k) \cdot \hat{u} = 0 \iff (\mathcal{B}(e_1, k) - \omega^2 \mathbf{1}) \cdot \hat{u} = 0, \quad (\text{D.14})$$

where:

$$A_5(e_1, \omega, k) = \begin{pmatrix} \frac{2\mu_M + \lambda_M}{\rho} k^2 - \omega^2 & 0 & 0 \\ 0 & \frac{\mu_M}{\rho} k^2 - \omega^2 & 0 \\ 0 & 0 & \frac{\mu_M}{\rho} k^2 - \omega^2 \end{pmatrix}, \quad (\text{D.15})$$

$$\mathcal{B}(e_1, k) = \frac{k^2}{\rho} \begin{pmatrix} 2\mu_M + \lambda_M & 0 & 0 \\ 0 & \mu_M & 0 \\ 0 & 0 & \mu_M \end{pmatrix}. \quad (\text{D.16})$$

Here, we observe that $A_5(e_1, \omega, k)$ is already diagonal and real. Requesting real wave velocities means $\omega^2 \geq 0$. For $k \neq 0$, this leads to the classical so-called *strong ellipticity condition*:

$$\mu_M > 0, \quad 2\mu_M + \lambda_M > 0, \quad (\text{D.17})$$

which is implied by the positive definiteness of the energy (D.10).

In classical (linear or nonlinear) elasticity, the condition of real wave propagation (D.17) is equivalent to *strong ellipticity* and *rank-one convexity*. Indeed, rank-one convexity amounts to set $(\xi = k \hat{\xi}$ with $\|\xi\|^2 = 1)$:

$$\left. \frac{d^2}{dt^2} \right|_{t=0} W(\nabla u + t \hat{u} \otimes \xi) \geq 0 \iff \langle \mathbb{C}(\hat{u} \otimes \xi), \hat{u} \otimes \xi \rangle_{\mathbb{R}^{3 \times 3}} \geq 0, \quad (\text{D.18})$$

where \mathbb{C} is the fourth-order elasticity tensor. Condition (D.18) reads then:

$$0 \leq 2 \mu_M \|\text{sym}(\hat{u} \otimes \xi)\|^2 + \lambda_M (\text{tr}(\hat{u} \otimes \xi))^2 = \mu_M \|\hat{u}\|^2 \|\xi\|^2 + (\mu_M + \lambda_M) \langle \hat{u}, \xi \rangle_{\mathbb{R}^3}^2.$$

We may express (D.19) given $\xi \in \mathbb{R}^3$ as a quadratic form in $\hat{u} \in \mathbb{R}^3$, which results in:

$$\mu_M \|\hat{u}\|^2 \|\xi\|^2 + (\mu_M + \lambda_M) \langle \hat{u}, \xi \rangle_{\mathbb{R}^3}^2 = \langle \mathcal{D}(\xi) \hat{u}, \hat{u} \rangle_{\mathbb{R}^3}, \quad (\text{D.19})$$

where the components of the symmetric and real 3×3 matrix $\mathcal{D}(\xi)$ read

$$\mathcal{D}(\xi) = \begin{pmatrix} (2\mu_M + \lambda_M)\xi_1^2 + \mu_M(\xi_2^2 + \xi_3^2) & (\lambda_M + \mu_M)\xi_1 \xi_2 & \\ (\lambda_M + \mu_M)\xi_1 \xi_2 & (2\mu_M + \lambda_M)\xi_2^2 + \mu_M(\xi_1^2 + \xi_3^2) & \\ (\lambda_M + \mu_M)\xi_1 \xi_3 & (\lambda_M + \mu_M)\xi_1 \xi_2 (\lambda_M + \mu_M)\xi_1 \xi_3 & \\ (\lambda_M + \mu_M)\xi_2 \xi_3 & & \\ 2\mu_M + \lambda_M)\xi_3^2 + \mu_M(\xi_1^2 + \xi_2^2) & & \end{pmatrix}. \quad (\text{D.20})$$

The three principal invariants are independent of the direction ξ due to isotropy and are given by:

$$\begin{aligned} \text{tr}(\mathcal{D}(\xi)) &= \|\xi\|^2 (4\mu_M + \lambda_M) = k^2 (4\mu_M + \lambda_M), \\ \text{tr}(\text{Cof } \mathcal{D}(\xi)) &= \|\xi\|^4 \mu_M (5\mu_M + 2\lambda_M) = k^4 \mu_M (5\mu_M + 2\lambda_M), \\ \det(\mathcal{D}(\xi)) &= \|\xi\|^6 \mu_M^2 (2\mu_M + \lambda_M) = k^6 \mu_M^2 (2\mu_M + \lambda_M). \end{aligned} \quad (\text{D.21})$$

Since $\mathcal{D}(\xi)$ is real and symmetric, its eigenvalues are real. The eigenvalues of the matrix $\mathcal{D}(\xi)$ are $k^2(2\mu_M + \lambda_M)$ and $k^2\mu_M$ (of multiplicity 2) such that positivity at $k \neq 0$ is satisfied if and only if¹:

$$\mu_M > 0, \quad 2\mu_M + \lambda_M > 0, \quad (\text{D.22})$$

which are the usual strong ellipticity conditions. We note here that the latter calculations also show that $B(e_1) = \frac{1}{\rho} k^2 \mathcal{D}(e_1)$. Alternatively, one may directly write the so-called *acoustic tensor* $B(\xi) \in \mathbb{R}^{3 \times 3}$ by

$$B(\xi) \cdot \hat{u} := [\mathbb{C}(\hat{u} \otimes \xi)] \cdot \xi, \quad \forall \hat{u} \in \mathbb{R}^3, \quad (\text{D.23})$$

in indices we have $(B(\xi))_{ij} = \mathbb{C}_{ikjl} \hat{u}_k \hat{u}_l \neq \mathbb{C}(\xi \otimes \xi)$. With (D.23) we obtain²:

$$\begin{aligned} \langle \hat{u}, B(\xi) \cdot \hat{u} \rangle_{\mathbb{R}^3} &= \langle \underbrace{[\mathbb{C}(\hat{u} \otimes \xi)] \xi}_{=: \hat{B} \in \mathbb{R}^{3 \times 3}}, \hat{u} \rangle_{\mathbb{R}^3} = \langle \hat{B} \cdot \xi, \hat{u} \rangle_{\mathbb{R}^3} = \langle \hat{B} \cdot (\xi \otimes \hat{u}), \mathbf{1} \rangle_{\mathbb{R}^{3 \times 3}} = \langle \hat{B}, (\xi \otimes \hat{u})^T \rangle_{\mathbb{R}^{3 \times 3}} \\ &= \langle \hat{B}, \hat{u} \otimes \xi \rangle_{\mathbb{R}^{3 \times 3}} = \langle \mathbb{C}(\hat{u} \otimes \xi), \hat{u} \otimes \xi \rangle_{\mathbb{R}^{3 \times 3}}, \end{aligned} \quad (\text{D.24})$$

and we see that strong ellipticity $\langle \mathbb{C}(\hat{u} \otimes \xi), \hat{u} \otimes \xi \rangle_{\mathbb{R}^{3 \times 3}} > 0$ is equivalent to the positive definiteness of the acoustic tensor $B(\xi)$.

D.2 Bulk wave propagation for the linear Cosserat model

In the isotropic hyperelastic case the elastic energy density and the kinetic energy density of the Cosserat model read:

$$\begin{aligned} W &= \mu_M \|\text{sym } \nabla u\|^2 + \mu_c \|\text{skew}(\nabla u - A)\|^2 + \frac{\lambda_M}{2} (\text{tr}(\nabla u))^2 + \frac{\mu_M L_c^2}{2} \|\text{Curl} A\|^2, \\ J &= \frac{\rho}{2} \|u_{,t}\|^2 + \frac{\eta}{2} \|A_{,t}\|^2. \end{aligned} \quad (\text{D.25})$$

¹The eigenvalues of $\mathcal{D}(\xi)$ are independent of the propagation direction $\xi \in \mathbb{R}^3$ which makes sense for the isotropic formulation at hand.

²The term $[\mathbb{C}(\hat{u} \otimes \xi)] \cdot (\hat{u} \otimes \xi)$ that in index notation reads $\mathbb{C}_{ijkl} \hat{u}_k \xi_l \hat{u}_j \xi_m$, is different from $\mathbb{C}[(\hat{u} \otimes \xi) \cdot (\hat{u} \otimes \xi)]$, i.e. $\mathbb{C}_{ijkl} \hat{u}_k \xi_m \hat{u}_m \xi_l$.

Introducing the canonical identification of R^3 with $\mathfrak{so}(3)$, A can be expressed as a function of $a \in \mathbb{R}^3$ as:

$$A = \text{anti}(a) = \begin{pmatrix} 0 & -a_3 & a_2 \\ a_3 & 0 & -a_1 \\ -a_2 & a_1 & 0 \end{pmatrix}. \quad (\text{D.26})$$

Here, we assume for clarity a uni-constant curvature expression in terms of only $\|\text{Curl } A\|^2$. Strict positive definiteness of the potential energy is equivalent to the following simple relations for the introduced parameters

$$2\mu_M + 3\lambda_M > 0, \quad \mu_M > 0, \quad \mu_c > 0, \quad L_c > 0. \quad (\text{D.27})$$

The dynamical formulation is obtained defining a joint Hamiltonian and assuming stationary action. The dynamical equilibrium equations are:

$$\begin{aligned} \rho u_{,tt} &= \text{Div} [2\mu_M \text{sym}(\nabla u - A) + 2\mu_c \text{skew}(\nabla u - A) + \lambda_M \text{tr}(\nabla u - A) \mathbf{1}], \\ \eta A_{,tt} &= -\mu_M L_c^2 \text{skew}(\text{Curl } \text{Curl } A) + 2\mu_c \text{skew}(\nabla u - A), \end{aligned} \quad (\text{D.28})$$

see also [104, 105, 177, 178] for formulations in terms of axial vectors. Note that for zero Cosserat couple modulus $\mu_c = 0$ the coupling of the two fields (u, A) is absent, in opposition to the relaxed micromorphic model (Equation (IV.3)). Considering plane and stationary waves of amplitudes \hat{u} and \hat{a} , we can express this system as:

$$A_6(\omega, k) \cdot (\hat{u}_1 \quad \hat{a}_1)^T = 0, \quad A_7(\omega, k) \cdot (\hat{u}_2 \quad -\hat{a}_3)^T = 0, \quad A_7(\omega, k) \cdot (\hat{u}_3 \quad \hat{a}_2)^T = 0, \quad (\text{D.29})$$

where

$$A_6(\omega, k) = \begin{pmatrix} k^2(2\mu_M + \lambda_M)/\rho - \omega^2 & 0 \\ 0 & (2\mu_M L_c^2 k^2 + 2\mu_c)/\eta - \omega^2 \end{pmatrix}, \quad (\text{D.30})$$

$$A_7(\omega, k) = \begin{pmatrix} k^2(\mu_M + \mu_c)/\rho - \omega^2 & -2ik\mu_c/\rho \\ ik\mu_c/\eta & (k^2\mu_M L_c^2 + 4\mu_c)/(2\eta) - \omega^2 \end{pmatrix}. \quad (\text{D.31})$$

As done in the case of the relaxed micromorphic model, we can equivalently express the problem with $A_6(\omega, k)$ and the following symmetric matrix:

$$\bar{A}_7(k) = \text{diag}_7 \cdot A_7(\omega, k) \cdot \text{diag}_7^{-1} = \begin{pmatrix} k^2(\mu_M + \mu_c)/\rho - \omega^2 & \sqrt{2}k\mu_c/\sqrt{\rho\eta} \\ \sqrt{2}k\mu_c/\sqrt{\rho\eta} & (k^2\mu_M L_c^2 + 4\mu_c)/(2\eta) - \omega^2 \end{pmatrix}, \quad (\text{D.32})$$

where

$$\text{diag}_7 = \begin{pmatrix} \sqrt{\rho} & 0 \\ 0 & i\sqrt{2\eta} \end{pmatrix}. \quad (\text{D.33})$$

Since ω^2 appears only on the diagonal, the problem can be analogously expressed as the following eigenvalue-problems:

$$\det(B_6(k) - \omega^2 \mathbf{1}) = 0, \quad \det(B_7(k) - \omega^2 \mathbf{1}) = 0, \quad (\text{D.34})$$

where

$$B_6(k) = \begin{pmatrix} k^2(2\mu_M + \lambda_M)/\rho & 0 \\ 0 & (2\mu_M L_c^2 k^2 + 2\mu_c)/\eta^2 \end{pmatrix}, \quad (\text{D.35})$$

$$B_7(k) = \begin{pmatrix} k^2(\mu_M + \mu_c)/\rho & \sqrt{2}k\mu_c/\sqrt{\rho\eta} \\ \sqrt{2}k\mu_c/\sqrt{\rho\eta} & (k^2\mu_M L_c^2 + 4\mu_c)/(2\eta) \end{pmatrix}, \quad (\text{D.36})$$

are the blocks of the *acoustic tensor* B

$$B(k) = \begin{pmatrix} B_6 & 0 & 0 \\ 0 & B_7 & 0 \\ 0 & 0 & B_7 \end{pmatrix}. \quad (\text{D.37})$$

The eigenvalues of the matrix $B_6(k)$ are simply the elements of the diagonal, therefore we have:

$$\omega_{\text{acoustic, long}}(k) = k \sqrt{\frac{2\mu_M + \lambda_M}{\rho}}, \quad \omega_{\text{optic, long}}(k) = \sqrt{\frac{2\mu_M L_c^2 k^2 + 2\mu_c}{\eta}}, \quad (\text{D.38})$$

while for $B_7(k)$, we find:

$$\omega_{\text{acoustic, trans}}(k) = \sqrt{a(k) - \sqrt{a(k)^2 - b^2 k^2}}, \quad \omega_{\text{optic, trans}}(k) = \sqrt{a(k) + \sqrt{a(k)^2 - b^2 k^2}}, \quad (\text{D.39})$$

where we have set:

$$a(k) = \frac{4\mu_c + \mu_M L_c^2 k^2}{\eta} + 2 \frac{\mu_M + \mu_c}{\rho} k^2, \quad b^2 = 8 \frac{\mu_M (4\mu_c + k^2 L_c^2 (\mu_M + \mu_c))}{\rho \eta}. \quad (\text{D.40})$$

The acoustic branches are those curves $\omega = \omega(k)$ as solutions of (D.33) that satisfy $\omega(0) = 0$. We note here that the acoustic branches of the longitudinal and transverse dispersion curves have as tangent in $k = 0^3$

$$c_l = \frac{d\omega_{\text{acoustic, long}}(0)}{dk} = \sqrt{\frac{2\mu_M + \lambda_M}{\rho}}, \quad c_t = \frac{d\omega_{\text{acoustic, trans}}(0)}{dk} = \sqrt{\frac{\mu_M}{\rho}}, \quad (\text{D.41})$$

respectively. Moreover, the longitudinal acoustic branch is non-dispersive, i.e. a straight line with slope (D.41)₁. The matrix $B_6(k)$ is positive-definite for arbitrary $k \neq 0$ if:

$$2\mu_M + \lambda_M > 0, \quad \mu_M > 0, \quad \mu_c \geq 0, \quad (\text{D.42})$$

Using the Sylvester criterion, $B_7(k)$ is positive-definite if and only if the principal minors are positive, namely:

$$(B_7)_{11} = k^2 \frac{(\mu_M + \mu_c)}{\rho} > 0, \quad (\text{D.43})$$

$$\det(B_7) = \frac{k^2}{2\eta\rho} (4\mu_M \mu_c + k^2 \mu_M L_c^2 (\mu_M + \mu_c)) > 0,$$

from which we obtain the condition:

$$\mu_M + \mu_c > 0, \quad \mu_M > 0, \quad \mu_c \geq 0. \quad (\text{D.44})$$

Considering these two sets of conditions, we can state a *necessary* and *sufficient* condition for the positive definiteness of $B_6(k)$ and $B_7(k)$ and therefore of the acoustic tensor $B(k)$:

$$2\mu_M + \lambda_M > 0, \quad \mu_M > 0, \quad \mu_c \geq 0. \quad (\text{D.45})$$

which are implied by the positive-definiteness of the energy (D.27). Eringen [67, p.150] also obtains correctly (D.42) and (D.44) (in his notation $\mu_c = \kappa/2$, $\mu_M = \mu_{\text{Eringen}} + \kappa/2$).

In [4, 64] strong ellipticity for the Cosserat-micropolar model is defined and investigated. In this respect we note that ellipticity is connected to acceleration waves while our investigation concerns real wave velocities for planar waves. Similarly to [171] it is established in [4, 64] that strong ellipticity for the micropolar model holds if and only if (the uni-constant curvature case in our notation):

$$2\mu_M + \lambda_M > 0, \quad \mu_M + \mu_c > 0. \quad (\text{D.46})$$

We conclude that for micropolar material models, (and therefore also for micromorphic materials) strong ellipticity (D.46) is too weak to ensure real plane waves since it is implied by but does not imply (D.45). This fact seems to have been appreciated also in the study of the Cosserat model [20, 79, 82, 135, 162].

³To obtain the slopes in 0, we search for a solution of the type $\omega = ak$ and then evaluate the limit for $a \rightarrow 0$, see [50] for a thorough explanation in the relaxed micromorphic case.

D.3 Inequality relations between material parameters

The macroscopic consistency conditions are based on the harmonic mean of two numbers κ_e and κ_m (or μ_e and μ_m). If the two numbers are positive, it is easy to see that:

$$\kappa_M \leq \min(\kappa_e, \kappa_m). \quad (\text{D.47})$$

Here, we show that the same conclusion still holds if we merely assume that $\kappa_e + \kappa_m > 0$. This allows for either $\kappa_e < 0$ or $\kappa_m < 0$. Therefore, considering that $\kappa_e + \kappa_m > 0$, even if the energy is not strictly positive, we find:

$$\begin{aligned} \kappa_M &= \frac{\kappa_m \kappa_e}{\kappa_e + \kappa_m} = \frac{\kappa_m \kappa_e + \kappa_e^2 - \kappa_e^2}{\kappa_e + \kappa_m} = \kappa_e \frac{\kappa_m + \kappa_e}{\kappa_e + \kappa_m} - \frac{\kappa_e^2}{\kappa_e + \kappa_m} = \kappa_e \underbrace{- \frac{\kappa_e^2}{\kappa_e + \kappa_m}}_{\leq 0} \leq \kappa_e, \\ \kappa_M &= \frac{\kappa_m \kappa_e}{\kappa_e + \kappa_m} = \frac{\kappa_m \kappa_e + \kappa_m^2 - \kappa_m^2}{\kappa_e + \kappa_m} = \kappa_m \frac{\kappa_m + \kappa_e}{\kappa_e + \kappa_m} - \frac{\kappa_m^2}{\kappa_e + \kappa_m} = \kappa_m \underbrace{- \frac{\kappa_m^2}{\kappa_e + \kappa_m}}_{\leq 0} \leq \kappa_m. \end{aligned} \quad (\text{D.48})$$

Considering similarly $\mu_e + \mu_m > 0$, we obtain:

$$\begin{aligned} \mu_M &= \frac{\mu_m \mu_e}{\mu_e + \mu_m} = \frac{\mu_m \mu_e + \mu_e^2 - \mu_e^2}{\mu_e + \mu_m} = \mu_e \frac{\mu_m + \mu_e}{\mu_e + \mu_m} - \frac{\mu_e^2}{\mu_e + \mu_m} = \mu_e \underbrace{- \frac{\mu_e^2}{\mu_e + \mu_m}}_{\leq 0} \leq \mu_e, \\ \mu_M &= \frac{\mu_m \mu_e}{\mu_e + \mu_m} = \frac{\mu_m \mu_e + \mu_m^2 - \mu_m^2}{\mu_e + \mu_m} = \mu_m \frac{\mu_m + \mu_e}{\mu_e + \mu_m} - \frac{\mu_m^2}{\mu_e + \mu_m} = \mu_m \underbrace{- \frac{\mu_m^2}{\mu_e + \mu_m}}_{\leq 0} \leq \mu_m. \end{aligned} \quad (\text{D.49})$$

Therefore, if $\mu_e + \mu_m > 0$ and $\kappa_e + \kappa_m > 0$, the macroscopic parameters are less or equal than the respective microscopic parameters, namely:

$$\kappa_e \geq \kappa_M, \quad \kappa_m \geq \kappa_M, \quad \mu_e \geq \mu_M, \quad \mu_m \geq \mu_M, \quad (\text{D.50})$$

and we can show that:

$$\begin{aligned} 2\mu_e + \lambda_e &= \frac{1}{3}(4\mu_e + 3\kappa_e) \geq \frac{1}{3}(4\mu_M + 3\kappa_M) = 2\mu_M + \lambda_M > 0, \\ 2\mu_m + \lambda_m &= \frac{1}{3}(4\mu_m + 3\kappa_m) \geq \frac{1}{3}(4\mu_M + 3\kappa_M) = 2\mu_M + \lambda_M > 0, \\ (2\mu_e + \lambda_e) + (2\mu_m + \lambda_m) &\geq 2(2\mu_M + \lambda_M) > 0, \\ 4\mu_M + 3\kappa_e &\geq 4\mu_M + 3\kappa_M = 3(2\mu_M + \lambda_M) > 0. \end{aligned} \quad (\text{D.51})$$

Therefore, the set of inequalities (IV.52) is implied from the smaller set:

$$\boxed{\mu_e > 0, \quad \mu_m > 0, \quad \mu_c \geq 0, \quad \kappa_e + \kappa_m > 0, \quad 2\mu_M + \lambda_M > 0.} \quad (\text{D.52})$$

We note here that $3(2\mu_e + \lambda_e) \geq 4\mu_M + 3\kappa_e \geq 3(2\mu_M + \lambda_M)$ because:

$$3(2\mu_e + \lambda_e) = 4\mu_e + 3\kappa_e \geq 4\mu_M + 3\kappa_e \geq 4\mu_M + 3\kappa_M = 3(2\mu_M + \lambda_M). \quad (\text{D.53})$$

D.4 The 12×12 acoustic tensor for arbitrary direction

We suppose that the space dependence of all introduced kinematic fields is limited to a direction defined by a unit vector ξ which is the direction of propagation of the wave. Therefore, we look for solutions of:

$$\begin{aligned} \rho u_{,tt} &= \text{Div} [2\mu_e \text{sym}(\nabla u - P) + 2\mu_c \text{skew}(\nabla u - P) + \lambda_e \text{tr}(\nabla u - P) \mathbf{1}], \\ \eta P_{,tt} &= -\mu L_c^2 \text{Curl Curl } P + 2\mu_e \text{sym}(\nabla u - P) + 2\mu_c \text{skew}(\nabla u - P) \\ &\quad + \lambda_e \text{tr}(\nabla u - P) \mathbf{1} - [2\mu_m \text{sym} P + \lambda_m \text{tr}(P) \mathbf{1}], \end{aligned} \quad (\text{D.54})$$

in the form:

$$\begin{aligned} u(x, t) &= \widehat{u} \underbrace{e^{i(k\langle \xi, x \rangle_{\mathbb{R}^3} - \omega t)}}_{s(x, t) \in \mathbb{R}/\mathbb{C} \text{ scalar}}, & \widehat{u} &\in \mathbb{C}^3, & \|\xi\|^2 &= 1, & (D.55) \\ P(x, t) &= \widehat{P} \underbrace{e^{i(k\langle \xi, x \rangle_{\mathbb{R}^3} - \omega t)}}_{s(x, t) \in \mathbb{R}/\mathbb{C} \text{ scalar}}, & \widehat{P} &\in \mathbb{C}^{3 \times 3}, \end{aligned}$$

where \widehat{u} is the polarization vector and \widehat{P} is the polarization matrix. We start by remarking that for $A, B \in \mathbb{R}^{3 \times 3}$ we have that:

$$\text{Curl}(A \cdot B) = L_B(\nabla A) + A \cdot \text{Curl}(B), \quad (D.56)$$

where $L_B : \mathbb{R}^{27} \rightarrow \mathbb{R}^{3 \times 3}$ is a linear operator with constant coefficients defined by the appropriate product rule of differentiation. Therefore we obtain:

$$\text{Curl}(\widehat{P} s(x, t)) = \text{Curl}(\widehat{P} \cdot \mathbb{1} s(x, t)) = \widehat{P} \cdot \text{Curl}(\mathbb{1} s(x, t)), \quad (D.57)$$

where:

$$\text{Curl}(\mathbb{1} s(x, t)) = \begin{pmatrix} 0 & \partial_3 s(x, t) & \partial_2 s(x, t) \\ -\partial_3 s(x, t) & 0 & \partial_1 s(x, t) \\ \partial_2 s(x, t) & -\partial_1 s(x, t) & 0 \end{pmatrix} \in \mathfrak{so}(3). \quad (D.58)$$

The derivatives of $s(x, t)$ are:

$$\nabla_x s(x, t) = \begin{pmatrix} \partial_1 s(x, t) \\ \partial_2 s(x, t) \\ \partial_3 s(x, t) \end{pmatrix} = e^{i(k\langle \xi, x \rangle_{\mathbb{R}^3} - \omega t)} \begin{pmatrix} i k \xi_1 \\ i k \xi_2 \\ i k \xi_3 \end{pmatrix} = e^{i(k\langle \xi, x \rangle_{\mathbb{R}^3} - \omega t)} i k \xi = i k \xi s(x, t). \quad (D.59)$$

We note that:

$$\text{Curl}(s(x, t)\mathbb{1}) = \text{anti}(\nabla s(x, t)) = e^{i(k\langle \xi, x \rangle_{\mathbb{R}^3} - \omega t)} i k \text{anti}(\xi) = s(x, t) i k \text{anti}(\xi). \quad (D.60)$$

Therefore, the $\text{Curl Curl } P$ is:

$$\begin{aligned} \text{Curl Curl}(\widehat{P} s(x, t)) &= \text{Curl}(\underbrace{\widehat{P} \cdot \text{anti}(\xi)}_{\in \mathfrak{so}(3)} i k s(x, t)) = i k \text{Curl}([\widehat{P} \cdot \text{anti}(\xi)] \cdot \mathbb{1} s(x, t)) & (D.61) \\ &= i k \widehat{P} \cdot \text{anti}(\xi) \text{Curl}(\mathbb{1} s(x, t)) = i k i k \widehat{P} \cdot \text{anti}(\xi) \cdot \text{anti}(\xi) s(x, t) \\ &= -k^2 \widehat{P} \cdot \text{anti}(\xi) \cdot \text{anti}(\xi) e^{i(k\langle \xi, x \rangle_{\mathbb{R}^3} - \omega t)}. \end{aligned}$$

On the other hand, the second derivative of P with respect to time is:

$$P_{,tt} = \partial_t^2 (\widehat{P} e^{i(k\langle \xi, x \rangle_{\mathbb{R}^3} - \omega t)}) = -\omega^2 \widehat{P} e^{i(k\langle \xi, x \rangle_{\mathbb{R}^3} - \omega t)} = -\omega^2 \widehat{P} s(x, t). \quad (D.62)$$

Analogously for u , the gradient and the derivatives with respect to time is:

$$\nabla_x u = i k s(x, t) \widehat{u} \otimes \xi, \quad u_{,tt} = -\omega^2 \widehat{u} s(x, t). \quad (D.63)$$

The sym, skew and tr of $\nabla u - P$ can then be expressed as:

$$\begin{aligned} \text{sym}(\nabla u - P) &= \text{sym}(i k \widehat{u} \otimes \xi - \widehat{P}) s(x, t) = (i k \text{sym}(\widehat{u} \otimes \xi) - \text{sym} \widehat{P}) s(x, t), \\ \text{skew}(\nabla u - P) &= \text{skew}(i k \widehat{u} \otimes \xi - \widehat{P}) s(x, t) = (i k \text{skew}(\widehat{u} \otimes \xi) - \text{skew} \widehat{P}) s(x, t), & (D.64) \\ \text{tr}(\nabla u - P) &= \text{tr}(i k \widehat{u} \otimes \xi - \widehat{P}) s(x, t) = (i k \langle \widehat{u}, \xi \rangle_{\mathbb{R}^3} - \text{tr} \widehat{P}) s(x, t). \end{aligned}$$

Therefore, we have:

$$\begin{aligned}
\text{Div sym}(\nabla u - P) &= \text{Div} \left[(ik \text{sym}(\hat{u} \otimes \xi) - \text{sym} \hat{P}) s(x, t) \right] = (ik \text{sym}(\hat{u} \otimes \xi) - \text{sym} \hat{P}) \cdot \nabla_x s(x, t) \\
&= (ik \text{sym}(\hat{u} \otimes \xi) - \text{sym} \hat{P}) \cdot (ik \xi s(x, t)) = -(k^2 \text{sym}(\hat{u} \otimes \xi) \cdot \xi + ik \text{sym} \hat{P} \cdot \xi) s(x, t), \\
\text{Div skew}(\nabla u - P) &= \text{Div} \left[(ik \text{skew}(\hat{u} \otimes \xi) - \text{skew} \hat{P}) s(x, t) \right] = (ik \text{skew}(\hat{u} \otimes \xi) - \text{skew} \hat{P}) \cdot \nabla_x s(x, t) \\
&= (ik \text{skew}(\hat{u} \otimes \xi) - \text{skew} \hat{P}) \cdot (ik \xi s(x, t)) = -(k^2 \text{skew}(\hat{u} \otimes \xi) \cdot \xi + ik \text{skew} \hat{P} \cdot \xi) s(x, t), \\
\text{Div}(\text{tr}(\nabla u - P) \mathbf{1}) &= \text{Div} \left[\left((ik \langle \hat{u}, \xi \rangle_{\mathbb{R}^3} - \text{tr} \hat{P}) \mathbf{1} \right) s(x, t) \right] = (ik \langle \hat{u}, \xi \rangle_{\mathbb{R}^3} - \text{tr} \hat{P}) \mathbf{1} \cdot \nabla_x s(x, t) \\
&= (ik \langle \hat{u}, \xi \rangle_{\mathbb{R}^3} - \text{tr} \hat{P}) \mathbf{1} \cdot (ik \xi s(x, t)) = -(k^2 \langle \hat{u}, \xi \rangle_{\mathbb{R}^3} + ik \text{tr} \hat{P}) \xi s(x, t).
\end{aligned} \tag{D.65}$$

Here, we have considered that, given a generic $B \in \mathbb{R}^{3 \times 3}$ and a scalar $s(x, t)$, we have:

$$\text{Div}[B s(x, t)] = \underbrace{\text{Div}[B]}_{=0} s(x, t) + B \cdot \nabla_x s(x, t), \tag{D.66}$$

Combining all the formulas above and simplifying $s(x, t)$ everywhere, we can write (D.54) as:

$$\begin{aligned}
-\rho \omega^2 \hat{u} &= - \left[2\mu_e (k^2 \text{sym}(\hat{u} \otimes \xi) \cdot \xi + ik \text{sym} \hat{P} \cdot \xi) + 2\mu_c (k^2 \text{skew}(\hat{u} \otimes \xi) \cdot \xi + ik \text{skew} \hat{P} \cdot \xi) \right. \\
&\quad \left. + \lambda_e (k^2 \langle \hat{u}, \xi \rangle_{\mathbb{R}^3} + ik \text{tr} \hat{P}) \xi \right], \\
-\eta \omega^2 \hat{P} &= \mu L_c^2 k^2 \hat{P} \text{anti}(\xi) \cdot \text{anti}(\xi) + 2\mu_e (ik \text{sym}(\hat{u} \otimes \xi) - \text{sym} \hat{P}) + 2\mu_c (ik \text{skew}(\hat{u} \otimes \xi) - \text{skew} \hat{P}) \\
&\quad + \lambda_e (ik \langle \hat{u}, \xi \rangle_{\mathbb{R}^3} - \text{tr} \hat{P}) \mathbf{1} - \left[2\mu_m \text{sym} \hat{P} + \lambda_m \text{tr}(\hat{P}) \mathbf{1} \right],
\end{aligned} \tag{D.67}$$

or analogously:

$$\begin{aligned}
&-\rho \omega^2 \hat{u} + k^2 (2\mu_e \text{sym}(\hat{u} \otimes \xi) \cdot \xi + 2\mu_c \text{skew}(\hat{u} \otimes \xi) \cdot \xi + \lambda_e \langle \hat{u}, \xi \rangle_{\mathbb{R}^3} \xi) \\
&\quad + ik (2\mu_e \text{sym} \hat{P} \cdot \xi + 2\mu_c \text{skew} \hat{P} \cdot \xi + \lambda_e \text{tr} \hat{P} \xi) = 0, \\
&-\eta \omega^2 \hat{P} - \mu L_c^2 k^2 \hat{P} \text{anti}(\xi) \cdot \text{anti}(\xi) + 2(\mu_e + \mu_m) \text{sym} \hat{P} + 2\mu_c \text{skew} \hat{P} + (\lambda_e + \lambda_m) \text{tr}(\hat{P}) \mathbf{1} \\
&\quad - 2\mu_e ik \text{sym}(\hat{u} \otimes \xi) - 2\mu_c ik \text{skew}(\hat{u} \otimes \xi) - \lambda_e ik \langle \hat{u}, \xi \rangle_{\mathbb{R}^3} \mathbf{1} = 0.
\end{aligned} \tag{D.68}$$

For a given $\xi \in \mathbb{R}^3$, this is a linear system in $(\hat{u}, \hat{P}) \in \mathbb{C}^{12}$ which can be written in 12×12 matrix format as:

$$\begin{pmatrix} \tilde{A}(\xi, \omega, k) \end{pmatrix} \begin{pmatrix} \hat{u}_1 \\ \hat{u}_2 \\ \hat{u}_3 \\ \hat{P}_{11} \\ \hat{P}_{12} \\ \hat{P}_{13} \\ \hat{P}_{21} \\ \hat{P}_{22} \\ \hat{P}_{23} \\ \hat{P}_{31} \\ \hat{P}_{32} \\ \hat{P}_{33} \end{pmatrix} = 0, \quad \begin{pmatrix} \tilde{B}(\xi, k) - \omega^2 \mathbf{1} \end{pmatrix} \begin{pmatrix} \hat{u}_1 \\ \hat{u}_2 \\ \hat{u}_3 \\ \hat{P}_{11} \\ \hat{P}_{12} \\ \hat{P}_{13} \\ \hat{P}_{21} \\ \hat{P}_{22} \\ \hat{P}_{23} \\ \hat{P}_{31} \\ \hat{P}_{32} \\ \hat{P}_{33} \end{pmatrix} = \begin{pmatrix} 0 \\ 0 \\ 0 \\ 0 \\ 0 \\ 0 \\ 0 \\ 0 \\ 0 \\ 0 \\ 0 \\ 0 \end{pmatrix}. \tag{D.69}$$

Here, $\tilde{B}(\xi, k)$ is the 12×12 acoustic tensor. It is clear that even with the aid of up-to-date computer software, it is practically impossible to determine positive-definiteness of the 12×12 acoustic tensor \tilde{B} in dependence of the given material parameters. In the main body of our manuscript, we succeed by choosing immediately the propagation direction $\xi = e_1$ and by considering a set of new variables (IV.6). This allows us to obtain a certain pre-factorization of $\tilde{B}(e_1, k)$ in 3×3 blocks. Since the formulation is isotropic, choosing $\xi = e_1$ is no restriction, as argued before.



FOLIO ADMINISTRATIF

THESE DE L'UNIVERSITE DE LYON OPEREE AU SEIN DE L'INSA LYON

NOM : BARBAGALLO

DATE de SOUTENANCE : 19 Octobre 2017

Prénoms : Gabriele

TITRE : Modeling fibrous composite reinforcements and metamaterials: theoretical development and engineering applications

NATURE : Doctorat

Numéro d'ordre : 2017LYSEI098

Ecole doctorale : Mécanique, Energétique, Génie Civil, Acoustique (MEGA)

Spécialité : Mécanique des solides, des matériaux des structures et des surfaces

RESUME : L'utilisation systématique d'une théorie dite de Cauchy conduit souvent à des simplifications trop fortes de la réalité. En effet, certaines caractéristiques de la microstructure sont implicitement négligées dans ces approches. Des matériaux possèdent des microstructures à une échelle assez grande (micron, millimètre, centimètre), dont l'effet se répercute sur le comportement macroscopique. Le modèle de Cauchy est insuffisant pour décrire leur comportement global spécifique, lié par exemple à la concentration d'efforts ou de déformations, ou à des modes de déformations caractérisés par de forts gradients locaux induisant des comportements liés à ce qui se passe à des échelles plus petites.

Un des domaines d'application les plus prometteurs des théories de milieux continus enrichis concerne les renforts tissés de composites. Cette classe de matériaux est constituée par le tissage de mèche, dont les rigidités sont très différentes en traction et en cisaillement : les mèches sont très raides en traction mais l'angle entre deux mèches peut varier très facilement. Ce contraste très marqué des propriétés mécaniques de la mesostructure du matériau permet de décrire ses propriétés homogénéisées dans le cadre d'une théorie de deuxième gradient. La manifestation macroscopique de la mesostructure peut en effet jouer un rôle majeur lors de la mise en forme des renforts de composites.

Les modèles de Cauchy ne sont pas adaptés à la description de la réponse dynamique de certains matériaux microstructurés montrant des comportements dispersifs ou des band-gaps. Les théories de milieux continus enrichis sont de bonnes candidates pour modéliser les effets de la présence d'une microstructure. Elles peuvent également posséder des propriétés très particulières vis à vis de la propagation d'ondes, ce qui confère aux structures résultantes des solutions de choix comme écran ou absorbeur d'ondes qui peuvent être innovantes dans le domaine du contrôle des vibrations ou dans le domaine de la furtivité.

MOTS-CLÉS : milieux continus enrichis, modèle micromorphe détendu, théories de second gradient, renforts fibreux de composite, metamatériaux, band gaps, bias extension test, mise en forme, emboutissage.

Laboratoire (s) de recherche : Laboratoire de Mécanique des Contacts et des Solides
UMR CNRS 5514 - INSA de Lyon
20, avenue Albert Einstein
69621 Villeurbanne Cedex FRANCE

Directeurs de thèse: Fabrice MORESTIN
Angela MADEO

Président de jury :

Composition du jury : Philippe BOISSE
Bruno LOMBARD
Fabrice MORESTIN
Massimo CUOMO
Angela MADEO
Patrizio NEFF